BIELEFELD UNIVERSITY
FACULTY OF PHYSICS

DISSERTATION

Hadronic correlators from heavy to very light quarks

Spectral and transport properties from lattice QCD

Author:
Hauke Sören SANDMEYER

July 2, 2019

Contents

1. Introduction and motivation

One of the fundamental ingredients for all kinds of physics is the existence of different phases of matter, where the most commonly known ones are solid, liquid, gas and plasma. These different phases are connected via phase transitions, where small changes in a system variable, e.g. the temperature, lead to rapid changes of certain observables. Phase transitions are not only limited to phases of matter but are also found for other physical processes. For instance the two different phases of a spin system, that is the ferromagnetic phase and the paramagnetic phase, are connected by a phase transition. Important for many phase transitions is the concept of spontaneous symmetry breaking. This means that the theory that describes the system does not change under some kind of symmetry transformation, but the actual realization of the system is not invariant under the same transformation. For instance when water is cooled below the freezing point, the formed ice crystals are aligned along a certain direction and the rotational invariance of the corresponding Hamiltonian is broken. Comparably, the just mentioned ferromagnetic phase transition comes along with the breaking of the $\mathbf{Z}_2$ symmetry.

In the seventies, when the theory of sub-nuclear particles, the so-called Quantum Chromodynamics (QCD) describing the interaction between quarks and gluons, was just established, it was proposed that besides the four mentioned states of matter another state exists, where nuclear matter is dissolved and quarks and gluons become the relevant degrees of freedom without being confined into hadrons [1]. This state, the so-called quark gluon plasma (QGP), was expected to be found at very high temperatures or densities, and the corresponding symmetry was believed to be the flavor symmetry between the light quarks, the so called chiral symmetry. Indeed in 2005 growing evidence revealed the existence of the QGP in the heavy ion collisions at the Relativistic Heavy Ion Collider (RHIC) [2–5]. However, the details about the phase transition between hadronic matter and the quark gluon plasma are still open to intense research. For instance it was only shown recently that for small baryon density, the transition is actually given by a crossover [6, 7] instead of a true phase transition.

The main challenge when analyzing the QGP comes from the confinement of quarks. On the experimental side, it is very hard to produce a quark gluon plasma; indeed heavy ion collisions with very high collision energies are needed. The lifetime of the plasma is extremely short so that it is impossible to directly observe processes within the QGP. Instead most information relies on particles created at the chemical freeze-out, where the QGP has cooled so much that the quarks and gluons form hadrons again. What happens before can only be indirectly measured by investigating the particle spectrum and particle distribution or by analyzing electromagnetic probes produced in the whole evolution of the system. However, this requires additional knowledge about the processes in the QGP to correctly interpret the outcome.

On the theoretical side, the strong coupling of QCD makes perturbation theory difficult to apply as it relies on the assumption of approximately free particles. This is only the case at very high temperatures, where the temperature scale exceeds that of the underlying force and quarks are indeed asymptotically free.

Thus, many of the QCD results have to be calculated from other, first principle methods. Such a method is given by numerical solutions using so called lattice QCD. Lattice QCD, first introduced by K. G. Wilson in 1974 [8], discretizes space-time by introducing a four dimensional lattice in Euclidean space which serves as a UV-cutoff. Using Monte-Carlo techniques to simulate the medium, it is directly possible to extract information in the interesting, also experimentally accessible regime around the transition temperature. Nevertheless, lattice QCD also faces certain limitations. For instance due to the so called sign problem it is impossible to perform direct calculations at nonzero net baryon density. Moreover, lattice QCD lacks some of the symmetries that hold for the continuum. So called doublers prevent the realization of chiral symmetry on the lattice in most discretization schemes, while the number of quarks taking part in the interactions stays the same as in the continuum. Different discretization schemes exist to reduce these effects, but chiral symmetry may be fully restored only after an extrapolation to the continuum.

An important tool in the investigation of the QGP from lattice QCD are hadronic correlation functions, which are defined as the transition amplitude for a certain particle from one space-time point to another. As all kinds of different particles interact with the medium in a different way many properties of the QGP can be extracted by analyzing the corresponding correlators. On the theoretical side, correlators are connected to an integration over the so called spectral function. This is especially interesting as the spectral function related to the Euclidean correlator is the same as the one in Minkowski space and thus provides a possibility to calculate real time information from the lattice.

The spectral function contains all information about the modification of bound states in the medium, which is especially interesting for heavy quarkonium correlators, like charmonium or bottomonium correlators, as due to their heavy weight, they can only be created before the equilibration of the medium. However, they might dissolve in the medium and other, mixed flavor states are created. Thus, if a significant suppression of pure quarkonium states in heavy ion collisions compared to proton-proton events in the collider is found, this is a strong hint for the existence of a quark gluon plasma. This makes quarkonium states ideal probes to extract information from before the chemical freeze out. It is expected that tightly bound states survive longer compared to less strongly bound states [9]. This phenomenon is usually referred as sequential melting. Indeed, the suppression of quarkonium states [10–15] as well as sequential melting [16, 17] has been found at the two large heavy ion colliders RHIC and LHC. To interpret these data, information about the melting points of the corresponding heavy mesonic states needs to be known beforehand. Here, the extraction of the spectral function from lattice QCD provides a tool to find these points of deconfinement.

In addition to the information about modification of bound states, the spectral function of the vector channel of mesonic correlators also contains a so called transport peak which carries information about the transport properties of heavy quarks in the medium. Especially the heavy quark diffusion coefficient can be extracted from the spectral function. This coefficient is of particular interest as a non-zero elliptic flow of heavy quarkonia suggests that heavy quarkonia interact with the medium and adopt the collective momentum distribution [18–21]. Also here, the spectral function provides information from first principle calculations that may be used to understand experimental results by using transport coefficients as input to transport models.

Correlators corresponding to mesons consisting out of the lighter quarks may reveal information about the restoration of the chiral symmetry and the so called axial symmetry. These symmetries play a crucial role in the classification of the phase transition. While the chiral symmetry mixes different quark flavors, axial rotation only works on the different entries in Dirac-space. The mass term in the QCD action explicitly breaks the chiral symmetry and also the axial symmetry is broken by quantum effects. However, both symmetries are expected to be effectively restored at certain temperatures, which do not necessarily have to be the same. In fact, whether or not these two temperatures coincide in the massless (chiral) limit, determines to which universality class the chiral phase transition belongs. At this point, mesonic correlators serve as a tool to find the temperatures of the effective restoration of those symmetries. A restoration of the chiral symmetry will be reflected in the degeneracy of the axial vector and the vector channel, and a degeneracy of the pseudoscalar and the scalar channel reflects an effective restoration of the axial symmetry.

When it comes to the analysis of mesonic correlators, one problem is to perform corresponding fits to the correlator. This is especially the case when multiple states contribute to the correlator and one wants to extract the ground state mass of the corresponding meson. Higher states shift the results up or downward. Therefore, the standard procedure is to concentrate on the large distance region of the correlator, where higher states are suppressed. As this region is maximally noisy, lots of information are lost. Though, including higher states to the fit heavily destabilizes the fit itself.

Now, the goal of this thesis is to first develop a new fitting routine that can perform higher state fits without the need of intensively guessing fit parameters. This new fitting routine shall then be used to analyze different kinds of mesonic correlators. We will start with heavy quarkonium states on quenched lattices and use the results to perform a quark mass interpolation to match for perfect quark masses. After performing a continuum extrapolation on the level of the correlator, we compare the results to perturbative computations of the spectral function. We will then switch to dynamic QCD by using the action of highly improved staggered quarks (HISQ) and lower the quark mass until we reach the masses of the very light u- and d-quarks. Mainly focusing on screening masses, we search for the restoration temperatures of the chiral and the axial symmetry and also analyze the higher temperature region. To further investigate the phase transition in the chiral limit, we will use even lighter than physical quark masses in the end.

The structure of the thesis is as follows: In section 2, we give a brief introduction to the methods of lattice QCD. In section 3 we explicitly derive mesonic correlators and their connection to the spectral function. We also establish the connection to in medium modifications, transport properties and the different symmetries. The different methods being used to analyze the correlators are described in section 4. Here, we also develop the just mentioned new fitting routine and also describe a reliable method to perform continuum extrapolations. In section 5 we focus on the results from the heavy quarkonium correlators on quenched lattices. We proceed with correlators belonging to the lighter u, d-quarks and to the strange quark in section 6. Finally we conclude this thesis by summarizing the results and giving an outlook to future work in section 7.

2. Short introduction to Quantum Chromodynamics on the lattice

The sub-nuclear interaction, that means the interaction of quarks and gluons, is described by Quantum Chromodynamics (QCD). The whole theory of QCD is based on the definition of its Yang-Mills Lagrangian, that is

$$\mathcal{L} = \bar{\psi}\left(x\right)\left(i\gamma^{\mu}D_{\mu} - m\right)\psi\left(x\right) - \frac{1}{4}F^{i}_{\mu\nu}(x)F^{\mu\nu,i}(x), \tag{2.1}$$

where ψ is the vector of quark fields, $D_{\mu} = \partial_{\mu} - igT_{a}A^{a}_{\mu}$ is the covariant derivative, γ_{μ} are the Dirac matrices and $F_{\mu\nu}$ is the field strength tensor. As a direct solution of the corresponding equations of motion is inaccessible, one could think of a numerical approach to simulate the movement of quarks and gluons. However, due to the huge number of degrees of freedom, the computational power available is by far not enough to do so. Instead, one can only calculate expectation values of observables in statistical physics using a discretized space-time. This method is called lattice QCD and is heavily used in this thesis. In the following we will give a short introduction to lattice QCD. For more details see standard textbooks, e.g. [22–26].

2.1. Discretization of QCD

The key ingredient to statistical physics is the so called partition function which, for a general field theory with fields ϕ, may be defined using the path integral formulation:

$$\begin{aligned} Z(\beta) &= \mathrm{tr}\left(\mathrm{e}^{-\beta H}\right) \\ &= \int \mathcal{D}\phi \mathrm{e}^{-S_{E}(\phi,\beta)}, \end{aligned} \tag{2.2}$$

where β corresponds to the length of the imaginary, periodic time dimension and is given by the inverse temperature $\beta = 1/T$. Here, H is the Hamilton operator, $\mathcal{D}\phi$ is the path integral measure for our generalized fields and $S_{E}(\phi, \beta)$ is the Euclidean version of the corresponding action. Now, our task is to find the corresponding path integral for Quantum Chromodynamics. We start with a Wick rotation $-it \to \tau$ to find the Euclidean action corresponding to the Lagrangian in equation (2.1),

$$S_{E}(\bar{\psi}, \psi, \beta, m) = \int_{0}^{\beta} \mathrm{d}\tau \int \mathrm{d}\vec{x} \left\{ \bar{\psi}\left(x\right)\left(\gamma^{\mu}D_{\mu} + m\right)\psi\left(x\right) + \frac{1}{4}F^{i}_{\mu\nu}F^{\mu\nu,i} \right\}. \tag{2.3}$$

As a next step, we want to find a numerical, discrete approximation of the covariant derivative and the space-time integral. Therefore we introduce a 4d-lattice Λ defined as

$$\Lambda = \{n = \{n_{x}, n_{y}, n_{z}, n_{\sigma}\} | n_{i} \in \mathbb{N}_{0};\ n_{\sigma} \leq N_{\tau} - 1,\ n_{x}, n_{y}, n_{z} \leq N_{\sigma} - 1\}. \tag{2.4}$$

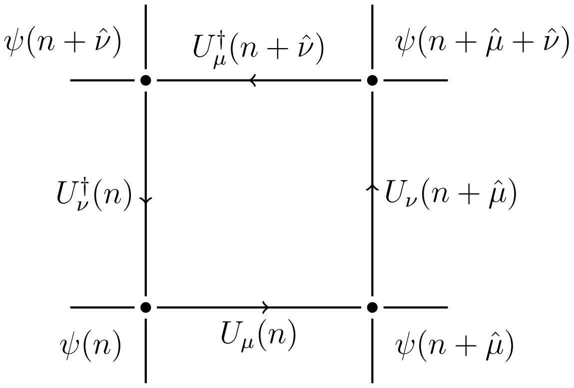

Figure 2.1: Visualization of the structure of the lattice. The product of the four shown link variables defines the plaquette $U_{\mu\nu}(n)$

Then, the connection to the continuum space-time point x is given by $x = an$, where a is the lattice spacing and carries the information of the physical scale. As a consequence, the temperature becomes a function of a with

$$T = \frac{1}{\beta} = \frac{1}{aN_\tau}. \tag{2.5}$$

Using a simple numerical approach to define the partial derivatives, we may now come up with a naive discretized version of the free fermionic part of the QCD action

$$S_F = a^4 \sum_{n\in\Lambda} \bar{\psi}(n) \left(\sum_{\mu=0}^{3} \gamma_\mu \frac{\psi(n+\hat{\mu}) - \psi(n-\hat{\mu})}{2a} + m\psi(n) \right), \tag{2.6}$$

where $\hat{\mu}$ is a unit vector pointing into the direction of μ. Now, in order to introduce quark interactions, we have to ensure gauge invariance under $SU(3)$ gauge transformations. This may be done introducing so called link variables defined as

$$U_\mu(n) = \mathrm{e}^{igaA_\mu(n)}. \tag{2.7}$$

which are, by definition, themselves members of the $SU(3)$ gauge group. These link variables sit in between the lattice points and connect two neighbouring quarks in direction of μ. See figure 2.1 for a visualization of the link variables and of the quark fields.

Putting everything together, we can now define a discretized version of the fermionic part of the QCD action

$$S_F = \sum_{n\in\Lambda} \bar{\psi}(n) \left(\sum_{\mu=0}^{3} \gamma_\mu \frac{U_\mu(n)\psi(n+\hat{\mu}) - U_\mu^\dagger(n-\hat{\mu})\psi(n-\hat{\mu})}{2} + m\psi(n) \right). \tag{2.8}$$

where we rescaled the fields with $a^{3/2}\psi(an) \to \psi(n)$ and the mass with $am \to m$. Note that we will use this notation from now on.

Taylor expanding the individual constituents, it is easy to see that this reproduces the continuum result up to order $\mathcal{O}(a)$.

To also discretize the gluonic part, we first have to define the so called plaquette as the product of four links in a closed loop

$$U_{\mu\nu}(n) = U_{\mu}(n)\, U_{\nu}(n+\hat{\mu})\, U_{\mu}^{\dagger}(n+\hat{\nu})\, U_{\nu}^{\dagger}(n)\,. \tag{2.9}$$

Then, we can write the gauge part as

$$S_G[U] = \beta \sum_{n\epsilon\Lambda} \sum_{\mu<\nu} \left(\mathbb{1} - \frac{1}{3} \operatorname{Re} \operatorname{tr}[U_{\mu\nu}(n)] \right), \tag{2.10}$$

with $\beta = 6/g^2$. Using the Baker-Campbell-Hausdorff formula, also here it easy to see that this gives the correct continuum result when performing $a \to 0$.

All in all, we have expressed the QCD action in terms of the fields U_μ, $\bar{\psi}$ and ψ and we can now define the path integral measure:

$$\int \mathcal{D}\bar{\psi}\mathcal{D}\psi \int \mathcal{D}U := \int \prod_{n\in\Lambda} \mathrm{d}\bar{\psi}(n)\mathrm{d}\psi(n) \int \prod_{n\in\Lambda} \prod_{\mu=0}^{3} \mathrm{d}U_{\mu}(n), \tag{2.11}$$

where $\mathrm{d}\psi(n)$ is the Grassmann integration measure and $\mathrm{d}U_\mu(n)$ is the Haar measure for $\mathrm{SU}(3)$ matrices. In fact, the Grassmann-valued fermionic part may be solved analytically, and we may express the partition function as a path integral over the link variables only:

$$\begin{aligned} Z &= \int \prod_f \mathcal{D}\bar{\psi}_f \mathcal{D}\psi_f \mathcal{D}U \mathrm{e}^{-S_F[U,\bar{\psi}_f,\psi_f,m_f]} \mathrm{e}^{-S_G[U]} \\ &= \int \mathcal{D}U \prod_f \det D[U,m_f] \mathrm{e}^{-S_G[U]}. \end{aligned} \tag{2.12}$$

Here, $D[U,m]$ is the so called Dirac matrix defined as the discrete version of the covariant derivative, that is

$$D_{nm}[U] = \sum_{\mu=0}^{3} \frac{U_\mu(n)\delta_{n,m-\hat{\mu}} - U_\mu^{\dagger}(n-\hat{\mu})\delta_{n,m+\mu}}{2} + m\delta_{nm}. \tag{2.13}$$

We have now found a way to calculate the partition function from a path integral over fermionic and gluonic fields. However, a direct computation of the partition function using this formulation is out of reach for current super computers. Instead, we may only compute expectation values of observables using importance sampling: In the scheme of the path integral formulation above, we can calculate expectation values of an observable $\mathcal{O}$ according to

$$\langle O \rangle = \frac{1}{Z} \int \prod_f \mathcal{D}\bar{\psi}_f \mathcal{D}\psi_f \mathcal{D}U \mathcal{O}[U,\bar{\psi}_f,\psi_f] \mathrm{e}^{-S_F[U,\bar{\psi}_f,\psi_f,m_f]} \mathrm{e}^{-S_G[U]} \tag{2.14}$$

For most observables, the Grassmann valued fermionic integrals are performed analytically using Wick's theorem, which again leads to the appearance of the fermion determinant,

$$\langle O\rangle = \frac{1}{Z}\int \mathcal{D}U\mathcal{O}_F[U]\mathrm{e}^{-S_G[U]}\prod_f \det D[U,m_f], \tag{2.15}$$

where $\mathcal{O}_\mathcal{F}$ is given by

$$\begin{aligned}\mathcal{O}_F &= \langle\mathcal{O}\rangle_F \\ &\equiv \frac{1}{Z_F[U]}\int\prod_f \mathcal{D}\bar{\psi}_f\mathcal{D}\psi_f\mathcal{O}[U,\bar{\psi}_f,\psi_f]\mathrm{e}^{-S_F[U,\bar{\psi}_f,\psi_f,m_f]}.\end{aligned} \tag{2.16}$$

At this point we may apply importance sampling to calculate the expectation value given in (2.14). The basic idea is to approximate the path integral using a finite set of so called gauge configurations C_i. Generally speaking, a gauge configuration defined as one possible realization of the gauge field in the path integral. If we distribute these gauge configurations according to the probability distribution

$$\mathrm{d}P[C] = \frac{\prod_f \det D[C,m_f]}{Z}\mathrm{e}^{-S_G[C]}\mathrm{d}C, \tag{2.17}$$

an approximation of the expectation value is given by

$$\langle\mathcal{O}\rangle \approx \frac{1}{N_\text{conf}}\sum_{i=1}^{N_\text{conf}} O[C_i], \tag{2.18}$$

where N_conf is the total number of gauge configurations.

Here, we can already notice one of the major challenges in lattice QCD: The Dirac matrix has dimension $|\Lambda| \times |\Lambda|$, and therefore, the computation of its determinant is computationally demanding. Even though computer power has increased in the past and new, more efficient algorithms have been developed, it is still impossible to perform lattice QCD including fermions with physical masses on lattices of sizes larger than $|\Lambda| \sim 100^4$.

Unfortunately, as we will see later, some observables indeed require lattices of such or even larger dimensions. Those observables may only be computed in the so called quenched approximation, where the fermionic part in the action is completely neglected. This corresponds to the infinite quark mass limit $m_f \to \infty$ or in other words implies $\det D[U,m_f] = 1$.

Physically speaking, the quenched approximation is equivalent to neglecting all kinds of quark loops that are not included in the gauge part of the action [24]. Even though this may seem rather drastic, the quenched approximation is still found to exhibit a phase transition of first order and is found to be suitable for qualitative studies [27]. For instance in the calculation of hadronic meson masses involving the strange and heavier quarks, the quenched approximation gives rise to only about 10% systematic error [28].

However, the generation of gauge configurations according to the probability distribution in equation (2.18) is not a trivial task. Among many different algorithms, a combination of overrelaxation [29, 30] and heatbath updates [31, 32] has been found to be most efficient for the quenched approximation, while for QCD including fermions the so called Hybrid Monte Carlo is widely used [33].

Due to the computation of observables using finite lattice sizes, and due to the finite number of configuration that enters importance sampling to approximate the true path integral, lattice calculations undergoes some uncertainties. At first place, it is directly clear that the approximation in equation (2.18) comes with a statistical error as we use only a finite set of configurations.

In addition to the statistical errors we also get systematic errors that arise from the finite lattice spacing. The above discrete version of the QCD action only reproduces the true continuum version for $a \to 0$. For finite a however, we still have higher order terms of a that do not vanish. This has two effects. First, the expectation values of observables come with an systematic error. Depending on the discretization scheme, this error usually scales with $\mathcal{O}(a)$ or $\mathcal{O}(a^2)$ and may be controlled by performing a continuum extrapolation: Based on results of the observable at different lattice spacings, one may extrapolate to $a \to 0$. A second error effects observables that are distributed among the lattice. For instance, many correlators are defined per time slice. For such observables, two neighbouring values undergo cut-off effects as the lattice version QCD action does not reflect the continuum at such scales.

Moreover, when choosing the size of the lattice, one has to make sure that uncertainties introduced by finite volume effects are controlled. For simulations around the transition temperature, we find an aspect ration of $N_\sigma/N_\tau \geq 4$ to be sufficient.

2.2. The Wilson action

While the derivation of the discretized QCD action in section 2.1 seems to be straightforward, it comes with one of the major problems in lattice QCD. Discretizating the Dirac operator in this way does not only introduce systematic errors, but it even changes the underlying physics! To see this we first have to look at discrete version of the free quark propagator, which is defined as

$$G(n) = \langle \bar{\psi}(n)\psi(0)\rangle_{\text{free}} \,, \tag{2.19}$$

where $\langle . \rangle_{\text{free}}$ denotes the fermionic expectation value for free quarks, that means all links set to $\mathbb{1}$.

After calculating the fermionic path integrals and after momentum projection, we find

$$\begin{aligned} \tilde{G}(p) &= \frac{1}{|\Lambda|}\sum_p \mathrm{e}^{ipn}\left(D^{-1}(n,0)\right) \\ &= \frac{m - i\sum_\mu \gamma_\mu \sin p_\mu}{m^2 + \sum_\mu \sin^2 p_\mu} \end{aligned} \tag{2.20}$$

For the limit $a \to 0$ with fixed $p_{\text{phys.}} = p_\mu/a$, this goes over to the correct continuum version with one pole at $p = 0$. Still, for finite a, 15 so called doublers arise, where $\omega(p) = \sum_\mu \sin^2(p_\mu) = m$. These additional poles correspond to extra particles with $E(p) = m$, where one or more entries of p are equal to π. For the free theory, these doublers might not be a problem, since they do not interact. But for an interacting theory, they simulate additional particles that do not exist in continuum.

To get rid of the doublers, the idea of Wilson fermions is to modify the discretized action in such a way that it still converges to the correct continuum result, but does not include doublers. One possibility is to add an extra term, that shifts the mass of the doubler to higher values. This extra term reads

$$\delta D_{n,m}[U] = -\sum_{\mu=0}^{3} \frac{U_\mu(n)\delta_{n+\hat{\mu},m} - 2\mathbb{1}\delta_{n,m} + U_{-\mu}(n)\delta_{n-\hat{\mu},m}}{2} \tag{2.21}$$

and vanishes linearly in a when performing the continuum limit. After rescaling the quark fields with $\psi(n) \leftarrow \sqrt{m+4}\psi(n)$, the total operator can now be written as

$$D_{nm}[U] = \delta_{n,m} - \kappa \sum_\mu \left((\mathbb{1} - \gamma_\mu) U_\mu(n) \delta_{n+\hat{\mu},m} + (\mathbb{1} + \gamma_\mu) U_\mu^\dagger(n-\hat{\mu}) \delta_{n-\hat{\mu},m} \right), \tag{2.22}$$

where the so called hopping parameter κ is given by

$$\kappa = \frac{1}{2m+8} \equiv \frac{1}{2}\left(\frac{1}{\kappa} - \frac{1}{\kappa_c}\right). \tag{2.23}$$

Here, κ_c is the so called critical hopping parameter which corresponds to the limit of massless quarks. In the free theory κ_c is obviously given by $\kappa_c = 1/8$. For interactions, however, this has to determined by tuning such that the resulting mass of the pion vanishes.

With these modifications, the free quark propagator becomes

$$\tilde{G}(p) = \frac{m(p) - i\sum_\mu \gamma_\mu \sin p_\mu}{m(p)^2 + \sum_\mu \sin^2 p_\mu} \tag{2.24}$$

where

$$m(p) = m + 2\sum_\mu \sin^2(p_\mu/2). \tag{2.25}$$

This explicitly shows that the unphysical poles are lifted to invalid values of the momentum, and therefore, the theory is free of doublers.

However, the so defined action still suffers from discretization errors of order $\mathcal{O}(a)$. In order to improve the this error, we have to add another term which may be chosen as [34]

$$\delta S = c_{sw} \sum_n \sum_{\mu<\nu} \bar{\psi}(n) \frac{1}{2} \sigma_{\mu\nu} \tilde{F}_{\mu\nu}(n) \psi(n), \tag{2.26}$$

where $\sigma_{\mu\nu} = [\gamma_\mu, \gamma_\nu]/(2i)$ and $\tilde{F}_{\mu\nu}$ is defined as

$$\tilde{F}_{\mu\nu} = -\frac{i}{8}(Q_{\mu\nu}(n) - Q_{\nu\mu}(n)) \tag{2.27}$$

with

$$Q_\mu = U_{\mu,\nu}(n) + U_{-\mu,-\nu}(n) + U_{\nu,-\mu}(n) + U_{-\nu,\mu}(n) \tag{2.28}$$

and $U_{\mu,\nu}(n)$ being the plaquette defined in equation (2.9). Due to the similar shape of a four leaf clover, this additional term is said to be as clover improved.

Here, the coefficient c_{sw}, also known as Sheikoleslami–Wohlert coefficient, has to be tuned according to the number of quarks involved. For a quenched theory where quarks only come as valance quarks, the coefficient has been determined both perturbatively [35] as well as non-perturbatively [36], where the latter results are summarized in an interpolating function given as

$$c_{sw}(g) = \frac{1 - 0.656g^2 - 0.152g^4 - 0.054g^6}{1 - 0.922g^2}, \tag{2.29}$$

where g is the bare coupling constant.

Despite its comparably high costs, one of the larger problems of the Wilson discretization scheme is the breaking of the so called symmetry. More about that in section 2.5.

2.3. The staggered discretization

In the above section we have introduced a possibility to remove the unphysical doublers from the discretized theory. However, we might also interpret this 16-fold degeneracy as additional degrees of flavor. Such a 16-flavor QCD is of course unphysical, so we have to reduce the number of flavors. One possibility to do so is the so called staggered action which reduces the number of degrees of freedom to 4 flavors. The further reduction to one or two-flavor QCD is then realized by taking roots of the staggered fermion determinant.

The basic idea of staggered fermions is to replace the quark fields using the following transformation:

$$\psi = \gamma_1^{n_1}\gamma_2^{n_2}\gamma_3^{n_3}\gamma_4^{n_4}\psi'(n)\,,\;\; \bar{\psi} = \bar{\psi}'(n)\,\gamma_4^{n_4}\gamma_3^{n_3}\gamma_2^{n_2}\gamma_1^{n_1}, \tag{2.30}$$

where the n_i correspond to the coordinates of the lattice points. When inserting the transformed spinors into the naive discretized fermion action in equation (2.8), we may interchange the gamma matrices, where each interchange produces a phase factor (-1), and we find

$$\bar{\psi}(n)\gamma_\mu\psi(n \pm \hat{\mu}) = \eta_\mu\bar{\psi}(n)'\mathbb{1}\psi(n \pm \hat{\mu}),' \tag{2.31}$$

where the so called staggered phases η_μ are given as

$$\eta_\mu = (-1)^{\sum_{\nu<\mu} n_\nu}. \tag{2.32}$$

Here, we notice that the action becomes diagonal in Dirac-space, which means each of the spinor entries carries the same information. In order to reduce the number of doublers, we drop three of the four components. Let us name these one dimensional quark fields $\chi(n)$. Then, the staggered fermionic action is given by

$$S_F = \sum_{n\epsilon\Lambda} \bar{\chi}\left(n\right) \left(\sum_{\mu=0}^{3} \eta_\mu\left(n\right) \frac{U_\mu\left(n\right)\chi\left(n+\hat{\mu}\right) - U_{-\mu}\left(n\right)\chi\left(n-\hat{\mu}\right)}{2} + m\chi\left(n\right) \right). \tag{2.33}$$

When dropping three of the four spinor components, the original Dirac–structure is hidden in the staggered phases only. However, these phases are also one-dimensional and therefore, cannot carry all the information of the original γ-matrices at each lattice point. Instead the information of the original Dirac structure is spread over lattice points and is now encoded within hypercubes of size 2^4. To see this, let us label the coordinates of each hypercube using $N = (\vec{N}, N_t)$[1]. We may now project back to the different spinor entries using

$$\psi^t_\alpha\left(N\right) = \frac{1}{8}\sum_\rho \Omega_{\alpha t,\rho}\chi\left(N+\rho\right), \tag{2.34}$$

where Ω is defined as

$$\Omega_{\alpha t,\rho} = (\gamma_1^{\rho_1}\gamma_2^{\rho_2}\gamma_3^{\rho_3}\gamma_4^{\rho_4})_{\alpha t} \tag{2.35}$$

and ρ is a sub-vector pointing to one of the corners of the hypercube.

However, we had to introduce the index t in order to capture the additional edges of the hypercube: There are 16 edges but the spin structure only exhibits four dimensions. Thus we have introduced another flavor-like component into the spinor. In analog to the flavor of quarks we name this structure taste.

Using this back-transformation, one finally gets for the total QCD action [24]

$$\begin{aligned} S_F =& 16\sum_N \left(\sum_{t=0}^{3} \left(m\bar{\psi}^t(N)\psi^t(N) + \sum_{\mu=0}^{3} \bar{\psi}^t(N)\gamma_\mu\nabla_\mu\psi^t(N) \right) \right. \\ & \left. - \sum_{t,t'=0}^{3}\sum_{\mu=0}^{3} \bar{\psi}^t(N)\gamma_5(\tau_5\tau_\mu)_{t,t'}(\nabla)^2_\mu\psi^{t'}(N) \right) \end{aligned} \tag{2.36}$$

with $\tau_\mu = \gamma_\mu^T$ and ∇_μ defining the discretized derivative on the lattice of hypercubes. The additional arising term removes the problem of fermion doublers and vanishes in the continuum limit. However, it also introduces a mixing of the different tastes, which is of course unphysical, and may be treated as a systematic error that has to be controlled for.

As a consequence of the taste structure, the staggered theory comes with four extra flavors by default. To get rid of them, we have to introduce rooting of the fermion determinant. For

---

[1] To distinguish the lattice dimension in time direction (N_τ) from the staggered hypercube coordinate N_t we use subscript t instead of τ, here.

instance, the path integral for a (2+1)-flavor QCD may be defined as

$$\langle O\rangle = \frac{1}{Z}\int \mathcal{D}U\mathcal{O}[U]\left(\det D[U,m_{u/d}]\right)^{1/2}\left(\det D[U,m_s]\right)^{1/4}\mathrm{e}^{-S_G[U]}. \tag{2.37}$$

In practice, this root is usually approximated using rational functions in the updating algorithm [37, 38].

Whether or not rooting of fermion determinant is allowed is controversial. Even though the extra term in the action vanishes in the continuum and the tastes decouple there, it is not yet clear whether the staggered action converges to the true continuum limit. See [23, 39] for further details. Nevertheless, the staggered action is found to give reasonable results and there is no evidence that the continuum limit does not reflect true physics. In any case, a reduction of the tastes mixing is to be preferred and may be realized by introducing extra terms into the staggered action. One way of doing so is to use so called "highly improved staggered quarks" (HISQ) [40]. Moreover, the HISQ action reduces the order of the discretization error to $O(a^2)$. A detailed description about the implementation of the HISQ action can be found in [41].

2.4. Connecting to physics

calculations In the last sections we have found a way to describe the theory of Quantum Chromodynamics using a lattice as regulator and we can now perform calculations on a computer. However, we are not yet fully prepared to extract physics from lattice QCD as we still have to find the connection between the dimensionless computations on a computer and real physics measured in units of GeV.

When constructing the formulation of lattice QCD, all direct occurrences of the lattice spacing a are absorbed into the definition of the involving fields or input constants. Therefore, the only parameters that are left to to tune the input to our actual computations are the bare coupling constant g via $\beta = 6/g^2$ and the bare quark masses m_q. However, the connection to the lattice spacing, which we initially introduced to discretize the theory, is lost and has to be regained from the measurement of physical quantities on the lattice.

Implicitly, the dependence on the lattice spacing a of an observable Γ_{lat} is hidden in a rescaling of the observable in powers of a. That means,

$$\Gamma_{\mathrm{lat}} = a^d\Gamma \Leftrightarrow \Gamma = a^{-d}\Gamma_{\mathrm{lat}}, \tag{2.38}$$

where d is the dimension of the observable. In order to find a continuum extrapolation for the physical observable, it becomes clear that the only input parameter g has to be function of the lattice spacing and has to be scaled accordingly. At the same time, the continuum value itself must not depend on a. This leads us to the so called renormalization group equation.

$$a\frac{\mathrm{d}}{\mathrm{d}a}\Gamma = \left(a\frac{\partial}{\partial a} - \beta(g)\frac{\partial}{\partial g}\right)\Gamma = 0, \tag{2.39}$$

where $\beta(g)$ is called beta function and is defined as

$$\beta(g) = -a\frac{\mathrm{d}g}{\mathrm{d}a}. \tag{2.40}$$

A general solution to the above differential equation is given by

$$\frac{a}{a_0} = \mathrm{e}^{\int_g^{g_0} \frac{1}{\beta(g')}\mathrm{d}g'}, \tag{2.41}$$

which justifies the arbitrarily seeming definition of the beta function as it relates the lattice spacing and the bare coupling. It also becomes clear that a continuum extrapolation $a \to 0$ only exists, if the beta function has a root.

For small a the beta function may be evaluated perturbatively and we get [42]

$$\begin{aligned} \beta(g) &= -\beta_0 g^3 - \beta_1 g^5 + \mathcal{O}(g^7), \\ \beta_0 &= \frac{1}{(4\pi)^2}\left(\frac{11}{3}N_c - \frac{2}{3}N_f\right), \\ \beta_1 &= \frac{1}{(4\pi)^4}\left(\frac{34}{3}N_c^2 - \frac{10}{3}N_f - \frac{N_c^2-1}{N_c}N_f\right). \end{aligned} \tag{2.42}$$

This implies that the continuum limit of lattice QCD is given by $g \to 0$ or equivalently $\beta \to \infty$.

However we still have to find another correspondence between β and a as the above perturbative results are only valid for small a and we also do not know the integration constant a_0. Such a connection can be established by comparing lattice results to physical observables for which experimental results exists. A detailed review which compares the different scales obtained from different quantities is given in reference [43].

A typical choice is the static quark potential which is defined as the non-relativistic potential between two heavy quarks and is precisely known from experiments. Its general structure is given by

$$V(r) = A + \frac{B}{r} + \sigma r, \tag{2.43}$$

where A and B are simple constants and σ is the so called string tension. Now, the so called Sommer scale r_0 is defined using the force $F(r) = dV(r)/dr$ and by requiring

$$r_0^2 F(r_0) = b + \sigma r_0^2 \overset{!}{=} 1.65. \tag{2.44}$$

From comparisons to Υ splittings, the corresponding Sommer scale in physical units has been determined to be $r_0 = 0.469(7)\,\mathrm{fm}$ [44].

On the lattice, the potential can be computed using Wilson loops and is a function of the lattice coordinates n. After interpolating the potential, we can also compute a value n_0 at which we have $F(n_0) = 1.65$. Then, the lattice constant a is set by $a = r_0/n_0$.

For quenched theory, the r_0 scale has been precisely determined and can summarized in the following interpolating formula [45, 46]:

$$\ln\left(\frac{r_0}{a}\right) = \left[\frac{\beta}{12b_0} + \frac{b_1}{2b_0^2}\ln\left(\frac{6b_0}{\beta}\right)\right]\frac{1+c_1/\beta+c_2/\beta^2}{1+c_3/\beta+c_4/\beta^2} \tag{2.45}$$

with $b_0 = 11/(4\pi)^2$, $b_1 = 102/(4\pi)^2$, $c_1 = -8.9664$, $c_2 = 19.21$, $c_3 = -5.25217$ and $c_4 = 0.606828$.

For dynamical QCD, one may choose the decay constant of the Kaon f_K as a quantity to set the scale. By comparing the physical value $f_K = 156.1 \pm 0.2 \pm 0.8 \pm 0.2$ [47] to the lattice observable af_K computed from two point correlation functions, one can define the set the so called f_K-scale.

For the staggered HISQ action this has been done in reference [48] for (2+1)-flavor QCD with a quark mass ratio $m_s/m_l = 20$. In this thesis, we have updated the interpolating coefficients using the additional data in given reference [49] using the following interpolation formula:

$$af_K = \frac{c_0 f(\beta) + c_2(10/\beta)f(\beta)^3}{1+d_2(10/\beta)f(\beta)^2}, \tag{2.46}$$

where $f(\beta)$ is inspired by the perturbative results inserted into equation (2.41) and is given by

$$f(\beta) = (\beta_0 10/\beta)^{-\beta_1/(2\beta_0^2)}\mathrm{e}^{-\beta/(20\beta_0)}. \tag{2.47}$$

After the fit we find the coefficients to be given by $c_0 = 7.49415$, $c_2 = 46049.0$ and $d_2 = 3671.0$. In figure 2.2 we compare the new and the old scale and find that only for large β-values there is a significant difference.

2.5. Chiral, $U_A(1)$ symmetry and the QCD phase transition

So far quarks have never been observed as quasi free particles directly. They only appear confined, as color neutral objects like mesons or baryons. However, it is known that this does not hold for extreme conditions at very high temperature or pressure. Under such conditions, quarks and gluons appear as free particles, forming the quark-gluon plasma. These two different phases are connected by a phase transition. See figure 2.3 for a visualization of the QCD phases and reference [50] for further details. Even though a direct relation is still open to be found, the phase transition between the confined and deconfined phases is probably related to the spontaneous breaking of the so called chiral symmetry [51, 52]. Nonetheless, this symmetry is not an exact symmetry of the QCD action as it is explicitly broken by the quark mass term. Still, one finds that in the limit of massless quarks, that means where the chiral symmetry becomes an exact symmetry, the classification of the phase transition is of crucial importance for the phase transition at physical quark masses [48, 50, 53–56]. In the following we first give an introduction to chiral symmetry and then draw the connection to the phase transition itself.

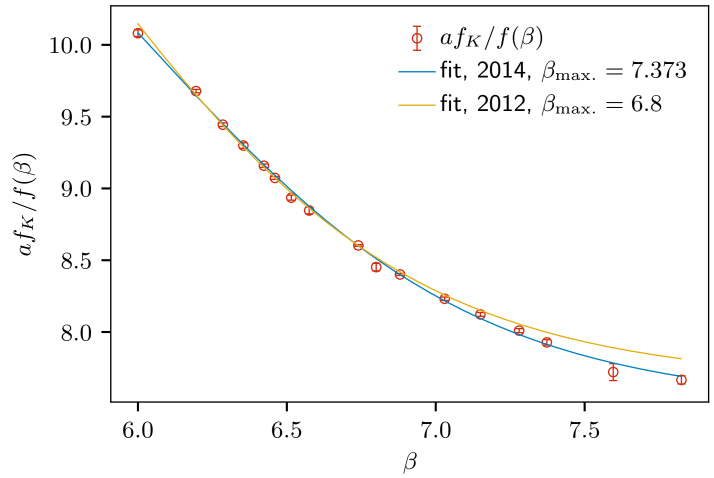

Figure 2.2: Comparison of the f_K scale from reference [48] (yellow) and with the new fit based on the data set in reference [49]

We start with the definition of the chiral projection operators

$$P_\pm = \frac{\mathbb{1} \pm \gamma_5}{2} \tag{2.48}$$

and then write $\psi = \psi_L + \psi_R$ with

$$\begin{aligned} \psi_R = P_+\psi,\ \psi_L = P_-\psi \\ \bar\psi_L = \bar\psi P_-,\ \bar\psi_L = \bar\psi P_+. \end{aligned} \tag{2.49}$$

When we put this into the total QCD action, we observe that all mixed terms cancel except those that are related to the quark mass. Thus, in the chiral limit we may decouple ψ_L and ψ_R and write

$$\mathcal{L} = \mathcal{L}_R + \mathcal{L}_L, \tag{2.50}$$

where $\mathcal{L}_R$ and $\mathcal{L}_L$ are defined as usual with $\psi_{L/R}$ instead of ψ.

Let us now extend the one-dimensional massless theory to a Lagrangian with N_f massless quarks. Then, we can perform a rotation in flavor space

$$\psi_{R,L} \to e^{iT^a\theta_{L,R}}\psi_{R,L}, \tag{2.51}$$

where $\theta_{L,R}$ is the vector of rotation angles and the T^a are the generators of the $SU(N_f)$-group. We find that the massless action is invariant under such mixing of the different flavors. Additionally, we may also find an invariance under

$$\psi \to e^{i\theta}\psi \tag{2.52}$$

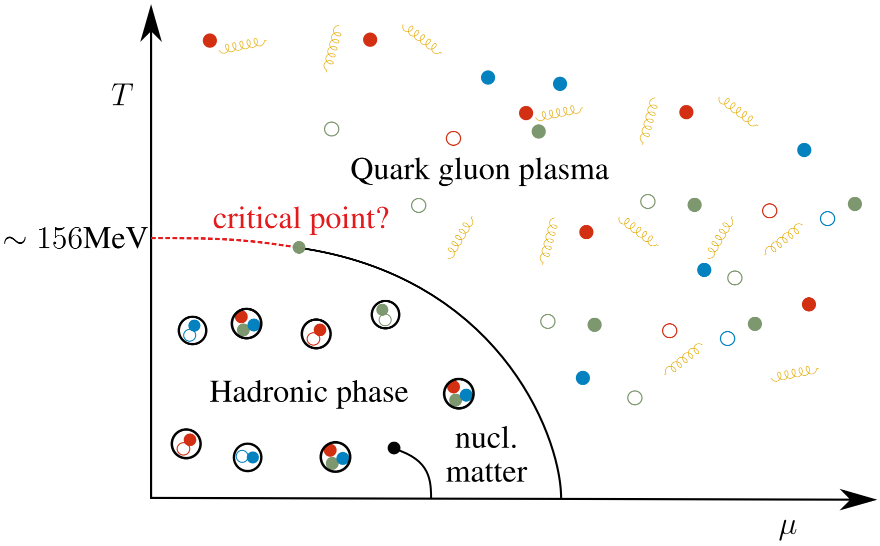

Figure 2.3: A sketch of the QCD phase diagram as a function of temperature and baryon chemical potential. The three phases of strongly interacting matter are classified as follows: For high temperatures and densities, quarks are asymptotically free and form, together with the force-carrying gluons, the quark-gluon plasma. At lower temperatures, quarks are confined in hadronic structures like mesons and baryons. Within this phase, there is another phase transition between the hadronic phase and nuclear matter. In the latter, remnants of the strong force keep different hadrons together, forming so called nuclear matter. This is the phase of matter where we actually live in. For low baryon density, the transition between the hadronic phase and the quark-gluon plasma is known to be an analytic crossover, visualized by the red dashed line. For higher densities the situation is unknown. In this sketch, a critical end point of a second order phase transition may exist (green). Beyond that, the phase transition is of 1st order (black line)

and

$$\psi \to e^{i\gamma_5\theta}\psi. \tag{2.53}$$

Putting everything together, we find that the massless N_f-flavor QCD Lagrangian is invariant under the following symmetry group:

$$SU(N_f)_L \otimes SU(N_f)_R \otimes U(1)_V \otimes U(1)_A. \tag{2.54}$$

This symmetry holds for a Lagrangian with degenerate massless quarks. Though, it does not hold for a fully quantized theory as the $U_A(1)$ is explicitly broken in the measure the of the path integral. This breaking is known as the axial anomaly [57, 58].

Further introducing a non-degenerate mass term into the QCD action, the total symmetry reduces to

$$\bigotimes_{i=1}^{N_f} U(1)_V, \tag{2.55}$$

whose corresponding conserved quantity is the baryon number.

Though chiral symmetry is explicitly broken by the mass term in the QCD action, it still has important consequences. Compared to the typical scale of QCD of $\sim 1\,\mathrm{GeV}$, the masses of the up and down quarks are small ($m_u = 2.3(7)\mathrm{MeV}$, $m_d = 4.8(5)\mathrm{MeV}$ in $\overline{\mathrm{MS}}$-scheme, $\mu = 2$ GeV [47]). Thus, remnants of a two-flavor chiral symmetry should still be visible in an approximate degeneracy of variables related to the chiral symmetry.

However, one finds that chiral symmetry is spontaneously broken for low temperatures. For example this manifests in the non-degeneracy of the proton mass ($\sim 940\,\mathrm{MeV}$) and the N^* mass ($\sim 1535\mathrm{MeV}$). In a chirally symmetric world, these two masses should be degenerate [24]. Also the very small mass of the Goldstone pion originates from the breaking of chiral symmetry.

Spontaneously broken symmetries are closely related to phase transitions. The phase transition associated with chiral symmetry is the already mentioned QCD phase transition from the hadronic phase to the quark-gluon plasma. The related order parameter is the chiral condensate, defined as

$$\langle\bar{\psi}_l\psi_l\rangle = \frac{T}{V}\frac{\partial \ln Z}{\partial m_l}, \tag{2.56}$$

where m_l refers to the mass of the light quarks. From its invariance under chiral rotations it is directly clear that it is only zero if chiral symmetry is restored. Likewise, we may also define the chiral susceptibility as

$$\chi_{m_l} = \frac{\partial}{\partial m_l}\left\langle\bar{\psi}_l\psi_l\right\rangle, \tag{2.57}$$

which has a peak in the vicinity of the transition temperature T_c.

The order of the phase transition in the chiral limit is still unknown. If it is of second order though, one may describe the behavior of observables near the transition temperature using universal scaling [59]. Universal scaling that means that quantities in different phase

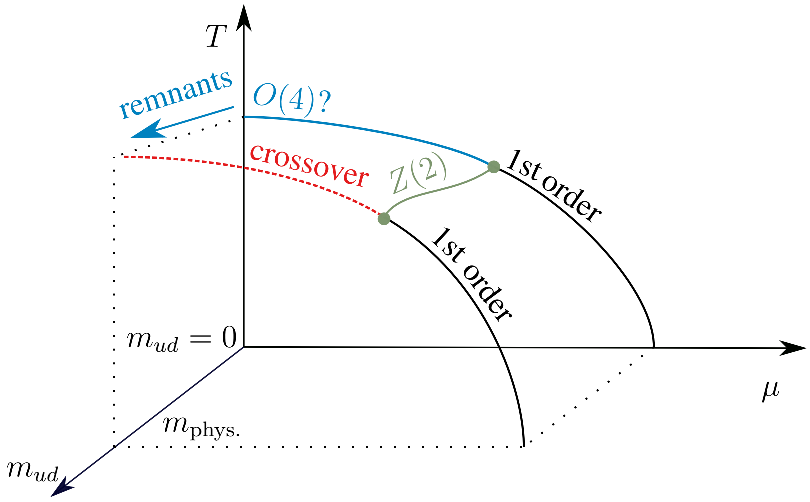

Figure 2.4: A sketch of the QCD phase diagram extended by a third axis regarding the mass of the two light quarks. As in figure 2.3 we assume the existence of a critical end point of a first order transition line. For quark masses below the physical value, the situation is unclear. In this example we assume that the phase in the chiral limit at low densities corresponds to the $O(4)$ universality class. In that case, remnants of this $O(4)$-scaling may still be important at the crossover at physical quark masses.

transitions behave in the same way and are grouped into universality classes, which also holds for the above quantities.

At the physical point, it has been shown that the QCD transition for physical quark masses is an analytic crossover rather than a true phase transition [6, 7] and happens at around $156.5(1.5)$ GeV [60]. Therefore, neither the shape of the peak of the susceptibility nor the drop off of the chiral condensate do fully correspond to a universality class as the finiteness of the light quark masses gives rise to scaling violations. Thus, these quantities may not be used for scaling analysis directly. Instead one has to add a regular term that takes care of the scaling violations.

To do so, we still need to know which universality class the chiral phase transition corresponds to. Then, remnants of this universal scaling may be used to determine further quantities, like for instance the transition temperature [60]. In figure 2.4 we visualize the influence of the phase transition in the chiral limit on the transition at physical quarks by extending the QCD phase diagram by a third axis corresponding to the mass of the light quarks.

Though there are many indications that the chiral phase transition may be described by the $O(4)$-spin model [54, 55, 61–63], there are also lattice QCD studies that state the opposite [64–66] and the situation remains unclear. Therefore, it is still unclear which universality class shall be used for further scaling analysis.

In figure 2.5 we show two possible scenarios in the plane of the two quark masses. For the infinite mass limit as well as for the 3-flavor chiral limit, it has been shown that the phase transition is of first order [67, 68]. For the two-flavor chiral limit with an additional strange

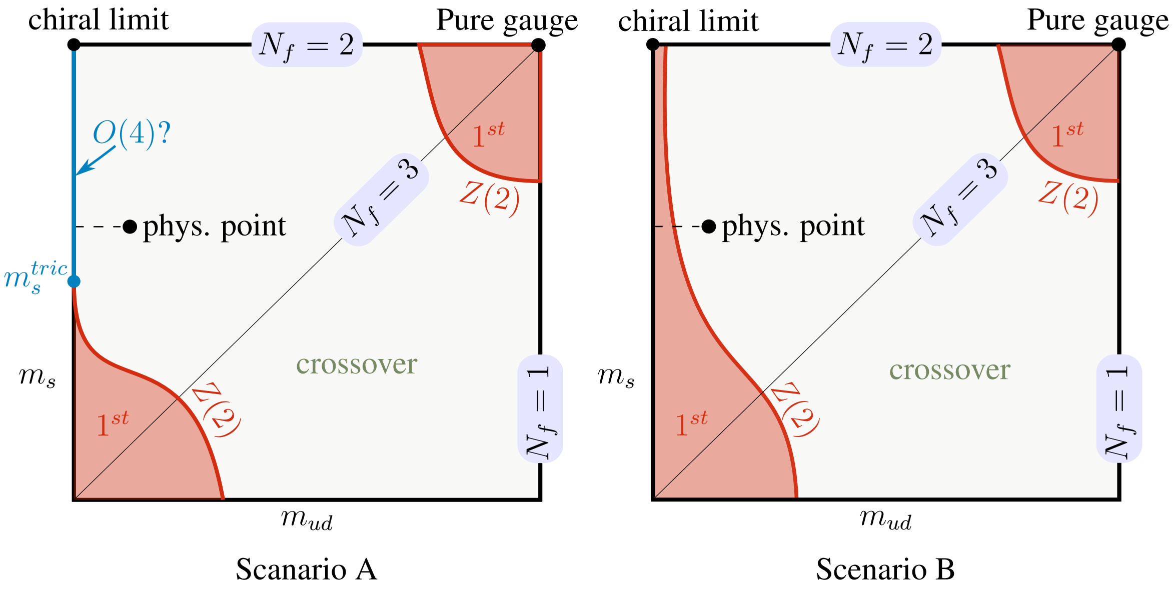

Figure 2.5: Two possible realizations of the QCD-phase diagram in the quark mass plane of two degenerate light m_{ud} and one strange quark m_s. Left: Phase diagram where the classification of the phase transition in the chiral limit depends on the strange quark mass. For light strange quarks, the transition is of first order. For larger strange quark masses, the transition eventually becomes of second order classified by the $O(4)$ universality class. Right: Phase diagram where the chiral phase transition is of first order independent of the strange quark mass. The region between a first order transition and a crossover is separated by a line of second order transitions belonging to the $Z(2)$ universality class.

quark, the region of first order transition at low strange quark masses may either end in a tricritical point (scenario A) or may even hold up to pure two-flavor QCD (scenario B). The physical point lies in the crossover region in any case. Beyond the tricritical point in scenario A, the chiral phase transition will be of second order belonging either to the $O(4)$ or to the $U_L(2) \otimes U_R(2)$ universality class. In that case, the position of the tricritical point determines which universality class is mostly relevant for physical quarks. In the example shown in figure 2.5, the tricritical point lies below the physical one, and the relevant universality class is either $O(4)$ or $U_L(2) \otimes U_R(2)$. In a possible realization where the tricritical point corresponds to a quark mass which is larger than physical, remnants of the $Z(2)$ symmetry become more important.

A useful tool to determine which of the scenarios takes place is the restoration of the $U_A(1)$ symmetry. In 2-flavor QCD it is found that if the $U_A(1)$ remains broken in the chiral limit, the phase transition will be of second order in the $O(4)$ universality class [68]. In case of a restoration of the $U_A(1)$ symmetry, both scenarios are possible. If the phase transition is of second order the chiral phase transition will probably lie either in the $U(2) \otimes U(2) \to U(2)$ [69, 70] or in the $SU(2) \otimes SU(2) \otimes Z_4 \to SU(2)$ [71, 72] universality class. Unfortunately, because of the explicit breaking of the $U_A(1)$ symmetry due to quantum effects it lacks an order parameter. Therefore, its restoration or likewise brokenness has to be estimated from other quantities. An example for such a quantity based on mesonic susceptibilities will be given in section 3.1.5.

At this point it is important to mention that the above defined discretized versions of the lattice QCD Lagrangian do not exhibit the same symmetries as in the continuum. In fact it can be shown that it is impossible to propose a QCD action in a way that it includes chiral symmetry and is free of doublers at the same time [73]. For the Wilson action, the chiral symmetry is explicitly broken as the extra terms behaves like a mass term. For the staggered symmetry, the action is not invariant under flavor mixing and the chiral symmetry reduces to $U_L(1) \otimes U_R(1)$. In both cases, the true chiral symmetry gets restored only in the continuum limit. Thus, to analyze quantities related to the chiral symmetry a continuum extrapolation has to be performed first.

To reduce the effect of the explicit symmetry breaking by discretizing the QCD action, different approaches have been suggested. For instance see the overlap operator [74, 75] or Domain Wall fermions [76–78]. Both are found to be way more computationally demanding: While the former replaces the Dirac operator by a much more complex structure to fulfill the so called index theorem, the latter introduces a fifth dimension.

3. Hadronic correlators and spectral functions

One of the key observable in lattice QCD is the hadronic correlator. It serves as a direct method to compute hadronic energy eigenstates from the lattice. This is used to tune input parameters such as the quark masses [79, 80]. On the other hand, energy eigenstates may be used to reproduce physical masses from the lattice, which verifies the underlying theory [81]. Furthermore, studying in-medium properties of excited states reveals information about the relevant degrees of freedom in the quark-gluon plasma [82]. Its connection to the spectral function makes correlators an important tool to investigate transport properties of the quark-gluon plasma [83].

In the following section we define hadronic correlators and describe its computation on the lattice, where we mainly follow [24]. See also [22] and [26] for a practical guide of hadronic mass extraction from lattice QCD and [84] for a detailed review over a broad range in lattice QCD. Additionally, we derive the connection to bound mesonic states in both the Wilson and staggered actions. In section 3.3 we relate the correlator to the spectral function, from which transport properties may be derived. A perturbative approach to spectral functions at high temperatures is given in section 3.5.

3.1. Hadron spectroscopy on the lattice

To define Euclidean hadronic correlators we start with a one particle propagator defined as the transition probability from an initial state $|O(0)\rangle$ to a final state $\langle O(\tau)|$:

$$G(\tau) \equiv \langle O(\tau)\, O^{\dagger}(0)\rangle = \langle 0|\, O(\tau)\, O^{\dagger}(0)\, |0\rangle \tag{3.1}$$

Here, $O^{\dagger}(\tau)$ represents an operator that has the same quantum numbers as the particle of interest. Explicitly introducing the time evolution and inserting a full set of energy eigenstates, we get

$$\begin{aligned} G(\tau) &= \langle 0|\, e^{H\tau} O(0)\, e^{-H\tau} O^{\dagger}(0)\, |0\rangle \\ &= \sum_{n} \langle 0|\, O^{\dagger}(0)\, |n\rangle \langle n|\, O(0)\, |0\rangle\, e^{E_0\tau} e^{-E_n\tau} \end{aligned} \tag{3.2}$$

When we further set the vacuum energy to zero, $E_0 = 0$, all other energy states may be interpreted as the energy difference that is necessary to create the quantum state from the vacuum. This also includes a possible momentum. We finally end up with

$$G(\tau) = \sum_{n} \langle 0|\, O^{\dagger}\, |n\rangle \langle n|\, O\, |0\rangle\, e^{-\tau E_n}. \tag{3.3}$$

Note that in the sum over energy states each state with the correct quantum number is represented. So it may be the case that one is measuring decay products instead of the quantum state itself.

When switching to the lattice version of the above correlator, we have to take periodic boundaries into account. This means we also have a quantum state traveling backward in imaginary time, which adds $A_n \exp(-E_n(1/T - \tau))$ with T being the temperature to the correlator. Even more, each propagation wraps around the lattice and appears again with suppression factor $A_n \exp(-kE_n/T)$, where $k \in \mathbb{N}$.

Summing up the resulting geometric series and redefining the amplitude, we get [84],

$$G(\tau) = \sum_n A_n \frac{\cosh[E_n(\tau - 1/(2T))]}{\sinh[E_n/(2T)]}. \tag{3.4}$$

In order to draw the connection to the spectral function $\rho(\omega)$ which will be introduced in section 3.3, we may rewrite the above result as

$$G(\tau) = \int_0^\infty \frac{\mathrm{d}\omega}{2\pi} \rho(\omega) \frac{\cosh[w(\tau - 1/(2T))]}{\sinh[w/(2T)]}, \quad \rho(\omega) = \sum_n A_n \delta(E_n - \omega). \tag{3.5}$$

Here, we have introduced the spectral function with a discrete sum over δ-peaks representing the discrete energy spectrum. However, for finite temperature these discrete energy levels start to broaden and the spectral function turns into a continuous function. This case will be discussed in section 3.3.

As the denominator in equation (3.4) is constant in τ, it often is absorbed into the amplitude A_n as

$$G(\tau) \equiv \sum_n A_n \cosh[E_n(\tau - 1/(2T)] \tag{3.6}$$

This formula is the basic tool to extract energy eigenstates from correlators computed on the lattice. More about that in section 4.3.

3.1.1. Correlators on the lattice

We still need to know how to compute such a correlator from lattice QCD. The first task is to find a lattice version of the operator O that shares the same symmetries with the particle of interest and has a non-vanishing overlap with its wave function. In this work we will focus on mesons. For baryons see e.g. [24].

A general local meson interpolator may be defined as

$$O_{H,f1,f2}(n) = \bar{\psi}(n)_{f1} \Gamma_H \psi_{f2}(n), \tag{3.7}$$

where n is the lattice point at which the state should be created. Γ_H is a combination of γ-matrices and defines the particle's quantum numbers (vector, pseudoscalar etc.). The flavor of the involved quarks is referred to by indices $f1$, $f2$. In the following, we might use the abbreviations $\psi_u = u$, $\psi_d = d$ and $\psi_s = s$ as well.

channel	J^{PC}	Γ_H	particle example
scalar (S)	0^{++}	$\mathbb{1}$	a_0 (δ), f_0 (σ), K^*, D_0^*, D_{s0}^*, χ_{s0}
pseudoscalar (PS)	0^{+-}	γ_5	$\pi^\pm$, $K^\pm$, $D^\pm$, $D_s^\pm$, η_c
vector (V)	1^{--}	γ_i	ρ, K^*, ϕ, D^*, $D_s^{*\pm}$, J/ψ
axial vector (AV)	1^{++}	$\gamma_i\gamma_5$	a_1, $K_{1,}$, f_1, D_1, $D_{s1}^\pm$, χ_{c1}

Table 3.1: Quantum numbers and Dirac-structure of commonly used meson interpolators as well as typical particle names.

In order to represent a certain particle state we have to choose Γ_H according to the symmetries of the particle. See table 3.1 for a list of particle channels, corresponding Dirac structure and particle examples. For the light quark sector, one has to distinguish between isospin-triplet ($I = 1$) and isospin singlet ($I = 0$) states. According to the isospin Clebsch-Gordon coefficients, the latter has the general form

$$O_{I=0}(n) = \frac{1}{\sqrt{2}} \left(\bar{u}(n)\Gamma_H u(n) + \bar{d}(n)\Gamma_H d(n)\right). \tag{3.8}$$

Likewise, the $I_z = 0$ iso-triplet is given by:

$$O_{I_z=0}(n) = \frac{1}{\sqrt{2}} \left(\bar{u}(n)\Gamma_H u(n) - \bar{d}(n)\Gamma_H d(n)\right). \tag{3.9}$$

The $I_z = \pm 1$ states of the isospin-triplet states are more simple and can be constructed by just putting a γ-matrix between the two quark fields, e.g.

$$\begin{aligned} O_{\pi^+}(n) &= \bar{d}(n)\gamma_5 u(n) \\ O_{\pi^-}(n) &= \bar{u}(n)\gamma_5 d(n). \end{aligned} \tag{3.10}$$

In lattice QCD, the masses of the light quarks are often assumed to be degenerate. As pure QCD does not involve electrical charge, this leads to a degeneracy of all the iso-triplet states which in turn simplifies the computations on the lattice.

Note that physical states may also involve additional contributions by combinations of the strange quark. For instance, the η-meson is known to be a combination of up, down and strange quarks. See [47] for more details.

Now, we can compute the expectation value of these interpolators by inserting them into the lattice version of the path integral expectation value, eq. (2.14). Afterwards, it is possible to integrate out the Grassman valued fermionic part. For simple interpolators which involve only one single term, like the iso-triplet interpolators in (3.10), we get [24]

$$\begin{aligned} \langle O_H(n) O_H^\dagger(m)\rangle_F &= \langle \bar{d}(n)\Gamma_H u(n)\bar{u}(m)\Gamma_H d(m)\rangle_F \\ &= \frac{1}{Z_F}\int \mathcal{D}\bar{d}\mathcal{D}d\mathcal{D}\bar{u}\mathcal{D}u\ \bar{d}(n)\Gamma_H u(n)\bar{u}(m)\Gamma_H d(m)\mathrm{e}^{-S_F[U,u,d]} \\ &= -\operatorname{Tr}\left[\Gamma_H D_u^{-1}(n,m)\Gamma_H D_d^{-1}(m,n)\right], \end{aligned} \tag{3.11}$$

where D_u^{-1} and D_d^{-1} is the inverse of the Dirac-operator in equation (2.13) and the fermionic partition function Z_f is given by $Z_f = \det D_u \det D_d$. Please note that the fermionic partition function canceled a factor $\det D_u \det D_d$ appearing in the numerator. This is only possible as the integral over gluonic fields is not performed at this point. For a full expectation value which also involves the path integral over links, the gluonic integral over the determinants arising in the partition function Z_f is performed separately.

For interpolators that involve more terms like the iso-singlet interpolator in (3.9) additional terms appear in the calculation of the correlator: For instance for the iso-singlet η-state, we get

$$\begin{aligned}\langle O_H(n)O_H^\dagger(m)\rangle_F = &-\frac{1}{2}\operatorname{Tr}\left[\Gamma_H D_u^{-1}(n,m)\Gamma_H D_u^{-1}(m,n)\right]\\ &+\frac{1}{2}\operatorname{Tr}\left[\Gamma_H D_u^{-1}(n,n)\Gamma_H D_u^{-1}(m,m)\right]\\ &+\frac{1}{2}\operatorname{Tr}\left[\Gamma_H D_u^{-1}(n,n)\Gamma_H D_d^{-1}(m,m)\right] + u \leftrightarrow d.\end{aligned} \tag{3.12}$$

Instead of connecting two different lattice points, the additional terms connect to the starting points themselves. As the computation of such disconnected diagrams on the lattice is computationally demanding, these contributions are usually neglected in lattice simulations. Therefore, comparisons are only possible for states whose mixing angle is small. In the light sector, this corresponds to iso-nonsinglets only.

When also considering the gluonic path integral, the final formula for pure flavor mesonic propagators reads

$$\begin{aligned}\langle O_H\left(m\right)O_H^\dagger\left(n\right)\rangle = &-\frac{1}{Z}\int \mathcal{D}\left[U\right]e^{-S_G[U]}\det D_u \det D_d\\ &\times \operatorname{Tr}\left[\Gamma_H D_u^{-1}(n,m)\Gamma_H D_d^{-1}(m,n)\right]\\ Z = &\int \mathcal{D}\left[U\right]e^{-S_G[U]}\det D_u \det D_d.\end{aligned} \tag{3.13}$$

This may now be approximated using importance sampling as defined equation (2.18). However, the full propagator matrix $\langle O_H\left(m\right)O_H^\dagger\left(n\right)\rangle$ is too large to be computed on each configuration. Moreover, as links at nearby lattice points are highly correlated, computing all of the propagator's entries does not help to increase the information from one single configuration. Instead it is adequate to compute only a few rows of this matrix. To do so, we introduce the so called quark source spinor ψ_0 as,

$$\psi_{0,a,f}(m) = \delta(m-m_0)\delta_{a,a_0}\delta_{f,f0}, \tag{3.14}$$

where a is a color index and f is a Dirac index. The lattice point m_0 is often called source of the propagator. We can now compute one row $G(n)_{a_0,\alpha_0} \equiv D^{-1}(n,m_0)_{a_0,\alpha_0}$ of the full quark propagator by solving for G in

$$DG = \psi_0. \tag{3.15}$$

This has to be repeated for each color and flavor index, such that in total 12 inversions are necessary. To avoid the computation of the backward running term in (3.11), we use the γ_5-hermiticity of the Dirac operator ($\gamma_5 D^{-1} \gamma_5 = D^{-1^\dagger}$) and write

$$\langle O_H(n) O_H^\dagger(m_0) \rangle_F = \mathrm{Tr}\left[\Gamma_H D^{-1}(n, m_0) \Gamma_H \gamma_5 D^{-1^\dagger}(n, m_0) \gamma_5 \right]. \tag{3.16}$$

From this equation it is directly obvious that the inversion of the Dirac-matrix on each gauge configuration is the most time consuming part. For lattice QCD, Krylov-Solver or Multigrid algorithms turn out to be the most effective tools. A review about the different inversion methods can be found in [85].

A typical problem that arises when computing meson correlators using the above formula on a finite set of configurations is a bad signal to noise ratio. This may be improved by introducing more complicated meson interpolators compared to the one in equation (3.7). These improved meson interpolators are generally of the form

$$O_H(n) = \sum_{n_1, n_2} \bar{\psi}(n_1, n_\tau) F_H(n; n_1, n_2) \psi(n_2, n_\tau) \tag{3.17}$$

and are chosen in such a way that the overlap between the initial and final state increases. Additionally, excited states may be suppressed when using different interpolators. For some interpolators, the overlap of the excited states may even become negative which leads to negative amplitudes of the excited states in the correlator.

In practice, such interpolators are introduced by choosing a different quark source that enters equation (3.15). It might also be necessary to perform a gauge fixing to ensure gauge invariance of the meson operators.

As a last step, a momentum projection of the correlator is required. Due to the finiteness of the lattice, only integer valued momenta are possible:

$$p_i = \frac{2\pi k_i}{N_\sigma a}. \tag{3.18}$$

Now, we get the momentum projected correlator via the discrete Fourier transformation on the spatial coordinates,

$$G_H(n_\tau, \vec{p}) = \sum_{n_x, n_y, n_z} \exp\left(i \sum_{i=x,y,z} p_i n_i \right) \langle O_H(n) O_H^\dagger(m_0) \rangle. \tag{3.19}$$

In many cases, one restricts the momentum to be zero, and the correlator becomes just a sum over spatial coordinates of the mesonic propagator. In that case, energies implicitly defined in equation (3.4) correspond to the particle mass at rest.

One exception is the G_{γ_0} correlator which appears to be constant in the Euclidean time direction due to the exact $U_V(1)$-symmetry from equation (2.55). To see this, we first have to extend our theory by the quark number chemical potential μ_q and define the corresponding quark number density ρ_q as

$$\rho_q \equiv \frac{1}{V}\frac{\mathrm{Tr}\,[N_q \exp(-\beta(H-\mu_q N_q))]}{\mathrm{Tr}\,[\exp(-\beta(H-\mu_q N_q))]}, \tag{3.20}$$

where the quark number operator N_q is defined as

$$N_q = \int \mathrm{d}^3x j_0(0,\vec{x}), \tag{3.21}$$

with $j_\mu(\tau,\vec{x})$ being the vector current

$$j_\mu(\tau,\vec{x}) = \bar{\psi}(\tau,\vec{x})\gamma_\mu\psi(\tau,\vec{x}). \tag{3.22}$$

Note that due to the periodic boundary conditions of the lattice, the choice of τ is arbitrary and is usually set to $\tau = 0$. Further, we define the quark number susceptibility as the response of the quark number density to small variations in the quark number chemical potential:

$$\chi_q(T) \equiv \left.\frac{\partial\rho_q}{\partial\mu_q}\right|_{\mu_q=0}. \tag{3.23}$$

When applying the derivative to equation (3.20) we find

$$\chi_{q,\tau}(T) = \frac{1}{T}\int \mathrm{d}x \left\langle j_0(\tau,\vec{x})j_0(0,\vec{0})\right\rangle, \tag{3.24}$$

which is exactly the definition of the Euclidean correlator for $\Gamma_H = \gamma_\mu$. As the total quark number is conserved, this is a Kubo relation and the quark number susceptibility appears to be constant in τ [86].

Though, because of cut-off effects on the lattice, this is not the case for short distances. Only for large distances, the correlator becomes constant in τ. This may be used to estimate the typical range of cut-off effects in correlators.

Another application is the use for renormalization. As the correlator G_{γ_i} undergoes the same renormalization effects as G_{γ_0}, ratios G_{γ_i}/χ_q are renormalization independent, which we will use in section 5 to perform a renormalization independent continuum extrapolation.

3.1.2. Screening correlators

Correlators calculated on the lattice serve as input for further analysis, such as the ground state extraction described in section 4.3 or extraction of spectral functions as described in section 3.3. To get precise results, this requires many data points in the time direction. However, for finite temperatures, the temporal extent of the lattice is rather short. This makes it difficult to apply fits, as there are only few data points available. Moreover, also the physical distances are short so that excited states are likely to give large contributions to the correlator at all available distances, i.e. it is hard to project onto the ground state. Therefore, at finite temperatures, correlators are usually evaluated in one of the spatial directions, instead. A typical choice is the z-direction. In that case, the momentum projection is defined as

$$G_{\mathrm{scr}.H}(n_z, p) = \sum_{n_x, n_y, n_\tau} \exp\left(i \sum_{i=x,y,\tau} p_i n_i \right) \langle O_H(n) O_H^\dagger(m_0) \rangle \, . \tag{3.25}$$

This has a few consequences. The corresponding energies in equation (3.6) do not refer to particle masses as an inverse of the decay time. Instead the inverse of such a mass may be interpreted as a length, at which the corresponding particle is effectively screened. This is why the correlator and its corresponding masses are named screening correlator and screening masses, respectively. Due to the isotropy of the lattice, screening and pole masses are degenerate at zero temperature. However, this is not the case at finite temperature. For very high temperatures, that means in the free limit, the temporal correlator may not be broken down into separate bound states as in equation (3.5). Instead, a continuum of states contributes through the spectral function. We ill give more details about that in section 3.3. On the other hand, for screening correlators, one still finds an exponential behavior with the screening mass of [87]

$$m_{\mathrm{scr.}} = 2\sqrt{\pi^2 T^2 + m_q^2}, \tag{3.26}$$

where m_q is the quark mass and πT is the lowest Matsubara frequency. This may be used to identify at which temperatures the medium starts to influence mesonic bound states: By comparing the ground state mass of screening correlators to the cases at $T = 0$ and $T \to \infty$, one can identify whether quarks are still bound in mesonic states or already free.

3.1.3. Staggered correlators

In the previous section we defined mesonic correlators on the lattice only for Wilson-like actions. In this section we will define mesonic correlators for staggered fermions and discuss consequences that arise from the taste violations.

Again, we start with the definition of the meson interpolator, which shall be defined in analog to equation (3.7). Due to the mixing of the taste and Dirac-structure within a hypercube, this requires to introduce another Γ_T-matrix that lives in the taste space. Thus, a general local staggered meson interpolator living on the hypercube with coordinates $N = (\vec{N}, N_t)$ can be defined as [88]

$$O_{\mathrm{stagg}}(N) = \bar{\psi}(N)(\Gamma_D \otimes \Gamma_T^*)\psi(N) \tag{3.27}$$

Because of this additional taste structure, each meson comes with 16 additional representations, where each representation comes with a different Γ_T. As those combinations carry the correct quantum numbers in Dirac-space but differ in taste-space, these representations are referred to as taste partners. As a next step, we want to map the staggered interpolator (3.27) back to the staggered spinor fields $\chi(n)$. According to equation (2.34), we get,

$$\begin{aligned} O_{\text{stagg}}(N) &= \bar{\psi}(N)(\Gamma_D \otimes \Gamma_T^*)\psi(N) \\ &= \frac{1}{64}\sum_{\rho,\rho'} \bar{\chi}(2N+\rho)\Omega^\dagger_{\alpha t,\rho}\Gamma_D^{\alpha\beta}\Gamma_T^{*ts}\Omega_{\beta s,\rho'}\chi(2N+\rho') \\ &= \frac{1}{64}\sum_{\rho,\rho'} \Omega^\dagger_{\alpha t,\rho}\Gamma_D^{\alpha\beta}\Omega_{\beta s,\rho'}\Gamma_T^{\dagger st}\bar{\chi}(2N+\rho)\chi(2N+\rho'). \\ &= \frac{1}{16}\sum_{\rho,\rho'} \phi_{DT}(\rho,\rho')\bar{\chi}(2N+\rho)\chi(2N+\rho'), \end{aligned} \tag{3.28}$$

with $\phi_{DT}(\rho,\rho')$ defined as

$$\phi_{DT}(\rho,\rho') = \frac{1}{4}\,\mathrm{Tr}\left[\Omega_\rho^\dagger\Gamma_D\Omega_{\rho'}\Gamma_T^\dagger\right]. \tag{3.29}$$

Thus, all information about the particle channel went into $\phi_{DT}(\rho,\rho')$. For $\Gamma_T \neq \Gamma_D$, this becomes a complex structure and $\phi_{DT}(\rho,\rho')$ connects different points of the hypercube. This is why such combinations are referred as “non-local” operators. However, for $\Gamma_H = \Gamma_D = \Gamma_T$ this factor simplifies to just a phase factor

$$\phi_{HH}(\rho,\rho') = \phi_H(\rho)\delta_{\rho,\rho'}, \tag{3.30}$$

and therefore such interpolators are named “local” operators. For example, for the scalar operator with $\Gamma_H = \mathbb{1}$ we get

$$\phi_{\mathbb{1}}(\rho) = \frac{1}{4}\,\mathrm{Tr}\,[\gamma_4^{\rho_4}\gamma_3^{\rho_3}\gamma_2^{\rho_2}\gamma_1^{\rho_1}\mathbb{1}\gamma_1^{\rho_1}\gamma_2^{\rho_2}\gamma_3^{\rho_3}\gamma_4^{\rho_4}\mathbb{1}] \tag{3.31}$$

$$= 1. \tag{3.32}$$

Similarly for the pseudoscalar-like state $\Gamma_H = \gamma_4\gamma_5$ we get,

$$\phi_{\gamma_4\gamma_5}(\rho) = \frac{1}{4}\,\mathrm{Tr}\,[\gamma_4^{\rho_4}\gamma_3^{\rho_3}\gamma_2^{\rho_2}\gamma_1^{\rho_1}\gamma_4\gamma_5\gamma_1^{\rho_1}\gamma_2^{\rho_2}\gamma_3^{\rho_3}\gamma_4^{\rho_4}\gamma_5\gamma_4] \tag{3.33}$$

$$= (-1)^{\rho_4}. \tag{3.34}$$

Further computation of the propagator and the momentum projection are analogous to the Wilson case, though we sum over the staggered coordinates $\vec{N}$ here. Restricting ourselves to zero momentum only, we end up with

$$G_H(N_t) = -\sum_{\vec{N}}\sum_{\rho,\rho'} \phi_H(\rho)\phi_H(\rho')\,\mathrm{Tr}\left[D^{-1\dagger}(2N+\rho',\rho)D^{-1}(\rho,2N+\rho')\right]. \tag{3.35}$$

Unfortunately, this formula is not ready to use. Because of the two sums over ρ, the distance between the source and the sink varies between $N_t - 1$ to $N_t + 1$, which is impractical when measuring correlator decays in the time direction.

This can be solved by adding another state to the correlator by replacing $\Gamma_D \otimes \Gamma_T^*$ with

$$\Gamma_D \otimes \Gamma_T^* \to \Gamma_D \otimes \Gamma_T^* + (\gamma_4\gamma_5\Gamma_D) \otimes (\gamma_4\gamma_5\Gamma_T)^*. \tag{3.36}$$

Speaking of correlators, this means we replace G_H by $G_{H+H'}$, where $\Gamma_{H'}$ is given by $\Gamma_{H'} = \gamma_4\gamma_5\Gamma_H$. We may motivate the choice of $\gamma_4\gamma_5$ by noticing that, similar to the two examples of ϕ_H above, the relation between ϕ_H and $\phi_{H'}$ is given by

$$\phi_{H'}(\rho) = (-1)^{\rho_4}\phi_H(\rho). \tag{3.37}$$

Therefore, contributions from time slices in time direction at $\rho_4 = 1$ exactly cancel and the new phase $\phi_{H+H'}$ does not depend on ρ_4 any more.

Since mixed terms with different quantum numbers cancel, the full correlator now reads

$$\begin{aligned}
G_{H+H'}(N_t) = &- \sum_{\vec{N},\rho,\rho'} (\phi_H(\rho) - \phi_{H'}(\rho'))(\phi_H(\rho) - \phi_{H'}(\rho')) \\
&\qquad\qquad \cdot \operatorname{Tr}\left[D^{-1\dagger}(2N+\rho',\rho)D^{-1}(\rho,2N+\rho')\right] \\
= &- \sum_{\vec{N}} \sum_{\substack{\rho \\ \rho\neq\rho_0}} \sum_{\substack{\rho' \\ \rho'\neq\rho'_0}} \phi_{H+H'}(\rho')\phi_{H+H'}(\rho) \\
&\qquad\qquad \cdot \operatorname{Tr}\left[D^{-1\dagger}(2N+\rho',\rho)D^{-1}(\rho,2N+\rho')\right] \\
= &- \sum_{\vec{n}} \sum_{\rho,\rho\neq\rho_0} \phi_{H+H'}(\vec{n})\phi_{H+H'}(\rho) \operatorname{Tr}\left[D^{-1\dagger}(n,\rho)D^{-1}(\rho,n)\right],
\end{aligned} \tag{3.38}$$

where we have combined the sum over N and ρ' into one sum over the whole lattice in the last step.

As a remaining task, we have to remove the ρ dependence in $D^{-1}(\rho,n)$ as it is impractical to compute $D^{-1}(\rho,n)$ at more than one source point. Similar to the step in equation (3.36) we add additional states to the correlator. This time we only add them to the source operator as the remaining ρ's stem from the source itself. Instead of adding only one state, we add all possible states. Such a source operator acts as a broad spectrum operator as it creates all states at once. By quantum number conservation, it follows that the sink operator selects the desired states. The phase of such a source operator simplifies to

$$\phi_\Sigma(\rho) = \sum_S \phi_S(\rho) = \delta_{\rho,0}. \tag{3.39}$$

Accordingly all contributions of ρ in equation (3.38) cancel out and we are left with

$$G_{H+H'}(N_t) = -\sum_{\vec{n}} \phi_{H+H'}(\vec{n}) \operatorname{Tr}\left[D^{-1\dagger}(n,0)D^{-1}(0,n)\right], \tag{3.40}$$

As a final step we exploit $D(n,0) = (-1)^{n_1+n_2+n_3+n_4}D^{-1\dagger}(0,n)$ and the above formula simplifies to

$$G_{H+H'}(N_t) = -\sum_{n} \zeta_{H+H'}(\vec{n}) \operatorname{Tr}\left[D^{-1\dagger}(n,0)D^{-1}(n,0)\right], \tag{3.41}$$

where $\zeta_{H+H'}(\vec{n})$ is defined as

$$\zeta_{H+H'}(\vec{n}) = (-1)^{n_1+n_2+n_3}\phi_{H+H'}(\vec{n}). \tag{3.42}$$

Note that we ignored $(-1)^{n_4}$ in the definition of $\zeta_{H+H'}(n)$ as we do not sum over n_4 anyway.

This correlator still lives at the hypercube time N_t. That means, when speaking of lattice coordinates n_τ, we only know how to compute the correlator for even distances $n_\tau = 2N_t$. For odd distances ($n_\tau = 2N_t + 1$), we have to redefine the sink operator in equation (3.36). Instead of adding the extra state, we subtract it:

$$\Gamma_D \otimes \Gamma_T^* \to \Gamma_D \otimes \Gamma_T^* - \gamma_4\gamma_5\Gamma_D \otimes (\gamma_4\gamma_5\Gamma_T)^*. \tag{3.43}$$

This time, all contributions from $\rho_4 = 0$ cancel in the phase $\phi_{H-H'}(\rho)$ and we get only contributions for time slice $2N_t+1$. Afterwards, the definition of the correlator $G_{H-H'}$ goes through in analogy to to equation (3.41). The only difference is that our correlator has distance $2N_t+1$ now and thus, is defined for odd distances only. Combining $G_{H+H'}$ and $G_{H-H'}$, we get the full correlator $G_{H\pm H'}(n_\tau)$.

At this point, it should be mentioned that $\zeta_{H+H'}(\vec{n})$ and $\zeta_{H-H'}(\vec{n})$ are identical, as both do not depend on n_4. Therefore we only speak of $\zeta_{H\pm H'}(\vec{n})$ from now on. The different signs in equations (3.36) and (3.43) were only introduced to understand what states $G_{H\pm H'}(2N_t)$ and $G_{H\pm H'}(2N_t + 1)$ correspond to, but the computation of the correlator itself is independent of that sign.

Nevertheless, that sign appears in the measured correlation function: Instead of measuring only one correlator at a given time n_τ, we always have a mixture of two states, where the second states is oscillating with $(-1)^{n_\tau}$. By using $\gamma_4\gamma_5\Gamma_H$ to construct the second state, it appears to be the parity partner of the first state. Consequently, a second decay channel also appears in equation (3.6) and the correlator decay is given by

$$\begin{aligned} G(n_\tau) =& \sum_n A_{no,n} \cosh[E_{no,n}(\tau - 1/(2T)] \\ &- (-1)^{n_\tau} \sum_n A_{osc,n} \cosh[E_{osc,n}(\tau - 1/(2T)]. \end{aligned} \tag{3.44}$$

A list of phase factors, corresponding states and their symmetries as well as abbreviations further used in this thesis can be found in table 3.2 for the temporal and in table 3.3 for the spatial correlators.

The only exception to equation (3.44) is the pseudoscalar correlator $\mathcal{M}2$ where $A_{osc,i} = 0$ holds for degenerate quarks. This is because the operator $\gamma_4 \otimes \gamma_4$ is the density of a conserved charge (eq. (3.20)), and as it is not a taste singlet, it cannot excite a purely gluonic state from the vacuum [23]. Thus, the contribution from this operator is zero, and the $\mathcal{M}2$ channel is the only one without oscillations.

So far, we have only looked at local operators with $\Gamma_D = \Gamma_T^*$. These local operators exhibit the smallest taste violations. Moreover, for the pseudoscalar channel only the local operator

	$\zeta(x)$	Γ		J^{PC}		states	
		non-osc.	osc.	non-osc.	osc.	non-osc.	osc.
$\mathcal{M}1$	$(-1)^{x+y+z}$	$\gamma_4\gamma_5$	$\mathbb{1}$	0^{-+}	0^{++}	π_2	a_0
$\mathcal{M}2$	1	γ_5	γ_4	0^{-+}	0^{+-}	π	–
$\mathcal{M}3$	$(-1)^{y+z}$	$\gamma_1\gamma_4$	$\gamma_1\gamma_5$	1^{--}	1^{++}	$\rho_2^{\mathcal{T}}$	$a_1^{\mathcal{T}}$
$\mathcal{M}4$	$(-1)^{x+z}$	$\gamma_2\gamma_4$	$\gamma_2\gamma_5$	1^{--}	1^{++}	$\rho_2^{\mathcal{T}}$	$a_1^{\mathcal{T}}$
$\mathcal{M}5$	$(-1)^{x+y}$	$\gamma_3\gamma_4$	$\gamma_3\gamma_5$	1^{--}	1^{++}	$\rho_2^{\mathcal{L}}$	$a_1^{\mathcal{L}}$
$\mathcal{M}6$	$(-1)^{x}$	γ_1	$\gamma_2\gamma_3$	1^{--}	1^{+-}	$\rho_1^{\mathcal{T}}$	$b_1^{\mathcal{T}}$
$\mathcal{M}7$	$(-1)^{y}$	γ_2	$\gamma_1\gamma_3$	1^{--}	1^{+-}	$\rho_1^{\mathcal{T}}$	$b_1^{\mathcal{T}}$
$\mathcal{M}8$	$(-1)^{z}$	γ_3	$\gamma_1\gamma_2$	1^{--}	1^{+-}	$\rho_1^{\mathcal{L}}$	$b_1^{\mathcal{L}}$

Table 3.2: List of staggered phases for local mesonic interpolators in the temporal direction and their corresponding γ-structure. The corresponding light quark physical states are listed as well [23].

$\gamma_5 \otimes \gamma_5^*$ corresponds to a Goldstone meson. However, the computation of the different taste partners may still be interesting to quantify the size of taste violations. For non-local operators, the computation of staggered correlators is involved and requires a group theoretical approach. Here we only quote the results for the different taste partners of the pseudoscalar channel. For other channels and further details see [89–92].

In general, staggered operators can be grouped according to the number of points that are connected within the hypercube: Depending on the taste structure (Γ_T in equation (3.27)), staggered operators fall into one of the following classes of operators [93]:

$$O_{\text{local}}(n) = \phi(n)\bar{\chi}(n)\chi(n) \tag{3.45}$$

$$O_{\text{one-link},i}(n) = \phi(n)\bar{\chi}(n)\Delta_i\chi(n) \tag{3.46}$$

$$O_{\text{two-link},k}(n) = \phi(n)\epsilon_{ijk}\bar{\chi}(n)\Delta_i\Delta_j\chi(n) \tag{3.47}$$

$$O_{\text{three-link}}(n) = \phi(n)\bar{\chi}(n)\Delta_1\Delta_2\Delta_3\chi(n). \tag{3.48}$$

Here Δ_i is the so called shift operator and is defined as

$$\Delta_i\chi(n) = \frac{1}{2}\left(\chi(x+\hat{i}) + \chi(x-\hat{i})\right), \tag{3.49}$$

and $\phi(n)$ is a phase factor again. The name of these operators corresponds to the number of links that connect different points within the hypercube. For the pseudoscalar channel, we get two local, six one-link, six two-link and one three-link operator which are listed in table 3.4.

Due to the taste symmetry breaking, the masses of these taste partners become degenerate only in the continuum and therefore, they may be used to quantify the magnitude of taste-symmetry violations. A typical way of doing so, is to calculate all taste partners of the pion and to compare their root mean square mass defined as

$$m_\pi^{\text{RMS}} = \sqrt{\frac{1}{16}\left(m_{\gamma_5}^2 + m_{\gamma_4\gamma_5}^2 + 3m_{\gamma_i\gamma_5}^2 + 3m_{\gamma_i\gamma_j}^2 + 3m_{\gamma_i\gamma_4}^2 + 3m_{\gamma_i}^2 + m_{\gamma_4}^2 + m_{\gamma_1}^2\right)} \tag{3.50}$$

	$\zeta(x)$	Γ		J^{PC}		states	
		non-osc.	osc.	non-osc.	osc.	non-osc.	osc.
$\mathcal{M}1$	$(-1)^{x+y+\tau}$	$\gamma_3\gamma_5$	$\mathbb{1}$	0^{-+}	0^{++}	π_2	a_0
$\mathcal{M}2$	1	γ_5	γ_3	0^{-+}	0^{+-}	π	–
$\mathcal{M}3$	$(-1)^{y+\tau}$	$\gamma_1\gamma_3$	$\gamma_1\gamma_5$	1^{--}	1^{++}	$\rho_2^{\mathcal{T}}$	$a_1^{\mathcal{T}}$
$\mathcal{M}4$	$(-1)^{x+\tau}$	$\gamma_2\gamma_3$	$\gamma_2\gamma_5$	1^{--}	1^{++}	$\rho_2^{\mathcal{T}}$	$a_1^{\mathcal{T}}$
$\mathcal{M}5$	$(-1)^{x+y}$	$\gamma_4\gamma_3$	$\gamma_4\gamma_5$	1^{--}	1^{++}	$\rho_2^{\mathcal{L}}$	$a_1^{\mathcal{L}}$
$\mathcal{M}6$	$(-1)^{x}$	γ_1	$\gamma_2\gamma_4$	1^{--}	1^{+-}	$\rho_1^{\mathcal{T}}$	$b_1^{\mathcal{T}}$
$\mathcal{M}7$	$(-1)^{y}$	γ_2	$\gamma_1\gamma_4$	1^{--}	1^{+-}	$\rho_1^{\mathcal{T}}$	$b_1^{\mathcal{T}}$
$\mathcal{M}8$	$(-1)^{\tau}$	γ_4	$\gamma_1\gamma_2$	1^{--}	1^{+-}	$\rho_1^{\mathcal{L}}$	$b_1^{\mathcal{L}}$

Table 3.3: List of staggered phases for local mesonic interpolators in the spatial direction and their corresponding γ-structure. The corresponding light quark physical states are listed as well [82].

to the mass of the Goldstone pion m_{γ_5} [48].

The additional oscillations in the correlator in equation (3.44) make it complicated to extract information from the correlator. This is especially the case for light quarks in the vector and axial vector channels, whose correlators tend to have a low signal to noise ratio. In order to still get a signal, improved quark sources have to be used. For staggered correlators, the so called corner wall source has been found to give a much better signal [94]. At the same time, it reduces the contributions of excited states to the correlator.

In the staggered coordinates of the hypercubes, a corner wall operator can be written as

$$O_{H,\mathrm{CW}}(N_t) = \sum_{\vec{N}} \bar{\psi}(\vec{N}, N_t)(\Gamma_D \otimes \Gamma_T^{\dagger})\psi(\vec{N}, N_t). \tag{3.51}$$

Speaking of sources, this means that for computation one has to use a source where one of three color entries at each corner of the hypercubes in one time slice is set to one and the rest to zero. The subsequent computation goes through as in the case of point source.

To ensure gauge invariance, Coulomb gauge is a good choice, as it does not introduce ghosts, like e.g. the Landau gauge [94]. Gauge fixing is computationally demanding and therefore, corner wall source should only be used if a significant improvement can be expected. However, this is not the case for high temperatures where quarks are deconfined, and thus improving the overlap to mesonic states does not increase the signal significantly.

3.1.4. Even odd splitting

When computing mesonic correlators, the main computational effort goes into the inversion of the Dirac operator. This effort can be reduced roughly by a factor two by using even odd preconditioning, which we describe using staggered quarks here. The corresponding implementation for Wilson fermions goes completely analogously.

Operator	$\Gamma_D \otimes \Gamma_T$		states	
	non-osc.	osc.	non-osc.	osc.
$\eta_4\zeta_4\bar{\chi}\chi$	$\gamma_5 \otimes \gamma_5$	$\gamma_4 \otimes \gamma_4$	π	$-$
$\bar{\chi}\epsilon\zeta_i\Delta_i\chi$	$\gamma_4 \otimes \gamma_i\gamma_4$	$\gamma_5 \otimes \gamma_i\gamma_5$	$-$	π
$\epsilon_{ijk}\eta_4\zeta_4\bar{\chi}\zeta_i\Delta_i(\zeta_j\Delta_j\chi)$	$\gamma_5 \otimes \gamma_k\gamma_4$	$\gamma_4 \otimes \gamma_k\gamma_5$	π	$-$
$\eta_4\zeta_4\bar{\chi}\eta_1\Delta_1(\eta_2\Delta_2(\eta_3\Delta_3\chi))$	$\gamma_4 \otimes \gamma_5$	$\gamma_5 \otimes \gamma_4$	$-$	π
$\frac{1}{2}[\eta_4\zeta_4(\bar{\chi}\chi_+ - \bar{\chi}_+\chi)]$	$\gamma_4 \otimes \mathbb{1}$	$\gamma_5 \otimes \gamma_4\gamma_5$	π	$[f_0]$
$\frac{1}{2}[\bar{\chi}\epsilon\zeta_i\Delta_i\chi_+ + \bar{\chi}_+\epsilon\zeta_i\Delta_i\chi]$	$\gamma_4 \otimes \gamma_i$	$\gamma_5 \otimes \gamma_j\gamma_k$	$[a_0]$	π
$\frac{1}{2}\epsilon_{ijk}\eta_4\zeta_4[\bar{\chi}\zeta_i\Delta_i(\zeta_j\Delta_j\chi_+) - \bar{\chi}_+\zeta_i\Delta_i(\zeta_j\Delta_j\chi)]$	$\gamma_5 \otimes \gamma_k$	$\gamma_4 \otimes \gamma_i\gamma_j$	π	$[a_0]$
$\frac{1}{2}\eta_4\zeta_4[\bar{\chi}\eta_1\Delta_1(\eta_2\Delta_2(\eta_3\Delta_3\chi_+))$ $+\bar{\chi}_+\eta_1\Delta_1(\eta_2\Delta_2(\eta_3\Delta_3\chi))]$	$\gamma_4 \otimes \gamma_4\gamma_5$	$\gamma_5 \otimes \mathbb{1}$	$[a_0]$	η'

Table 3.4: Operators for the 16 pseudoscalar taste partners, their γ-structure and the corresponding physical states in the continuum [92]. Notation is as follows: Δ_i defined in equation (3.49), $\eta_\mu(n) = (-1)^{\sum_{\nu=0}^{\mu-1} n_\nu}$, $\zeta_\mu(n) = (-1)^{\sum_{\nu=\mu}^{4} n_\nu}$, $\epsilon(n) = (-1)^{\sum_{\nu=0}^{4} n_\nu}$ and $\chi_+(n) = \chi(\vec{n}, n_\tau + 1)$. The sum over n is omitted.

Noticing that the staggered Dirac operator in equation (2.33) only connects even and odd points, we split the spinors into an even χ_e and an odd part χ_o. In that case, the Dirac operator reads

$$D\chi = \begin{pmatrix} m\mathbb{1} & D_{eo} \\ D_{oe} & m\mathbb{1} \end{pmatrix} \begin{pmatrix} \chi_e \\ \chi_o \end{pmatrix}, \tag{3.52}$$

where D_{eo} and D_{oe} connect even and odd points or odd and even points, respectively. Note that these do not include a mass term. With this notation, equation (3.15) transforms to

$$D \cdot \begin{pmatrix} G_e \\ G_o \end{pmatrix} = \begin{pmatrix} \chi_{0,e} \\ \chi_{0,o} \end{pmatrix}, \tag{3.53}$$

where χ_0 is the staggered version of the source. Further we notice that $D_{eo}^\dagger = -D_{oe}$. When restricting the point source from equation (3.14) to even lattice points, and multiplying with $D^\dagger + m$ from the left, we get

$$\left(m^2 - D_{eo}D_{oe}\right)\chi_{0,e} = mS_e - D_{eo}S_o = m\chi_{0,e}, \tag{3.54}$$

where we used $G_o = 0$. Instead of solving for G in $DG = \chi_0$, we can solve for G_e, which needs less computational effort as we work only with spinors of half the lattice size. Afterwards, one gets the other half of the quark propagator by multiplying out equation (3.53):

$$G_o = -\frac{1}{m}D_{oe}\chi_{0,e}. \tag{3.55}$$

With this method we have computed the full quark propagator $G = (G_e, G_o)$ and the further correlator computation goes through as usual.

$$\begin{tikzcd}
a_1 : \bar{\psi}\gamma_5\gamma_\mu\psi \arrow[r, leftrightarrow, "SU_L(2)\times SU_R(2)"] & \rho : \bar{\psi}\gamma_\mu\psi \\
\pi : \bar{\psi}\gamma_5\frac{\tau^i}{2}\psi \arrow[r, leftrightarrow, "SU_L(2)\times SU_R(2)"] \arrow[d, leftrightarrow, "U_A(1)"'] & f_0\ (\sigma) : \bar{\psi}\psi \arrow[d, leftrightarrow, "U_A(1)"] \\
a_0\ (\delta) : \bar{\psi}\frac{\tau^i}{2}\psi \arrow[r, leftrightarrow, "SU_L(2)\times SU_R(2)"'] & \eta : \bar{\psi}\gamma_5\psi
\end{tikzcd}$$

Figure 3.1: Symmetry transformation between different meson states. Here we use Pauli matrices to denote the three iso-triplet states of the scalar and the pseudoscalar state. States connected with arrows will become degenerate if the corresponding symmetry is restored

3.1.5. Hadronic correlators and chiral symmetry

In section 2.5 we stressed the importance of the chiral and $U_A(1)$ symmetries in QCD. Having defined the mesonic correlators in the above way, we may now notice that a restoration of these symmetries is reflected in the degeneracy of certain correlators. For instance let us look at the iso-vector particles π and a_0: We may obtain the pseudoscalar interpolator O_π from the scalar interpolator O_{a_0} by performing a $U_A(1)$ rotation of $\theta = \pi/4$:

$$\begin{aligned}
O_{a_0} = \bar{u}d \rightarrow & \bar{u}\mathrm{e}^{i\theta\gamma_5}\mathrm{e}^{i\theta\gamma_5}d \\
&= \frac{1}{2}\bar{u}(1+i\gamma_5)(1+i\gamma_5)d \\
&= i\bar{u}\gamma_5 d.
\end{aligned} \tag{3.56}$$

Thus, if the $U_A(1)$ symmetry is restored the corresponding correlators should be degenerate. A visualization of which states should become degenerate under chiral or $U_A(1)$ restoration is given in figure 3.1. As it is computationally demanding to compute the disconnected part of correlators, it is reasonable to look at the axial vector a_1 and the vector ρ to analyze the chiral symmetry restoration and to compare the scalar a_0 and pseudoscalar π to look for a restoration of the $U_A(1)$ symmetry.

Useful tools to analyze the degeneracy of correlators are the so called mesonic susceptibilities defined as the temporal sum over the correlator

$$\chi_H = \sum_{n_\tau} G_H(n_\tau, \vec{p} = 0). \tag{3.57}$$

For instance a common quantity to estimate the brokenness of the $U_A(1)$ symmetry is to look at the difference $\chi_\pi - \chi_{a_0}$. Note that this definition for the susceptibility also holds for screening correlators were one has to sum over n_z instead.

Summing over the correlator may seem to be a loss of information as the degeneracy should appear already at the level of the correlator itself. However, this is not necessarily the case for staggered correlators as they consist of two states. Therefore, the degeneracy may only become visible in the screening mass of the special correlator or in the staggered version of the mesonic susceptibility. In doing so, the latter has to be defined with spatial care in order to remove the contribution of one of the two states: Again we start with the interpolator definition in equation (3.28). We also use the point like source from equation (3.39). Then the susceptibility χ_H is given by

$$\begin{aligned}
\chi_H &= -\sum_N \sum_\rho \phi_H(\rho)\,\mathrm{Tr}\left[D^{-1\dagger}(2N+\rho,0)D^{-1}(0,2N+\rho)\right] \\
&= -\sum_n \phi_H(n)\,\mathrm{Tr}\left[D^{-1\dagger}(n,0)D^{-1}(0,n)\right] \\
&\equiv -\sum_n \tilde{\zeta}_H(n)\,\mathrm{Tr}\left[D^{-1\dagger}(n,0)D^{-1}(n,0)\right], \qquad (3.58)
\end{aligned}$$

with $\tilde{\zeta}_H(n) = (-1)^{n_1+n_2+n_3+n_4}\phi_H$. We have used $D^{-1}(0,n) = (-1)^{n_1+n_2+n_3+n_4}D^{-1}(n,0)$ in the last step. Here, we can make an important observation regarding the phases in the correlator and in the susceptibility: By construction, the phase of the susceptibility $\tilde{\zeta}_H(n)$ and the phase of the corresponding correlator from equation (3.42) $\zeta_{H\pm H'}(n)$ will only differ in at most n_4. For instance, we may have a look at the examples in section 3.1.3 and compare $\zeta_{\mathbb{1}\pm\gamma_4\gamma_5}(n) = (-1)^{n_1+n_2+n_3}$ and $\tilde{\zeta}_{\mathbb{1}}(n) = (-1)^{n_1+n_2+n_3+n_4}$ or $\tilde{\zeta}_{\gamma_4\gamma_5}(n) = (-1)^{n_1+n_2+n_3}$. Therefore, we can simply sum over the correlator $G_{H\pm H'}$ multiplied by a n_4-dependent phase factor to compute the susceptibilities. For example, to get the susceptibility of the scalar channel we use

$$\chi_{\mathbb{1}} = \sum_{n_4}(-1)^{n_4}G_{\mathbb{1}\pm\gamma_4\gamma_5}(n_4). \qquad (3.59)$$

This means that we can compute pure, single state susceptibilities from staggered correlators, even though the correlators themselves mix two different states.

However, when using staggered correlators to analyze symmetry restorations, we have to make an important note regarding the scalar channel for light quarks and staggered correlators. Due to taste violations, the staggered version of the scalar iso-vector may decay into two pions and other unphysical states [95]. Thus, the mass of the corresponding correlator appears to be too light. Nevertheless, as the corresponding state still does involve the correct quantum numbers, the quantity $\chi_\pi - \chi_{a_0}$ still reflects a measure of the brokenness of the $U_A(1)$ symmetry.

3.2. Renormalization

Our construction of lattice QCD is based on the bare QCD action and when describing observables, like the correlators above, we carelessly ignored renormalization. Indeed the lattice formulation of QCD serves as a regulator and thus, in order to perform a correct continuum extrapolation, hadronic correlation functions have to be renormalized. Here we shortly summarize the renormalization constants for hadronic correlators in quenched theory for clover improved Wilson fermions used in this work.

In general the renormalization of a local hadronic interpolator O_H is summarized by

$$O_{H,\text{ren.}} = \frac{2\kappa}{a^3} Z_H O_H, \tag{3.60}$$

where Z_H is the renormalization factor and κ is the hopping parameter.

For the vector channel the renormalization constant Z_V has been determined non-perturbatively for almost vanishing quark masses and is given by [96]

$$Z_V(g^2) = \frac{1 - 0.7663g^2 + 0.0488g^4}{1 - 0.6369g^2}. \tag{3.61}$$

When introducing quark masses, this has to be modified according to

$$Z_V(g^2, m_q) = Z_H(g^2)(1 + b_H(g^2)m_q), \tag{3.62}$$

with m_q being the bare quark mass. Also b_H has been determined non-perturbatively and can be calculated according to

$$b_V = \frac{1.0 - 0.6518g^2 - 0.1226g^4}{1.0 - 0.8467g^2}. \tag{3.63}$$

In our calculations we estimated the quark masss from equation (2.23) using the values for the critical hopping parameter given in reference [36].

For the pseudoscalar channel, no non-perturbative renormalization constants are currently available, and therefore, we use the perturbative one- and two-loop results from reference [97]. The final formula for the two-loop renormalization constant Z_P reads

$$\begin{aligned} Z_H^{bare}(g^2, a\mu) =& 1 + \frac{g^2}{16\pi^2}(6\ln(a\mu) + z_1) \\ &+ \left(\frac{g^2}{16\pi^2}\right)^2 (l_1 \ln(a\mu)^2 + l_2 \ln(a\mu) + z_2), \end{aligned} \tag{3.64}$$

where the coefficients l_1, l_2, z_1 and z_2 are functions of the clover coefficient c_{sw} and can be read off in [97]. Here μ corresponds to the renormalization scale in the $\overline{\text{MS}}$-scheme. Note, that the one-loop result is given by the first line. In order to estimate the uncertainties stemming from the renormalization, it makes sense to compare the one and two-loop results.

As the non-perturbatively calculated renormalization constants deviate far from the perturbative ones, tadpole improvement was introduced to include information from lattice results into the perturbative calculation [98, 99]. After doing so, the pseudoscalar renormalization constant reads [100]

$$\begin{aligned} Z_H(g^2_{LAT}, a\mu) = u_0 \Bigg(& 1 + \frac{g^2_{LAT}}{16\pi^2}(6\ln(a\mu) + z_1 + C_F\pi^2) \\ & + \left(\frac{g^2_{LAT}}{16\pi^2}\right)^2 (l_1 \ln(a\mu)^2 + (l_2 - 16\pi^2 p_1 6) - r_1 6 \ln(a\mu)) \\ & + z_2 - r_2 - 16\pi^2 p_1 (z_1 - r_1) + r_1^2 - r_1 z_1) + \mathcal{O}(g^6_{LAT}) \Bigg), \end{aligned} \tag{3.65}$$

where u_0 may be approximated using the fourth root of the plaquette

$$u_0 \approx \Big\langle \frac{1}{N_c} \sum_n \operatorname{Re}\operatorname{Tr} U_{\mu\nu}(n) \Big\rangle^{1/4} \tag{3.66}$$

and with $C_F = 4/3$, $g^2_{\text{LAT}} = g^2/u_0^4$, $p_1 = 1/3$ and $p_2 = -\frac{2r_2+3r_1^2}{128\pi^4}$. The coefficients r_1 and r_2 may be found in [101]. In order to perform the computation, we still need to know how to compute $g_{\overline{MS}}$ from the lattice coupling g. One possibility is to use the potential scheme (V-scheme) as an intermediate step. In that scheme, the plaquette may be expanded as

$$-\ln(u_0^4) = \frac{C_F g_V^2(\mu^\star)}{4}\left(1 - \frac{g_V^2(\mu^\star)}{4\pi}\left(\frac{11N_c}{12\pi}\ln\left(\frac{6.7117}{\mu^\star a}\right)^2\right)\right) + \mathcal{O}(g_V^6(\mu^\star)). \tag{3.67}$$

Choosing the scale to be $\mu^\star = \frac{3.4018}{a}$ gives the best matching [102]. Together with the relation $\Lambda_{\overline{\text{MS}}} = 0.6252\Lambda_V$ [98] and

$$g^{-2}(a) = 2\beta_0 \ln\left(\frac{1}{a\Lambda}\right) + \frac{\beta_1}{\beta_0}\ln\left(2\ln\left(\frac{1}{a\Lambda}\right)\right) \tag{3.68}$$

g_V is used to evaluate the coupling in the $\overline{\text{MS}}$ scheme.

The change from the lattice to the $\overline{\text{MS}}$ scheme has consequences for the pseudoscalar renormalization. In order to have the same anomalous dimension as the scalar correlator, the pseudoscalar correlator needs to be computed with an additional factor Z_5 given as [46, 103]

$$Z_5 = 1 - \frac{g^2 C_F}{2\pi^2} + \frac{g^4 C_F}{128\pi^4}\frac{N_c + 2N_f}{9} + \mathcal{O}(g^6). \tag{3.69}$$

3.3. Spectral functions

In section 3.1 we have already defined the so called spectral function as a sum over delta peaks corresponding to different states with the same quantum numbers for zero temperature. For higher temperature, however, the delta peaks start to broaden and we get a continuous function that holds the entire information about the modification of bound states in the hot medium. In this section we will give an overview about the general definition of the spectral function as well as its connection to Euclidean current-current correlators in lattice QCD. Later, we derive the connection between the spectral function and transport properties. Note, that we mainly follow [104] and [105] here.

We start by rewriting the two-point function of hadronic correlators in a more general way called Wightman correlation functions:

$$\begin{aligned} G^{>}(t) &\coloneqq \langle O(t)O(0)\rangle \\ G^{<}(t) &\coloneqq \langle O(0)O(t)\rangle = G^{>}(-t), \end{aligned} \tag{3.70}$$

where $O(t)$ is any kind of operator in the Heisenberg picture. Note that t corresponds to real time here. Let us now calculate the thermal average using the density matrix

$$\rho = \frac{1}{Z} e^{-\beta H} \tag{3.71}$$

as a sum over the energy eigenstates:

$$\langle A\rangle = \mathrm{Tr}[\rho A] = \frac{1}{Z}\sum_n e^{-\beta E_n} \langle n|\, A\, |n\rangle\,. \tag{3.72}$$

With the standard definition of time evolution in the Heisenberg picture,

$$\mathrm{e}^{-\beta H} A(t) e^{\beta H} = A(t+i\beta) \tag{3.73}$$

we find the Kubo-Martin-Schwinger (KMS) relation,

$$G^{>}(t) = G^{>}(-t-i\beta). \tag{3.74}$$

Translating this relation into frequency space by Fourier transforming the Wightman correlation functions

$$\begin{aligned} G^{>}(\omega) &= \int_{-\infty}^{\infty} \mathrm{d}t \mathrm{e}^{i\omega t} G^{>}(t) \\ G^{<}(\omega) &= \int_{-\infty}^{\infty} \mathrm{d}t \mathrm{e}^{i\omega t} G^{<}(t) \end{aligned} \tag{3.75}$$

we arrive at

$$G^{<}(\omega) = G^{>}(-\omega) = \mathrm{e}^{-\beta\omega} G^{>}(\omega). \tag{3.76}$$

At this point we also look at the expectation value of the commutator,

$$G(t) = i\,\mathrm{Tr}\{\hat{\rho}[O(t), O(0)]\} = i\left(G^{>}(t) - G^{<}(t)\right), \tag{3.77}$$

which satisfies

$$G(-t) = -G(t) \quad \text{and} \quad G^{\dagger}(t) = G(t^{*})^{*}, \tag{3.78}$$

and now we can define the spectral function as its Fourier transform:

$$\rho(\omega) := \frac{1}{2\pi i}\int_{-\infty}^{\infty} \mathrm{d}t e^{i\omega} G(t) = G^{>}(\omega) - G^{<}(\omega). \tag{3.79}$$

Using the KMS relation we may also write this the other way around, so that the Wightman correlators are expressed as a function of the spectral function itself:

$$G^{>}(\omega) = \frac{2\pi \mathrm{e}^{\beta\omega}}{\mathrm{e}^{\beta\omega}-1}\rho(\omega) \quad \text{and} \quad G_{<}(\omega) = \frac{2\pi}{\mathrm{e}^{\beta\omega}-1}\rho(\omega). \tag{3.80}$$

In order to connect to the Euclidean lattice correlator as well as drawing the connection to linear response theory, we will need the so called retarded correlator defined as the positive half Fourier integral over the commutator in equation (3.77)

$$G_R(\omega) = \int_0^{\infty} \mathrm{d}t \mathrm{e}^{i\omega t} G(t). \tag{3.81}$$

Then, through the properties (3.78) we rewrite the spectral function as

$$\rho(\omega) = \frac{1}{2\pi i}\left(G_R(\omega) - G_R(\omega)^*\right) = \frac{1}{\pi}\operatorname{Im} G_R(\omega). \tag{3.82}$$

This means that the spectral function is given just by the imaginary part of the retarded correlator. However, the retarded correlator is defined in real time, for which we do not have a path integral formulation. Let us now establish the connection to lattice correlators by switching to imaginary time τ and define the Euclidean correlator as

$$G_E(\tau) = G_{>}(-i\tau). \tag{3.83}$$

Now, we have all ingredients to find the spectral distribution of the hadronic correlator defined in equation (3.13). But now, we also have to take care about momentum and space coordinates $\vec{p}$ and $\vec{x}$.

Accordingly, our Euclidean correlator of interest is given by

$$G^H(\tau, \vec{p}) = \int \mathrm{d}x \left\langle O^H(\tau, \vec{x}) O^H(0, \vec{0}) \right\rangle, \tag{3.84}$$

where $O^H(\tau,\vec{x})$ is the meson interpolator from equation (3.7). Using relation (3.83) we find

$$\begin{aligned}
G^H(\tau,\vec{p}) &= \int \mathrm{d}^3\vec{x}\mathrm{e}^{i\vec{p}\vec{x}} G^H_>(-i\tau,\vec{x}) \\
&= \int \frac{\mathrm{d}\vec{\omega}}{2\pi}\mathrm{e}^{\omega\tau} G^H_>(\omega,\vec{p}) \\
&= \int_0^\infty \frac{\mathrm{d}\vec{\omega}}{2\pi}\left(\mathrm{e}^{-\omega\tau}G^H_>(\omega,\vec{p}) + \mathrm{e}^{\omega\tau}G^H_<(\omega,\vec{p})\right). \\
&= \int_0^\infty \mathrm{d}\omega \left(\frac{\mathrm{e}^{\beta\omega-\omega\tau}}{e^{\beta\omega}-1} + \frac{\mathrm{e}^{\omega\tau}}{e^{\beta\omega}-1}\right)\rho^H(\omega,\vec{p}) \\
&= \int_0^\infty \mathrm{d}\omega \frac{\cosh(\omega(\tau-\beta/2))}{\sinh(\omega\beta/2)}\rho^H(\omega,\vec{p}) \\
&=: \int_0^\infty \mathrm{d}\omega K(\omega,\tau)\,\rho^H(\omega,\vec{p}),
\end{aligned} \tag{3.85}$$

where $K(\omega,\tau)$ is often called the kernel.

Here, a major problem in the reconstruction of the spectral function becomes visible: The exact determination of the spectral function using the above equations is impossible, as the inversion of the integral is a so called ill-posed problem. This means that, due to the many degrees of freedom, a solution is not available even for arbitrary fine lattices. Methods to still extract spectral information from the hadronic correlator are presented in the next section.

3.4. Linear response theory and the qualitative shape of the spectral function

Till now we have only considered physics in equilibrium. However, the quark-gluon plasma created in heavy ion collisions obviously cannot be fully in equilibrium as the system cools down and expands at the same time. Moreover, when the resulting particles hit the detectors, the medium is totally gone and we only observe non-interacting particles created at the chemical freeze out. Thus, the evolution of the medium cannot be observed directly and its former state can only be estimated using descriptive models. These models heavily depend on transport properties of the medium.

For the same reasons, these transport properties cannot be measured directly. Also, due to the strong coupling in QCD, an analytic approach is difficult to apply. At this point, lattice QCD may help to find the transport properties of the medium. In the following we will use linear response theory to find that the spectral function contains information about the transport properties of the medium as well. The advantage of linear response theory is that the deviation from the equilibrium is introduced as a small external source. Subsequently we can infer transport properties even from hadronic correlators calculated in equilibrium.

The idea of linear response theory is to disturb the medium by introducing a small potential to the Hamiltonian as

$$H'(t) = H + H_{\text{ext}}(t). \tag{3.86}$$

Then, the expectation value is modified according to

$$\langle\psi'|\, O(\vec{x},t)\,|\psi'\rangle = \langle\psi|\, U^{-1}(t)O(\vec{x},t)U(t)\,|\psi\rangle\,, \tag{3.87}$$

where the time evolution operator is defined as usual:

$$U(t) = \exp\left(-i\int_{-\infty}^{t}\mathrm{d}t' H_{\mathrm{ext}}(t')\right). \tag{3.88}$$

Since the disturbance is small we may expect that the reaction of the medium is of linear order. Therefore, we consider only linear terms and summarize the effects of of the perturbation by subtracting the unperturbed expectation value:

$$\begin{aligned}\delta\,\langle O(t)\rangle &\equiv \langle\psi'|\, O(\vec{x},t)\,|\psi'\rangle - \langle\psi|\, O(\vec{x},t)\,|\psi\rangle \\ &= \int_{-\infty}^{t}\mathrm{d}t'\,\langle\psi|\,[H_{\mathrm{ext}}(t'),O(\vec{x},t)]\,|\psi\rangle\,. \end{aligned}\tag{3.89}$$

Considering an external source $h(\vec{x},t)$ that couples to the observable itself,

$$H_{\mathrm{ext}} = \int \mathrm{d}^3x h(\vec{x},t)O(\vec{x},t), \tag{3.90}$$

we find the connection to the retarded correlator

$$\begin{aligned}\delta\,\langle O(\vec{x},t)\rangle &= -i\int_{-\infty}^{t}\mathrm{d}t'\int\mathrm{d}x' h(\vec{x}',t')\,\langle[O(\vec{x},t),O(\vec{x}',t')]\rangle \\ &= \int_{-\infty}^{t}\mathrm{d}t'\int\mathrm{d}x' h(\vec{x}',t')G_R(\vec{x},t,\vec{x}',t') \end{aligned}\tag{3.91}$$

Then, equation (3.82) leads to the connection to the spectral function. When switching to frequency-momentum space, this transforms to

$$\delta\,\langle O(\vec{x},t)\rangle = h(\omega,\vec{p})G_R(\omega,\vec{p}). \tag{3.92}$$

Thus, the change in the medium is given by the external source multiplied with the unperturbed retarded correlator. It follows that linear response theory allows to compute transport properties of the medium from an ensemble that itself is in equilibrium.

The choice of the potential H_{ext} depends on the observable for which we want to compute transport properties. In this thesis, we focus on the diffusion of heavy quarks through the medium. From the heavy quark mass $M >> T$ and its momentum $p \sim \sqrt{T/M}$, it follows that it needs a lot of collisions with the thermal medium to change the momentum substantially. Therefore, it is possible to use the Langevin formalism to describe the motion of the heavy quarks [106]. As a result, the low frequency region of the spatial components of the vector spectral function $\rho_{ii}(\omega)$ for heavy quarks gets an extra contribution which is usually called transport peak and is given by [107]

$$\rho_{ii}(\omega) = \chi_s \frac{T}{M\pi} \frac{\omega\eta}{\omega^2 + \eta^2} = \chi_s \frac{D}{\pi} \frac{\omega\eta^2}{\omega^2 + \eta^2}, \tag{3.93}$$

where η is the momentum drag coefficient, D is the heavy quark diffusion coefficient and χ_s is the susceptibility for the zero component of the vector channel, given by

$$\chi_s = \int_0^{1/T} \mathrm{d}\tau G_{\gamma_0}(\tau). \tag{3.94}$$

From equation (3.93) we find, that the heavy quark momentum diffusion coefficient may be directly computed from the spectral function as

$$D = \frac{\pi}{3\chi_s} \lim_{\omega\to 0} \sum_{i=1}^{3} \frac{\rho_{ii}(\omega)}{\omega}. \tag{3.95}$$

However, we still have to extract the spectral function from the lattice correlator first. To reduce the amount of parameters, we need as much information about the spectral function as possible. Some of this information can be inferred from qualitative considerations:

In equation (3.5) we have already motivated that, in the case of zero temperature, the spectral function consists of peaks corresponding to the different energy eigenstates of a hadronic particle interpolator. While these peaks are of narrow, δ-like structure for relatively stable particles, unstable particles like the ρ resonance produce rather broad contributions to the spectral function. For higher temperatures, the medium starts to influence the bound states and the peaks start to broaden. In the high frequency region of the spectral function, quarks are already asymptotically free, and a continuum of states arises in the spectral function. When further increasing the temperature above the QCD phase transition, quarks are no longer confined, so we cannot expect expect bound states at all. The spectral function will then be an analytic, continuous function throughout its whole range. At even higher temperatures, that is in the completely free quark limit where no interactions are relevant, it is possible to derive an analytic expression for the spectral function which reads [108, 109][2],

$$\begin{aligned}\rho_{\text{free}}(\omega, m_q) = {} & \frac{N_c}{16\pi^2}\theta(\omega^2 - 4m_q^2)\omega^2 \tanh\left(\frac{\omega}{4T}\right)\sqrt{1 - \left(\frac{2m_q}{\omega}\right)^2} \\ & \cdot \left[\left(a_H^{(1)} - a_H^{(2)}\right) + \left(\frac{2m}{\omega}\right)^2 \left(a_H^{(2)} - a_H^{(3)}\right)\right] \\ & + N_c \left[\left(a_H^{(1)} + a_H^{(3)}\right) I_1 + \left(a_H^{(2)} - a_H^{(3)}\right) I_2\right] \omega\delta(\omega),\end{aligned} \tag{3.96}$$

---

[2] Note, that the formula in [108] had a typo. This one is taken from [109]

	$a_H^{(1)}$	$a_H^{(2)}$	$a_H^{(3)}$
ρ_S	1	-1	1
ρ_P	1	-1	-1
ρ_V^{ii}	3	-1	-3
ρ_V^{00}	1	1	1
ρ_{AV}^{ii}	3	-1	3
ρ_{AV}^{00}	1	1	-1

Table 3.5: Coefficients for the free spectral function in equation (3.96) for different meson channels

where

$$I_1 = -2\int_k \frac{\partial n_F(\omega_k)}{\partial \omega_k} \quad \text{and} \quad I_1 = -2\int_k \frac{k^2}{\omega_k}\frac{\partial n_F(\omega_k)}{\partial \omega_k} \tag{3.97}$$

and $n_F = 1/(e^{\omega/T}+1)$. The coefficients $a_H^{(i)}$ are given in table 3.5.

Independent of the particle channel, this formula reveals a threshold at $2m_q$ below which the spectral function is, except for the zero mode at vanishing frequency, equal to zero. Above this threshold, a continuum contribution takes place. This threshold has a descriptive interpretation: As the quarks appear to be free, the propagator is not restricted to bound states only, and a transition is possible at all kinds of energies that exceed the mass of the two participating quarks. This is in stark contrast to the discrete spectral function at zero temperature. Nevertheless, it is intuitive to expect a smooth transition between these two extreme cases.

In figure 3.2 we display a sketch of the spectral function for heavy quarkonium, e.g. charmonium, at different temperatures above the transition temperature. In the limit $T \to \infty$, we plot the free spectral function for the vector channel. When lowering the temperature, the continuum threshold shifts upwards and starts to smooth out. At the same time, the peak structure corresponding to certain bound states gets restored. For heavy quarks one may expect that bound states even survive in the hot medium. In that case, a peak would may be located also in the continuum region. In addition, the transport peak in the form of a δ-function at zero frequency starts to broaden and takes the form of a Lorentzian.

Even though we now have a rough understanding of the shape of the spectral function, we still have to deal with a lot of unknown parameters and the inversion problem is still ill-posed. In order to tackle the problem, many statistical methods have been suggested. The widely used maximum entropy method (MEM) as well as the rather recent BR-method [110] calculate the most probable spectral function based on a default model as input using Bayesian theory [111, 112]. Other Bayesian methods, like statistical analytic interference (SAI) [113, 114] or the stochastic optimization method (SOM) [115] use Monte Carlo averaging over many possible realizations and assign a certain weight to it. For a detailed comparison of these methods, see also [116]. Instead of reconstructing the spectral function itself, the method of Backus and Gilbert estimates an averaged version thereof [117, 118].

All these methods come with large statistical errors, and often it is not possible to get reliable information. Still, it is possible to observe changes of the spectral function at different

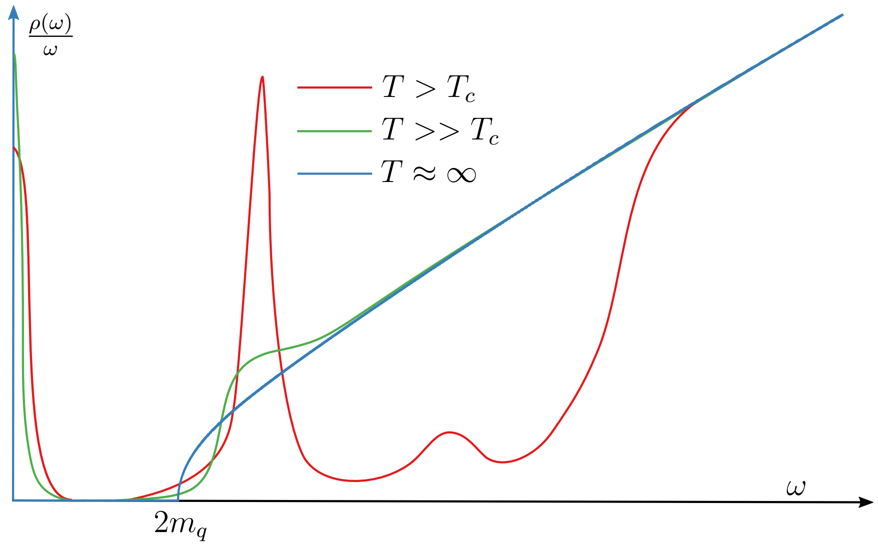

Figure 3.2: Sketch of a heavy quark current-current spectral function for the vector channel at different temperatures. The high temperature limit corresponds to the free spectral function from equation for the vector channel (5.1).

temperatures indirectly: As changes in the spectral functions also change the correlator itself, one may compare ratios of correlators with different temperatures to indirectly observe temperature effects. However, such temperature effects may also stem from the change of the kernel. One way to get rid of the kernel's contribution is the so called reconstructed correlator which is defined as

$$G_{\text{rec}}(\tau, T; T') = \int_0^\infty \rho(\omega, T') K(\omega, \tau, T) d\omega \tag{3.98}$$

where $T' < T$, $T' = (aN_t')^{-1}$, $N_\tau' = mN_\tau$, $m \in \mathbb{Z}$. By construction, in the reconstructed correlator we evaluate the spectral function at a different, warmer temperature than the temperature of the kernel. By using the relation

$$\frac{\cosh[\omega(\tau - N_\tau/2)]}{\sinh(\omega N_\tau/2)} = \sum_{\tau'=\tau;\tau'+=N_\tau}^{N_\tau'-N_\tau+\tau} \frac{\cosh[\omega(\tau' - N_\tau'/2)]}{\sinh(\omega N_\tau'/2)} \tag{3.99}$$

we may rewrite the reconstructed correlator as

$$G_{\text{rec}}(\tau, T; T') = \sum_{\tau'=\tau;\tau'+=N_\tau}^{N_\tau'-N_\tau+\tau} G(\tau', T'). \tag{3.100}$$

Therefore, we can calculate the constructed correlator simply by resumming another existing correlator calculated on the lattice. By comparing the reconstructed correlator at temperature

T' with a correlator at temperature T, the changes are directly related to changes in the spectral function itself.

Another way to indirectly observe changes of the spectral function is to look at the screening correlator. It can be shown that its relation to the spectral function is given by

$$G_{\mathrm{scr}.H}(n_z, T) = \int_0^\infty \mathrm{d}\omega \frac{2}{\omega} \int_\infty^\infty \mathrm{d}^3 p e^{ip_z n} \rho(\omega, p_z, T). \tag{3.101}$$

Therefore, one can conclude that all changes in the screening correlator are directly linked to changes in the spectral function. The same holds for the screening mass. It follows that the screening mass is a simple, easy to calculate quantity that reveals any kind of thermal modification of hadronic bound states.

3.5. Perturbative approach

In the last section we have motivated the shape of the spectral function at different temperatures. As those considerations where mainly based on qualitative arguments, we need to find a way to connect these considerations with the hadronic correlator measured on the lattice. One possibility is to model the general shape of the spectral function and fit this model to the correlator. Such a model may be given by connecting different perturbative results for heavy quarks at different frequency regions. This connection procedure has been described in detail for the pseudoscalar channel in reference [46]. For the vector channel the calculation goes through fully analogously. Here we will give a short summary about the different perturbative regions and how to connect them.

To do so, we first need to distinguish the regions in the spectral function in which different physics takes place. In this work we only consider particles at rest, and therefore, the energy of the decay products is of order $\omega/2$. For very high energies, $\omega \gg 2M \gg \pi T$, where M denotes the mass of any kind of decay particle, thermal effects are suppressed as the kinetic energy of the decay products is larger than the kinetics from the medium. In this region vacuum perturbative calculations may be performed [46, 119]. For frequencies of the order $\omega \sim 2M$, thermal effects start to become important. Here, one may use potential non-relativistic QCD (pNRQCD). However, for even smaller frequencies, way below the threshold of $\omega \approx 2M$, the thermal results overestimate the spectral function again. This has to be corrected with a phenomenological damping factor.

In the UV-region, the spectral function has been computed up to $\mathcal{O}(\alpha_s^3)$ for the pseudoscalar correlator [46] and up to $\mathcal{O}(\alpha_s^4)$ for the vector channel [120, 121]. When rewriting the spectral function in the vector channel as

$$\rho_V(\omega) = \frac{3\omega^2}{4\pi} R(\omega^2) \tag{3.102}$$

and in the pseudoscalar channel as

$$\rho_P(\omega) = \frac{3\omega^2}{8\pi} m^2(\mu) R(\omega^2) \tag{3.103}$$

it may be expanded in the $\overline{\mathrm{MS}}$-scheme as

$$\begin{aligned}R(\omega^2) = r_{0,0}& \\ &+ r_{1,0}\frac{\alpha_s(\bar{\mu})}{\pi} \\ &+ \left(r_{2,0} + r_{2,1}\ln\left(\frac{\bar{\mu}}{\omega}\right)\right)\frac{\alpha_s^2(\bar{\mu})}{\pi^2} \\ &+ \left(r_{3,0} + r_{3,1}\ln\left(\frac{\bar{\mu}}{\omega}\right) + r_{3,2}\ln^2\left(\frac{\bar{\mu}}{\omega}\right)\right)\frac{\alpha_s^3(\bar{\mu})}{\pi^3} \\ &+ \left(r_{4,0} + r_{4,1}\ln\left(\frac{\bar{\mu}}{\omega}\right) + r_{4,2}\ln^2\left(\frac{\bar{\mu}}{\omega}\right) + r_{4,3}\ln^3\left(\frac{\bar{\mu}}{\omega}\right)\right)\frac{\alpha_s^4(\bar{\mu})}{\pi^4},\end{aligned} \tag{3.104}$$

where the coefficients $r_{i,j}$ for the pseudoscalar channel can be found in [46] and for the vector channel in [121] and $m(\mu)$ is the quark mass in the $\overline{\mathrm{MS}}$-scheme. A way to relate $m(\bar{\mu})$ in the $\overline{\mathrm{MS}}$-scheme and the pole mass M in the on-shell scheme is described in [46].

In the thermal region ($\omega \approx 2M$) and non-relativistic regime ($v \ll 1$), the spectral function for the pseudoscalar channel and the vector spectral function are related through [46]

$$\rho_P^{\mathrm{NRQCD}} = \frac{M^2}{3}\rho_V^{\mathrm{NRQCD}}. \tag{3.105}$$

The latter may be computed from the Wightman correlator [122]:

$$\rho_V^{\mathrm{NRQCD}}(\omega) = \frac{1}{2}\left(1 - e^{-\frac{\omega}{T}}\right)\int_{-\infty}^{\infty}\mathrm{d}t e^{i\omega t}G_>(t;\vec{0},\vec{0}), \tag{3.106}$$

where we get $G_>(t,\vec{0},\vec{0})$ by solving the Schrödinger equation with

$$\left\{i\partial_t - \left[2M + V(r) - \frac{\nabla_r^2}{M}\right]\right\}G_>^V(t;\vec{r},\vec{r}') = 0, \quad t \neq 0 \tag{3.107}$$

$$G_>^V(t;\vec{r},\vec{r}') = 6N_c\delta^{(3)}(\vec{r} - \vec{r}'). \tag{3.108}$$

The interaction modelling potential $V(r)$ has been computed using Hard Thermal Loop resummed perturbation theory in [123] to first non-trivial order and is given by

$$V(r) = -\alpha_s C_F\left[m_D\frac{\exp(-m_D r)}{r}\right] - i\alpha_s C_F T\phi(m_D r) + \mathcal{O}(\alpha_s^2), \tag{3.109}$$

where m_D is the Debye mass and $\phi(x)$ reads

$$\phi(x) \equiv 2\int_0^{\infty}\frac{\mathrm{d}z z}{(z^2+1)^2}\left[1 - \frac{\sin(zx)}{zx}\right]. \tag{3.110}$$

For short distances $r \ll 1/m_D$, the potential should be replaced with the free vacuum static potential given in [124].

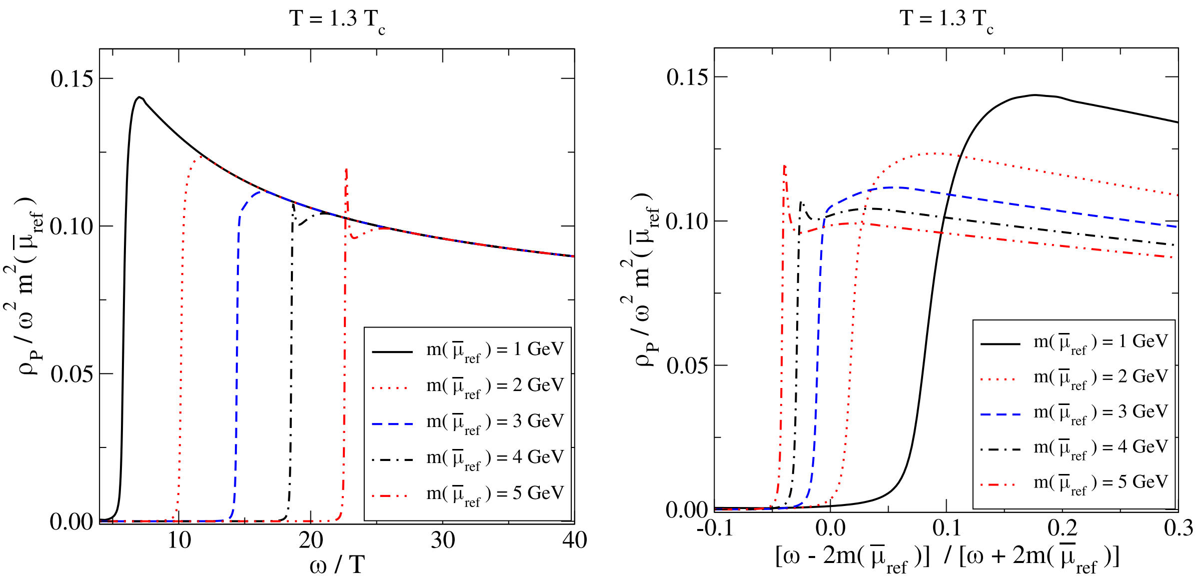

Figure 3.3: Pseudoscalar spectral functions with different quark masses as input in the vicinity of the threshold at $2M$. Taken from reference [46].

As already mentioned, below the threshold, the spectral function overshoots the true result [46]. In order to compensate for that effect one may multiply the function ϕ with

$$\theta(2M-\omega)e^{-|\omega-2M|/T}. \tag{3.111}$$

As a final step, we have to connect the UV-region and the thermal part. As there are large uncertainties in the amplitude of ρ^{NRQCD}, we normalize it with a free coefficient $\rho^{\mathrm{QCD}} = A\rho^{\mathrm{NRQCD}}$ such that the connection between the two regions is continuous. Further we require that the derivative at some certain $\omega_{\mathrm{con.}} \sim 2.3...2.6M$ is continuous as well. In figure 3.3, we show the resulting spectral functions for the pseudoscalar channel as an example.

4. Methodology

On encounters many statistical and technical complications during the practical analysis of lattice QCD. For instance one major problem of analysing screening masses is the convergence of the corresponding fits. In this section we collect different techniques that we have used and developed to circumvent such problems.

4.1. Correlations in lattice QCD

In lattice QCD, observables undergo statistical autocorrelations due to importance sampling using Markov chains. As each configuration is generated based on the previous configuration, correlations between these configurations appear. This is why the use of standard statistical tools underestimate the statistical error of observables. One can solve this problem by throwing away intermediate configurations, so that subsequent configurations are uncorrelated. However, this drastically increases the computational effort. Instead one usually chooses a step size where correlations are still present.

The remaining autocorrelation can be examined through the so called autocorrelation time. It can be obtained by first defining the autocorrelation function

$$C_O(t) = \langle O_i O_{i+t} \rangle - \langle O_i \rangle \langle O_{i+t} \rangle \tag{4.1}$$

for different values of t. In a typical Markov chain, the autocorrelation function has an exponential descent,

$$\frac{C_O(t)}{C_O(0)} \sim \mathrm{e}^{-t/\tau}, \tag{4.2}$$

where τ is the so called exponential autocorrelation time. Often, the descent is composed of several exponential terms,

$$\frac{C_O(t)}{C_O(0)} \sim \sum_i A_i \mathrm{e}^{-t/\tau_i}. \tag{4.3}$$

The exponential autocorrelation time is then given by the largest value of those τ_i.

Additionally, correlations between different observables might occur. For instance, when analyzing quantities calculated along one of the lattice axes. Typical examples are Polyakov loop correlators or meson correlators, where each entry is correlated to its neighbors: As neighboring lattice points within one configuration are correlated, the quantity to be computed will also exhibit correlations.

In both cases, the analysis of the simulated data has be done using tools that take care of the correlations. Such tools are bootstrapping or the jackknife method which will be described in the following.

4.1.1. Bootstrapping

The idea of bootstrapping is to estimate the distribution of the central value of an observable by using random samples: Let us assume, we want to calculate the expectation value of an observable O from a data set D of size N. The computation of the observable does not undergo any limits. For example, it can be the result of a fit. First, one draws M random samples D_m of size N from the original data set D, where repetitions are allowed. The observable is then calculated on each of these samples giving a set of estimates for the observable $O_m = O(D_m)$. As an estimator for $\langle O \rangle$ and its error one might use

$$\tilde{O} = \frac{1}{M} \sum_{m=1}^{M} O_m, \quad \sigma_O = \sqrt{\frac{1}{M} \sum_{m=1}^{M} (O_k - \tilde{O})^2}. \tag{4.4}$$

However, if the distribution is highly non-Gaussian, it is better to use the median and 68% percentiles to estimate the expectation and its error.

Bootstrapping is a great tool to reduce correlations between different observables. To do so, one needs to use different samples per observable. As each observable is calculated on a different data set, this breaks up the correlations between this observables. However, it is not possible to use bootstrapping to reduce the effects of autocorrelation.

It is also possible to nest bootstraps. For instance when the final observable is computed by a fit, where one needs errors on the data to be fitted. The first bootstrap is performed to generate different samples for the fit. The errors on the data points that enter the fit may be computed by a second bootstrap that is based on the samples of the first bootstrap. Here it is important, that the second bootstrap is performed on the sample of the first bootstrap and not on the original data set.

4.1.2. Jackknife

Again, let us look at an observable O which shall be calculated on a data set D of length N. Now, one divides the data set into n blocks of length m with $N = n \cdot m$. To fulfill the last condition, one may need to drop a few data points. Next, one computes the observable O on partial data sets D_i where one of the n data blocks has been dropped. One ends up with n values $O(D_i)$ which are computed on $N - m$ data points. These values $O(D_1) \dots O(D_n)$ are transformed into so called pseudo values,

$$O_i = n \cdot O(D) - (n-1) O(D_i). \tag{4.5}$$

These pseudo values may be used to estimate expectation value and its error as usual:

$$\tilde{O} = \frac{1}{n} \sum_{i=1}^{n} O_i, \quad \sigma_O = \sqrt{\frac{1}{N(N-1)} \sum_{i=1}^{n} (O_i - \tilde{O})^2} \tag{4.6}$$

The jackknife method corrects for effects of the autocorrelation of observables, but it is not possible to remove correlations between different observables.

The choice of the block length should be larger than the autocorrelation length. On the other hand a too large block size leads to too few values of O_i. In practice one should reduce the number of blocks, until a maximum in the error size is reached. This is usually the case for roughly 20 blocks.

4.2. Correlated fits

When performing fits on lattice data, it often happens that the data points that enter the fit are not independent. This means that the data points actually carry less information than if they are independent. This effect has to be corrected using correlated fits which we describe in the following.

We start with the definition of a fit in the sense of maximum likelihood estimation. Assume we have observed the outcome $\bar{\mathbf{y}} = \{\bar{y}_1, \bar{y}_2, \ldots, \bar{y}_N\}$ of an experiment given the input data $\mathbf{x} = \{x_1, x_2, \ldots, x_N\}$. We have put the bar above $\bar{\mathbf{y}}$ to indicate that this outcome may stem from averaging over several individual measurements of some observable y_i:

$$\bar{y}_i = \frac{1}{M_i} \sum_{k=1}^{M_i} y_{i,k}. \tag{4.7}$$

Now, we are interested in finding those parameters $\theta = \{\theta_1, \theta_2, \ldots, \theta_M\}$ of some model $f(\theta, \mathbf{x})$ that maximize the probability that we observe $\bar{\mathbf{y}}$ given θ and $\mathbf{x}$. In other words, we search for a maximum of the so called likelihood function $L_{\bar{\mathbf{y}},\mathbf{x}}(\theta) = P(\bar{\mathbf{y}}|\theta, \mathbf{x})$. Usually, the probability density function $P(\bar{\mathbf{y}}|\theta, \mathbf{x})$ is not known a priori and assumptions based on the spread of the data points have to be made about it.

In many cases the spread of the individual elements $\bar{y}_i$ is found to follow a Gaussian distribution. In that case, the outcome of the experiment often also provides an estimator for the variance σ_y^2, and the likelihood function is given by

$$L_{\bar{\mathbf{y}},\sigma_y,x}(\theta) = \left(\prod_{i=1}^{n} \frac{1}{\sqrt{2\pi\sigma_{y,i}^2}} \right) \exp\left(\sum_{i=1}^{n} -\frac{(\bar{y}_i - f(\theta, x_i))^2}{2\sigma_{y,i}^2} \right). \tag{4.8}$$

Maximizing this function is equivalent to minimizing its exponent

$$\chi^2 = \sum_{i=1}^{n} \frac{(\bar{y}_i - f(\theta, x_x))^2}{\sigma_{y,i}^2}, \tag{4.9}$$

which is the usual least square fitting that is widely used. In most cases, an analytical solution for this minimization is not available and numeric algorithms have to be used. This becomes tricky if there is more than one local minimum of χ^2. In that case on has to use start parameters that are near the global minimum as an initial guess for the minimization algorithm.

Note that the above equations are only valid if the individual elements of $\bar{\mathbf{y}}$ are completely independent of each other. This is indeed the case for many experiments, but for data observed from lattice QCD, many observables are correlated. This means that there is actually less information in the data than it seems. To take care of this, the covariance C takes the place of the variance, and the likelihood functions is given by

$$L_{\bar{\mathbf{y}},C}(\theta) = \frac{1}{(2\pi)^{n/2}\sqrt{\det C}} \exp\left(-\frac{1}{2}\chi^2\right), \tag{4.10}$$

$$\chi^2 = \sum_{i,j=1}^{n} \left[\bar{y}_i - f(\theta, x_i)\right] (C^{-1})_{ij} \left[\bar{y}_j - f(\theta, x_j)\right]. \tag{4.11}$$

The covariance matrix either has to be known from theoretical considerations or can be estimated from individual measurements of our observable y_i:

$$C_{ij} = \frac{1}{N-1} \sum_{k=0}^{N} (y_{i,k} - \bar{y}_i)(y_{j,k} - \bar{y}_j). \tag{4.12}$$

Note that this is the covariance matrix of the individual values. To get the covariance matrix of the mean values, this has to be normalized with an extra $1/N$. As we commonly want to fit the mean values, this is what should be used in the fit.

To calculate the covariance matrix in this way, lots of statistics are needed. Too few statistics often leads to strange fit results that are far off or leads to numerical uncertainties. Even for good statistics, correlated fits are found to be less stable. This is especially the case if the fit model does not reasonably match to the data. It is also essential to start with good initial parameters, as correlated fits tend to have lots of local minima. At this point we found it reasonable to try as many minimization algorithms as possible and select the one with the smallest χ^2.

In addition, the covariance matrix is almost singular in many situations, and inverting it leads to numerical uncertainties. This can be reduced by using the correlation matrix

$$X_{ij} = \frac{C_{ij}}{\sigma_i \sigma_j} \tag{4.13}$$

instead of the covariance matrix. This has to be compensated in the residual:

$$\chi^2 = \sum_{i,j=1}^{n} \left(\frac{\bar{y}_i - f(\theta, x_i)}{\sigma_i}\right) (X^{-1})_{ij} \left(\frac{\bar{y}_j - f(\theta, x_j}{\sigma_j}\right). \tag{4.14}$$

The correlation matrix should have a smaller condition number and therefore, is less singular. Nevertheless, one should always check for numerical problems by comparing $X^{-1}X$ against the identity matrix.

Despite all these problems, it is not possible to simply use a non-correlated fit instead, as this will underestimate the errors of the fit parameters and may even give wrong results. If a correlated fit does not work one can use bootstrapping to keep track of the correlations. This can also be used if the data are non-Gaussian distributed and will be addressed later.

Having found the minimum of the chi-squared, we still have to compute the errors or, more generally, the covariance matrix of the fit parameters. Suppose we know the best fit parameters θ_k for each individual measurement $\mathbf{y}_k$ (k refers to the measurement and not to the observable). Defining $\delta\theta_{a,k} = \bar{\theta}_a - \theta_{a,k}$ with $\bar{\theta}_a$ the mean over all $\theta_{a,k}$, the covariance matrix of the fit parameters will be given by

$$P_{ab} = \frac{1}{N-1}\sum_{k=1}^{N}\delta\theta_{a,k}\delta\theta_{b,k} \tag{4.15}$$

One way to compute $\delta\theta_{a,k}$ is to bootstrap from the original data set. However, assuming that $\theta_{a,k}$ behaves approximately linearly for small deviations in $\mathbf{y}_k$, we can also use error propagation with

$$\delta\theta_{a,k} = \sum_i \frac{\partial\theta_a}{\partial y_i}\delta y_{i,k}, \tag{4.16}$$

where $\delta y_{i,k}$ is defined as $\delta y_{i,k} = \bar{y}_i - y_{i,k}$. Inserting this into equation (4.15), we end up with

$$\begin{aligned} P_{ab} &= \sum_{i,j}\frac{\partial\theta_a}{\partial y_i}\frac{\partial\theta_b}{\partial y_j}\frac{1}{N-1}\sum_k \delta y_{i,k}\delta y_{j,k} \\ &= \sum_{i,j}\frac{\partial\theta_a}{\partial y_i}\frac{\partial\theta_b}{\partial y_j}C_{ij}. \end{aligned} \tag{4.17}$$

To perform the computation, we still do not know the derivatives $\partial\theta_a/\partial y_i$ because we do not know how θ depends on y_i. However, we know how y_i is expected to depend on θ, as this dependency is given by the fit model. With J being the Jacobian of $f(x,\theta)$, we can assume $J_{ia} = \partial f(x_i,\theta)/\partial\theta_a = \partial y_i/\partial\theta_a$ and one can easily show that the covariance matrix of the fit parameters is finally given by

$$P = (J^T C^{-1} J)^{-1}. \tag{4.18}$$

With this formula, the errors can be computed directly from the errors of the data set, but the quality of the fit has not been taken into account which results in heavily underestimated errors for bad fit models. This can be corrected by multiplying the result with $\chi^2/d.o.f$, where $d.o.f.$ is the number of degrees of freedom, i.e. $N - M$ with N being the number of data points and M being the number of fit parameters.

4.3. Ground state extraction

Having computed the correlators on the lattice, we need to extract the ground state mass according to equation (3.6) or (3.44), respectively. The methods to extract the ground state are the same for pole and screening masses. Therefore in this section we only use the notation for the pole mass, which means we are measuring the correlator in temporal direction n_τ.

There are different ways to extract the ground state, where most of them rely on the fact that higher states are sufficiently suppressed for large distances. For non-oscillating correlators, a first estimate is given by the so called effective mass m_{eff} which is implicitly defined by

$$\frac{C(n_\tau)}{C(n_\tau+1)} = \frac{\cosh(m_{\text{eff}}(n_\tau - N_\tau/2))}{\cosh(m_{\text{eff}}(n_\tau + 1 - N_\tau/2)}, \tag{4.19}$$

which has to be solved numerically for m_{eff}.

For staggered correlators, i.e. with an oscillating part, the definition of the effective mass is more involved [125]. The idea is to use four subsequent points to solve the non-linear equation system of the four parameters given by the two ground states. To be able to solve this equation system analytically, we have to neglect contributions from the periodic boundary conditions and assume

$$G(n_\tau) \approx A_{no}\exp(-m_{no}n_\tau) - (-1)^{n_\tau} A_{osc}\exp(-m_{osc}n_\tau). \tag{4.20}$$

Further defining $g_i = G(n_\tau = i)$, $x_- = \exp(-m_{no})$ and $x_+ = \exp(-m_{osc})$ leads to two equations:

$$Ax_\pm \mp Bx_\pm + C = 0. \tag{4.21}$$

These may be solved under the condition $AC < 0$ and we get

$$x_\pm = \pm\frac{B}{2A} + \frac{\sqrt{B^2 - 4AC}}{2|A|} \tag{4.22}$$

where A, B, and C are defined as $A = g_1^2 - g_2 g_0$, $B = g_3 g_0 - g_2 g_1$ and $C = g_2^2 - g_3 g_1$.

From this we define the effective oscillating and non-oscillating correlator, as well as their effective mass:

$$\begin{aligned} G_{no}(n_\tau) &= A_{no}\exp(-m_{no,\text{eff}}n_\tau) = \frac{g_1 + g_0 x_+}{x_- + x_+} \\ G_{osc}(n_\tau) &= A_{osc}\exp(-m_{osc,\text{eff}}n_\tau) = \frac{g_1 - g_0 x_-}{x_- + x_+}. \end{aligned} \tag{4.23}$$

Assuming that for large distances higher states are suppressed, the so defined effective masses should reproduce the ground state mass. The problem with this method is that the errors of correlators typically rise for large distances. This is why the effective mass becomes imprecise exactly in the region of interest. One way to tackle this problem is to perform an exponential fit on the mass plateau of the effective masses [53]. Yet, for staggered correlators, the neglected boundary conditions in (4.20) start to become relevant in the large distance region, and the effective mass does not settle but drops down to too small values (see figure 4.1 for an example). So this method is not applicable any more.

Instead, the usual approach for staggered correlators is to perform fits on the correlator instead. As there are in principle infinitely many excited states, it is difficult to perform these fits. Adding many states to the fit function will make the fit unstable and highly dependent on the initial guess. We find that fits with up to four parameters usually work when the initial guess is roughly estimated. For staggered fits, this corresponds to a one state fit in both the oscillating and non-oscillating channels. Such a one state fit is not able to follow the correlator at short distances as higher states start to become important. Thus, the standard way to extract the ground state of a correlator is to restrict the fit to only a few states (usually two states for non-oscillating and one state for oscillating fits). This fit is performed on different intervals $[n_{\tau,\min}, n_{\tau,\max}]$ until the resulting mass settles in a plateau. For large enough $n_{\tau,\min}$ (and small enough $n_{\tau,\max}$) the higher states are sufficiently suppressed.

However, the same problem as for the effective masses arises. The region where higher states are suppressed exhibits larger errors compared to points at short distances. Therefore, points including higher states are more dominant, and the fit will follow mostly these points (see figure 4.1, left plot). This is why a plateau is usually reached only if the centered, most noisy points of the correlator are used for the fit (figure 4.1, right plot). Moreover, a one state fit often does not exhibit a plateau, as excited states contribute even at large distances (compare one state and two state fits in 4.2).

Different approaches have been suggested to solve these issues. The variational method [126, 127] computes the different states from eigenvalues of the cross correlation matrix of different interpolators. This method requires additional computation of correlators and is difficult to apply for staggered fermions.

In [128], a method that extracts excited states by subtracting the result from the effective ground state mass is introduced. As the ground state is estimated from a one state effective mass, this requires a precise correlator at large distances as well.

Another method that works with fits is to constrain the fits with beforehand known values of the fit parameters, so called priors [129]. These priors and their errors have to be known before the fit from other theoretical considerations or by experiments. There are methods to extract priors from the data itself [130]. Though, without prior knowledge, it is impossible to find priors that do not introduce a bias to the fit.

4.3.1. Automated initial guess estimation

To overcome the problems of all these methods, non-constraint, higher state fits are needed and the instabilities have to be removed. Indeed, we find that such higher state fits are possible, if the initial guess is very close to the final result. Nevertheless, the initial guess has to be known so precisely, that it is impossible to tune by hand for each parameter set. Therefore we have developed an automated fit parameter estimation routine based on a sequence of fits. This routine calculates an initial guess even for high states, which is precise enough to perform the final fit afterwards. This makes it possible to perform higher state fits for large fit intervals and this gives a reasonable plateau even for very short distances.

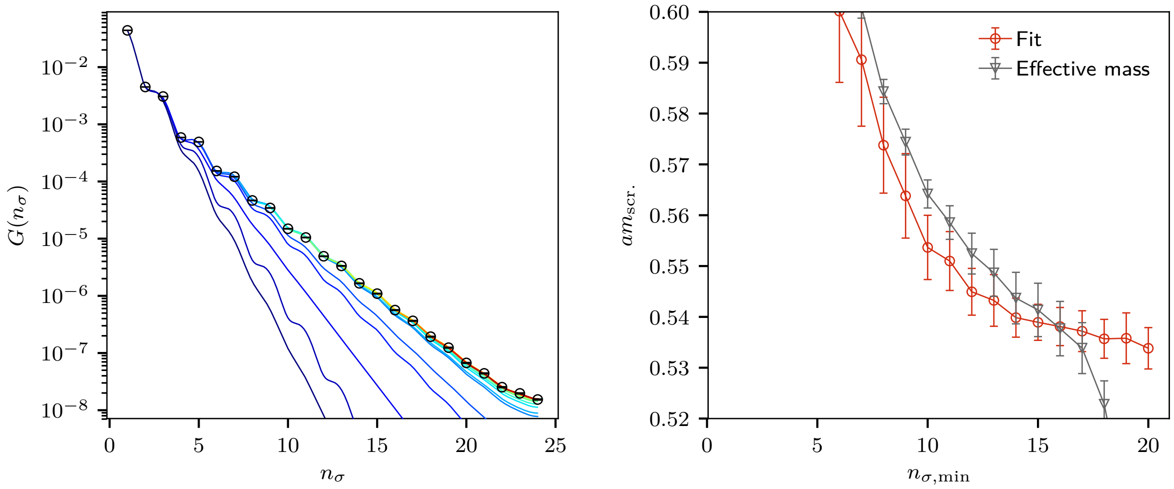

Figure 4.1: Example for a one state staggered correlator fit in a spatial direction. (HISQ action, $m_s = 20m_l$, lattice size: $48^3 \times 12$, axial vector channel for two light quarks, point source, $\beta = 8.71$). The correlator has been symmetrised and we fit only half of the correlator. Left: The correlator fit for different fit intervals. The upper limit of the fit interval has been fixed to $n_{\sigma,\mathrm{max}} = 24$, while the lower limit is varied from 1 to 20. Each fit result is visualized with a different color: For larger intervals the fit is colored in blue while for smaller intervals the color is changed to red. For a better visualization we plot only the real part, i.e. $\mathrm{Re}(-(-1)^{n_\tau}) = -\cos(\pi n_\tau)$. Right: The screening mass of the non-oscillating part in lattice units for this fit as a function of $n_{\sigma,\mathrm{min}}$ and the effective mass. In order to guide the eye we connect the data points by straight lines

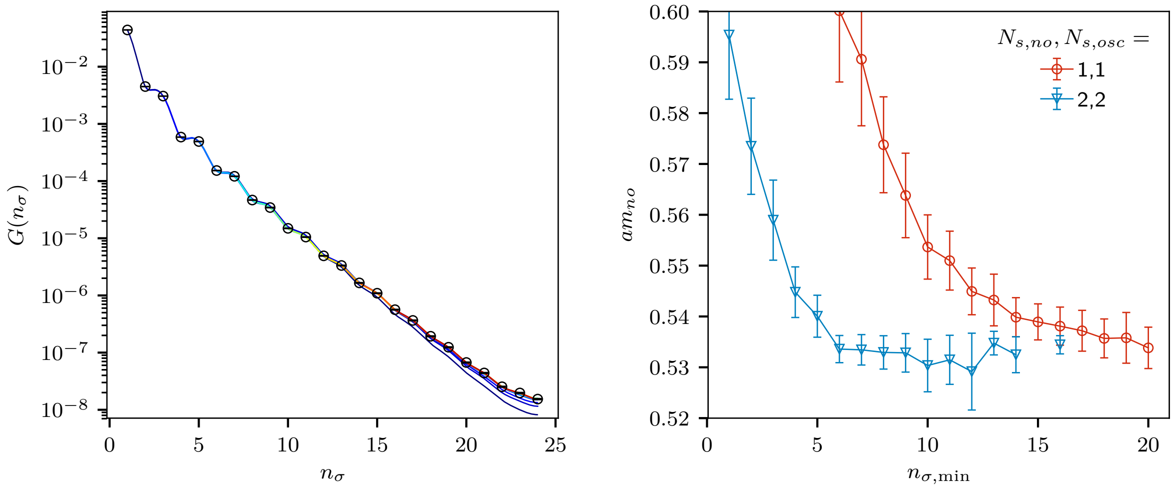

Figure 4.2: Left: Same as figure 4.1 for $N_{s,no} = N_{s,osc} = 2$. Right comparison of the corresponding mass plateaus for one and two state fits respectively. In order to guide the eye we connect the data points by straight lines

First, let us define a most general fit ansatz as

$$\begin{aligned} G_{\text{fit}}(n_\tau) = &\sum_{i=1}^{N_{s,no}} A_{no,i} \cosh[m_{no,i}(n_\tau - N_\tau/2)] \\ &- (-1)^{n_\tau} \sum_{i=0}^{N_{s,osc}} A_{osc,i} \cosh[m_{osc,i}(n_\tau - N_\tau/2)] \end{aligned} \tag{4.24}$$

where the second part is only relevant for staggered correlators. For simplicity, we restrict to $N_{s,osc} = 0$ first and will show how deal with oscillating fits later. Using the following steps it is now possible to generate an initial guess, that is close enough to perform higher states fits. As we introduce another method later, we call this routine method A.

1. First, choose a fit interval, where contributions of excited states are mostly suppressed. On this interval, we may estimate the initial guess for a simple one state fit. For $n_\tau < N_\tau/2$, we may approximate

   $$A \cosh(m(n_\tau - N_\tau/2)) \sim A' \exp(-mn_\tau) \tag{4.25}$$

   Now, if we fit the log-scaled data with a linear function $\ln(A') + mn_\tau$, we get good estimates for the start parameters.

2. Use the parameters from step 1 as initial guess to perform a one state fit on the small fit interval. The resulting parameters may be named A_1, m_1 and the resulting correlator $G_{1,\text{fit}}(n_\tau)$

3. Increase the fit interval such that roughly the next excited state is included. Then, compute $G_{2,\text{diff}}(n_\tau) = G(n_\tau) - G_{1,\text{fit}}(n_\tau)$. As we subtract the one state from the correlator, this quantity will contain information about the second state mostly.

4. Perform a one state fit on $G_{2,\text{diff}}(n_\tau)$. The resulting parameters may be named A_2, m_2.

5. The parameters A_2, m_2 can be improved: Perform a two-state fit, where parameters for the first state are used from 2 and kept fixed. Use the parameters from step 4 as start parameters for the second state. Update A_2, m_2.

6. Perform a full two-state fit using the parameters from steps 2 and 5 as start parameters. Update parameters A_1, m_1, A_2, m_2.

7. Repeat steps 3 to 6 for higher states, until the desired number of states $N_{s,no}$ is reached.

A visualization of this procedure can be found in figure 4.3.

Due to the instability of correlated fits, is is reasonable to apply the above method using uncorrelated fits. Afterwards, one final correlated fit is performed. Furthermore, we may use the symmetry of the correlator and perform the fit only on the half of the correlator: First we symmetrize the correlator:

$$G_{\text{new}}(n_\tau) = \frac{1}{2}\left(G(n_\tau) + G(N_\tau - n_\tau)\right). \tag{4.26}$$

Afterwards, the upper bound of the fit interval is kept fixed to $n_{\tau,\max} = N_\tau/2$ and only the lower bound is varied (see left plot of figure 4.1). This helps to improve the quality of the estimated covariance matrix.

Additionally it helps to normalize the correlator such that $G(N_\tau/2) = 1$. This leads to a ground state amplitude close to one, which helps a lot of minimization algorithms converge.

Note that this method also works if an excited state has a negative amplitude. One only has to change the sign of the correlator in the logarithmic estimation fits.

To apply the method A to staggered correlators, we have to split the correlator according to equation (4.23). This allows one to estimate the initial guess for the oscillating and non-oscillating part separately by applying non-oscillating fits using the above method to the split correlators. As already mentioned, the split correlators are often of bad quality. This is especially the case for noisy data. In that case, the initial guess estimated by the split correlators is not precise enough to apply the final fit. For that case, we have developed an additional routine, that works directly on the oscillating correlator. This method relies on the fact that the ground state fit of the oscillating and non-oscillating part are usually of similar size. We name the following sequence of fits method B.

1. At a small fit interval, Perform one state fits on all even points of the correlator and we name the resulting fit parameters A_e, m_e. Repeat the same for the odd points (A_o, m_o).

2. Assuming similar size of the non-oscillating and oscillating masses, the fit parameters for the combined fit may be estimated with $A_{no,1} = (A_e + A_o)/2$, $A_{osc,1} = (A_e - A_o)/2$ and $m_{no,1} = m_{osc,1} = (m_e + m_o)/2$.

3. Using the parameters from step 2 as initial guess, perform a full one state fit with oscillating and non-oscillating part.

4. Increase the fit interval. Guess the mass of the next excited state of either the even or the odd part (we use $m_{no/osc,2} = 5/4 m_{no/osc,1}$). Adjust the corresponding amplitude ($A_{osc,2}$ or $A_{no,2}$) such that the first point of the correlator in the fit interval is reproduced.

5. Perform a full fit with higher states. Use the parameters from steps 4 and 3 as the initial guess.

6. Repeat steps 4 to 5 until the desired number of states is reached.

When applying the fits in practise, one should apply both methods and choose the one with the better (=smaller) χ^2. We find that method A is superior for correlators with rather small

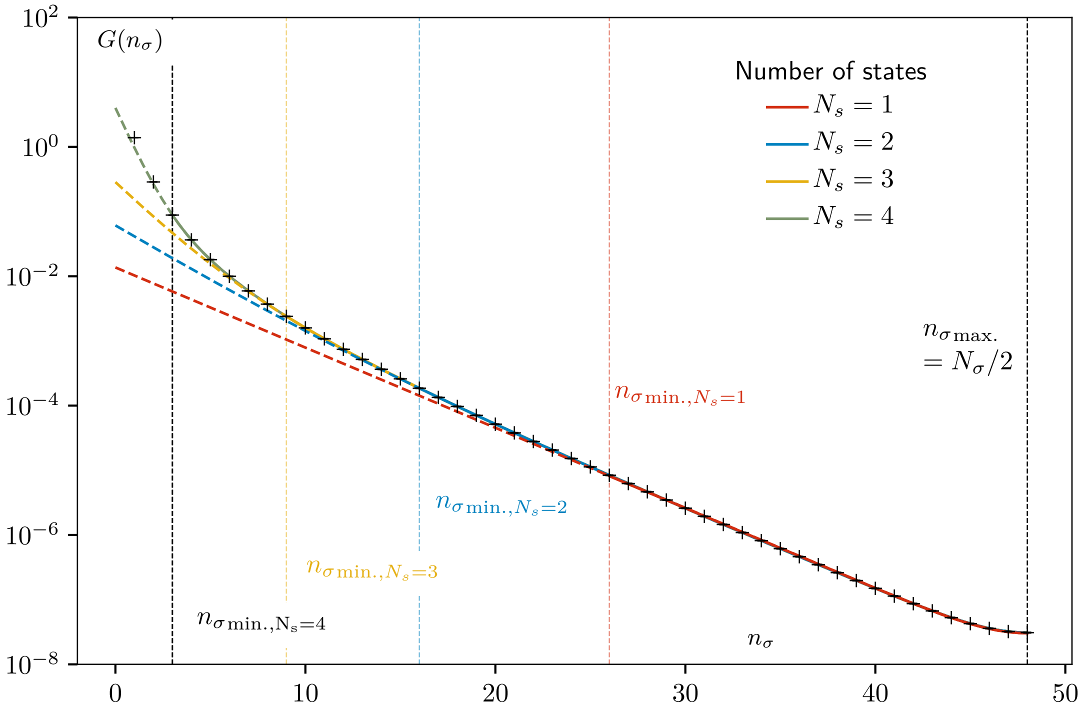

Figure 4.3: Visualization of the different fits that are performed to estimate the start parameters of a non oscillating four state fit to a Wilson charmonium pseudoscalar correlator on a quenched lattice. While the lattice has 96 points in the spatial direction, the fit has been restricted to $n_{\tau\,\text{min.}} = 3$ and $n_{\tau\,\text{max.}} = N_\tau/2 = 48$. First, a one state fit is performed on a small fit interval with $n_{\tau\,\text{min.},N_s=1} = 26$ and $n_{\tau\,\text{max.},N_s=1} = n_{\tau\,\text{max.}} = 48$. From the results of this fit, the start parameters for a two state fit are estimated (see text). Then this two state fit is performed on a larger interval ($n_{\tau\,\text{min.},N_s=2} = 16$). The results are used for a three state fit ($n_{\tau\,\text{min.},N_s=3} = 9$) and finally we can estimate the start parameters for the four state fit. The fit intervals have been calculated based on equation 4.27 with weights given in table 4.1 and are visualized by vertical lines.

method	$N =$	1	2	3	4	5
A	$\omega_1 =$	2	4	6	6	6
	$\omega_2 =$	1	1	1	1	1
B	$\omega_1 =$	8	8	10	10	10
	$\omega_2 =$	1	1	1	1	1

Table 4.1: Weights to estimate the fit intervals according to equation (4.27). N denotes the total number of states, $N = N_{s,no} + N_{s,osc}$, for which we want to calculate the fit interval based on our current fit interval.

errors, while method B works better for very noisy data. When iterating through the mass plateau, we also recommend to reuse the result from the previous fit as a third initial guess.

To have a fully automated fitting routine, we still need to know how to choose the fit intervals for the different steps. We found it sufficient to calculate the next smaller interval based on the following formula:

$$n_{\tau,\text{min,sub}} = \frac{(\omega_1 n_{\tau,\text{min}} + \omega_2 n_{\text{up}})}{\omega_1 + \omega_2}. \tag{4.27}$$

Here $n_{\tau,\text{min,sub}}$ is the lower bound of the smaller fit interval that we want to compute from the current lower bound $n_{\tau,\text{min}}$ while n_{up} is defined as $\min(n_{\tau,\text{max}}, N_\tau/2)$. The parameters ω_1 and ω_2 can be arbitrarily chosen depending on how many states we are looking at. In table 4.1 we present weights that we found work best for methods A and B. However one should not hesitate to try different ones.

Another problem that usually arises in practise is the selection of the ground state: If a multi state fit successfully runs into a minimum it is not directly clear which of the states actually corresponds to the ground state. Even though the above fitting routines affect the ordering of the states in principle, it might still happen that the ground state is not given by the first state in the fit. One might assume that simply ordering the fit result according to the resulting masses should represent the corresponding ordering of states. However we find that this is not sufficient. It might also happen, that a two state effectively becomes a one state fit, where the amplitude of the second state is unphysically small. In that case, the corresponding mass does not reflect any meaningful state. To overcome similar problems with imprecise fit results we came up with a sorting algorithm:

We iterate over pairs of states, and interchange them if one of the following conditions is true:

1. The amplitude of the first state is lower than the second one's;
2. the mass of the first state is unrealistic small or large;
3. the amplitude of the first state is negative and the amplitude of the second state is positive.

This algorithm is optimized for sources, where all states come with a positive amplitude. For results where negative amplitudes appear, this will still extract the correct ground state. Only excited states come in a different order.

4.3.2. Error estimation

Having found the best fit values using the methods in the previous section, we still need to compute the error of the fit parameters. In the following, we will give a short overview over the many possibilities to do so.

Using the jackknife method to estimate the final fit error has a few problems that stem from the chaotic behavior of the fit. Even though the initial guess estimation routines described in section 4.3.1 help to find a reasonable fit result, it still may happen that a fit fails and the fit parameters are off. This happens especially if the estimate of the covariance matrix is of low quality and the number of states is larger. When using the jackknife method, fewer data enter the computation of the covariance matrix. Therefore, it is likely that one of the fits within the jackknife fails. One fit result that is completely off destroys the whole jackknife method. This is why we found that the jackknife method does not work for correlated higher state fits.

The same argument holds for a bootstrapping where one computes the covariance matrix on each bootstrap sample. However, bootstrapping allows to break the correlation of the different values in the correlator by using different samples per n_τ-value. In that case, the covariance matrix becomes diagonal and uncorrelated fits are possible. Indeed, we find that this method gives reasonable results even for higher state fits, though using different samples per n_τ-value adds noise to the correlator. This noise removes the correlations but it also may hide excited states which results in larger error bars for excited state fits.

An additional problem arises when the fit ansatz does not reflect the data. For instance, if a one state fit is performed on a large interval where excited states are not suppressed. In that case, the fits keep running into a minimum, whose $\chi^2/\mathrm{d.o.f}$ is too large. As all these run into a similar minimum, this results in an underestimated error. Both of these effects are visible in figure 4.4. The error from bootstrapping of the (2,2)-fit is overestimated for separations $n_{\sigma,\mathrm{min}} \geq 10$. At the same time, the error of the (1,1)-fit is underestimated for separations $n_{\sigma,\mathrm{min}} \leq 15$ At separations where the bootstrapping method works, the results of direct fits and bootstrapping agree in error size as well as central value. This serves an independent check for the correctness of the correlated fit.

All in all, we find that the best working method is to use only one direct correlated fit which error is estimated by correlated error propagation.

4.3.3. Selecting the best fit

With the methods in section 4.3.1 it is now possible to perform higher state fits at arbitrary fit intervals. We still have to chose an optimal fit regarding the number of states. Too few states leads to the usual problem of excited state influence. Too many states leads to overfitting and the error bars become large again. To select the appropriate number of states, we

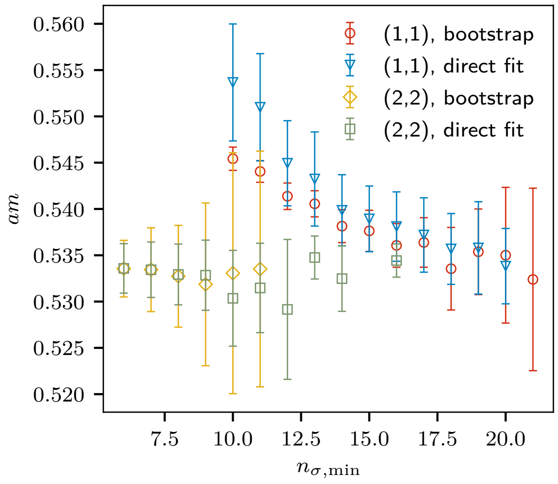

Figure 4.4: Ground state screening mass for different number of states using bootstrapping and direct fits. In the case of one direct fit, the error stems from the fit error itself. Parameters are the same as in figure 4.1.

use the Akaike Information criterion (AIC) [131] which is a criterion to select the best among different fit models. It is defined as

$$\mathrm{AIC} = 2k - \ln(\hat{L}), \tag{4.28}$$

where k is the number of parameters and $\hat{L}$ is the likelihood function from equation (4.11). The best model is then given by the model with the lowest AICc. Though, equation (4.28) is only valid for data sets where the number of data points n is much larger than k. For smaller data sets, one has to correct for over-fitting. This may be done by using the corrected AIC (AICc) [132] which is defined as

$$\mathrm{AICc} = \mathrm{AIC} + \frac{2k^2 + 2k}{n - k - 1}. \tag{4.29}$$

For each given interval $[n_{\tau,\min}, N_\tau/2]$, we perform fits with different numbers of states. For staggered correlators, we also try different numbers of states for the oscillating and non-oscillating channel, respectively. Then, the fit with the lowest AICc is selected as the best fit for this interval.

In figure 4.5, we show this selection process for a data set with small errors. As the AICc is only a relative comparison, it is impossible to compare the result from different fit intervals. Only a comparison between different states is possible: Even though it seems that the fits with larger fit intervals are favored by the AICc, this is not the case. In the end, the resulting plateau is totally stable throughout the whole range, but lies below all results of the one state fit. This stresses the importance of higher state fits.

In figure 4.6 we show another example for a very noisy correlator. Here, we only get a signal from the short distance region, where the correlator is less noisy, but higher states contribute. Using higher state fits and the AICc-selection routine, we may still extract the ground state.

4.3.4. Plateau averaging

Having computed the final plateau, using the many state fitting routine and the AICc selection, we still average over the plateau to find the final value and error. As the data points within the plateau stem from the same data set, they are not independent. This forbids us to use standard statistical tools like standard mean and standard error.

One way to solve this problem is to use bootstrapping to find the covariance matrix between the data points within plateau. Afterwards the final value and error may be computed using the correlated weighted average. However, this has two drawbacks: First, this requires a factor 100-1000 more computation time, as each fit has to be repeated on bootstrap samples. This increases the computational effort for the fits so much that the data analysis is about as expensive as the computation of the correlators themselves. Second, a covariance matrix estimated from bootstrap samples is usually of low quality. In our test we found that this often leads to mean values which are completely off.

Instead it easier to assume 100% correlation between the points and use Gaussian bootstrapping to estimate the final value and error. To do so, we draw Gaussian noise around each of the data points. We then add the resulting distributions to one final distribution. The median is then quoted as the final error, while the error comes from a 68% percentile around the median. Example plots for this procedure can be found in figure 4.7.

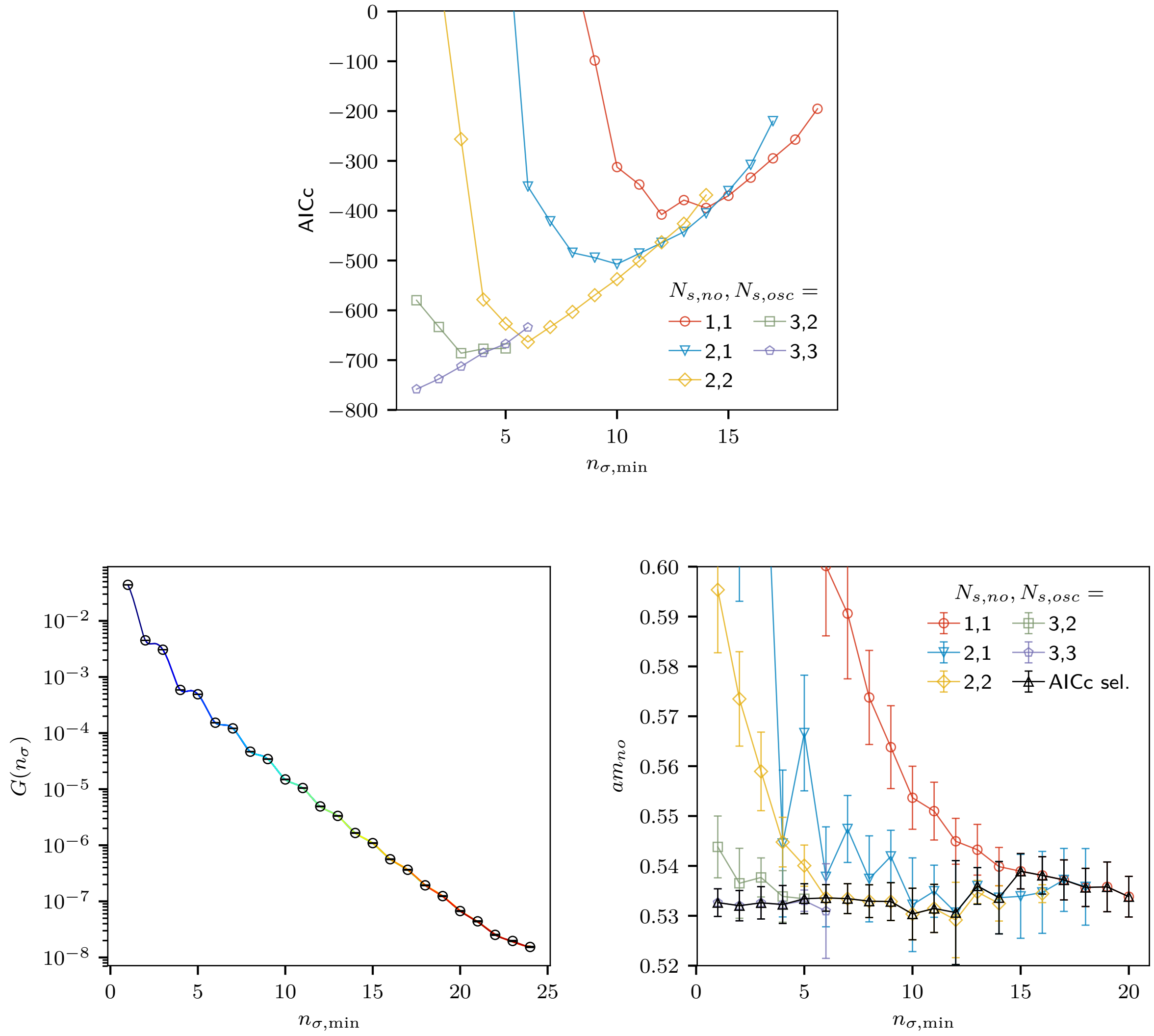

Figure 4.5: Top: Corrected Akaike information criterion (AICc) for different numbers of states as a function of $n_{\sigma,\min}$. Note that the AICc may only be compared for the same data set. In this case this means that one should not compare horizontally. Left: Same as figure 4.1 but with a higher number of states. For each interval we plot the fit model selected by the AICc. Right: Ground state mass for the non-oscillating part for different fit models. Black: Ground state mass selected by AICc. In order to guide the eye, we connected the data points with straight lines in the upper and right plot.

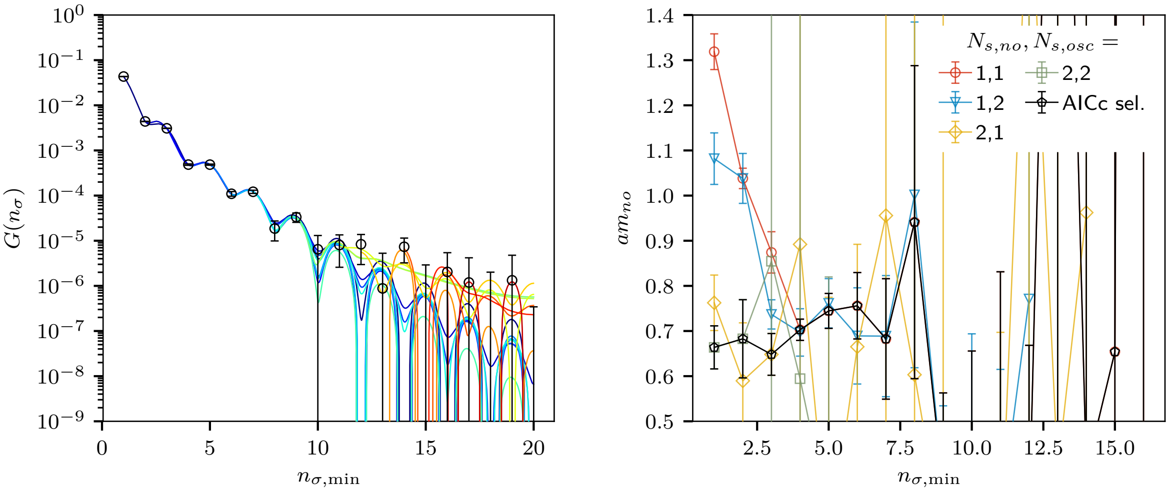

Figure 4.6: Same as figure 4.5 but for a noisy data set (HISQ action, $m_s = 20m_l$, lattice size: $40^3 \times 10$, axial vector channel for two light quarks, point source, $\beta = 6.575$). Left: For each interval we plot the fit model selected by the AICc. Right: Ground state mass for the non-oscillating part for different fit models. Black: Ground state mass selected by AICc

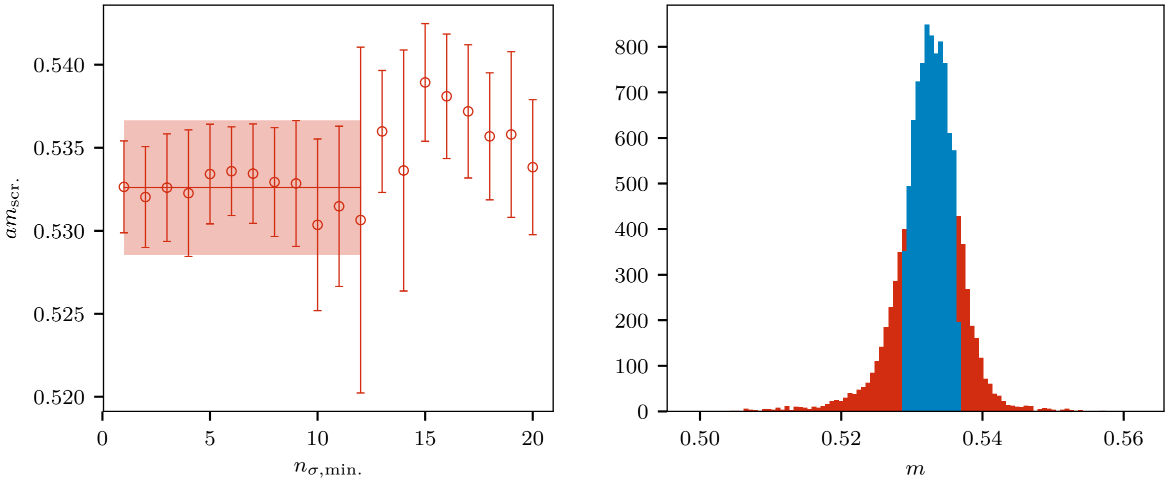

Figure 4.7: Example for the plateau averaging. The data stem from the same lattice as in figure 4.5. Left: Final mass plateau as a function of $n_{\sigma,\mathrm{min.}}$. The shaded area marks the selected plateau, its median and the error. Right: Histogram, which shows the 68%-percentile that has been used for the error computation

4.4. Continuum extrapolation

Physical observables computed on the lattice undergo cut-off effects. That means that the result of these observables does not reflect the true physical value, but comes with systematic errors instead. These errors stem from the discretization of the action and the observable itself. Therefore, the size of these cut-off effects depends on the discretization scheme itself. In the so called continuum limit, where the lattice spacing goes to zero ($\lim_{a\to 0}$), this cut-off vanishes. Due to the limit in computer power, this limit is never reached, and cut-off effects stay relevant even for large lattices. To still be able to calculate continuum observables, an extrapolation $a \to 0$ based on finite lattices is necessary.

In many cases, such an extrapolation should be done at many different realizations of an observable concurrently. A typical example is an observable that is measured at different temperatures. If the temperatures between the different lattice spacings do not match exactly, a point wise continuum extrapolation is impossible. Often, it is even impossible to match data points for each lattice spacing. For instance a correlator at smaller lattice sizes has less data points that the largest one. The lattice points of the finer lattice do not match to those of the coarsest lattice. This is why an interpolation at each lattice spacing has to be done first. Such an interpolation may be done by using any appropriate interpolation ansatz.

In this work, we used splines as an interpolation ansatz, as they make it easy to combine the continuum extrapolation and the interpolation in one step. A spline contains of piece-wise defined polynomials, which are constructed in such a way that a certain number of derivatives stay steady at the transition points. These transitions points are called knots and may be distributed arbitrarily within the interval that should be interpolated. To define such a spline, we first define the so called jump function as

$$(x)_+ = \begin{cases} 0: & x \leqq 0 \\ x: & x > 0. \end{cases} \tag{4.30}$$

A spline, where all but the n-th derivatives are steady, may then be defined as

$$p(x) = \sum_{n=0}^{d} a_n (x - x_0)^n + \sum_{k=0}^{n} c_k (x - x_k)_+^d, \tag{4.31}$$

where d is the degree of the underlying polynomials, n is the number of knots, x_k are the knot positions and a_i, c_i are the spline coefficients. Here, the coefficients a_i are the coefficients of the underlying base polynomial while the c_i belong to each knot. If less than $n-1$ derivatives should stay steady, the above formula changes to

$$p(x) = \sum_{n=0}^{d} a_n (x - x_0)^n + \sum_{k=0}^{n} \sum_{i=d-s+1}^{d} c_{k,i} (x - x_k)_+^{d-i}, \tag{4.32}$$

where s is the number of derivatives that are not steady.

The spline interpolation itself may now be performed by fitting the given data points over the coefficients a_i and c_i. The number of knots and the degree of the polynomial have to be selected by hand for each data set.

For a continuum extrapolation, one may interpolate each data set corresponding to a different lattice spacing separately. Then the continuum extrapolation can be performed on the interpolated data. A better way is to combine the extrapolation and the interpolation into one single fit. To do so, we replace the spline coefficients by a function that depends on the lattice spacing a or equivalently on $1/N_\tau$. This function itself contains coefficients that are used in the fit. For example, if the action is quadratically improved in a, a typical ansatz is $a_k(N_\tau) = a/N_\tau^2 + b$. The error of the spline interpolation may then be estimated by bootstrapping.

When working with splines, typically oscillations in the fitted spline occur. This is mostly the case when some parts of the data show a lot of curvature while others are rather smooth. In the following we give a few practical hints for how to reduce those oscillations. We demonstrate this using mock data which are Gaussian generated around a non-trivial function:

$$f(x) = \{\arctan[5(x-\pi)] + \pi/2\}\cos(x-\pi) + 30/N_\tau. \tag{4.33}$$

The density of data points is chosen to follow the details of the function. This means that most of the data points are given at the peak structure. In the top left plot of figure 4.8, we show an example with $d = 3$ and nine knots that are evenly distributed within the given interpolation interval. We also show the analytically given continuum extrapolation. It can be found that the spline results oscillate a lot, which is a typical behavior for splines. Moreover, the spline is not able to follow the details of the data at the peak structure. This is due to the insufficient distribution of the knot position. While the high number of knots at the flat area leads to oscillations, more knots are needed at the peak structure.

Thus, a better way is to distribute the knots according to the data point density: We choose the positions of the knots in such a way that the same number of data points lies between each pair of subsequent knots. The result is displayed in the top right plot of figure 4.8. The oscillations are almost gone. However, the continuum extrapolation still partially misses the correct result. This may be solved by adding splines with a different number of knots to the bootstrap sample. As a result (bottom left plot of figure 4.8), the continuum extrapolation is more smooth.

Especially at the flat region for $x < 2.5$, there still a few oscillations mainly in the error bars. These may be reduced even further by slightly randomizing the knot positions in each bootstrap realization. One way to randomize the knot positions is to calculate them according to the point density only on a randomly chosen fraction of the data set.

Additionally one can use existing information to force the splines to fulfill certain constraints. For instance, one constrains the derivative at special x-values. This can be realized by excluding some of the spline coefficients from the fit. These coefficients are chosen in such a way that the constraints are fulfilled: Let us assume, we have a function $f(\mathbf{c}, x)$ linear in its M different coefficients $c_i,\ i \in \{0, 1, \ldots, M\}$. Further, we have an array of N constraint positions x_i and the constraint values C_i itself:

$$f^{(n_i)}(x_i) \overset{!}{=} C_i. \tag{4.34}$$

Here $f^{(n_i)}(x_i)$ denotes the n-th derivative of f. Now, we choose N coefficients c_j which we use to fulfill the constraint. The indices j of these coefficients may be grouped in $J = \{j \in \{0, 1, \ldots, M\}\}$. Given these coefficients, we define $f_{0,j}^{(n)} = f^{(n)}(\{0, \ldots, 0, 1, 0, \ldots, 0\}, x)$, which contains only the contribution of coefficient c_j to the function. The set of coefficients where all coefficients used to fulfill the spline are set to zero but all other coefficients stay unchanged may be defined as

$$\mathbf{c_0} = \begin{cases} c_i : & i \notin J \\ 0 : & i \in J. \end{cases} \tag{4.35}$$

Then the constraints are fulfilled if the following equation system is solved:

$$\begin{gathered} f^{(n_1)}(c_\mathbf{0}, x_1) + \sum_{j \in J} c_j f_{0,j}^{(n_1)}(x_1) = C_1 \\ f^{(n_2)}(c_\mathbf{0}, x_2) + \sum_{j \in J} c_j f_{0,j}^{(n_2)}(x_2) = C_2 \\ \vdots \\ f^{(n_N)}(c_\mathbf{0}, x_N) + \sum_{j \in J} c_j f_{0,j}^{(n_N)}(x_N) = C_N. \end{gathered} \tag{4.36}$$

A spline is only linear in those coefficients that belong to nodes below the constraining x-value. This is why only those coefficients may be chosen to constrain the spline. We found that the fits work best if the spline coefficient belonging to the nearest, lower knot is used for constraining the fit. In the lower left plot of figure 4.8, the derivative has been constraint to match the correct value at $x = 0$ and $x = 2\pi$. The spline clearly performs better at the edge of the interpolation region.

In practice, the choice of the number of knots, the degree of the polynomials and the constraint need to be tuned by hand. In many cases, it helps to use more than one constraint outside of the interpolation region. It especially helps to use constraints below the first knot.

4.5. Technical implementation

When it comes to the technical implementation of analysis methods in physics they are often implemented in a “quick and dirty” way, where a lot of parameters have to be hard coded. This includes the high risk of introducing bugs into the analysis of the data. A common mistake are wrong parameters that have not been changed after an existing script has been reused for something else.

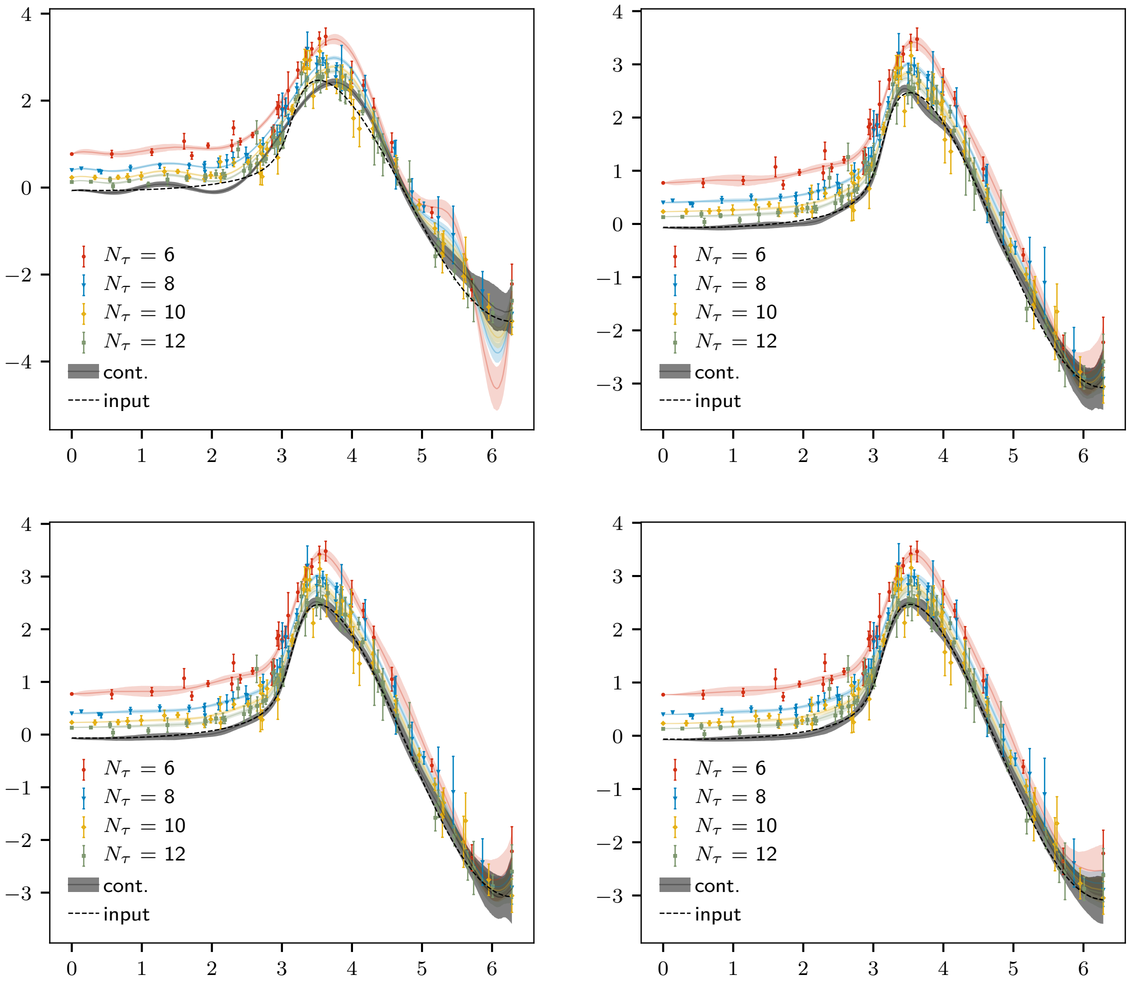

Figure 4.8: Different steps to improve the continuum extrapolation. The shown data are generated with Gaussian noise around $f(x) = (\arctan[5(x-\pi)] + \pi/2)\cos(x-\pi) + 30/N_\tau$. All splines are of degree 4. The gray band denotes the continuum, while the black dashed line shows the input function $f(x)$. The colored bands show the resulting interpolation at the given N_τ. Top left: Simple spline with nine evenly distributed knots. Top right: Density of the nine knots adapted to the number of data points. Bottom left: Like top right but here we average over the results from 8, 9 and 10 knots. Bottom right: Like bottom left but with slightly randomized knot positions and constraints to the derivative at $x = 0$ and $x = 2\pi$.

To avoid such problems, all of the programs used for data analysis in this thesis have been written in a modular, reusable and most general way. The entire amount of software used in this thesis is written in python, making heavy use of the numpy and scipy packages. All programs are available in a library that we lazily named “AnalysisToolBox”. Among others, we provide statistical tools, like Jackknife or Bootstrapping which may be applied for arbitrary functions and multi-dimensional data, a very general tool to perform correlated and non-correlated fits, numerical solvers for integrals, differential equations and root finding and a library for easily generating plots. In addition the algorithms for the screening mass determinations as well as for the continuum extrapolation in the last subsections are available. These tools may executed directly from the command line.

In the following we demonstrate the modularity of the library by explicitly writing a small script to perform screening mass fits. Let us start with a simple one state fit for a staggered correlator with an oscillating and a non-oscillating part. The corresponding implementation can be found in listing 1.

```
#!/usr/bin/env python3
from latqcdtools.readin import *
from latqcdtools.fitting import *
from latqcdtools.statistics import *
import numpy as np


def one_state(x, A_no, m_no, A_o, m_o, Nt):
    return A_no * np.cosh(m_no * (x - Nt/2))\
            - np.cos(np.pi*x) * A_o * np.cosh(m_o * (x - Nt/2))

xdata, data, nconfs = read_in_pure("corr_pure.txt", symmetrize = True)
Nt = len(xdata)


ydata, cov = mean_and_cov(data, axis = 1)
cov /= nconfs

fitter = Fitter(one_state, xdata, ydata, cov, args = (Nt,))

res, res_err, chi_dof = fitter.try_fit(xmin = 7, xmax = Nt / 2)

fitter.plot_fit("plot.pdf", ylog = True, xmax = Nt/2,
        xlabel = "$n_\\tau$", ylabel = "$G(n_\\tau)$")
```

Listing 1: A simple script to perform a one state screening mass fit

First, we import the necessary tools. In this case, we need a reading routine, the tool for fitting and the statistics module to compute the covariance matrix. All this is included in the packaged `latqcdtools`. Afterwards we define the fit function, which is just a possible implementation of equation (4.24). Next, we need the data that shall be fitted and we read them using the `read_in_pure`-function. After calculating and normalizing the covariance

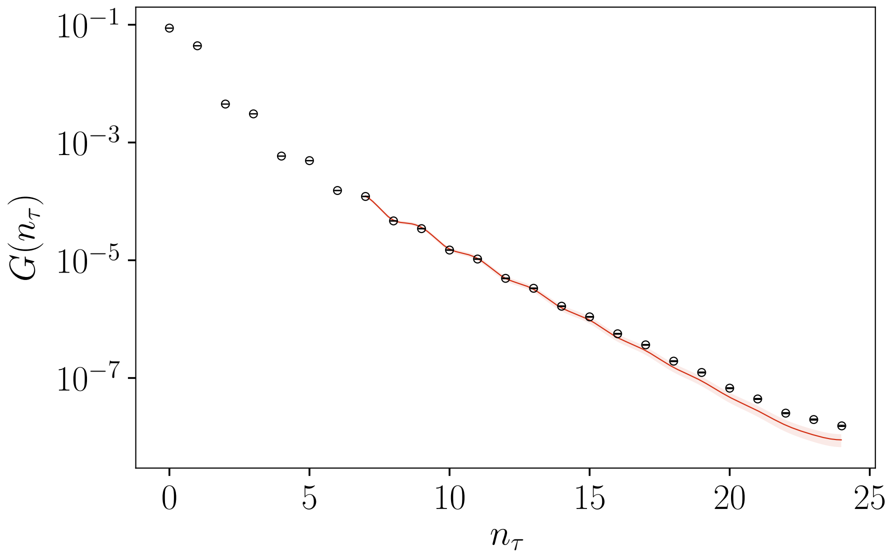

Figure 4.9: Result of the script in listing 1.

matrix in lines 16 and 17, we initialize the fitting module called `Fitter`, which we passed the function to be fitted. Then, in line 21 we perform the fit. We use the member function `try_fit`, as this function tries all available minimization algorithms and chooses the result with the smallest $\chi^2/\mathrm{d.o.f.}$. As a last step we generate a plot of the fit which includes those data points and a visualization of the fit. This plot may simply be generated by calling `plot_fit`. The resulting plot may be found in figure 4.9.

```
1  #!/usr/bin/env python3
2  from latqcdtools.readin import *
3  from latqcdtools.fitting import *
4  from latqcdtools.jackknife import *
5  from latqcdtools.bootstr import *
6  from latqcdtools.statistics import *
7  from latqcdtools.corr_fitting import *
8  import numpy as np


11 def one_state(x, A_no, m_no, A_o, m_o, Nt):
12     return A_no * np.cosh(m_no * (x - Nt/2))\
13             - np.cos(np.pi*x) * A_o * np.cosh(m_o * (x - Nt/2))

15 xdata, data, nconfs = read_in_pure("corr_pure.txt", symmetrize = True)
16 Nt = len(xdata)


19 def one_state_fit(data, Nt):
```

```
20      ydata, cov = mean_and_cov(data, axis = 1)
21      cov /= nconfs

23      fitter = Fitter(one_state, xdata, ydata, cov, args = (Nt,))
24      res, res_err, chi_dof = fitter.try_fit(xmin = 10, xmax = Nt / 2)
25      return res

27  res, res_err = jackknife(one_state_fit, data,
28          numb_blocks = 10, args = (Nt,))

30  res, res_err = bootstr(one_state_fit, data,
31          numb_samples = 100, args = (Nt,))
```

Listing 2: Improved version of the script in 1 in order to use a Jackknife or bootstrapping for error computation.

In the script in listing 1, the error is given by fit error which is calculated according to equation (4.17). As already mentioned, we find that this error is reliable in most of the cases. One still might compare it to errors computed from bootstrapping or by using the Jackknife method. In the listing in 2, we show how this may be realised by just adding a few lines to the script.

First, we put the whole functionality of the script in listing 1 into a function that we call `one_state_fit`. It is important that this function takes the raw data as a first argument, as the jackknife and bootstrap routines expect it to do so. After that argument one passes an arbitrary number of optional arguments. In this case we pass `Nt`. The function has to return the result for which we want to compute the error. In this case, this is the array of fit parameters. It is also possible to return more than one observable.

The calls to the Jackknife and bootstrap routine happen in lines 27 and 30, respectively. Both work the same way: As a first argument they take the function which calculates the observable. The second argument is the array of raw data that shall be used for the error calculation. The following arguments are optional: For the Jackknife we specify the number of blocks and for the bootstrap we specify the number of samples that shall be used. As a last argument, we have to tell the routines about the optional parameter `Nt` by passing a tuple which contains the necessary variables. After the call, both the Jackknife and the bootstrap routine return the final result as well as its corresponding error.

When looking at the script again, we notice that we did not have to care about the implementation of the Jackknife or of the bootstrap at all. All we had to do was to write a function that calculates the desired observable from the array of raw input data. So how does it work then? The idea is to call the function `one_state_fit` multiple times with a different data set. For the bootstrap, each data set corresponds to a different sample. The result of the function will be stored for each sample. Afterwards, we compute the final value and error based on that array. For the Jackknife, each data set contains the raw data, where one block is removed. The result of the function enters the computation of the pseudo values, which are further used to calculate the unbiased estimator as well as the Jackknife error.

In figure 4.9 we can directly notice that a one state fit for this correlator is not enough. The fit clearly does not match to the data, so higher states are required. However, a simple fit like in listings 1 and 2 is not possible without a precise initial guess. To estimate an initial guess as described in section 4.3, we have to use another module. In listing 3 we show how to use the so called `PerformCorrFit` class. This class does all the parameter estimation automatically and higher state fits are no problem. Also the whole input/output and data management is encapsulated in that class. All we have to do is initialize the class in line 4 and to perform the fit in line 7. In this case, we used the `direct_fit`-method. This method returns the error directly from the fit. There are many more possible options to that class. For instance, if a nested bootstrap should be used, we would pass `btstr_fit = True, scnd_btstr = True` instead of `jack_fit = True`. A documentation of all the available options for this class can be found in the class itself.

```
1 #!/usr/bin/env python3
2 from latqcdtools.performcorrfit import *

4 fitter = PerformCorrFit(filename = "corr_pure.txt", nstates = 2,
5         nstates_osc = 2, correlated = True, direct_fit = True)

7 res, res_err, chi_dof, aicc = fitter.perform_fit(xmin = 7,
8         xmax = fitter.get_Nt()/2)
9 fitter.plot_corr()
```

Listing 3: Use the PerformCorrFit module to perform a higher state fit.

Even though the presented scripts are rather short, it is still quite some effort to write an individual script for each problem. This problem increases if a potential user is not familiar with python. Thus, all the methods and algorithms used in this thesis have been merged into single executables that may be directly used from the command line. Here we summarize those commands that have been used to generate that data in this thesis. For the many more options, see appendix A or simply pass `--help` to the executable of interest.

For correlator fitting, we use the `corrfitter.py` command. A typical example to perform multiple state fits for a staggered correlator is given in listing 4. Before performing the actual fit we do not know how many states work best. Therefore, we loops over the number of states that shall enter the fit. Then, the program will automatically iterate over possible fit intervals and perform a fit on each of these fit intervals. The results are stored in a different folder whose name we specified with the `--folder` flag. In this folder different output files are generated. Among others, plots of the fits, of the covariance matrix and its eigenvalues are generated. The results of the fit are stored in a file whose name starts with `fitmass_`. The rest of the filename depends on the other parameters that are passed to the executable. The flag `-auto-sign` automatically multiplies -$(-1)^{n_z}$ to the correlator if there are more negative than positive odd data points. This interchanges the oscillating and non-oscillating states, but it may help to find better convergence of the fit. We use `--correlated` to make sure that correlated fits are used. Finally the flags `--nstates` and `--nstates-osc` specify the number of states.

```
for nso in 1 2 3; do #number of oscillating states
    for ns in 1 2 3; do #number of non-oscillating states
        corrfitter.py --auto-sign --correlated --nstates $ns --nstates-osc $nso --folder fit_out_ns${ns}_nso${nso} corr_pure.txt
    done
done
```

Listing 4: Typical usage of the `corrfitter.py` command.

Having performed the fits (this may take some time), we want to figure out how many states are most suitable according to the Akaike information criterion. To do so, we perform the following command:

```
best_fit.py fit_out_ns?_nso?/fitmass_* --folder best_fit --corr-file corr_pure.txt --auto-signu
```

where we pass the names of files which contain the results of the fits as arguments. The `best_fit.py` command will automatically figure out which fit was the most optimal according to the AICc. Here, the `--auto-sign` has the same meaning as before. Additionally we pass the file name of the original data. This will generate an extra plot that displays the best fit for each fit interval. The ground state results of the best fits are summarized in the two files `best_fit/mass_m_no.txt` and `best_fit/mass_m_no.txt` for the non-oscillating and the oscillating state, respectively.

In order to extract screening masses from these files, we have to choose a plateau for the final computation of the ground state mass. Choosing the points that enter the plateau by hand is tedious. One may use a tool called `find_plateau.py` instead. For example by calling

```
find_plateau.py best_fit/mass_m_no.txt
```

a window will open with a plot of the results from the `best_fit.py` command. Simply by doing two clicks, one may select a final plateau. Afterwards the final value and error are computed as described in section 4.3.4 and are printed to the command line.

For most lattice results one wants to perform a continuum extrapolation in the end. For that purpose, we have developed the so called `extrapolator.py` program. With this tool, a continuum extrapolation as described in section 4.4 may be performed:

```
extrapolate.py input_Nt8.txt input_Nt12.txt input_Nt16.txt --order 3 --nknots 3 4 5 --constraints 1.0 1 0 --Nts 6 8 10 12 16 --method gauss_btstr --nsamples 1000 --randomization-factor 0.4
```

In this example, the files containing the data for the continuum extrapolation are given in files named `input_files_Nt8.txt, input_files_Nt12.txt`, etc. and are passed as the first arguments to the extrapolator. The meaning of the other flags is as follows: `--order` specifies the order of the spline. The numbers following `--nknots` specify how many knots for the spline shall be used. If more than one number as given an average over the results from different knots is performed. Using the `--constraints` flag, we may introduce constraints to the spline. The first number following this flag is the x-position of the spline. In this case, we constrained the spline at $x = 1.0$. The next number is the order of the derivative that shall be constraint. Here we want to constraint the first derivative. The last value is the constrain itself. All in all this means that, we require the first derivative of the spline to be 0 at $x = 0$. The extrapolator performs the extrapolation linear in $1/N_\tau^2$. Thereby, it has to know the temporal dimension of the lattice. Using the `--Nts` flag we pass which N_τ values corresponding to the input files. In this example, we do not work on the original lattice data. Therefore, we cannot perform a bootstrap on the original data. Instead we perform a bootstrap by generating Gaussian noise around the data points. For that purpose, we have to pass `--method gauss_btstr`. With `--nsamples` we define the number samples that are used in the bootstrap. Finally, the last flag specifies what fraction of data point shall enter into the random knot position calculation (see section 4.4).

5. Heavy quarkonium correlators on quenched lattices

The only way to get insights into the properties of the quark gluon plasma in heavy ion collisions is to measure the many different particles that hit the detectors long after the medium is already dissolved. Heavy quarkonium states, such as $\bar{c}c$ or $\bar{b}b$ have been found to be ideal probes to study the hot medium [9]: Due to their high masses, these states have to be created early in the collision before the medium equilibrates. Afterwards, when the medium is in equilibrium these states interact with the medium. If a quark-gluon plasma is indeed created, the length of the color Debye screening radius may exceed the binding radius of certain heavy quarkonium states. Therefore these states will melt and other, mixed flavor states like $\bar{c}u$ or $\bar{c}s$ are more likely to be created at the chemical freeze out. This means that if the number of pure charmonium or bottomonium events, like J/ψ, χ_{c0}, $\psi(2S)$ or Υ hits in the detectors, is lower than in comparable proton-proton collisions, this strongly indicates the existence of a quark-gluon plasma. Additionally, within the melting process, less tightly bound states are expected to melt at lower temperatures compared to strongly bound states. This phenomenon is called sequential melting [133, 134] and leads, for instance, to a higher suppression of $\psi(2S)$ states compared to J/ψ states.

As already mentioned in the introduction, a suppression of J/ψ-yields has been found at all three large colliders SPS, RHIC and LHC and also Υ suppression has been reported at the LHC [10–15]. Sequential melting has been observed as well [16, 17]. However to interpret these data, the corresponding melting temperatures of the different states have to be known beforehand. This is especially important, as different models suggest a regeneration of charmonium yields at even higher temperatures [135, 136]. This effect is based on the interaction charm quarks stemming from two different nuclei collisions. Also these models heavily depend on the melting temperatures and the bound energy of charmonia.

Another evidence for the existence of a quark-gluon plasma in heavy ion collision is the non-zero elliptic flow of heavy quarkonia [18–21]. This indicates a collective motion of heavy quarkonium, which in turn implies that heavy quarkonia interact with the medium and adopt its momentum anisotropy. For a better understanding of the hydrodynamic effects going on in thermalization of heavy quarkonia, detailed information about the transport properties are needed. In particular the heavy quark diffusion constant is of interest as it as related to the energy loss of heavy quarks.

In section 3 we have seen that both in medium modification as well as transport properties of heavy quarkonia are encoded in the spectral function. There, we also mentioned the problems that arise in the reconstruction of the spectral function from hadronic correlators. Because of these, one needs lots of data points in order to extract any reliable information. Currently the only way to generate lattice configurations that have enough data points in time direction at finite temperature is to use the quenched approximation. There exist several studies that work with hadronic correlators based on quenched configurations [137, 138]. However, a continuum extrapolation for heavy quarkonium has never been performed.

In this section, we want to extend these studies by performing a continuum extrapolation on the level of correlators. Afterwards we analyze the results by using the reconstructed correlator and by comparing against the results from perturbative spectral functions. The methods and results presented in this section are partially published in [139] and [46]. We start with the description of the lattice setup and with the basic quark mass tuning in section 5.1. After we describe a method to ensure perfectly tuned quark masses, and after giving details about the continuum extrapolation in section 5.2, we present the results in section 5.3.

5.1. Lattice setup and quark mass tuning

The calculations have been performed using large quenched lattices with the standard Wilson gauge action on isotropic lattices whose parameters and statistics are listed in figure 5.1. Within the Markov chain we used configurations separated by 500 sweeps, where each sweep consisted of four overrelaxation updates and one heatbath update. The thermalization time has been set to 6000 sweeps. We used four different spatial extents with sizes $N_\sigma = 96$, 120, 144 and 192. According to the scale in 2.45 we tuned the β value such that all lattices roughly have the same physical spatial dimension of $8.44\,\mathrm{GeV}^{-1}$. For each lattice, except for $N_\sigma = 120$, we used five different temporal extents so that the resulting temperatures roughly correspond to values of $T/T_c = 0.75$, 1.1, 1.3, 1.5 and 2.25. We used $r_0 T_c = 0.7457(45)$ from [45] to convert to units in of T_c. For $N_\sigma = 120$ there is no possible choice for $T/T_c = 1.3$ with an even number of lattice points in the temporal direction. Therefore for this lattice size, this temperature is skipped.

The hadronic correlators have been calculated using the non-perturbatively improved clover action defined in equation (2.27) with the Sheikholeslami-Wohlert coefficient calculated according to (2.29). The input quark masses or rather the hopping parameters have been roughly tuned such that the resulting vector meson masses match to the physical values of the J/ψ and the Υ. To measure the zero temperature masses from the lattice, we used the screening correlator instead of the correlator in time direction. At small temperatures the corresponding masses are expected to be the same, but due to the longer physical distance and the higher number of available points, the screening mass is expected to be of higher precision.

Afterwards, using a multi-shift conjugate gradient [140], we calculated the hadronic correlators for multiple different κ-values between the charm and the bottom mass. For the vector correlators, we summed over the three spatial components for temporal correlators. The corresponding spatial correlators were calculated along the z-axis and, therefore, we summed over the first two components only. The tuning as well as the further mass computation is carried out in the deeply confined phase at the lowest temperature, that means roughly at $T = 0.75T_c$. In order to increase the statistics on the final lattice, we measured the correlator at five different source point for those κ-values nearest to bottomonium or charmonium, respectively.

The screening masses have been computed using the method described in section 4.3. For the fits we used up to five states in order to get stable results for the ground state mass throughout the whole range of the fit intervals. The final plateau for the determination of the screening mass has been chosen individually for each lattice by hand. Besides a plateau in the resulting screening masses, we also searched for a region where the minimal $\chi^2/\mathrm{d.o.f}$ was closest to one. In figure 5.1, we give an example for the fit results. As is visible in the upper left plot of

β	a[fm](a^{-1}[GeV])	κ-range	N_σ	N_τ	T/T_c	#meas.
7.192	0.0177 (11.18)	0.12257-0.13194	96	48	0.74	237
				32	1.12	476
				28	1.27	336
				24	1.49	336
				16	2.23	237
7.394	0.0137 (14.23)	0.124772-0.132245	120	60	0.76	258
				40	1.13	220
				30	1.51	354
				20	2.27	253
7.544	0.0116 (16.99)	0.12641-0.13236	144	72	0.75	221
				48	1.13	462
				42	1.29	660
				36	1.51	288
				24	2.26	237
7.793	0.0087 (22.75)	0.12798-0.13221	192	96	0.76	224
				64	1.13	291
				56	1.30	291
				48	1.51	348
				32	2.27	235

Table 5.1: Lattice setup of quenched lattices used for the charmonium and bottomonium correlator calculations. The scale has been determined using (2.45).

that figure, it sometimes happened that selection of the Akaike information criterion was not optimal and it preferred a fit with fewer states even though a fit with higher states gave a more reasonable result. For instance see the transition between the two state and the three state fit results. In such a case we made sure not to include such points into the fit plateau (see upper right plot of figure 5.1). Surprisingly we found that large fit intervals worked better compared to fit intervals that only included the large temporal distance region.

The final results for the vector screening masses can be found in the lower plot of figure 5.1. The visible uncertainties in the quark mass tuning will be corrected by quark mass interpolation in the next section.

5.2. Continuum limit

In the following section we will describe the different steps that are necessary to perform the continuum extrapolation. We mainly focus on the vector channel here, but the steps for the pseudoscalar channel are analogous. (See also [46].)

To visualize fine details of the correlator, we normalize the correlators using the free con-

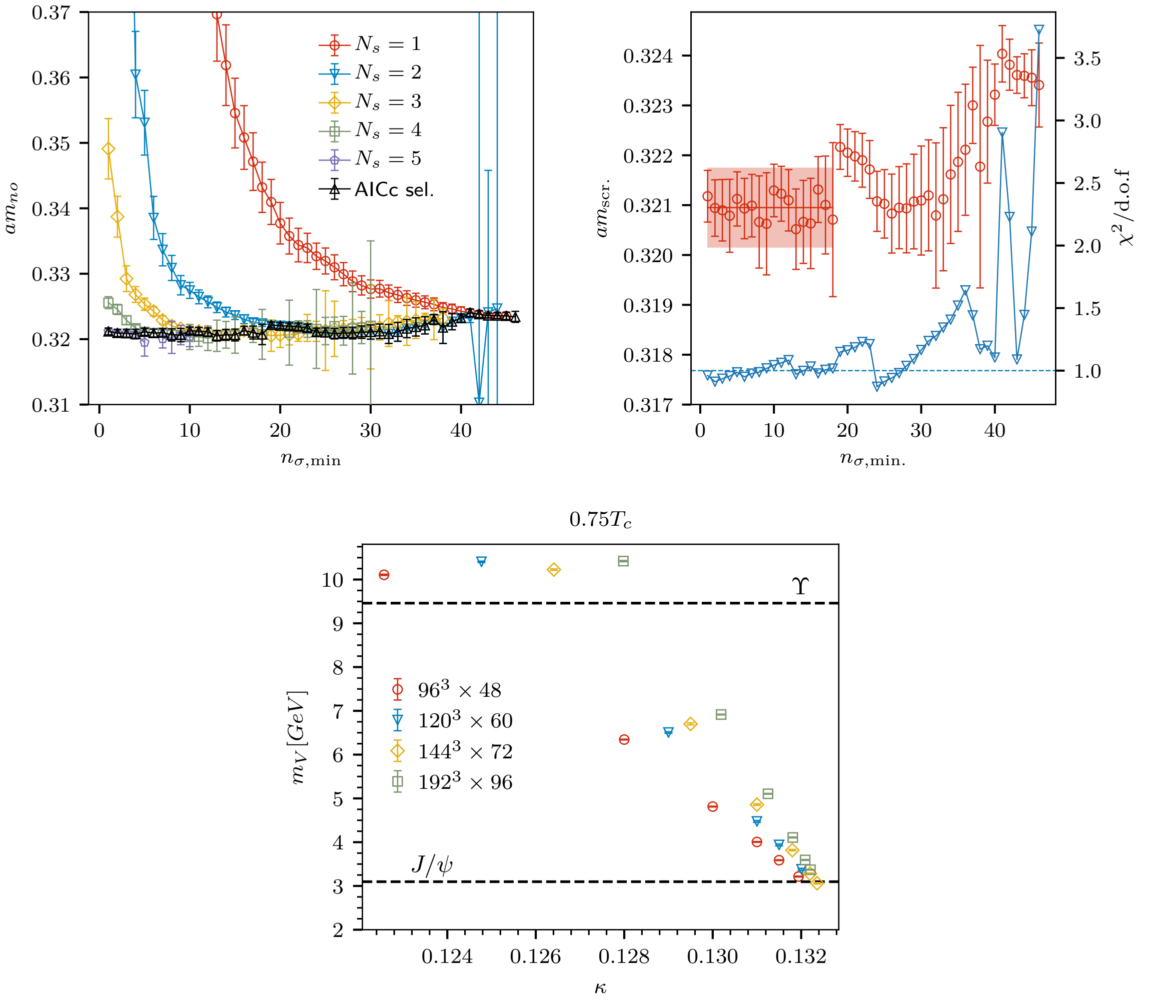

Figure 5.1: Top left: Screening mass plateaus of the multiple state fits and the mass selected by the Akaike information criterion for the $96^3 \times 48$ lattice with hopping parameter $\kappa = 0.1315$ at $T = 0.75T_c$. Top right: Correspondingly selected mass plateau as well as the fit quality $\chi^2/\mathrm{d.o.f.}$ Bottom: Measured ground state screening masses for the vector channel using the correlators on the quenched lattices in table 5.1. The horizontal lines correspond to the physical values of the J/ψ and the Υ meson.

tinuum correlator

$$\frac{G_{\text{free}}(\tau)}{T^3} = \frac{1}{T^3}\int_{2m_q}^{\infty} \rho_{\text{free}}(\omega, m_q) K(\omega, \tau) d\omega, \tag{5.1}$$

which we evaluate at the corresponding lattice points. Here, ρ_{free} is the free spectral function from equation (3.96). For the quark mass, we chose $m_q = 1.5\,\text{GeV}$ for charmonium and $m_q = 5\,\text{GeV}$ for bottomonium, respectively.

Regarding the renormalization, we use the perturbative two-loop calculations given in equation (3.64) for the pseudoscalar channel. For the vector channel we use renormalization independent ratios by dividing by the quark number susceptibility χ_q from the lattice with the same β-value at $T = 2.25T_c$ whenever possible. Thereby, we compute the quark number susceptibility by taking the centered point from the time component of the vector correlator. This way, we ensure that discretization effects are smallest. Later on, we will also need to renormalize the quark number susceptibility itself. For that, we use the non-perturbative renormalization given in equation (3.62).

In the left plot of figure 5.2, we show example plots for the vector correlator at different κ-values. Clearly a very strong mass dependence is visible. Even for small changes in the corresponding ground state mass, we observe a significant change of the correlator. This becomes a problem, when it comes to the continuum extrapolation of the correlator. In the right plot, we show the different correlators whose mass is closest to the J/ψ mass. It can be seen that the ordering of the correlators does not correspond to the order of the lattice sizes. This effect stems from the slightly mistuned quark masses.

To compensate for that, we perform an interpolation in quark masses. This is done by performing a fit at each temporal distance τT of the correlator according to

$$G\left(\frac{m_V}{T}, \tau T\right) = \exp\left(\alpha_1(\tau T)\left(\frac{m_V}{T}\right)^2 + \alpha_2(\tau T)\left(\frac{m_V}{T}\right) + \alpha_3(\tau T)\right), \tag{5.2}$$

where α_0, α_1 and α_3 are the fit parameters. As the quark mass is not available, we use the measured vector ground state mass m_V for the interpolation. This means that this interpolation is equivalent to a quark mass tuning based on the vector meson mass. After the fit is performed we evaluated the result at the physical masses $m_{J/\psi}$ and m_{Υ}. In principle, this quark mass interpolation can be performed on each configuration separately. However, due to statistical fluctuations, some of the correlator values might become negative, such that the above fit ansatz fails. Thus, we chose to compute the errors of the interpolated correlator by performing this interpolation on 1000 bootstrap samples. Using the same random numbers for the sample generation, we may keep correlations preserved.

Because of the large differences between the correlators of different mass, we did not use all six available different κ-values. Instead we only used the closest four correlators for charmonium and the closest three for bottomonium.

In the upper plot of figure 5.3 we show an example for the mass interpolation and in the lower left plot we compare the result against the other measured correlators. Though the

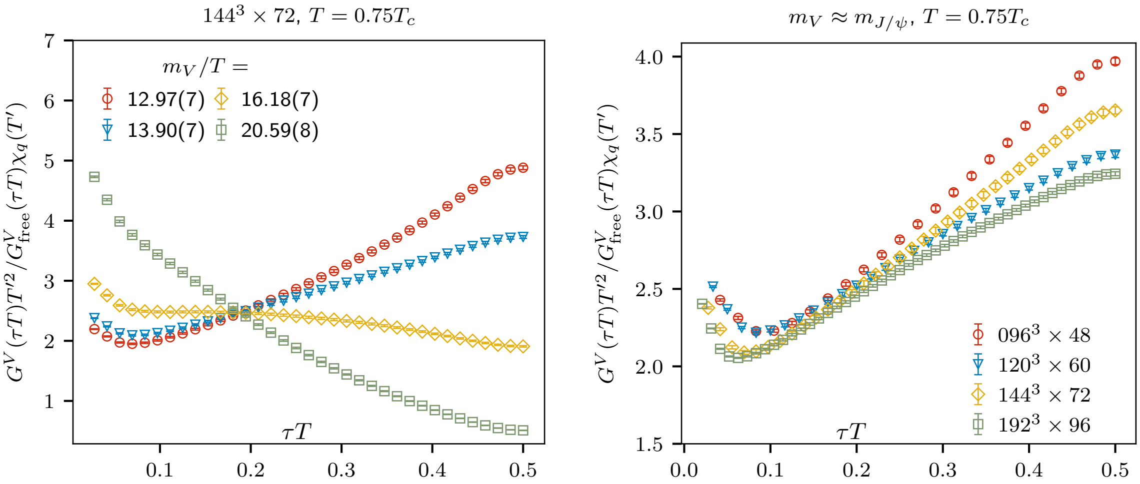

Figure 5.2: Vector correlators from the lattice divided by the free continuum correlator defined in equation (5.1) with an input quark mass of $m_q = 1.5\,\mathrm{GeV}$. In order to have renormalization independent ratios, we additionally divide by the quark number susceptibility χ_q taken from the corresponding lattices at $T' = 2.25T_c$. Left: Correlators for the $144^3 \times 72$ lattice with different input κ-values. The labels show the corresponding measured ground state screening mass. Right: Correlators closest to the J/ψ-mass for different lattice sizes at $T = 0.75T_c$.

resulting changes seem to be small, we find that the interpolation shifts the correlators such that the ordering is correct and we are now ready to perform the continuum extrapolation.

The continuum extrapolation and the interpolation of the correlators is performed in one single step using simple splines with the techniques defined in section 4.4. We extrapolated linearly in $1/N_\tau^2$ on the interpolated correlators normalized with the free correlator (5.1). An extrapolation quadratic in $1/N_\tau^2$ or linear using only the finest three lattice spacings gave comparable results. For the quark mass, we chose $m_q = 1.0\,\mathrm{GeV}$ for charmonium and $m_q = 4.5\,\mathrm{GeV}$ for bottomonium. These values differ from the values used above, but the resulting correlators exhibit less curvature which results in better spline interpolation.

We used fourth order splines and increased the number of knots until the resulting $\chi^2/\mathrm{d.o.f}$ reached a plateau. For the randomization of the knots, we used half of the data points in each bootstrap sample for the position calculation (see section 4.4). To stabilize the splines, we required the interpolation to have a derivative of zero at $\tau T = 0.5$. The fits worked well for most most parts of the correlators. Only for short temporal distances, $\tau T < 0.1$, the cut-off effects were too large, so that the combined extrapolation could not match all data points. This is why the resulting $\chi^2/\mathrm{d.o.f}$ often was a bit larger than one. In figures 5.4 and 5.5 we show the continuum extrapolation for the vector channel for bottomonium and charmonium. All four lattice sizes are included into the extrapolation except for temperatures $T = 1.25T_c$, where only three different lattice spacings are available. The whole continuum extrapolation is realized on each bootstrap sample that has already been used for the quark mass interpolation.

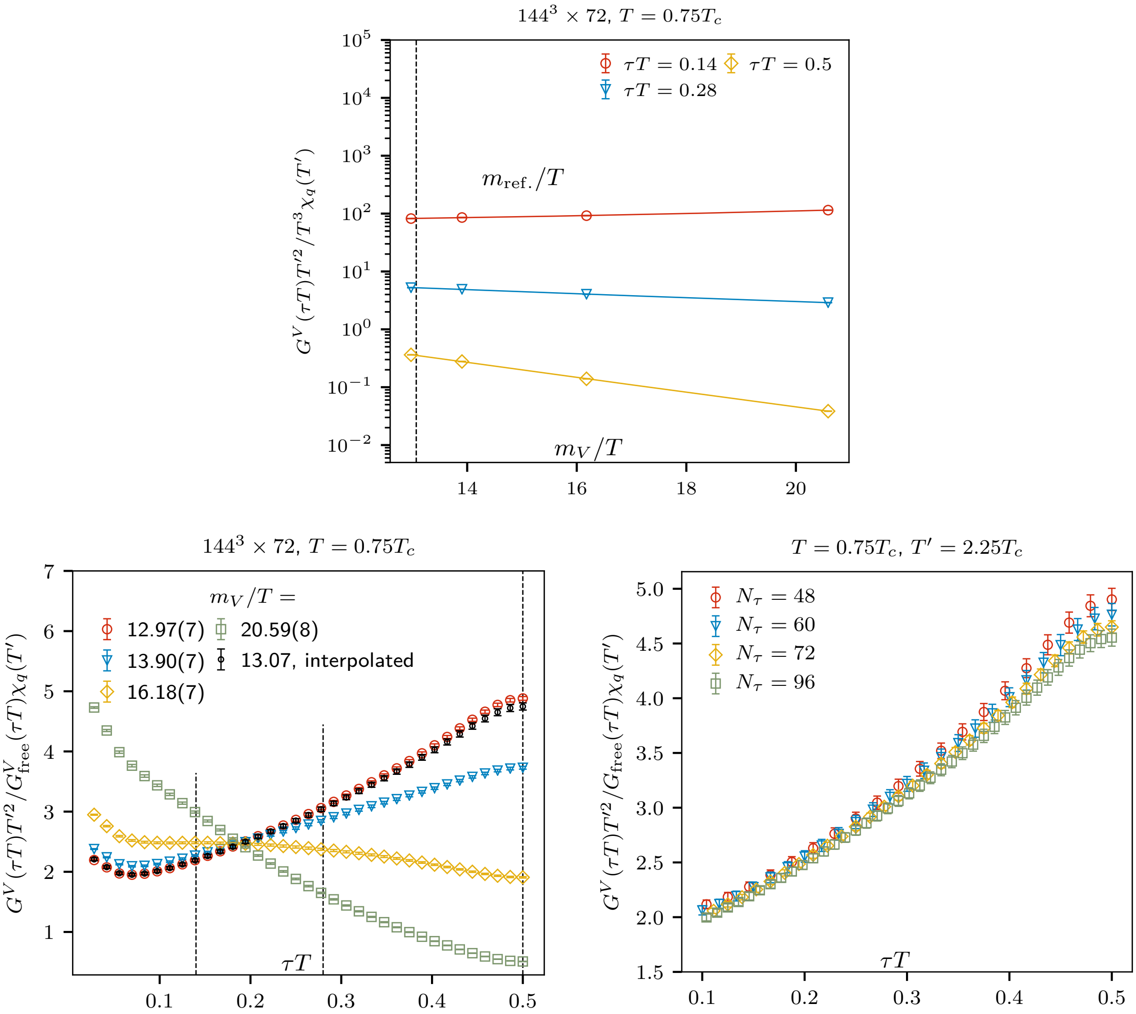

Figure 5.3: Top: Example for the mass interpolation at three different temporal extents. This examples show one out of the 1000 bootstrap samples. The vertical line corresponds to the reference mass used for the interpolation. In this case it is the mass of the J/ψ. Lower left: Same as left plot in figure 5.2, where the interpolated correlator for the J/ψ reference mass has been inserted (black). The vertical lines correspond to the τT values in the examples lines in the upper plot. Lower right: The resulting interpolated correlators for different lattice sizes at $T = 0.75T_c$.

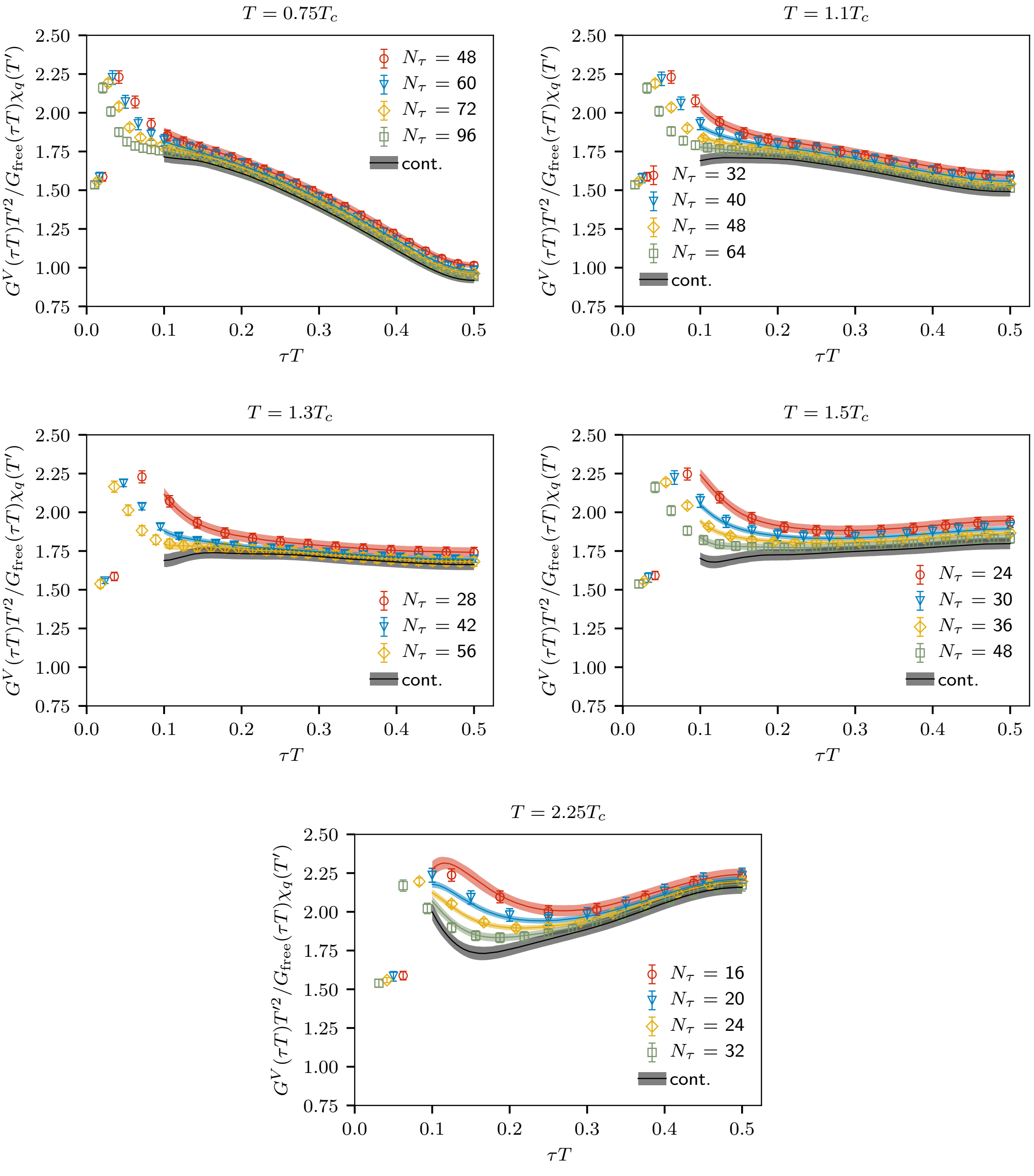

Figure 5.4: Continuum extrapolation of the interpolated charmonium vector correlators. In order to perform a spline interpolation, we divided by the free continuum correlator defined in equation (5.1) with an input quark mass of $m_q = 1.0\,\text{GeV}$. The renormalization is taken care of by dividing by quark number susceptibility χ_q, which is taken from the corresponding lattices at $T' = 2.25T_c$. The extrapolation and the interpolation is performed in one step using simple splines with the techniques described in section 4.4 to reduce the spline typical oscillations.

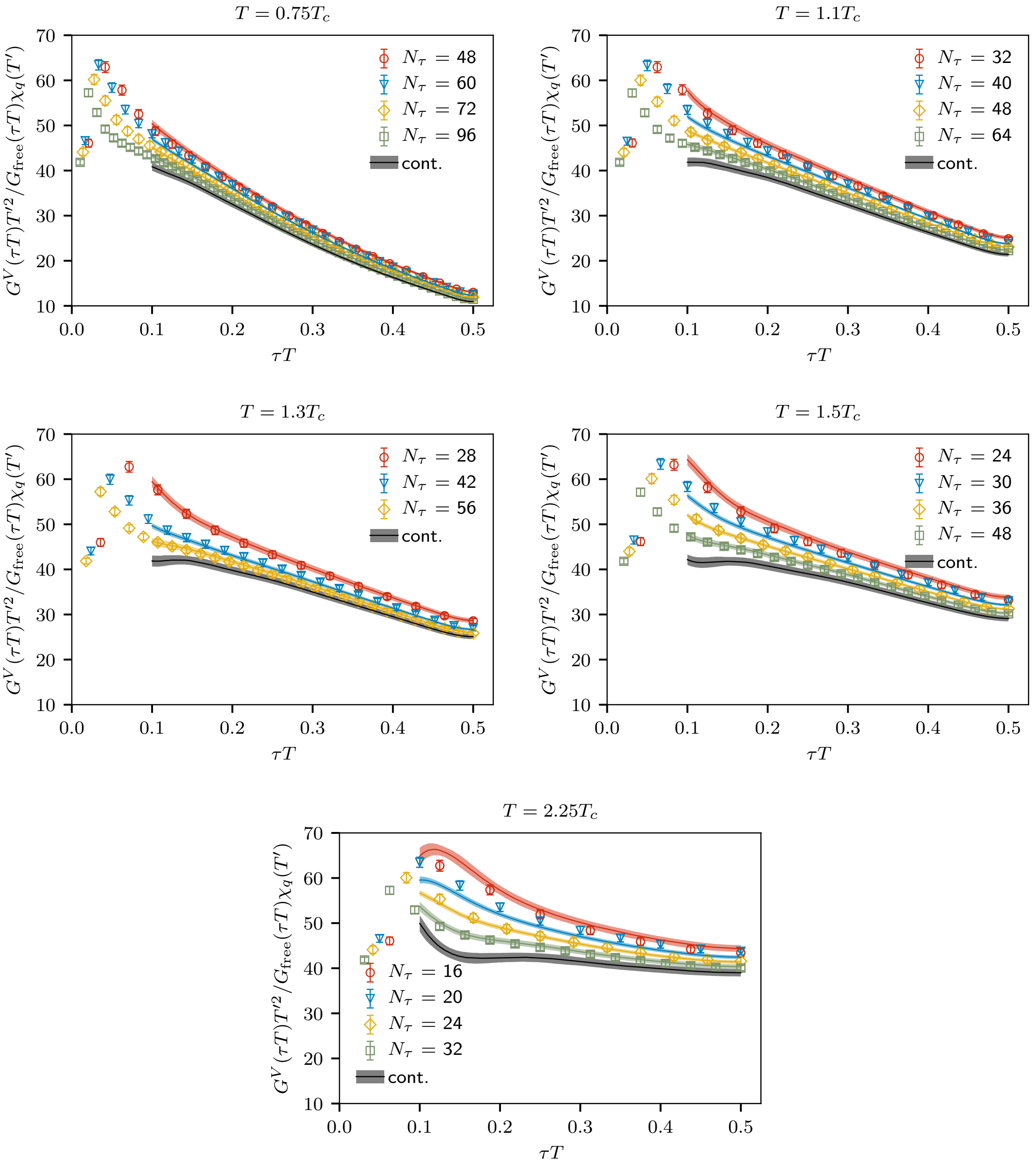

Figure 5.5: Continuum extrapolation of the interpolated bottomonium vector correlators. In order to perform a spline interpolation, we divided by the free continuum correlator defined in equation (5.1) with an input quark mass of $m_q = 4.5\,\mathrm{GeV}$. The renormalization is taken care of by dividing by quark number susceptibility χ_q, which is taken from the corresponding lattices at $T' = 2.25T_c$. The extrapolation and the interpolation is performed in one step using simple splines with the techniques described in section 4.4 to reduce the spline typical oscillations.

5.3. Results

The final results of the continuum extrapolated correlators are shown in figure 5.6. For short temporal distances ($\tau \approx 0.05\,\mathrm{fm}$), all measured correlators show almost no temperature effects and approach each other. This is expected as, due to asymptotic freedom, temperature and mass dependency should vanish asymptotically. Though we have to stress that in this region the cut-off effects may still be relevant. For larger temporal distances, we do not observe any significant temperature dependence within error bars except for the charmonium vector channel corresponding to the J/ψ. Here, we observe significant deviations for all temperatures. The correlator at $T = 1.1T_c$ starts to deviate at around $\tau \approx 0.2\,\mathrm{fm}$. For higher temperatures, the starting point at which deviations become relevant shifts to lower τ values. For $T = 2.25T_c$, the correlator deviates from the correlator at $T = 0.75T_c$ already at $\tau \approx 0.07\,\mathrm{fm}$. Overall, the largest deviation is found at $T = 2.25T_c$ at $\tau = 0.12\,\mathrm{fm}$, where the correlator takes about 30% larger values compared to correlator at $0.75T_c$.

However, changes in the correlator do not necessarily come from a change in the underlying spectral function as the kernel also contains temperature dependent information. Therefore we look at the comparison of the finite temperature correlators compared to the reconstructed correlator as defined in equation (3.100) as a next step. Our choice of lattice sizes allows to compute the reconstructed correlator for three different temperature combinations. Based on the coldest lattice at $T = 0.75T_c$, we may compute the reconstructed correlator at $T' = 1.5T_c$ and $T' = 2.25T_c$. Additionally, we can reconstruct the correlator at $T' = 2.25T_c$ based on the lattice at $T = 1.1T_c$. In order to show the deviations from the true correlators at those temperatures, we plot the ratio of the correlator divided by the corresponding reconstructed correlator in figure 5.7.

Here, the situation changes and we find significant temperature dependence in all of the correlators. The temperature effects are found to be largest at maximal temporal distance. The values at short temporal distances do not exhibit any significant deviations. We find that the ratios $G(T' = 2.25T_c)/G_{\mathrm{rec}}(T = 0.75)$ and $G(T' = 2.25T_c)/G_{\mathrm{rec}}(T = 1.1)$ perfectly agree except for the pseudoscalar channel in the charm sector. There, we find slightly smaller values, when the reconstructed correlator is calculated at $T = 0.75T_c$. From this, we may conclude that all of the channels are not yet significantly affected by temperature effects at $T = 1.1T_c$ except for the just mentioned channel corresponding to the η_c meson.

For the charm sector we find and up to 15% increase of the vector correlator compared to the reconstructed correlator at $T = 2.25T_c$ and an up to 10% rise at $T = 1.5T_c$. For the pseudoscalar channel we observe that the correlator is maximally about 10% smaller than the reconstructed one at $T = 2.25T_c$ and about 6% smaller at $T = 1.5T_c$. In the bottom sector, the temperature effects are less pronounced. In the vector channel, we notice only a small change at a temporal distance of $\tau = 0.25\,\mathrm{fm}$ at $T = 1.5T_c$. Within error bars this change is in agreement with a ratio of $G/G_{\mathrm{rec.}} = 1$. Nevertheless for $T = 2.25T_c$ we find temperature effects of about 10% (positive) at $\tau = 0.14\,\mathrm{fm}$. The pseudoscalar channel does not show any temperature influence at $T = 1.5T_c$ and is also only slightly affected at $T = 2.25$. Here the sign changes and we also find that the reconstructed correlator is smaller than the true one.

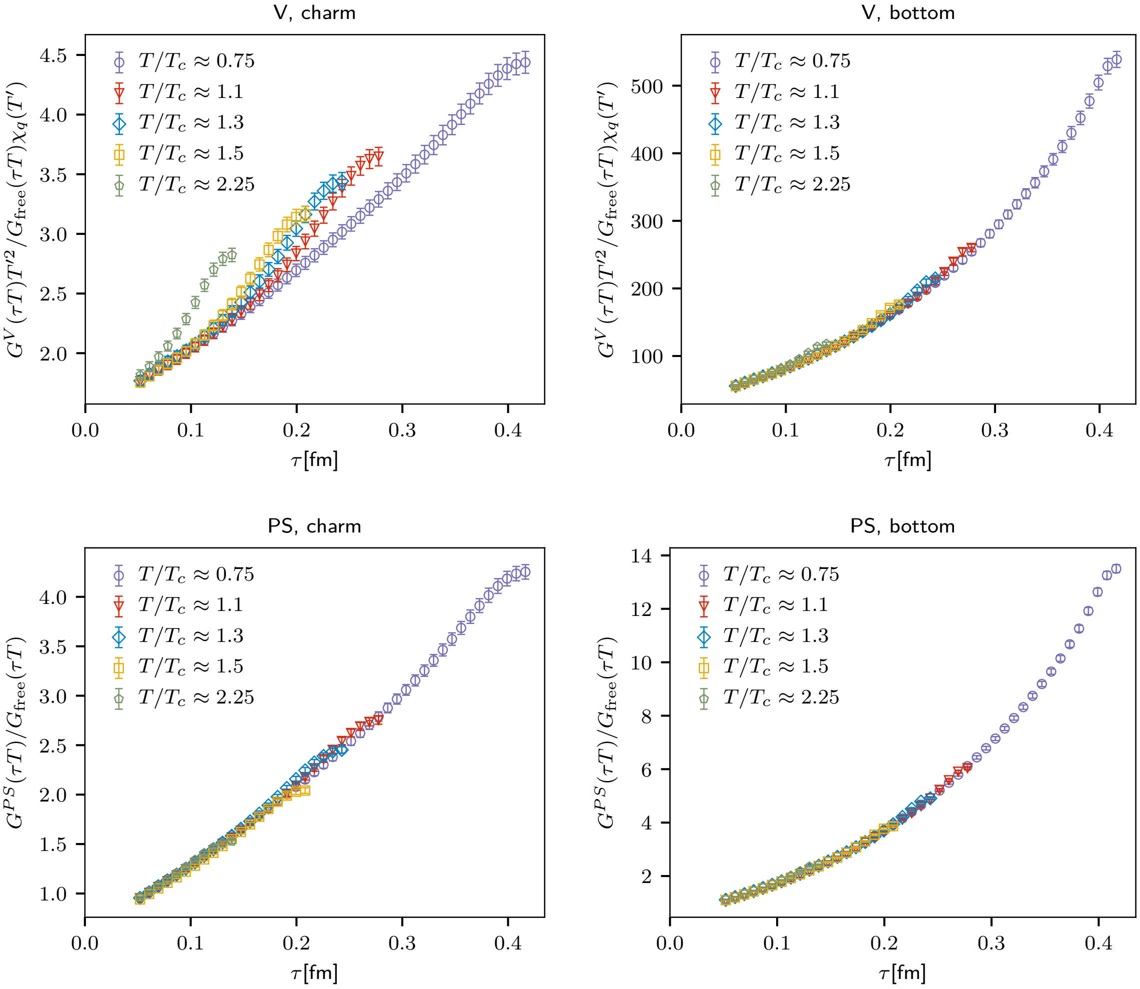

Figure 5.6: Continuum extrapolated correlators for the vector channel (top) and the pseudoscalar channel (bottom). We plot the results for charmonium (left) and bottomonium (right). The correlators are normalized using the corresponding free correlator in equation (5.1) with $m_q = 1.5\,\mathrm{GeV}$ for charmonium and $m_q = 5\,\mathrm{GeV}$ for bottomonium. While the pseudoscalar correlators are renormalized using the two-loop renormalization from equation (3.64), we divide by the quark number susceptibility χ_q at $T' = 2.25T_c$ for the vector channel to get a renormalization independent ratio.

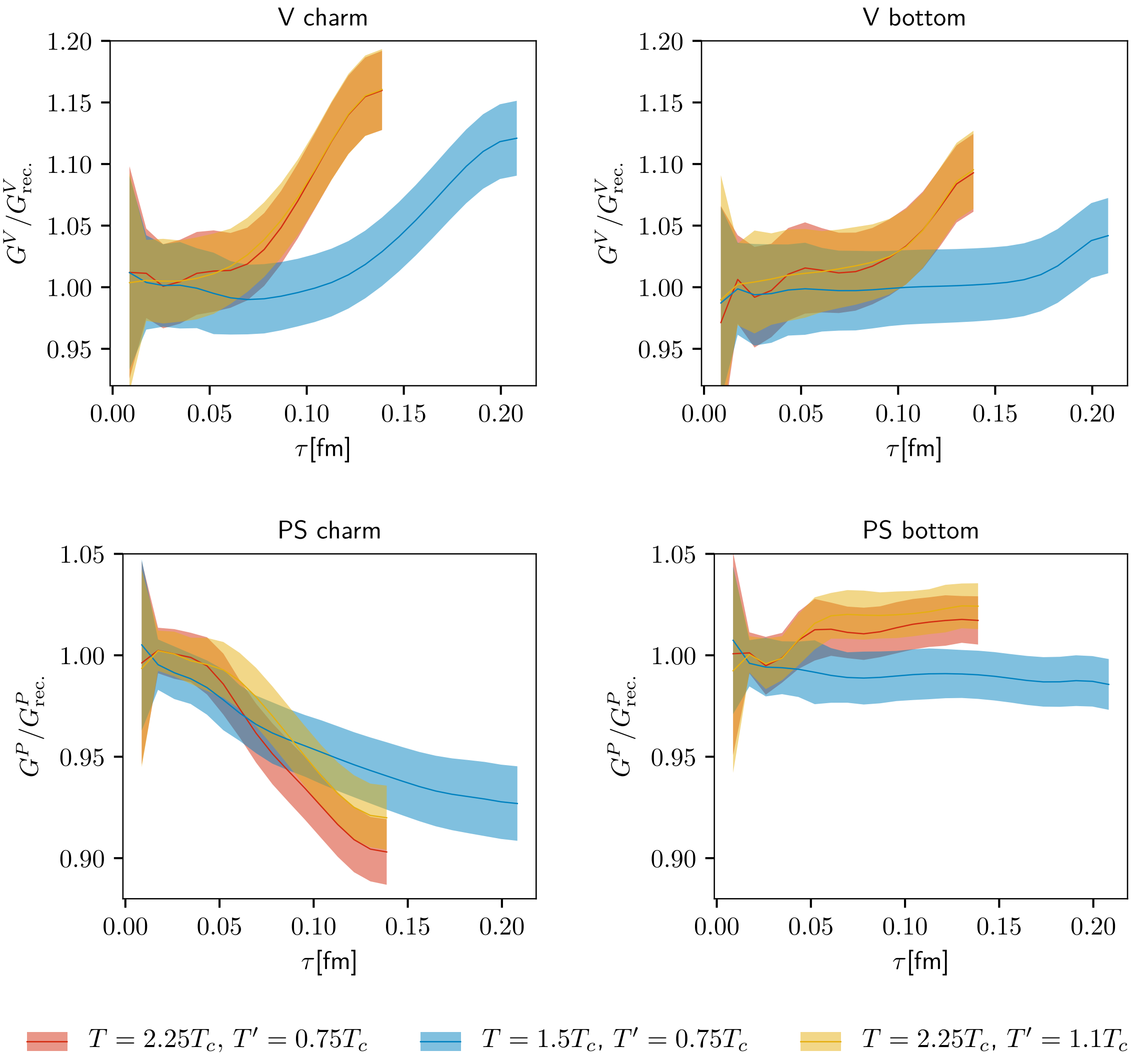

Figure 5.7: Ratio of the correlator and the corresponding reconstructed correlator defined in equation (3.100) evaluated on the continuum extrapolated correlators in figure 5.6. The reconstructed correlator is calculated using the data at $T = 0.75T_c$ and $T = 1.1T_c$, respectively

For a better understanding of the effects found in figure 5.7, we first integrate different parts of a model spectral function in order to understand which parts mainly contributes to the correlator at different τT. As a model spectral function we chose the vector spectral function developed in section 3.5. The transport peak is either modeled by a delta-peak or by a Breit-Wigner peak. We differentiate between a transport part, a part belong to the bound state region and a high frequency part. The results may be found in figure 5.8. In can be found, that the high frequency part mainly contributes to the short temporal distance region of the correlator. As none of the ratios $G/G_{\text{rec.}}$ exhibits any deviations from one at short temporal distances, we may conclude that the high frequency region of the spectral function stays unchanged throughout the whole temperature range.

The mid frequency range of the spectral function (yellow) mainly contributes at larger τ. In this region we expect possible peaks corresponding to bound states. Therefore, in medium modifications should mainly result in changes at larger temporal distances. In particular if a particle starts to melt, we expect the resonance peak to shrink and therefore, expect the ratio $G/G_{\text{rec.}}$ to become smaller than one at larger τ. Thus, the decline of in the lower left plot of figure 5.7 suggests, that the η_c state is effected already at $T = 1.5T_c$. At higher temperature, $T = 2.25T_c$ we observe even stronger temperature dependence, which suggests that the particle is melted at such temperatures. From the fact that the ratio $G(T' = 2.25T_c)/G_{\text{rec}}(T = 0.75)$ declines faster than $G(T' = 2.25T_c)/G_{\text{rec}}(T = 1.1)$, we may conclude that the state is even affected at $T = 1.1T_c$.

For the bottom sector in the pseudoscalar channel, we do not find a decline of the ratio $G/G_{\text{rec.}}$. Instead the ratio even rises for higher temperatures. This may be explained by a shift of the bound peak to lower frequency values, while its height does not shrink significantly. Though, as the ratio is compatible with $G/G_{\text{rec.}} = 1$ within 1 to 1.5σ, this might also be a statistical fluctuation. We will address this problem later again.

For the vector channel, another effect becomes relevant. With rising temperatures, the transport peak appears. As can be seen from figure 5.8, this transport peak also mainly contributes at larger temporal distances. Thus, in the vector channel, two effects overlay: At rising temperature, the bound states start to melt and we expect the correlator to take smaller values at larger τ. At the same time, the transport peak shifts the correlator upwards again. Therefore, from a change in the correlator one can only estimate which effects dominate.

We find a significant rise of the vector correlator in the charmonium sector at $T = 1.5T_c$ and an even higher rise at $T = 2.25T_c$. This clearly indicates the existence of a transport peak at those temperatures. As the ratio at $T' = 2.25T_c$ takes the same values regardless of whether the reconstructed correlator was computed using the $T = 0.75T_c$ or the $T = 1.1T_c$ data, we can deduce that there is no significant transport contribution at $T = 1.1T_c$. For bottomonium the temperature effects are not so pronounced. At $T' = 1.5T_c$ we only find a small effect at the end of the investigated temporal range. At $T = 2.25T_c$ the effects are larger, but still less than for the charmonium sector. This hints that the area under transport peak of the Υ is smaller then the one of the J/ψ.

Still, we do not get any information about modification of the bound state peak as the effects of the transport peak superimpose the contributions of the bound state peak. To compensate

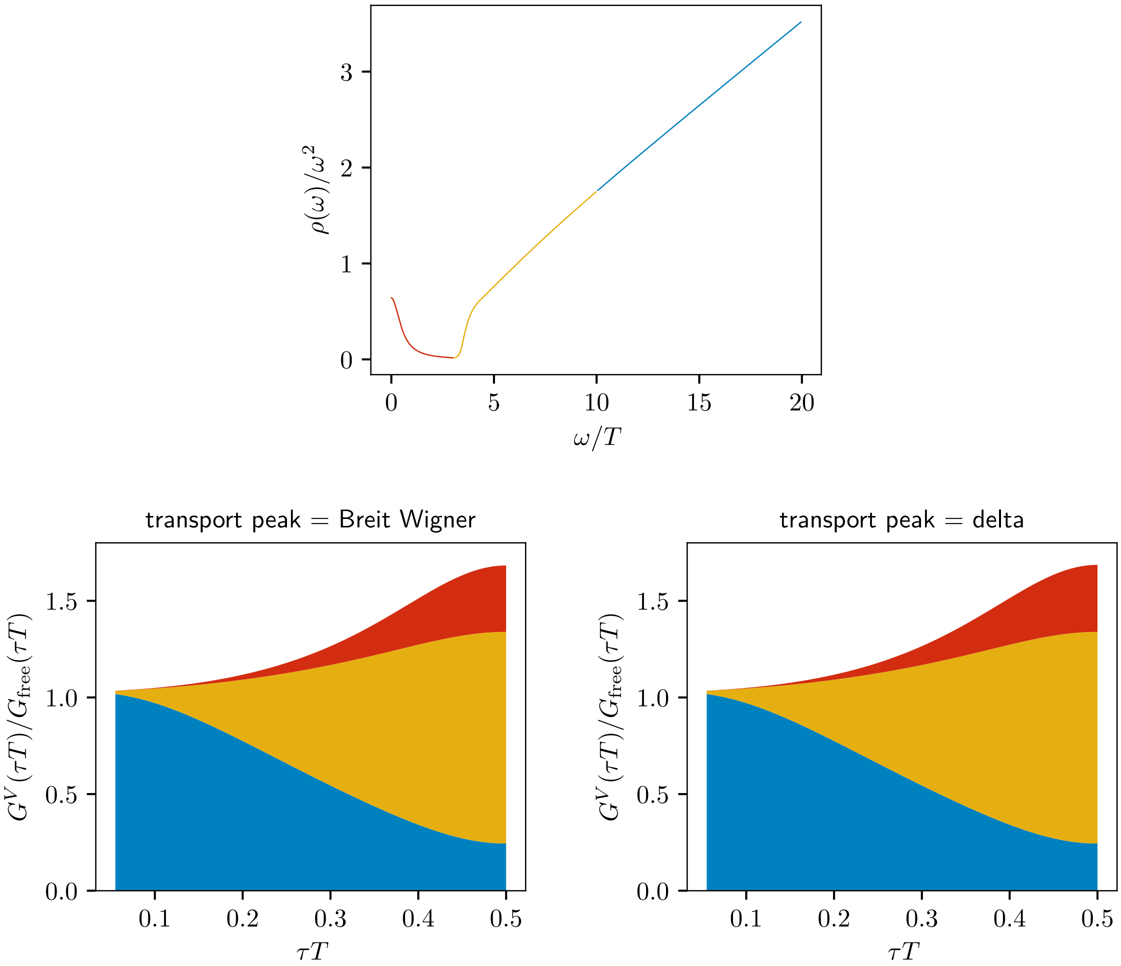

Figure 5.8: Visualization of which parts of the spectral function contribute to the correlator at different τT. Top: The spectral function that is integrated to calculate the corresponding correlator. The spectral function is the charmonium perturbative vector spectral function from section 3.5 at $T = 2.25 T_c$. The transport peak is modeled by a Breit-Wigner peak with $2\pi DT = 3$ and $\eta/T = 0.51$. Bottom left: Integrated correlator for the spectral function in the upper plot. The different colors bands correspond to the contribution of the different colored regions in the spectral function. Bottom right: The same as bottom left, but the transport contribution is modeled by a δ-peak with the same integrated contribution as as for the Breit-Wigner peak.

for that effect we try to remove the contributions from the transport peak by subtracting the correlator's value at $\tau T = 0.5$. The narrow peak structure of the transport peak leads to an almost constant part of the correlator. As can be seen in figure 5.8, the percentage of this constant part is maximal at $\tau T = 0.5$. Thus, the ratio of the so defined subtracted correlators

$$\frac{G_{\mathrm{sub}}(\tau T)}{G_{\mathrm{sub,rec.}}(\tau T)} \equiv \frac{G(\tau T) - G(0.5)}{G_{\mathrm{rec.}}(\tau T) - G_{\mathrm{rec.}}(0.5)} \tag{5.3}$$

should be free of most of the transport effects. However, we also remove a lot of parts from the mid range of the spectral function (yellow region in figure 5.8). Therefore we can not exclude that we also removed contribution of the bound state peak as well.

The results are given in figure 5.9. The error bars of the continuum extrapolated correlators become large, as the continuum extrapolation itself introduces a lot of uncertainties. Hence, we also plot the results from the finest lattice. Overall, we find agreement between the lattice data and the continuum extrapolated data within one sigma. For the pseudoscalar channel we still observe temperature effects for the charm sector. However, the effects are less pronounced compared to the ratio of G/G_{rec}. This suggests that we already removed parts of the resonance peaks which we should consider when analyzing the vector data. There, in the charm sector, the correlator now slightly decreases at $T' = 1.5T_c$. For $T' = 2.25T_c$ the decrease is a bit more distinct. This suggests that also J/ψ might be influenced already at $1.5T_c$. In the bottom sector, we do not observe any significant temperature effects in the lattice data, both in the vector as well as in the pseudoscalar channel. In the continuum extrapolated correlator, there is a slight increase of the subtracted correlator compared to the reconstructed subtracted correlator in the pseudoscalar channel. It is unsure whether this increase stems from a shift of the bound state peak to lower frequencies or if there is an unknown systematic error in the continuum extrapolation.

5.4. Comparing to perturbative computations

To get more insights into the changes of the spectral function and how to interpret the above results, we now have a closer look at a comparison to the perturbative spectral functions constructed in section 3.5. As a traditional reference scale, we chose $\mu_{\mathrm{ref.}} = 2\,\mathrm{GeV}$. For the charm quark we assumed a mass of $m(\mu_{\mathrm{ref.}}) = 1$ GeV and for the bottom mass we chose $m(\mu_{\mathrm{ref.}}) = 5$ GeV. In order to estimate the errors stemming from the uncertainties of the quark mass, we varied the input mass $m(\mu_{\mathrm{ref.}})$ by 10% for the charm sector and by 2% for the bottom sector. To compare to the lattice data, the perturbative spectral functions have been integrated numerically. We start with the results for the pseudoscalar channel in figure 5.11 for charmonium and in figure 5.12 for bottomonium. We find a general agreement of the shape of lattice data compared to the shape of the perturbative data. The perturbative data show a higher curvature, so that they overshoot the lattice data. For the charmonium data, this is mainly the case for higher values of τT. In the bottom sector, the relative difference is largest for smaller distances.

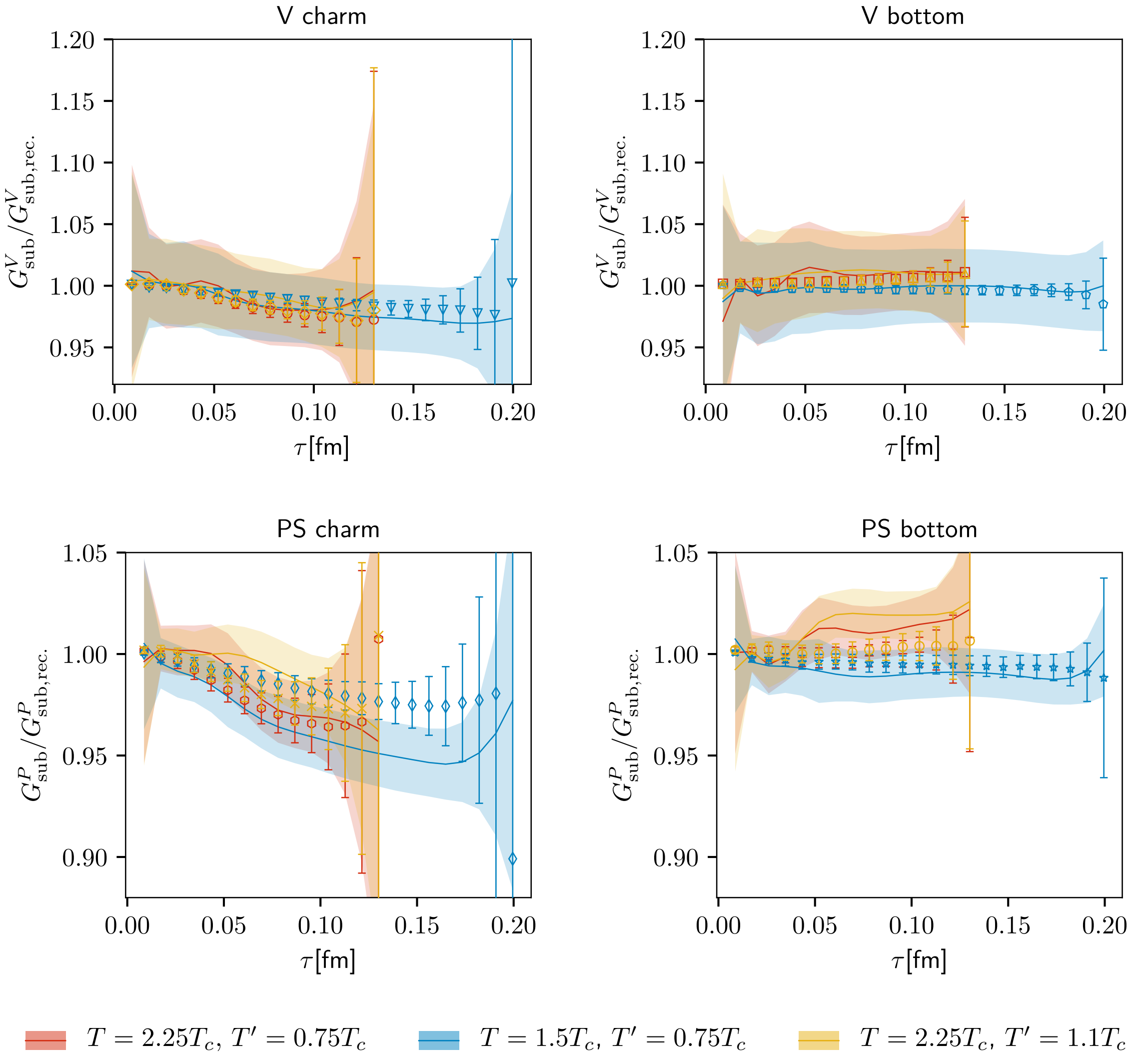

Figure 5.9: Ratio of the subtracted correlator and the corresponding subtracted reconstructed correlator defined in equation (5.3) evaluated on the continuum extrapolated correlators in figure 5.6 (bands) and on the finest lattice (dots). The reconstructed correlator is calculated using the data at $T = 0.75T_c$ and $T = 1.1T_c$, respectively.

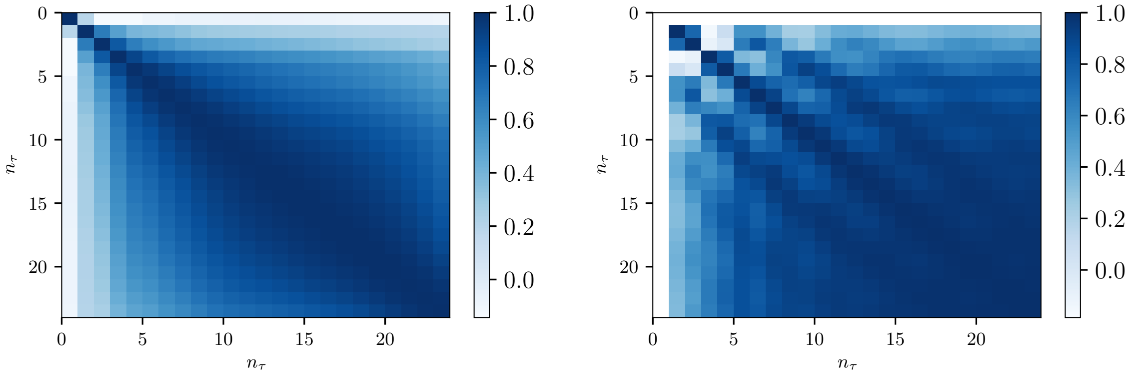

Figure 5.10: Correlation matrix for the lattice data (left) and for the continuum extrapolated correlator (right) for the vector channel of charmonium at $T = 1.5T_c$.

However, the perturbative as well as the non-perturbative lattice results undergo some uncertainties, which we try to overcome by introducing a model spectral function as

$$\rho_{\text{model.}} = A\rho_{\text{pert.}}(\omega + b). \tag{5.4}$$

Here, we modify the overall amplitude to compensate uncertainties on the lattice site stemming from the renormalization. The shift b has been introduced to correct for the uncertainties of the estimate of pole-type masses as well as non-perturbative thermal mass shifts in the threshold region. This model has then been fitted to the lattice data. To exclude cut-off effects on the lattice site from the fit, we only used lattice points above $\tau T = 0.15$. In principle these fits need to take care of the correlations between the individual data points in the correlator.

The resulting modeled correlators are also plotted in figures 5.11 and 5.12 and the corresponding fit parameters are given in tables 5.2 and 5.3. We find a perfect representation of the lattice data for both bottomonium and charmonium at all temperatures. Note that the $\chi^2/\text{d.o.f.}$ is below one for almost all of the fits. This is due to the fact that the simple χ^2-fits do not account for correlations, as there is no correlation matrix available in the extrapolated data.

By taking the same random number in the bootstrapping for each distance, in principle we may compute a continuum extrapolated covariance matrix. However, as it can be seen in figure 5.10, the spline interpolation introduces oscillations into the covariance matrix which heavily destabilize the fits. Thus, we only use decorrelated fits and therefore, all following fit results may be interpreted in a qualitative way only.

Regarding the fit parameters, we observe a slight increase in the amplitude of the correlators, which is well covered by the uncertainties of the perturbative renormalization used here. In addition, the spectral functions are shifted to the right, where the shift is largest at $T = 1.1T_c$ and decreases monotonically with increasing temperature. This may be explained by non-perturbative thermal mass effects, which induce a temperature dependent mass shift.

For bottomonium, the mass shifts are less significant. Here, the spectral function is slightly

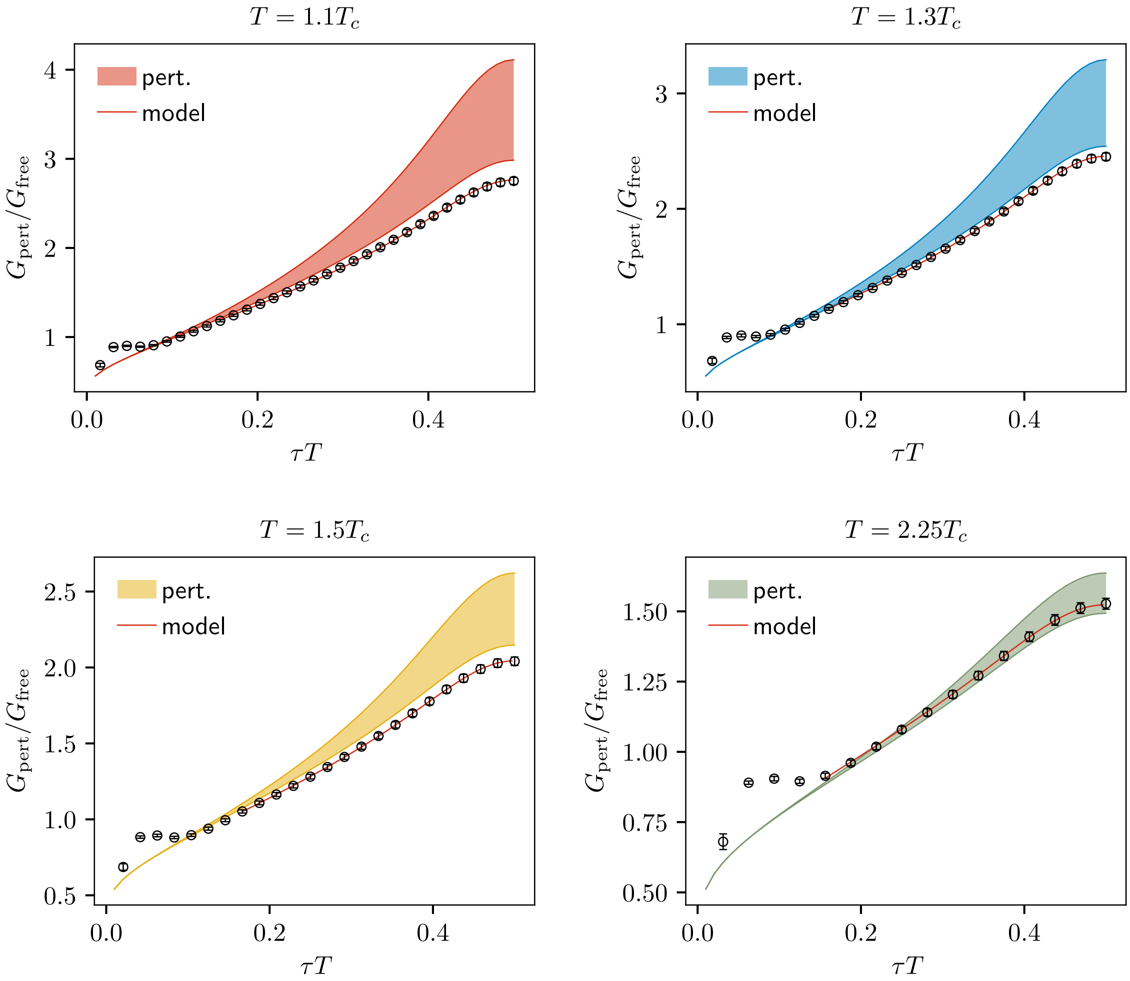

Figure 5.11: The perturbative correlator (band) as well as the lattice results (dots) in the pseudoscalar channel at different temperatures for charmonium. Both are divided by the free correlator in equation (5.1) with an input quark mass $m_q = 1.5\,\mathrm{GeV}$. Additionally, we plot the best model according to equation (5.4). The uncertainty bands of the perturbative correlator stem from varying $m(\bar{\mu}_{\mathrm{ref}}) = 1\,\mathrm{GeV}$ by 10%.

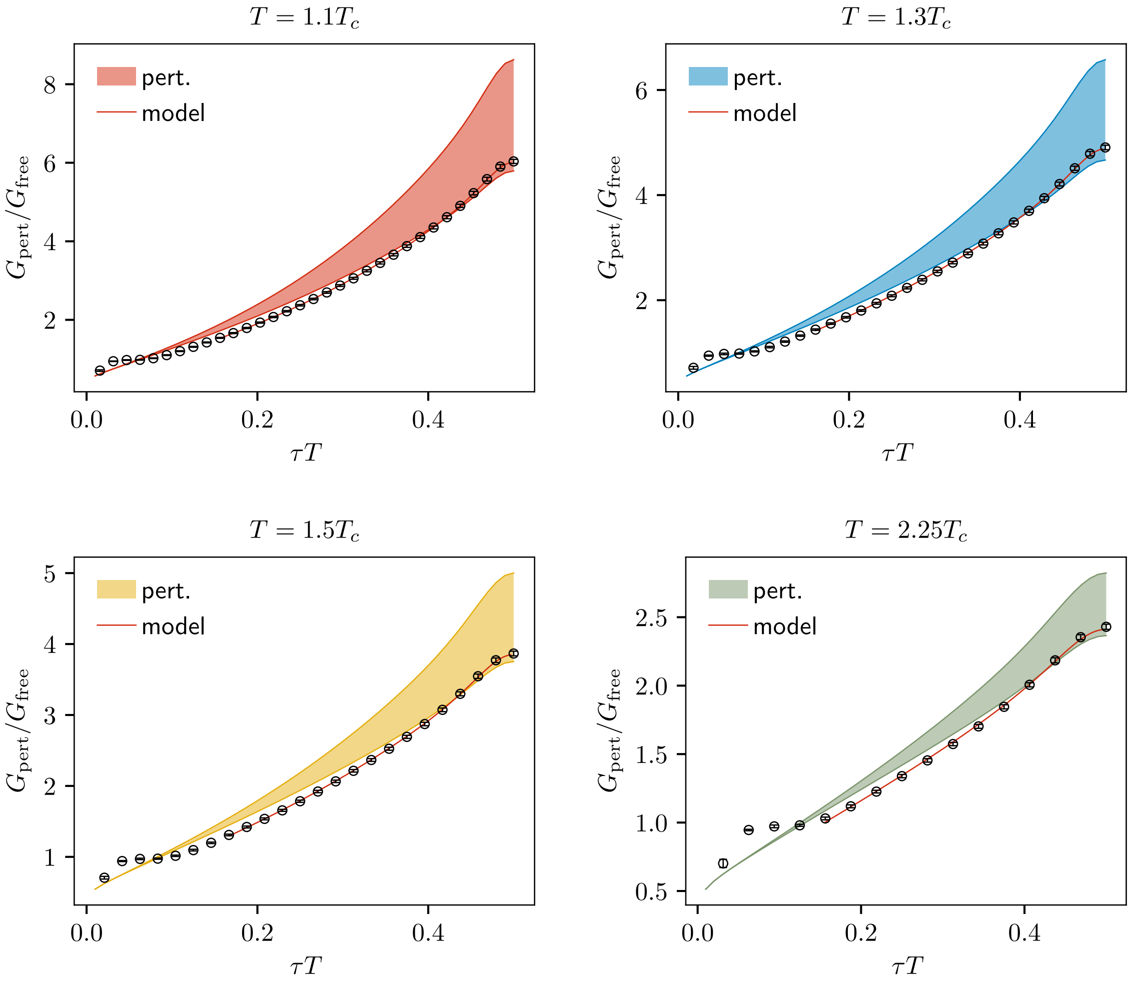

Figure 5.12: The perturbative correlator (band) as well as the lattice results (dots) in the pseudoscalar channel at different temperatures for bottomonium. Both are divided by the free correlator in equation (5.1) with an input quark mass $m_q = 5\,\text{GeV}$. Additionally, we plot the best model according to equation (5.4). The uncertainty bands of the perturbative correlator stem from varying $m(\bar{\mu}_\text{ref}) = 5\,\text{GeV}$ by 2%.

fit parameters	$T = 1.1T_c$	$T = 1.3T_c$	$T = 1.5T_c$	$T = 2.25T_c$
A	1.052(3)	1.042(2)	1.0214(9)	1.043(4)
b/T	-0.574(8)	-0.407(4)	-0.340(3)	-0.13(2)
$\chi^2/\mathrm{d.o.f.}$	0.1	0.02	0.009	0.1

Table 5.2: Fit results according to equation (5.4) for the pseudoscalar channel in the charmonium sector. The data points enter as independent points. The given errors stem from the fit itself.

fit parameters	$T = 1.1T_c$	$T = 1.3T_c$	$T = 1.5T_c$	$T = 2.25T_c$
A	0.846(2)	0.854(3)	0.851(4)	0.897(9)
b/T	0.046(6)	0.094(9)	0.11(2)	0.10(3)
$\chi^2/\mathrm{d.o.f.}$	0.1	0.2	0.3	1.3

Table 5.3: Same as 5.2 for the bottomonium sector.

shifted to the left. Moreover, the mass shift seems to be less temperature dependent for temperatures of $T = 1.3T_c$ and above. Only at $T = 1.1T_c$, the shift differs significantly from the values at other temperatures. Here, the amplitude takes values smaller than one and is corrected by a larger amount compared to charmonium. This may be expected because of the larger cut-off effects due to the higher quark mass.

Due to the transport contribution, the situation becomes more complicated in the vector channel. Already in figure 5.8, it became clear that the detailed shape of the transport peak is difficult to estimate from lattice data, as a difference to a δ-peak is very small. This has been analyzed in more detail in [141] and it could be shown that it becomes challenging to reconstruct the shape of the transport peak if $2\pi TD$ takes values larger than 2. Therefore, we model the transport peak by simply adding a constant to the correlator or, equivalently, by introducing a δ-function the spectral function:

$$\rho_{\mathrm{model.}} = A\rho_{\mathrm{pert.}}(\omega + b) + c/T\delta(\omega). \tag{5.5}$$

For the choice of the constant c we now have three options: First we can take it as an additional fit parameters. Another possibility is to use perturbative calculations given in [141]. As a last option, we also analyze if a transport peak is necessary at all by setting $c = 0$.

For the vector channel, we normalized with the quark number susceptibility in order to get a renormalization independent ratio. However, the quark number susceptibility χ_q is not available at the perturbative site, so that we cannot create this renormalization independent ratio for the perturbatively computed correlator. Therefore, we also perform a continuum extrapolation on the quark number susceptibility itself at $T \sim 2.25T_c$. We used the non-perturbative renormalization given in equation (3.62). Afterwards, the quark number susceptibility has been removed from the lattice data.

The results for the corresponding fit parameters can be found in tables 5.4 and 5.5 and the corresponding plots in figures 5.13 and 5.14. The fits work reasonable for all different models of the transport peak. In the case of charmonium, the values for A and b heavily depend on

method	fit parameters	$T = 1.1T_c$	$T = 1.3T_c$	$T = 1.5T_c$	$T = 2.25T_c$
flexible	A	1.044(5)	1.034(3)	1.000(3)	0.969(8)
peak	b/T	-0.27(2)	-0.12(2)	0.01(2)	0.24(5)
	c/T^3	0.002(5)	0.038(4)	0.102(5)	0.34(3)
	$\chi^2/\mathrm{d.o.f.}$	0.02	0.004	0.002	0.01
fixed	A	1.16(2)	1.14(2)	1.08(1)	0.999(5)
peak	b/T	-0.81(5)	-0.60(4)	0.07(2)	0.07(2)
	c/T^3	0.125	0.176	0.245	0.444
	$\chi^2/\mathrm{d.o.f.}$	0.7	0.4	0.2	0.04
no	A	1.042(2)	1.012(3)	0.957(4)	0.890(8)
peak	b/T	-0.261(5)	-0.011(7)	0.24(2)	0.72(3)
	$\chi^2/\mathrm{d.o.f.}$	0.02	0.02	0.07	0.2

Table 5.4: Fit results according to equation (5.5) for the vector channel in the charmonium sector. The data points enter as independent points. The given errors stem from the fit itself. We used three different methods to model the transport peak. The “flexible peak” model takes the constant c as a fit parameter. For the “fixed peak”-method, the constant c was fixed to perturbative values computed using the methods described in [141]. For the method “no peak” we performed the fit while completely ignoring the transport contributions.

the choice of the method. Overall we find that the amplitude A is not independent of the temperature. While it takes values greater than one for $T = 1.1T_c$, it reduces with rising temperature, until it takes values smaller than one for the highest temperature at $T = 2.25T_c$ for all different methods. This is somewhat surprising, as the renormalization is independent of the temperature. Also for the shift we observe different effects at different temperatures: For low temperatures, the spectral function is shifted to the right, while for higher temperatures, we observe a shift to the left. The results for the transport peak from the method with the “flexible peak” method differ from the perturbative values. In fact, the perturbative results seem to be too large at all different temperatures when comparing to the three parameter fit. This has to be compensated by different shifts and amplitudes when fixing the area under the transport peak.

As all different methods perfectly lie within the error bars, it is difficult to decide which model works best. However, we should note that the size of the error bars mainly stems from the uncertainties of the continuum extrapolation of χ_q. This error is constant in τT. Thus, this error mainly transfers into uncertainties in the estimation of the amplitude. The values of the shift and the transport contribution should therefore be determined with higher accuracy. The constancy of the error does also imply that the values of the $\chi^2/\mathrm{d.o.f}$ might still be used to compare the results of the fit, even though the values are far below one. In that sense, we find that the three parameter fit gives the best results. Except for $T = 2.25T_c$, the second best option is to use no transport contribution at all. This seems to be reasonable as the results for the constant c of the three parameter fit are closer to zero than to the perturbative values. Only at $T = 2.25T_c$, the three parameter fit results lie closer to the perturbative predictions.

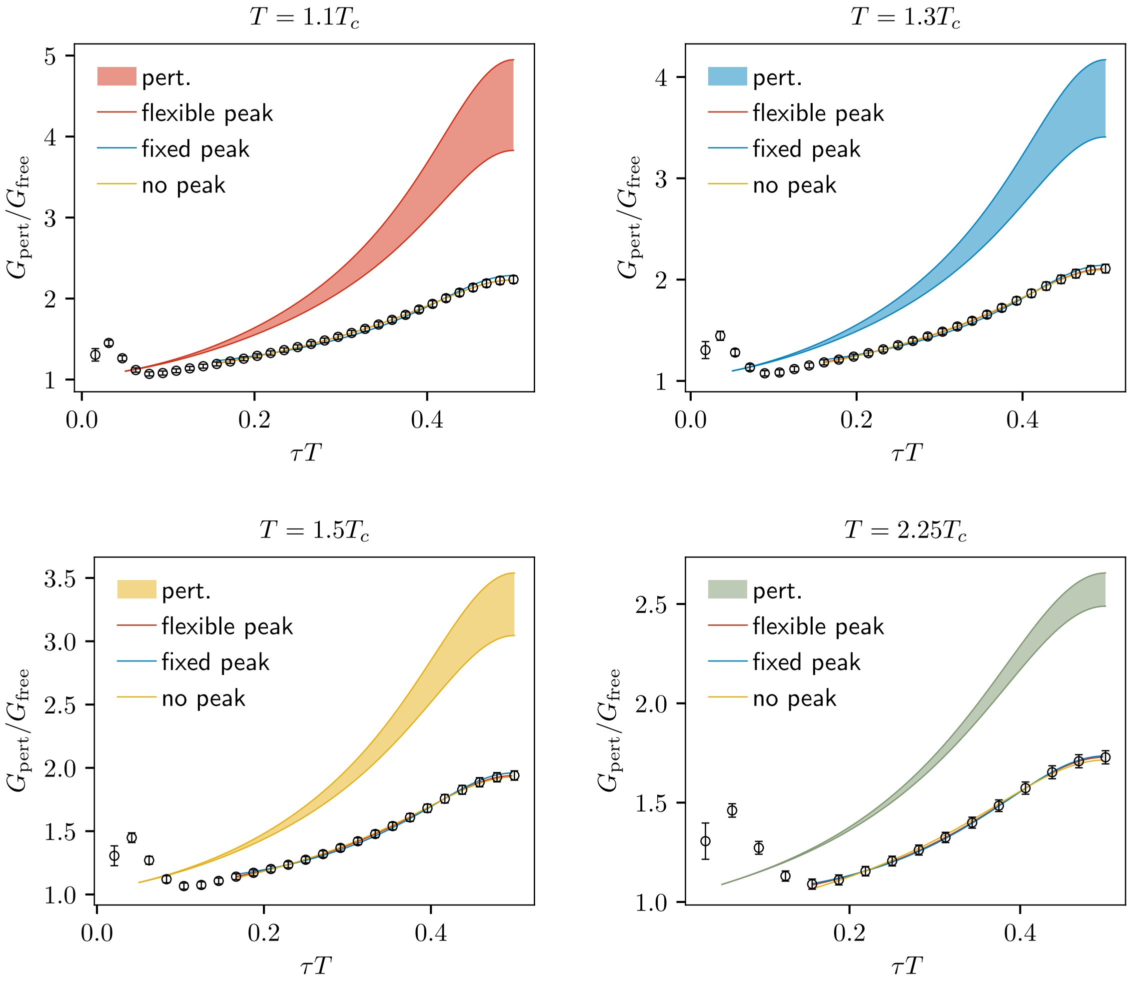

Figure 5.13: The perturbative correlator (band) as well as the lattice results (dots) in the vector channel at different temperatures for charmonium. Both are divided by the free correlator in equation (5.1) with an input quark mass $m_q = 1.5\,\text{GeV}$. Additionally, we plot the best model according to equation (5.4). The uncertainty bands of the perturbative correlator stem from varying $m(\bar{\mu}_{\text{ref}}) = 5\,\text{GeV}$ by 10%.

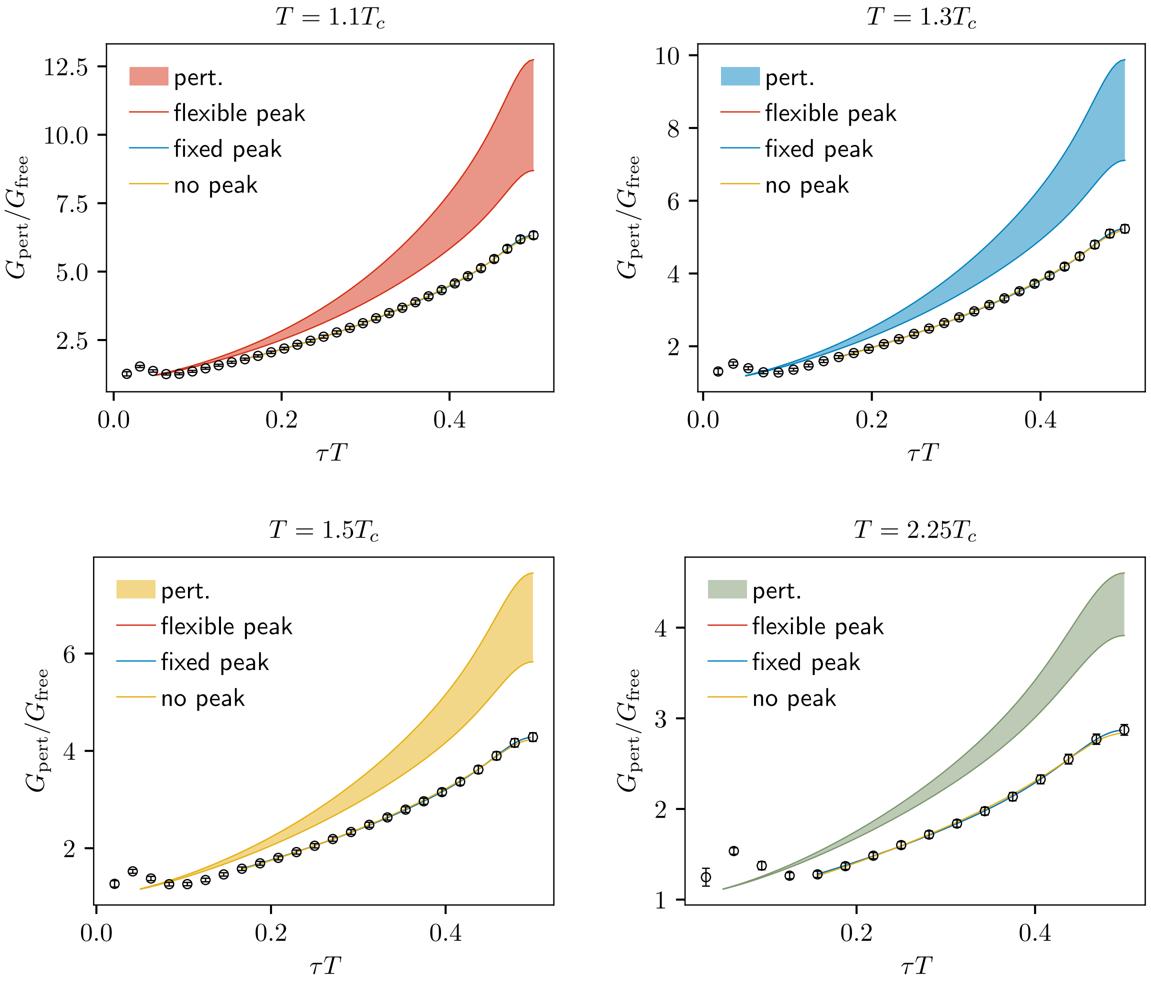

Figure 5.14: The perturbative correlator (band) as well as the lattice results (dots) in the vector channel at different temperatures for bottomonium. Both are divided by the free correlator in equation (5.1) with an input quark mass $m_q = 5\,\mathrm{GeV}$. Additionally, we plot the best model according to equation (5.4). The uncertainty bands of the perturbative correlator stem from varying $m(\bar{\mu}_{\mathrm{ref}}) = 5\,\mathrm{GeV}$ by 2%.

method	fit parameters	$T = 1.1T_c$	$T = 1.3T_c$	$T = 1.5T_c$	$T = 2.25T_c$
flexible	A	0.993(2)	0.992(2)	0.979(3)	0.955(6)
peak	b/T	-0.019(6)	0.056(7)	0.13(1)	0.27(3)
	c/T^3	$1.4(2) \cdot 10^{-5}$	$6.3(6) \cdot 10^{-5}$	$3.6(3) \cdot 10^{-4}$	0.0077(9)
	$\chi^2/\mathrm{d.o.f.}$	0.008	0.006	0.009	0.02
fixed	A	0.995(2)	0.995(2)	0.978(2)	0.954(4)
peak	b/T	-0.025(4)	0.045(5)	0.127(5)	0.27(1)
	c/T^3	$1.55 \cdot 10^{-5}$	$7.5 \cdot 10^{-5}$	$3.5 \cdot 10^{-4}$	0.0076
	$\chi^2/\mathrm{d.o.f.}$	0.008	0.007	0.008	0.02
no	A	0.981(4)	0.977(4)	0.954(6)	0.914(9)
peak	b/T	0.03(1)	0.12(2)	0.23(2)	0.46(3)
	$\chi^2/\mathrm{d.o.f.}$	0.05	0.06	0.1	0.2

Table 5.5: Same as 5.4 for the bottomonium sector.

In the bottom sector the contributions of the transport peak are small. ($c/T < 10^{-2}$ for all temperatures). Still, the results of the three parameter fit agree surprisingly well with the perturbative results. Only at $T = 1.3T_c$ the values differ more than one sigma of uncertainty. Even though the contribution of the transport peak are small, they still seem to help for the stability of the fit. The two parameter fit without transport contribution roughly gives a ten times larger $\chi^2/\mathrm{d.o.f.}$ This may be explained as following: Due to the larger gap between the transport and the threshold region, changes in the spectral function near the bound state can not compensate for the effects from the low frequency region. This means, the relative contribution of the transport peak becomes more important for larger values of τT.

For the amplitude we find consistent values slightly below one over the whole temperature range. For the shift we do not observe a pattern. It takes values above and below zero.

The plots of the resulting model spectral functions are given in figure 5.15 for the pseudoscalar channel and in figure 5.16 for the vector channel. The modification by the fit to model spectral functions are moderate, moving the threshold of the spectral function slightly without changing the qualitative behavior. After the fit, we do not observe any significant temperature dependent shift of the threshold of the spectral function, for all temperatures up to $1.5T_c$. Only for $2.25T_c$ we may observe a small shift of the threshold upwards in the pseudoscalar channel and to lower frequency values in the vector channel for bottomonium. These findings are in contrast to the results from NRQCD lattice calculations in [142, 143] and to the perturbative computations in [144], where in both cases a significant, negative mass shift is found. However, note that peak position in our perturbative model spectral functions are fixed and do not exhibit a temperature dependent shift. Due to the small contribution of the actual peak to the final correlator, also the fit is not sensitive to the peak position and thus, the total mass shift is mainly given by the shift of the threshold.

For both channels, no bound state for the vector channel is needed to describe the lattice data. Though, we find a decrease of the spectral function in the threshold region with rising

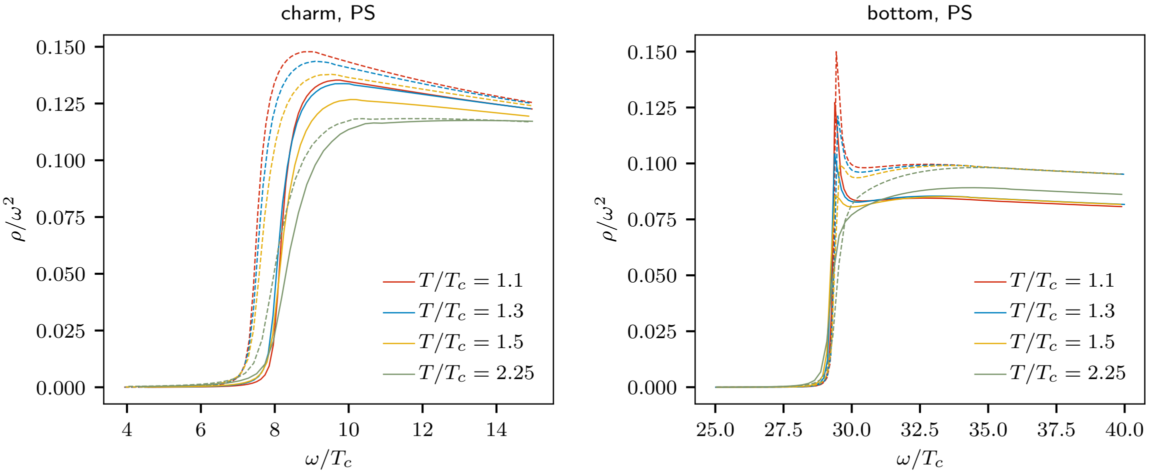

Figure 5.15: Perturbative pseudoscalar spectral functions (dashed) and their modifications according to equation (5.4) (continuous lines) for the charm sector (left) and the bottom sector (right). The modeled spectral functions correspond to the model in figures 5.11 and 5.12.

temperature: For $1.1T_c$ and $1.3T_c$, the spectral functions mainly lie almost on top of each other for both the pseudoscalar as well as the vector channel. At $T = 1.5T_c$, the spectral function lies below these values and at $T = 2.25T_c$ it takes even lower values. This effect is a bit more distinct in the case of the pseudoscalar channel. Here, the difference between the spectral function at $T = 1.1T_c$ and the spectral function at $T = 2.25T_c$ is maximally 15%, while it is about 8% for the vector channel. This behavior is in perfect accordance with the observations with the reconstructed correlator, where we observed stronger temperature effects for the pseudoscalar channel. Nevertheless, we have to state that this temperature dependence does not originate from a bound state. Due to the uncertainties of the perturbative calculations we cannot exclude non-perturbative effects which lead to a bound peak and are not covered here. Still, we find a perfect agreement with the lattice data, which once more shows how small effects of bound states may be. This especially becomes clear when looking at the bottom sector.

In contrast to charmonium, a clear bound state can be observed for $T \lesssim 1.5T_c$ for bottomonium. However, the narrowness of this peak reduces its impact on the correlator. Even though the peak shrinks with rising temperatures until it is totally gone at $T = 2.25T_c$, this barely effects the ratio of the subtracted correlator divided by the reconstructed subtracted correlator in figure 5.9. The small loss of the peak is compensated by other parts of the spectral function, which takes higher values. This is especially visible at $T = 2.25T_c$, where the spectral function lies above the other ones on the left and right side of the peak. Such a modification of the spectral function is not observable by ratios of the correlator divided the reconstructed correlator.

For bottomonium, the melting of bound states appears to be roughly in accordance with

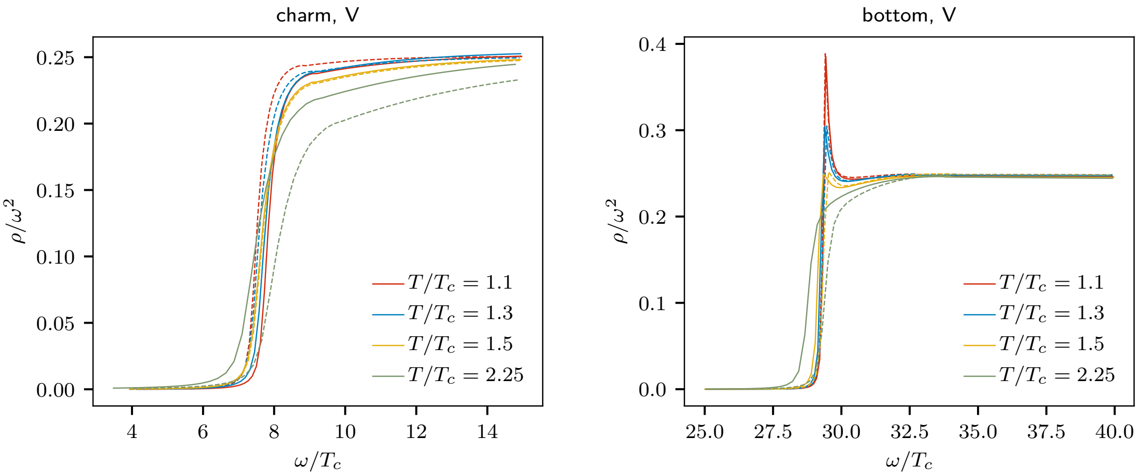

Figure 5.16: Same as figure 5.15 but for the vector spectral functions.

the NRQCD results from references [142, 143], where a clear peak up to $1.66T_c$ could be observed. For charmonium however, we do not observe a bound state peak for temperatures of $T = 1.1T_c$ and above which is contrast to the NRQCD results and probably originates from the fact that in the latter case, full QCD has been used instead of a quenched theory.

5.5. Concluding remarks

For the first time, we have presented a continuum extrapolation of the charmonium and bottomonium correlators in the vector and pseudoscalar channel on quenched lattices. To exclude any effects stemming from uncertainties in the tuning of the quark mass, we performed a quark mass interpolation by interpolating the correlators such that they correspond to the exact same meson vector mass at zero temperature. Afterwards, the continuum extrapolation has been performed linear in $1/N_\tau^2$. By analyzing the reconstructed correlator, we find thermal modifications for the charm sector for both channels. For the vector channel, we observe the existence of of a transport peak at higher temperatures. This transport peaks hides information about the modifications of the bound states. Therefore, we analyzed the subtracted correlator. Here we also find modifications of the bound state region. The modifications are less dominant compared to the pseudoscalar channel. We tentatively conclude that the η_c may melt at lower temperatures compared to the J/ψ. For the bottom sector, we do not find any modifications of the bound states. Though, we find indications for a small transport peak in the vector channel.

We compare the lattice correlators against perturbative results from resummed perturbation theory to get more insights into the modifications of the spectral function. To overcome the uncertainties of the renormalization and of the quark pole mass, we perform a model fit to the continuum extrapolated lattice correlators. For the vector channel, we also compare three different models of the transport peak. We find that a transport peak is not necessary to describe the lattice data but helps stabilize the fits. Regarding the area under the transport peak, we do not find a good agreement with the perturbative results from [141] for the charmonium and a model with variable transport contribution works better. However for bottomonium we find that the perturbative results and the results of the fit agree within error bars.

For the charm sector, no bound state is needed to describe the lattice data in both channels. Still, we find temperature dependent modifications starting at about $1.5T_c$. The pseudoscalar channel exhibits slightly stronger temperature dependence. For bottomonium, we observe a bound state peak up to roughly $1.5T_c$, whose height shrinks with rising temperature. As the spectral function gains contribution to the correlator at other frequencies, this is still in accordance with the results extracted from the reconstructed correlator.

In our models we did not analyze the detailed shape of the transport peak, as we found four parameter fits to be unreliable. Thus, we can not make any statements about the heavy quark diffusion constant. In a future study, this problem may be circumvented by first fitting to the midpoint subtracted correlator ($G_{\mathrm{mid-sub.}}(n_\tau) = G(n_\tau) - G(N_\tau/2)$) and afterwards fitting the transport peak, separately.

We cannot exclude the existence of non-perturbative features that are not covered in our analysis, within the resonance peak region. This holds especially for the charm sector as, due to the lighter quark mass, this is less close to non-relativistic QCD compared to the bottom sector. Therefore, we may use statistical tools like MEM [111] or SAI [113] to extract the spectral function independently. Among others, the perturbative spectral functions may serve as a default model. With this method, we may also find out details about the shape of the transport peak.

So far, our analysis is based on quenched QCD. Due to the higher transition temperature, this makes perturbation theory more applicable. However, the different temperatures as well as the larger effective coupling, may change the results for dynamic QCD. Indeed in [142] resonance peaks have also been found for charmonium at physical quark masses. Consequently an analysis based on unquenched lattice configurations is desirable. In [145] an analysis at non-physical pion masses without an continuum extrapolation has been performed. A starting point for an analysis at physical quark masses could be the staggered HISQ configurations used in the next section. These have sizes up to $64^3 \times 16$ and the mesonic correlators have already been calculated using the Wilson action as well as the HISQ action. Due to the oscillating two states that are present in staggered meson correlators (see section 3.1.3) the extraction of the spectral function is only possible for the pseudoscalar channel.

6. Screening masses for dynamic QCD

In the last section, we analyzed mesonic correlators for charmonium and bottomonium in the quenched approximation. As a next step, we want to analyze mesonic states that also include the lighter quarks. Due to their small masses, the systematic effects stemming from the quenched approximation will be larger when measured on quenched lattices. Thus, we switch to configurations generated using dynamical QCD. As the Markov update for dynamical QCD actions is far more expensive, we can not reach the large lattice sizes of the previous section. Consequently, an analysis of temporal correlators is currently out of reach for dynamical QCD at temperatures around the transition temperature, and therefore, we focus on spatial correlators here.

As already mentioned in section 3.1.2, screening correlators represent a perfect tool to investigate the restoration of chiral and $U_A(1)$ symmetry: Chiral symmetry should manifest in a degeneracy of the screening correlators of the ρ and the a_1 particles, while a degeneracy of the π and a_0 indicates an effective restoration of the $U_A(1)$ symmetry.

The screening correlator is connected to the same spectral function as the temporal one through equation (3.101) so that changes in the screening correlator also correspond to changes in the spectral function. Hence, modifications of the corresponding screening masses also indicate an influence of the medium on the bound states.

Another application of screening masses is a validity check of resummed perturbation theories. In the free limit one expects a behavior of $m_{\text{scr.}} \sim 2\pi T$ according to equation (3.26). Results of resummed perturbation theory predict that this limit should be reached from above, as the leading order perturbative corrections of $\mathcal{O}(g^2T)$ are found to be positive and identical for all mesonic channels [146]. A non-perturbative measurement of the screening masses at high temperatures thus may be used to check the applicability of Perturbative theory.

To summarize: the intention of this section is to analyze the restoration of the chiral and the $U_A(1)$ restoration, to investigate modifications of mesonic states and to check the applicability of resummed perturbation theory at high temperature. A comparably computationally favorable dynamic lattice QCD action is the staggered HISQ action, which we will use in the following. As mesonic correlators mix two states and involve oscillations of one of the states, a detailed analysis on the level of the correlator itself is difficult. Therefore we mainly look at the corresponding screening masses and the susceptibilities instead.

We start with the description of the lattice setup in section 6.1, where we also analyze the amount of taste violations that goes into the correlators. After having a closer look at the difference between different sources used for calculating the correlator, we describe the methods being used to perform the continuum limit. Afterwards, we present the results for different quark combinations in section 6.2. We cover a large temperature range starting at about $140\,\text{MeV}$ going up to $3\,\text{GeV}$. Additionally we use four different values for the light quark mass to examine the effects in the chiral limit.

6.1. Lattice setup and continuum limit

The calculation of the correlators is based on $N_f = 2{+}1$ staggered HISQ configurations which all have been tuned to a physical strange quark mass by matching to the mass of the fictitious pseudoscalar meson $m_{\eta_s} = \sqrt{2m_K^2 - m_\pi^2}$ [48, 147]. For the light quark mass, we use values of $m_l = m_s/20$, $m_l = m_s/27$, $m_l = m_s/40$ and $m_l = m_s/80$. Here, the ratio of $m_s/m_l = 27$ corresponds to the physical point. For the ratio $m_s/m_l = 20$ we cover a wide temperature range from about $0.13\,\mathrm{GeV}$ up to $3\,\mathrm{GeV}$. For the other quark mass ratios, we concentrated on the crossover region from about $130\,\mathrm{MeV}$ to roughly $175\,\mathrm{MeV}$. All configurations are separated by 10 full trajectories.

The lattice sizes vary from $24^3 \times 6$ to $64^3 \times 16$, which allows for a continuum extrapolation of the resulting screening masses. For the mass ratios $m_s/m_l = 20$ and $m_s/m_l = 27$ we only used an aspect ratio of $N_\sigma/N_\tau = 4$. From the analysis in [148] we conclude that the corresponding systematic error is small compared to the statistical one for these quark mass ratios. For the lighter quark mass ratios, we also used large volumes to analyze for possible volume effects. Due to the high cost of the inversion of the Dirac matrix, the ratios $m_s/m_l = 40$ and $m_s/m_l = 80$ are calculated only at lattice size of $24^3 \times 6$, $32^3 \times 8$, $32^3 \times 6$ and $40^3 \times 6$. Therefore, a continuum extrapolation is not possible for these quark masses. For a complete list of the used configurations, see appendix C.

The scale being used to generate these configurations is taken from [48]. Since then, this scale has been updated in equation (2.46) so that the quark mass tuning may not be optimal. However, as the difference is maximally a 2% effect, the corresponding systematic error should mainly be hidden in the statistical uncertainties.

We calculated the connected mesonic correlators for all eight channels given in tables 3.3 and 3.2, respectively. For the axial vector channel and for the vector channel, we averaged over the different components in order to increase the statistics. In the following we will refer to the different parts using the following notation: “Axial vector” (A) for the summed components of the oscillating part of channel $\mathcal{M}3$ and $\mathcal{M}4$, “vector” (V) for the summed components of the non-oscillating part of channel $\mathcal{M}6$ and $\mathcal{M}7$, “scalar” (S) for the oscillating part of channel $\mathcal{M}1$ and “pseudoscalar”(P) for the non-oscillating part of channel $\mathcal{M}2$.

We used two different sources, namely the default point source and the extended corner wall source described in section 3.1.3. We compared the results of the different sources for each temperature and particle channel. For the point source data, we observe a convex curvature in the log scaled plots in any case, which in turn means that all excited states have a positive amplitude. However, for the corner wall correlators, we find both excited states with a negative amplitude as well as a positive amplitude. Examples of these cases may be found in figure 6.1. In the upper plot, the excited states come with a positive amplitude, while the curvature in the lower plot reveals excited states with negative amplitude.

As expected, the corner wall correlators exhibits a smaller relative error and excited states are suppressed in both cases. Hence, one might expect that corresponding screening mass fits work better for the corner wall correlators. Nevertheless, we find that the fits using the point source work comparably well or even better for the majority of fits. As in section 5.1, we use

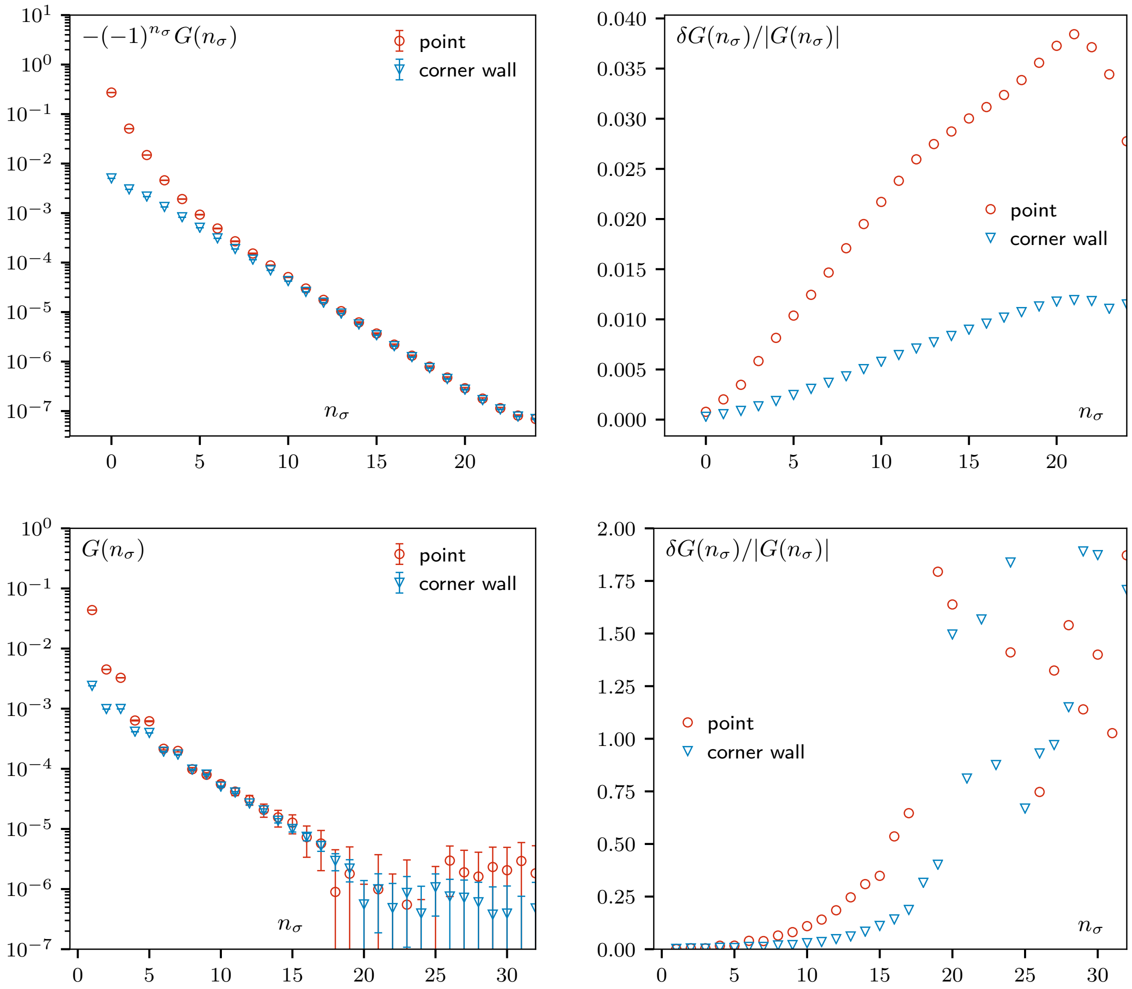

Figure 6.1: Comparison of point source versus corner wall source correlators with two light quarks on a $64^3 \times 16$ lattice with $m_s = 27m_l$ for the vector channel at $T = 0.146\,\mathrm{GeV}$ (bottom) and on a $48^3 \times 12$ lattice with $m_s = 20m_l$ for the scalar channel at $T = 0.769\,\mathrm{GeV}$ (top). Left: Direct comparison of the correlators. The correlators have been normalized such that they take same values in the center. Right: Comparison of the relative error.

the correlator fitting methods described in section 4.3. For the non-oscillating pseudoscalar channel for pure quarkonium states ($\bar{u}d$, $\bar{s}s$), we used up to four states. For all other oscillating channels, we used up two three states in the oscillating channel as well as in the non-oscillating channel.

Examples for the corresponding mass plateaus can be found in figure 6.2. In the first example in the top left plot, it is clear that a simple one state fit is not enough to extract the final screening mass. Both the corner wall as well as the point source data do not exhibit a final plateau. Due to the negative amplitude of the corner wall data, the corresponding plateau comes from below instead of above. Thus, one would expect an agreement of the corresponding screening masses only for large distances, where the fit is not influenced by higher states. However, even for the largest available distance at $n_{\sigma,\mathrm{min.}} = 20$ the data of both sources do not agree. This changes when switching to higher state fits and letting the AICc choose the best model. This reveals a plateau at shorter distances at which the two data for both sources perfectly agree. Even the size of the error bars is comparable.

In the lower plot of figure 6.2 we show an example where fits to the corner wall fail and we do not get a stable mass plateau. While the point source data show a stable plateau similar to the one in the upper left plot, the corner wall results keep oscillating and exhibit large error bars. We assume that the inconsistent sign of the amplitude of the excited state leads to an instability of the fits using corner wall source. In both cases, the statistics of 100 configurations each is rather small. Therefore, we assume that the poor fit behavior may also stem from a bad estimate of the corresponding covariance matrix.

The top right plot of figure 6.2 displays an example where the bad signal to noise ratio of the point source correlator prevents any reliable ground state screening mass extraction. In this case, a stable plateau is only available for the corner wall data. Please note that the plateau of corner wall data also comes from above here.

After carefully analyzing the different mass plateaus from the many different fits we decided to use the corner wall data only for the noisiest data, that is for the vector channel and the axial vector channel below $T = 0.3\,\mathrm{GeV}$. For all other channels and temperatures, we use point source results only. In both cases, the mass plateaus have been selected by hand for each parameter set.

Before starting to look at the final results of the continuum extrapolated screening masses, we should analyze the effects of the taste violation on the mesonic masses. To do so, we computed all 16 taste partners for the pseudoscalar channel on a 64^4 lattice at zero temperature with a quark mass ratio $m_s/m_l = 27$. We analyzed three different lattice spacings. For the vector like taste partners, we averaged over all three components. Additionally we computed the RMS mass given in equation 3.50. The results can be found in figure 6.3. As expected, the taste violation effects decrease with decreasing lattice spacing in all different quark combinations. For the $\bar{s}s$ and the $\bar{s}u$ combinations, the effect stays in the few percent region and therefore is on the same uncertainty level as the scale itself. For the light quark sector, we find up 30% of difference among the different taste partners. Thus, a correct comparison to physical statements free of taste violation effects may be only done with continuum extrapolated data in the light sector.

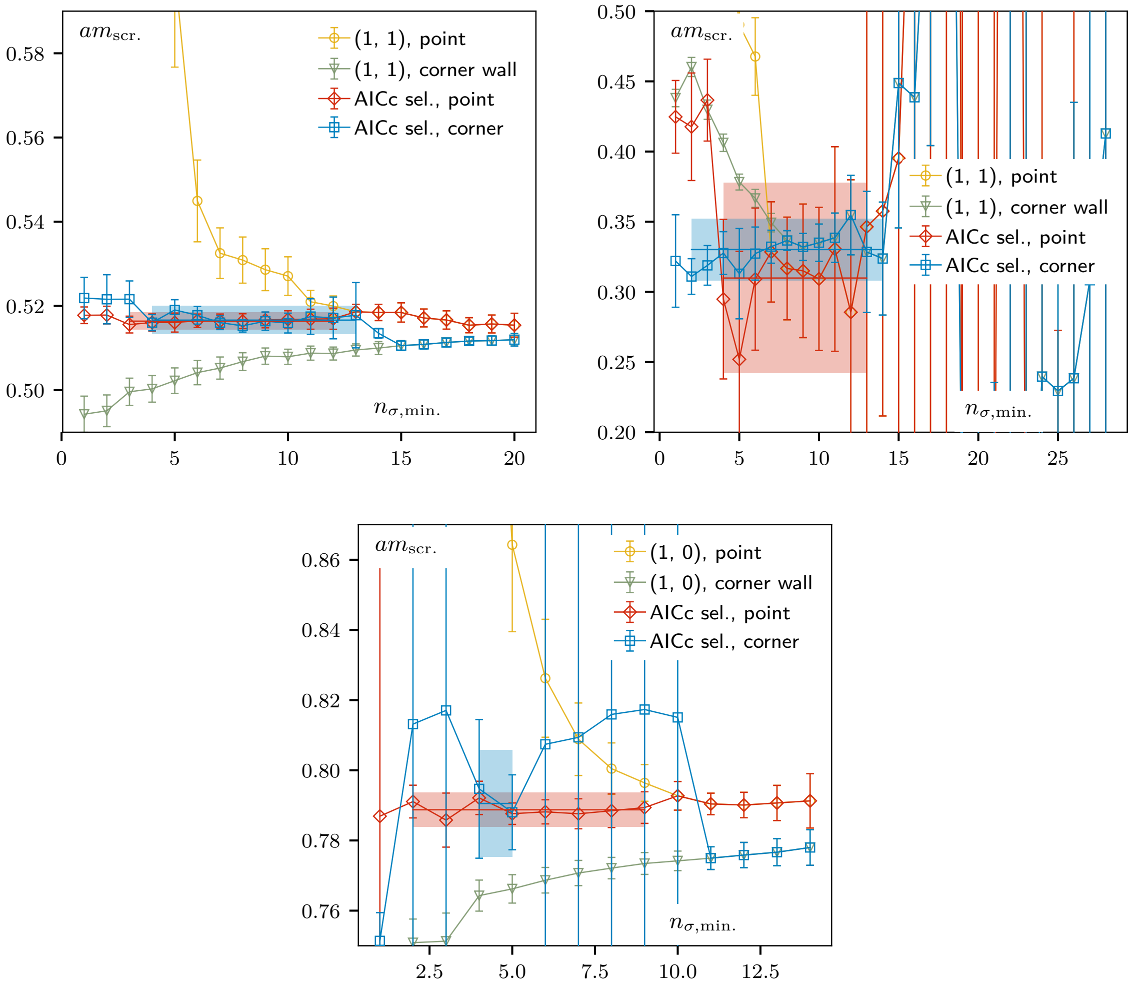

Figure 6.2: Top: Corresponding mass plateaus for the parameter sets in figure 6.1 (dots) and the finally selected plateaus (bands). Left: The scalar channel at $T = 0.769\,\text{GeV}$. Right: the vector channel at $T = 0.146\,\text{GeV}$. Bottom: Same as top but for $m_s = 20m_l$ on a $32^3 \times 8$ lattice at $T = 1.15\,\text{GeV}$.

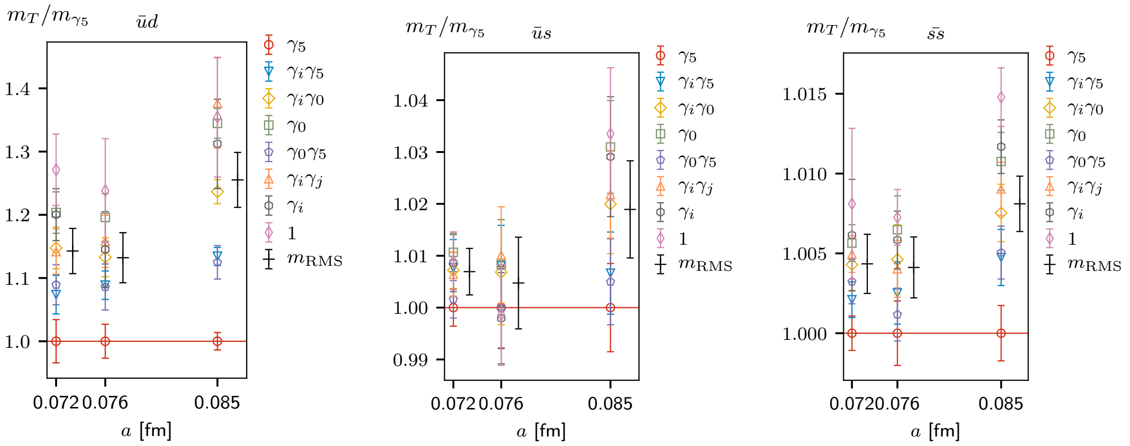

Figure 6.3: Zero temperature masses on a 64^4 lattice with $m_s = 27m_l$ for the 16 different taste partners of the pseudoscalar channel given in table 3.4 at different lattice spacings for the $\bar{u}d$ (left), $\bar{u}s$ (center) and $\bar{s}s$ (right) mesons. Vector like taste partners have been averaged over all three components.

In order to verify the results of the various steps that are necessary to compute the screening masses, we compare the results at zero temperature to the corresponding physical meson masses in figure 6.4. Overall we find a good agreement between the lattice data the physical values. Only in the axial vector channel in the light quark sector we underestimate the physical results. This might be due to the large taste violation effects in this region. Another explanation may be the use of the corner wall source here. As the axial vector correlators are particularly noisy in the center, it might happen that the fit still includes excited states. Due to the negative amplitude of these states, the screening mass might be shifted downwards.

In addition, we find slight deviations of the pseudoscalar masses of the $K^\pm$ and η_s mesons masses of up to 3%. This small effect may be explained easily by the slight uncertainties in the quark mass tuning, as the scale changed between the generation of the configurations and the measurement of the screening masses.

Due to the artificial decay of the scalar channel [95], we cannot find an agreement of the scalar channel with the corresponding physical value. The error bars are large and we find only a very rough agreement with the mass of the corresponding decay products, which are two pions in the light-light sector and $\pi K^\pm$ in the light-strange sector.

After computing all the screening masses, the data for the quark mass ratios $m_s/m_l = 20$ and $m_s/m_l = 27$ have been extrapolated to the continuum linearly in $1/N_\tau^2$ using the method described in section 4.4. We find that the difference of the extrapolated results for those two quark mass ratios is negligible for $T \gtrsim 160\,\mathrm{GeV}$. Therefore we combined those two quark mass ratios by using the $m_s = 27m_l$ results below $172\,\mathrm{GeV}$ and the $m_s = 20m_l$ data above. We performed a continuum extrapolation on these combined data as well.

We used 3^{rd} order splines were the numbers of knots has been adjusted manually to fit to the data set. In order to remove oscillations, for each of the data sets we used at least two different

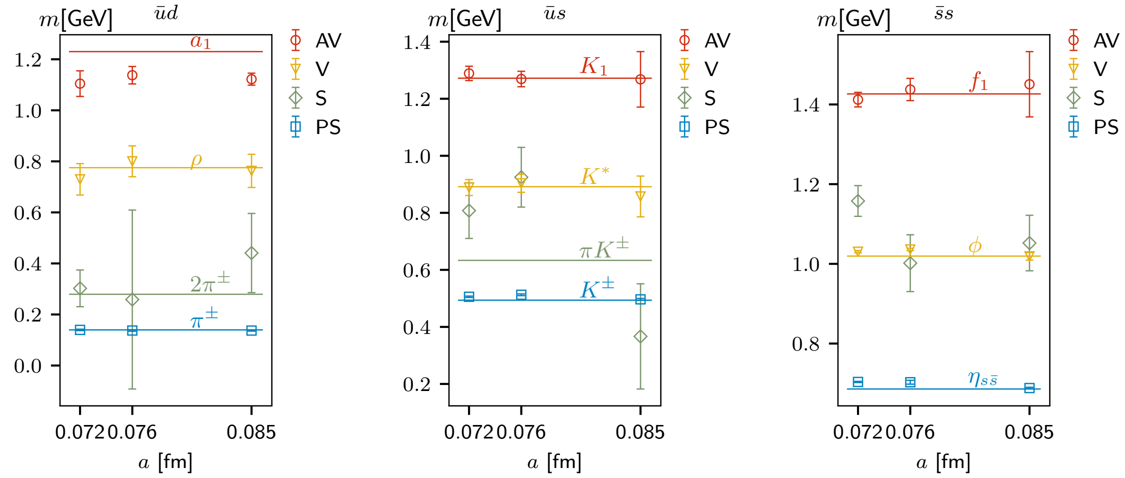

Figure 6.4: Zero temperature masses for a quark mass ratio $m_s/m_l = 27$ on a 64^4 lattice. The horizontal lines depict the physical meson masses. Due to the unphysical decay of the scalar channel for staggered mesons, we plot the total mass of the corresponding decay products for $\bar{u}d$ and $\bar{u}s$ instead. The mass of the η_s pseudoscalar meson is approximated using the fictitious mass $m_{\eta_s} = \sqrt{2m_K^2 - m_\pi^2}$ [48, 147].

number of knots. The number of knots greatly changed depending on the data set. While we used only four to five knots for the axial vector and vector channel, we used up to ten knots for the pseudoscalar and scalar channel. The position of the knots was chosen according to the density of the points using the method described in section 4.4. To randomize the knot positions in the bootstrapping, we use 20% randomly selected data points.

To stabilize the splines at the borders of the data sets, we used three different constraints on the derivative outside of the actual region of interest. At $T = 0.025\,\text{GeV}$ and $T = 0.05\,\text{GeV}$ we constrained the derivative to be 0 and, inspired by the free quark limit, we set the derivative to be 2π at $T = 1.5\,\text{GeV}$. The $\chi^2/\text{d.o.f.}$ was $\mathcal{O}(1)$ for all extrapolations except for the pseudoscalar channel for the strange-light and the strange-strange sector, where it was of order $\mathcal{O}(10)$. Here the error bars become so small that systematic effects become more important than the statistical error.

Examples for the continuum extrapolation in the light-light sector can be found in figure 6.5. For the scalar channel we find very strong cut-off effects, though the continuum extrapolation manages perfectly to cover the different data points. For the pseudoscalar channel, the cut-off effects are less dominant, but there still is an explicit separation of the different lattice sizes. In the case of the vector channel and the axial vector channel, the cut-off effects are mainly hidden in the size of the statistical error bars. Only the $N_\tau = 6$ data take values slightly above the data with finer lattice spacings. This observed behavior was similar in the case of the strange-light and strange-strange sector except that we observe smaller error bars in the vector channel and axial vector channel so that we also observe significant cut-off effects here.

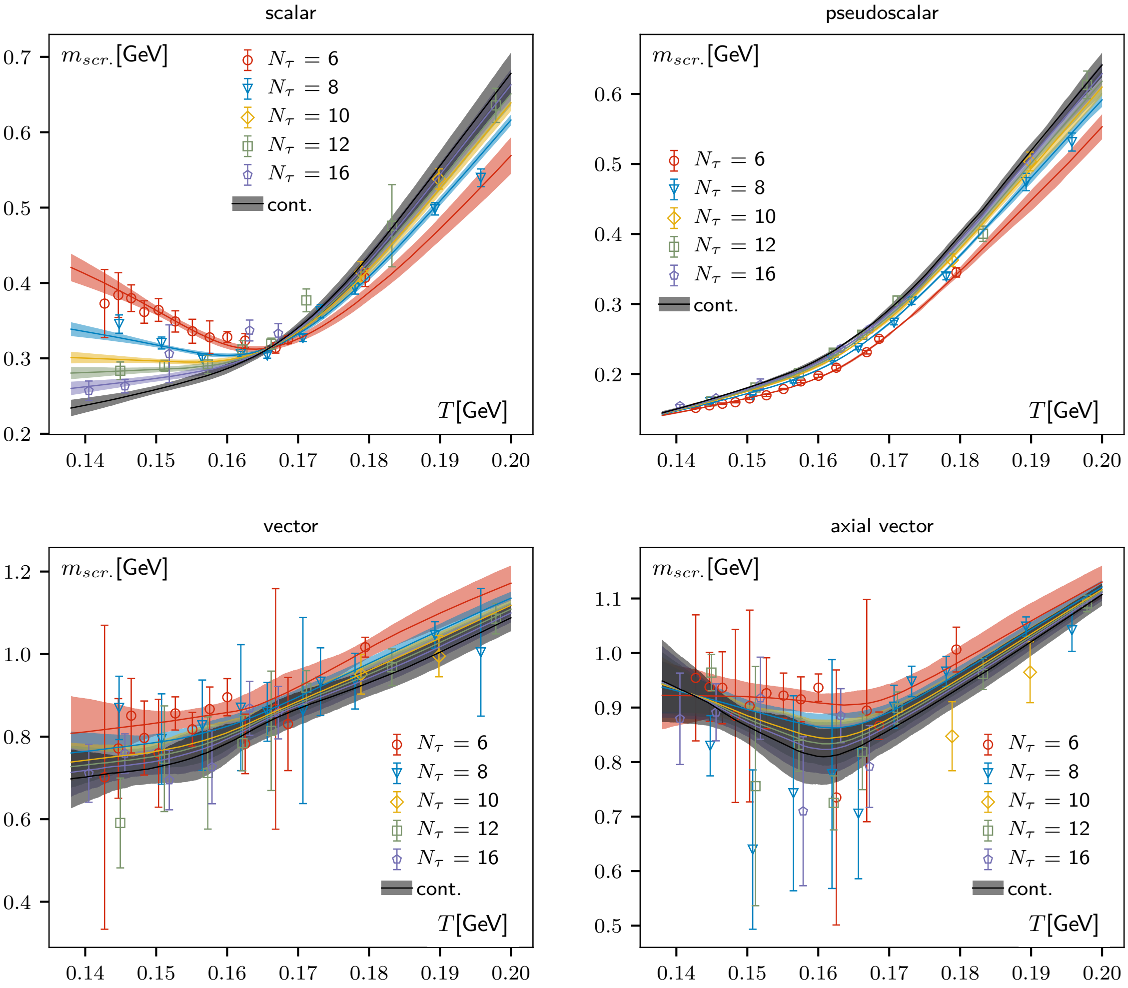

Figure 6.5: Continuum extrapolation of screening masses linearly in $1/N_\tau^2$ for the different channels with a quark mass ratio of $m_s/m_l = 20$ above 172 GeV and $m_s = 27m_l$ below.

6.2. Results at physical quark masses

The final results in the crossover region have been summarized in figure 6.6, where we plot the measured lattice data as well as the corresponding continuum extrapolation for the combined data set. A cleaner plot only showing the continuum bands is given in figure 6.7. We first concentrate on the vector and axial vector channel. At the left border of the examined temperature range at $T = 0.135\,\mathrm{MeV}$, both screening masses corresponding to these channels undershoot the physical values of the zero temperature masses. In the case of the axial vector, this is probably because the meson states are already modified by the medium at this temperature, as the corresponding screening mass is heavily decreasing with temperature. For the vector channel, this slight effect may either be of statistical nature or might be due to a systematic effect. As can be seen in figure 6.5, the data points in the transition region have rather large error bars. Thus, the corresponding spline mainly follows the curvature of the higher temperatures and pushes the result at lower temperature downwards.

With rising temperature, we find the mass of the axial vector to decrease, while the mass of the vector channel increases until both become degenerate. In the light quark sector, this roughly happens at the chiral crossover temperature of $T = 156.5(1.5)\,\mathrm{MeV}$ [60]. With increasing quark mass in the strange-light and strange-strange sector, the point of degeneracy shifts upwards. Once the vector and axial vector masses become degenerate, they remain degenerate at all temperatures. This is perfectly in agreement with the expectations of chiral symmetry restoration.

Next, we come to the pseudoscalar and scalar channel. At low temperatures, the mass of the pseudoscalar channel matches to the physical zero temperature mass. With rising temperature, the mass starts to increase with a positive curvature until around $T = 0.2\,\mathrm{GeV}$, an almost linear behavior appears.

The continuum extrapolated screening mass of the scalar channel greatly undershoots the physical zero temperature mass in the low temperature region in the light-light and light-strange sector. For the strange-strange sector, no physical state free of disconnected contributions exists, and therefore a comparison is not possible. With rising temperature, the results rise monotonically for the light-light and light-strange sector. For the strange-strange case the mass first drops and then starts to rise.

The discrepancy of the scalar mass and the physical values at low temperature very probably stems from unphysical decay of staggered mesons due to taste violations. Indeed, the results roughly approach the value of the mass of the unphysical decay products, that is 2π in the light-light sector and $\pi K^{\pm}$ in the light-strange sector. Apparently, the unphysical contributions are still relevant even at the smallest lattice spacings, and our fitting routine resolves this unphysical state as the ground state. This may also explain the direction of the continuum extrapolation, where the even finer lattices exhibit even smaller masses. To analyze this effect in more details, finer lattices are needed. For zero temperature, an estimate of the unphysical contributions is available based on chiral perturbation theory [149], and by using this estimation as input for the fit, it is possible to extract the physical state ground state. Unfortunately, for finite temperatures, such an analysis is not yet available.

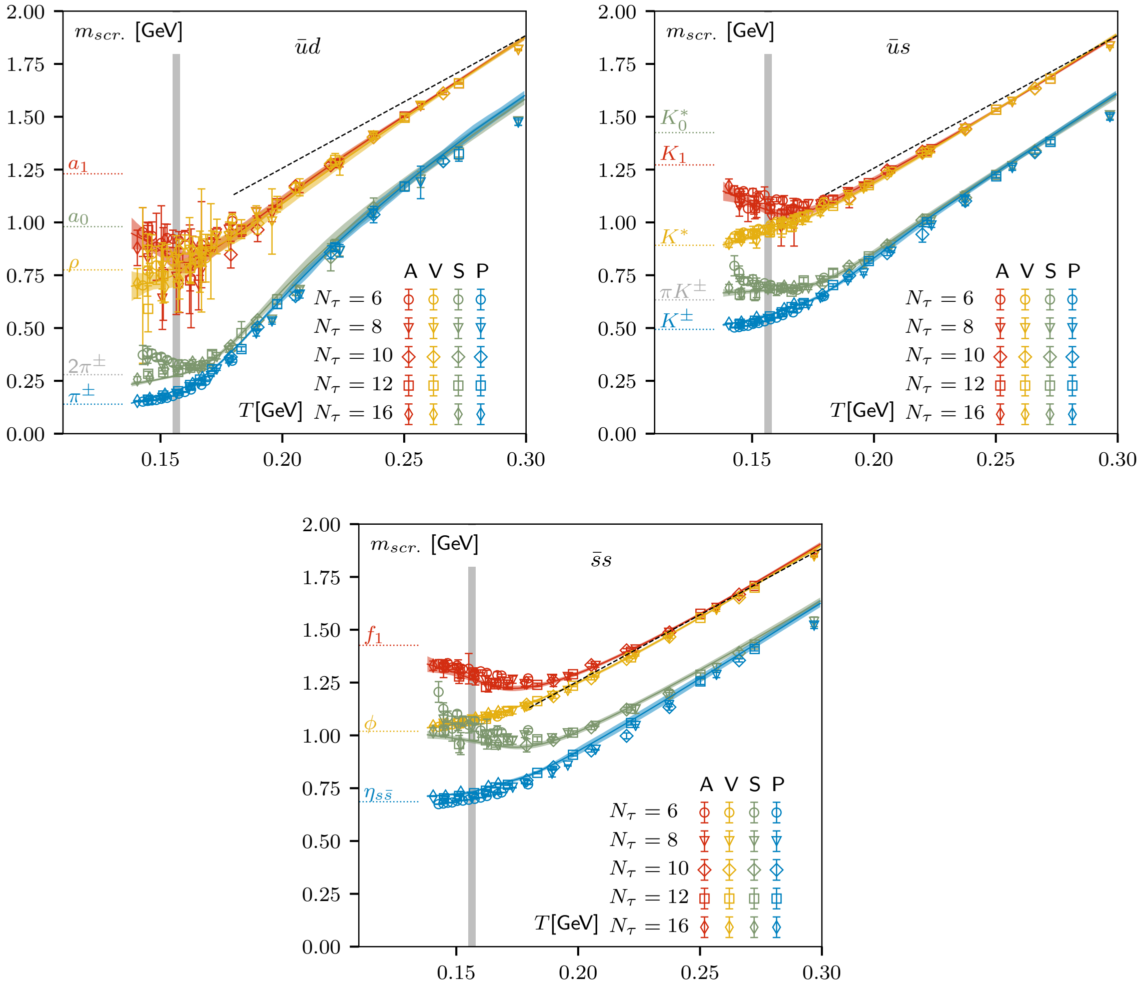

Figure 6.6: Measured screening masses (dots) and continuum extrapolation (bands) for the different channels for light-light (top left), strange-light (top right) and strange-strange (bottom) correlators in the crossover region. Below $T = 172\,\text{GeV}$ we use data with a quark mass ratio of $m_s/m_l = 27$, while we use $m_s = 20m_l$ above. The gray band corresponds to the chiral transition temperature at $T_{\text{pc}} = 156.5(1.5)\,\text{MeV}$ and the dotted line represents the free quark limit $m_{\text{scr.}} = 2\pi T$.

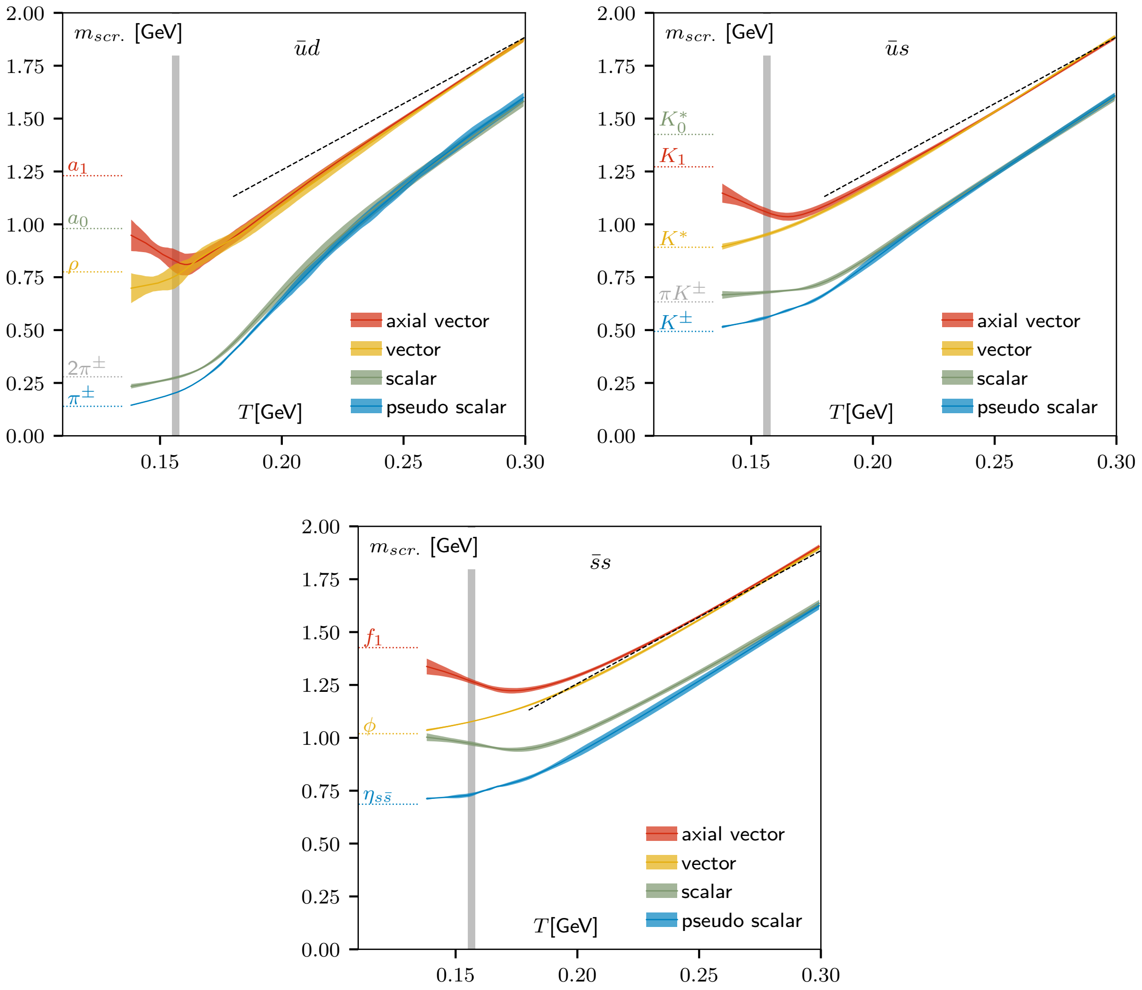

Figure 6.7: Continuum extrapolation for the different channels for light-light (top left), strange-light (top right) and strange-strange (bottom) correlators. Same as figure 6.6 but only showing continuum bands.

However, a possible effective restoration of the $U_A(1)$ symmetry should still become visible in a degeneracy of the mass of the scalar and pseudoscalar channel. With rising temperature, we find the two channels in the light-light sector become degenerate at around 0.22 GeV. This is clearly above the chiral transition temperature. For the light-strange sector, the degeneracy happens roughly at the same temperature, while for the strange-strange sector, the two masses do not become equal up to around 0.3 GeV.

We now try to further address the issue of the scalar channel by looking at the corresponding susceptibilities. The measured ground state screening masses mainly rely on the correlator values at large distances. This is exactly where contributions of the unphysical states in the scalar channel are largest. Thus, the results for the screening masses are mainly dominated by systematic errors. However at short distances, the also the physical, heavier states contribute. Due to the exponential drop off of the correlator, these short distance points mainly contribute to the corresponding scalar susceptibility defined in equation (3.59). Therefore, the scalar susceptibility should be relatively free of the unphysical effects. To investigate the restoration of the $U_A(1)$ symmetry, we may use $m_s^2(\chi_P - \chi_S)/T_c^4$ as a measure. In the case of a $U_A(1)$ symmetry restoration, this quantity should become equal to zero. The factor m_s has been introduced to ensure for a RG-invariant quantity so that a continuum extrapolation is possible.

As for the screening masses, we computed this quantity for all data sets and then combined the $m_s = 27m_l$ and $m_s = 20m_l$ data, where we choose the $m_s = 20m_l$ data for all temperature values above $T = 172$ GeV. In figure 6.8, we show the results of the continuum extrapolation for all three different quark combinations. The point of degeneracy of the scalar and the pseudoscalar channel agrees with the results from the screening mass analysis. For the light-light and light-strange sector, it is roughly located at around 0.2 GeV, while for the strange-strange combination, we do not find a degeneracy up to 0.3 GeV.

The findings for the $\bar{u}d$ combinations would favor a $O(4)$ universality scaling in the chiral limit, as the $U_A(1)$ symmetry is effectively not restored at the chiral transition temperature. To further quantify this conclusion, we also analyzed first configurations for lighter than physical quark masses. However, due to a missing continuum extrapolation, these results may only be interpreted as a first estimate. Again, we look at $m_s^2(\chi_P - \chi_S)/T_c^4$. The results for the different quark masses $m_s = 20m_l$, $m_s = 27m_l$, $m_s = 40m_l$ and $m_s = 80m_l$ are combined in figure 6.9. For temperatures above the transition temperature, the values for different quark mass do not show significant differences and clearly lie above zero. The points of the $m_s = 40m_l$ data take very similar values as the $m_s = 20m_l$ data. The two data points for $m_s = 80m_l$ that lie above the chiral transition temperature even exhibit slightly larger masses compared to physical quark masses. This strengthens the hints that the $U_A(1)$ remains broken in the chiral limit. The two lattices with different volume for $m_s = 80m_l$ differ with about one sigma uncertainty. Though, as there is no consistent ordering for different temperatures, we assume that this effect is of statistical nature.

As a last point, we analyze the high temperature region. For this region, we only have data for $m_s = 20m_l$. For temperatures larger than 1.0 GeV, only one single lattice of size $32^3 \times 8$ is available so that a continuum extrapolation of the screening masses is not possible. However, the cut-off effects for masses around 1 GeV are found to be small, as the data for all meson

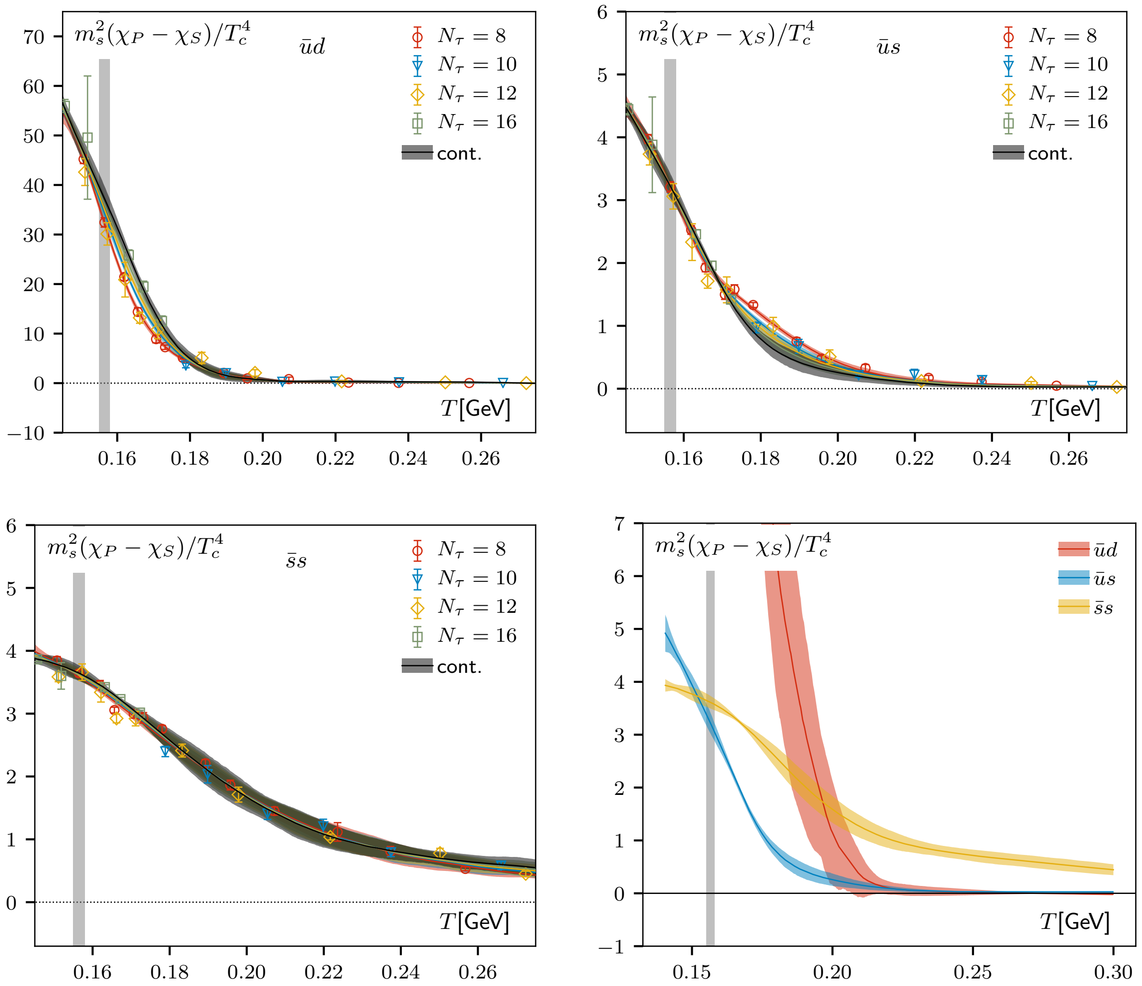

Figure 6.8: Continuum limit of the difference between the pseudoscalar and scalar susceptibilities as a function of the temperature for the light-light sector (top left), the light-strange sector (top right) and the strange-strange sector (bottom left). Bottom right: Combination of the continuum bands of the three other figures. The gray band denotes the chiral transition temperature.

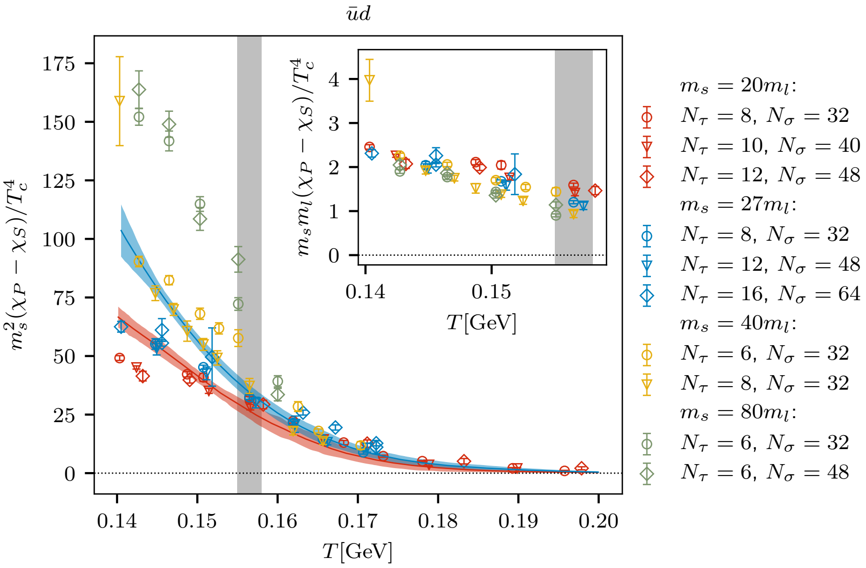

Figure 6.9: Same as top left plot of figure 6.8 but for different light quark masses approaching the chiral limit. Due to the high costs of the Dirac matrix inversion, no continuum extrapolation is possible for $m_s = 40m_l$ and $m_s = 80m_l$. The insert shows the region below T_c scaled with $m_l m_s$ rather than m_s^2.

channels do not show an ordering dependent on the lattice size. Thus we feel confident to also make reliable statements of higher temperatures.

The resulting screening masses are plotted in figure 6.10. The masses normalized by the temperature of all channels rise quickly with increasing temperature until they roughly settle in a plateau. For all results we find a very similar behavior for all three quark combinations $\bar{u}d$, $\bar{u}s$ and $\bar{s}s$. From 0.5 GeV and upward, they do not depend on the quark mass, and the screening masses of the different channel become equal. For the vector and axial vector channel, the plateau begins at around $T = 0.5\,\mathrm{GeV}$ and lies above the ideal gas approximation. Therefore, we expect a decrease of the screening masses for even higher temperatures, such that the ideal gas limit is eventually reached. Though, such a decrease cannot be found in the examined temperature window. However, when comparing to the data from perturbation theory taken from reference [146], we find that this behavior is somewhat expected as these data show a significant deviation from the free quark limit as well and also approach the free continuum limit from above. Nevertheless, the measured screening masses exhibit slightly smaller values compared to the perturbative ones. We may also find that the decreasing rate of the perturbative results is rather small so that a possible decrease of our measured results might be hidden in the error bars.

For the pseudoscalar channel and scalar channel the plateau lies lower, slightly above the free quark limit. We also observe a small increase of the screening mass in the temperature range from 1 to 3 GeV and cannot find a tendency towards the limit of infinite temperature.

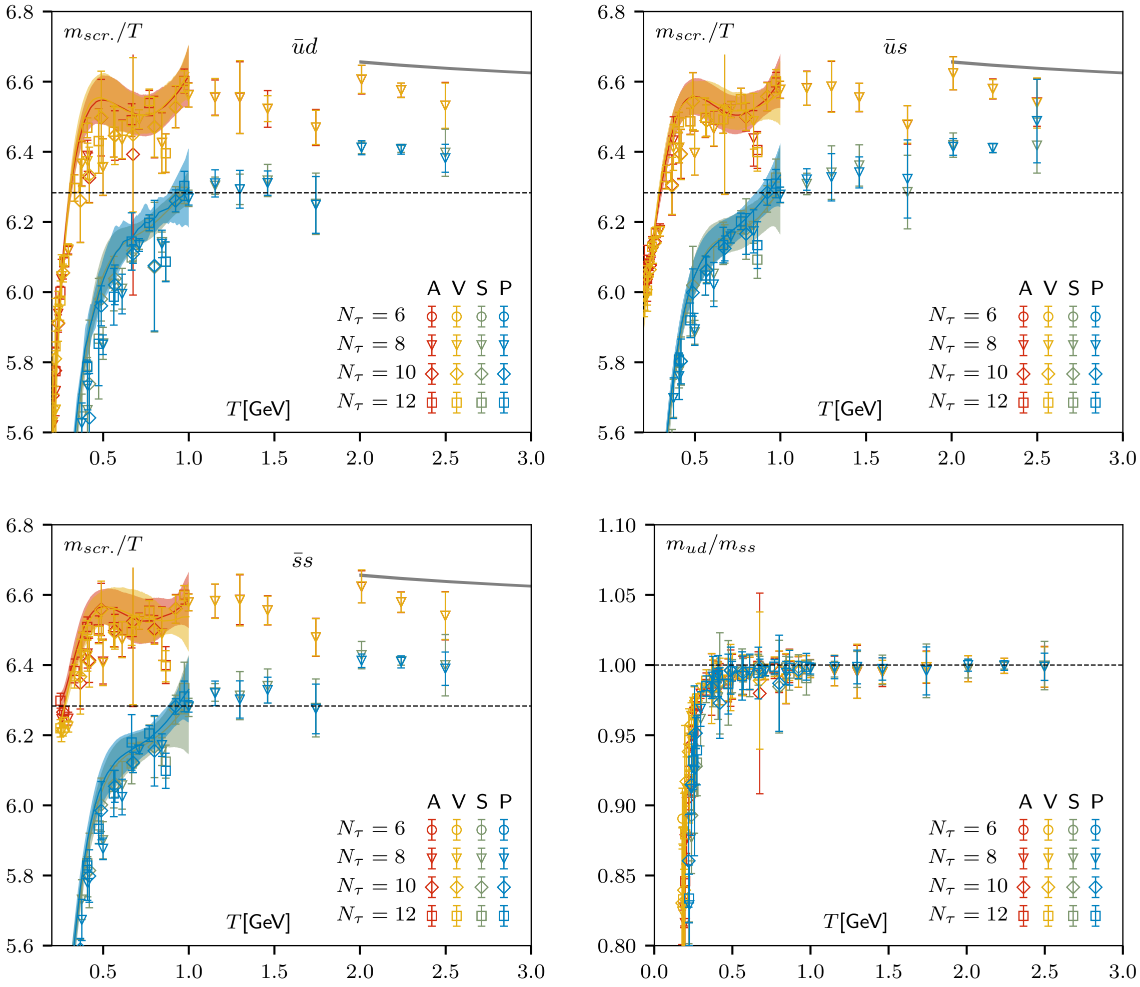

Figure 6.10: Top and bottom left: Same as figure 6.6 for the high temperature region. Here we plot the screening masses in units of the temperature, rather than GeV. The gray band corresponds to perturbative results taken from [146] with $N_f = 3$ and the 2-loop EQCD coupling g_E^2 from [150]. The constant g_E^2 was renormalized using the energy scale $\mu = 9.08$ and was varied by a factor of two to account for systematic errors. Bottom right: Ratio $m_{\bar{u}d}/m_{\bar{s}s}$ for all four meson channels. All data in this figure correspond to $m_s = 20m_l$.

Due to the large error bars this might be a statistical effect, though. We observe a significant deviation between the perturbative results and the lattice data. The measured masses lie approximately 3 to 4% below the perturbative results. A degeneracy of all four meson channels cannot be found in the analyzed temperature range. We conclude that the perturbative results still lack some spin dependent information to describe screening masses in this temperature range.

6.3. Concluding remarks

We have calculated mesonic screening masses based on the staggered HISQ action for (2+1)-flavor QCD at a wide temperature range and for various lattice sizes. For finest zero temperature lattices, we find a very good agreement with the physical values except for meson states corresponding to the a_1 particle, where the measured masses have slightly lower values. Small deviations in the pseudoscalar channel can be explained by a slight misstuning due to the scale update between generating the configurations and measurements. Due to the artificial decay of the scalar channel, the results from the scalar channel do not correspond to a physical counter part.

For the first time, we performed a continuum extrapolation on mesonic screening masses for physical values of the light quark mass using the staggered HISQ action. For all different channels and all quark combinations, we find temperature effects close to or even below the chiral transition temperature. Though, for the strange-strange sector, the curvature is less steep and the temperature effects are less pronounced.

As expected, for the $\bar{u}d$ combination, the axial vector channel and the vector channel become degenerate roughly at the chiral transition temperature. For the heavier quark combination the point of degeneracy shifts upwards. Due to the higher mass of the strange quark, this is expected. An effective restoration of $U_A(1)$ symmetry is observed above pseudo-critical temperature at around 0.2 GeV in the light-light sector. For the other quark combinations, this point also shifts upwards. These results favor an $O(4)$ scaling in the chiral limit. The findings are generally in agreement with the analysis of staggered screening masses in references [82, 151]. However, for the finer lattices in our analysis we find smaller values for the scalar mass, which is very probably due to the stronger cut-off effects in this channel. In comparison to the results in reference [53], we find a clear gap between the scalar and pseudoscalar screening mass at the transition temperature. This may be explained by the usage of Wilson fermions in [53] and also maybe by the fact that calculation of the screening masses is based on the effective mass instead of multiple state fits.

Due to the artificial decay of the scalar channel, we also analyzed the susceptibilities corresponding to the scalar and pseudoscalar channel. Here, we performed a continuum extrapolation as well. For the point of degeneracy we find similar results as the screening mass analysis. Including first lighter than physical results we do not find any hints that the point of $U_A(1)$ degeneracy shifts significantly downwards. This strengthens the assumption of second order phase transition corresponding to the $O(4)$ spin model in the chiral limit. This is in agreement with the analysis of the different mesonic susceptibilities in [6] and with the investigation of low lying eigenvalue spectrum of the Dirac operator for domain wall fermions in [152]. Our results also coincide with the results using the overlap operator on HISQ configurations in [153] and goes along with the findings in references [154, 155] but disagrees with the results in [156]. Also the results of the chiral extrapolation in [53] is not in accordance with our findings.

Further work is necessary address this issue and to classify the phase transition in the chiral limit. A screening mass based approach needs more and finer lattices approaching the chiral limit. Such configurations with quark masses down to $m_s/m_l = 320$ are currently being generated and the measurement of the corresponding screening masses is on its way. Additionally, the problem of the artificial decay of the scalar channel has to be addressed. One way could be to introduce chiral perturbative results into the fit to account for the unphysical parts in the correlator. However, this requires perturbative calculations at finite temperature first. Using finer lattices, which are closer to the continuum limit, the unphysical contributions should become less relevant, so that the ground state screening mass will eventually correspond to the physical a_0 mass. Though, as we could not find such a behavior in our data for lattices up to a size of $64^3 \times 16$, this will probably require extremely fine lattices. An alternative approach could be the use of a computationally more expensive discretization method, like for instance the domain wall action, instead. Also mixed action approaches could be an option here.

Regarding the high temperature region, we still found significant differences between the measured data and the free quark limit for temperatures up to 3 GeV. We also find disagreement with the perturbative computations in the pseudoscalar and scalar channel. To further address this issue, more configurations with larger lattice sizes are needed in the high temperature region, such that a continuum extrapolation is possible up to temperatures of 3 GeV. To quantify the behavior at even higher temperature, for instance to find the point of degeneracy of all four meson channels, configurations at even higher temperature are needed. For those configurations it will be also useful to perform a direct comparison to the corresponding free correlators as has also been done in [82].

7. Conclusion

In this short conclusion, we address the goals that have been set in the introduction. For more detailed conclusions about the physical results, see the two concluding remarks in the previous sections.

We developed a new universal fitting algorithm for the analysis of hadronic correlation functions and applied it to different kind of hadronic correlators. We first analyzed heavy quarkonium mesonic states in quenched lattice QCD and then investigated the light quark sector using the HISQ action. This fitting algorithm is able to stabilize multiple state fits even for oscillating, staggered mesonic correlators. Using subsequent fits with an increasing number of states, we successfully applied fits up to five states in the non-oscillating case, like for Wilson correlators. For staggered correlators we managed to perform up to three states in both the oscillating part as well as in the non-oscillating part. All this is possible without the need of initial guess estimation. For the selection of the number of states, we used the Akaike information criterion to select the best fit for each fit interval. This way, we got completely stable fit plateaus, which resulted in a better estimation for the final ground state mass.

The corresponding implementation of the fitting routine has been written in python in an easy to use, flexible and modular way. Along with the fitting routine we provide an analysis tool box including a jackknife routine, a bootstrapping module and an executable to perform continuum extrapolations directly from the command line.

In the heavy quark sector, our goal was to extract information about spectral and transport properties of heavy quarkonia by analyzing hadronic Wilson correlators for charmonium and bottomonium computed on large quenched configurations. The new fitting routine has been used to extract the corresponding meson vector mass, which then has been used as input for a further quark mass interpolation to perfectly match the corresponding quark mass. Afterwards the correlators have been extrapolated to the continuum. Using the reconstructed correlator we searched for modifications of the underlying spectral function for temperatures above the phase transition. From the rising ratio $G/G_{\mathrm{rec.}}$ we conclude that a transport peak arises in the vector channel, for both charmonium and bottomonium, though, the transport peak appears to be smaller in the latter case. By subtracting the low frequency region from the reconstructed correlator, we find that the bound state region of the spectral function in the pseudoscalar channel is more affected by the increasing temperature compared to the vector. This suggests that the pseudoscalar channel might melt before the vector channel. For bottomonium we do not find any temperature dependence up to $T = 2.25T_c$, which is in agreement with the expectations of sequential melting.

The continuum extrapolated charmonium and bottomonium correlators allowed for a comparison to results from resummed perturbation theory above the transition temperature and overall find a good agreement. The correlators could be reproduced perfectly by integrating the perturbative spectral function. In the case of the vector channel, an additional constant has been added to account for the area under the transport peak. For charmonium, this area under the transport peak does not agree with perturbative results in reference [141]. For bottomonium however, we find a perfect match of the result from the fit with the lattice data.

The perturbative spectral functions do not exhibit any bound state peak for charmonium. This changes when switching to bottomonium, where a small quasi bound peak may be observed for temperatures of $T = 1.5T_c$ and below. This is in contrast to the findings from the reconstructed correlator, where no modification of bound states was suggested for bottomonium. This might be explained by the relatively small width of the bound state and the fact that changes of the spectral function directly next to the peak could have canceled the corresponding area loss. Compared to the charmonium case, we also find sequential melting, as the bottomonium states survive longer compared to charmonium. More and finer lattices are needed to resolve this behavior in more detail. Also, dynamical QCD lattices are required to analyze the systematic uncertainties introduced by the quenching of the theory.

In the light sector, the goal was the extraction of screening masses for dynamical (2+1) flavor lattices using the staggered HISQ action to analyze the effective restoration of the chiral and the $U_A(1)$ symmetry. The used configurations covered a wide temperature range from about 135 MeV up to 3 GeV, and different quark masses from $m_s = 20m_l$ up to $m_s = 80m_l$ have been used. The resulting screening masses have been extrapolated to the continuum for the quark mass ratio of physical quarks with $m_s = 27m_l$. As expected, the restoration of the chiral symmetry, visualized by the degeneracy of the vector and axial vector channel for the light quarks, roughly happens at the transition temperature.

An effective restoration of the $U_A(1)$ symmetry should result in the degeneracy of the pseudoscalar channel and the scalar channel. From the continuum extrapolated results, we find that this degeneracy happens above the chiral transition temperature at about 200 MeV. However, as the results for the scalar channel appear to be heavily influenced by an artificial decay stemming from taste violations of staggered mesons, we also looked at the difference between the scalar susceptibility and the pseudoscalar susceptibility. The results support the findings from the screening mass analysis and also suggest a degeneracy at around 200 MeV. By analyzing first configurations with lighter than physical quark masses, we do not observe a significant shift of the point of degeneracy downwards towards the chiral transition temperatures. This would favor a second order phase transition with $O(4)$ scaling in the chiral limit. As the result for quark masses lighter than physical are based on small lattice sizes without a continuum extrapolation, further, larger configurations approaching the chiral limit need to be generated and measured using the new fitting routine. Also other discretization schemes, free of taste violations, may serve as a cross check to the observations in this thesis. For instance this could be done by the analysis of low lying eigenmodes of the overlap operator on HISQ configurations [153] or by switching to dynamical chiral fermions like overlap or domain-wall in the future.

A. Technical documentation

In this section, we collect the documentation of the software used in this thesis. Please note that the same documentation is available by passing `-help` to the executables.

corrfitter.py

This is a very general program to perform correlator fits. It can handle an arbitrary number of states for the non-oscillating as well as for the oscillating channel. Estimating the initial guess for the fit is completely automatized.

This routine works in two steps. First, the data are read in and processed, which means that the mean and the error of the correlator are computed. Additionally the raw input data are stored. Afterwards the fit is performed based on this mean and error. For some fitting options this mean and error are ignored and the fitting process works directly on the raw data. In that case, the mean and the error are only used for the generated plots (see below).

The way how errors and mean values of the correlator data are computed is controlled by flags that end with "`-data`" (See below). This also defines how the error-bars on the data points that appear in the plots are computed. The method to compute the errors of the fit parameters is defined by flags that end with "`-fit`". Please note that for bootstrapping and for the jackknife, the errors on the data points are ignored and the fit is calculated directly from the raw input. In that case, the errors defined by the "`-data`"-flag only show up in the plots but do not contribute to anything else. If no "`-data`"-flag is passed, the best method is chosen based on the fit method. This means in particular by default:
`--jack-fit` comes with `--jack-data`
`--btstr-fit` comes with `--btstr-data`
`--ratio-fit` comes with `--ratio-data`
`--direct-fit` comes with `--std-err-data` for correlated fits and
with `--jack-data` otherwise.

The results will be given in the output folder ("`results`" by default). You will find the final fit results in `fitmass_*.txt`. A plot of the correlator will be given in `corr_*.pdf`. The effective mass will be given in `effmass*.txt`. For the effective mass, some of the "`-data`"-keywords might be ignored and a jackknife is used instead.

If there is at least one oscillating state, you will find additional versions of the files mentioned above with "`_osc_`" or "`non-osc`" in the file names. This will contain information about the separated correlators (See section 4.3 how to separate correlators into oscillating and non-oscillating part). If the fit is correlated you will find a plot of the normalized covariance matrix in `cov_*.pdf` and a plot of its eigenvalues in `eig_*.pdf`. For the meaning of the rest of the abbreviations in the file names, please see below flags.

In the following is a complete list of options for the program:

Argument	description
`filename`	The file name of the data raw data file.
`-h, --help`	Show this help message and exit.
`--corr, --correlated`	Perform a correlated fit involving the covariance matrix of the data points. This will add "`_cov`" to the output file names.
`--sym`	Fit only half of the correlator. The correlator will be symmetrized. This will add "`_sym`" to the output file names.
`--asym`	Fit the full correlator. The correlator will not be symmetrized. This will add "`_asym`" to the output file names.
`--change-sign`	Multiply the correlator with $-(-1)^{n_t}$. This interchanges oscillating and non-oscillating part. Be careful with this option! This will add "`_sc`" to the output file names.
`--auto-sign`	Automatically change the sign of even data points if more than half of them have a negative sign. If this is the case, the oscillating and non-oscillating part are interchanged. Be careful with this option!
`--nstates NSTATES`	Number of non-oscillating states.
`--nstates-osc NSTATES_OSC`	Number of oscillating states.
`--cut-eig`	Cut lower eigenvalues of the covariance matrix.
`--cut-perc CUT_PERC`	Percentage how many eigenvalues should be cut.
`--min-cov-det`	Use the minimal covariance determinant method to estimate mean and covariance. We use the scikit-learn library to compute the covariance matrix ([157]). This will add "_mcd" to the output file names.
`--mcd-supp-frac MCD_SUPP_FRAC`	Support fraction for Minimum covariance method. (See above)
`--folder FOLDER`	Output folder.
`--title TITLE`	The title for all the plots.
`--file-string FILE_STRING`	String that will be put into the names of the output files.
`--nt-column NT_COL, -ntc NT_COL`	Column of the lattice points (n_τ or n_σ).
`--data-column DATA_COL, -dc DATA_COL`	Column of the data points.
`--error-col ERR_COL, -ec ERR_COL`	When reading direct data, this is the column of the error bars.

`--Nt NT, -Nt NT`	Do not compute N_τ from the data. Instead use this one. This prevents symmetrization of the correlator!
`--numb-samples NUMB_SAMPLES, -ns NUMB_SAMPLES`	Number of samples in the bootstrap for averaging data points.
`--numb-fit-samples NFIT_SAMPLES, -nfs NFIT_SAMPLES`	Number of samples in the bootstrap for fitting.
`--numb-blocks NUMB_BLOCKS, -nb NUMB_BLOCKS`	Number of jackknife blocks.
`--no-tex`	Do not use LaTeX for rendering labels.
`--log-level LOG_LEVEL`	Log level. Available are WARN, INFO, PROGRESS, DETAILS, DEBUG, NONE.
`--try-all`	Try fits with all available start parameter estimation methods. Very expensive.
`--start-params START_PARAMS [START_PARAMS ...]`	Initial guess for the fit.
`--fit-range FIT_INTERVAL FIT_INTERVAL, --fit-interval FIT_INTERVAL FIT_INTERVAL`	Range of $n_{\min}$ that shall be scanned.
`--nmax XMAX, --xmax XMAX`	Upper limit of the correlator fit.
`--priorval PRIORVAL [PRIORVAL ...], --prior-val PRIORVAL [PRIORVAL ...]`	Perform a constraint fit, this will be the prior values.
`--priorsigma PRIORSIGMA [PRIORSIGMA ...], --prior-sigma PRIORSIGMA [PRIORSIGMA ...]`	Perform a constraint fit, this will be the prior sigmas.
`--seed SEED`	Seed for the bootstrap analysis.
`--jack-data`	Compute the errors of the data points from a jackknife. This will add "`_jk-data`" to the output file names.
`--std-err-data`	Compute the errors of the data points from a standard error. This will add "`_std-err-data`" to the output file names.

`--btstr-data`	Compute the errors of the data points from a bootstrap. This will add "`_bs-data`" to the output file names.
`--sample-data`	Compute the errors of the data points from a standard deviation. This makes sense if the data are averages over bootstrap samples. This will add "`_fr-sample`" (from sample) to the output file names.
`--direct-data`	Read data that are already averaged. This will add "`_direct-data`" to the output file names.
`--ratio-data`	Read in data and compute the ratio $G(n_\tau)/G(n_\tau+1)$. This will add "`_ratio-data`" to the output file names.
`--jack-fit`	Compute the error on the fit parameters from a jackknife. This will ignore the errors that are given by the data-flag. Instead everything is computed directly on the raw data. This will add "`_jk-fit`" to the output file names.
`--direct-fit`	Compute the error on the fit parameters directly from the fit. This will add "`_direct-fit`" to the output file names.
`--btstr-fit`	Compute the error on the fit parameters from a bootstrap. This will ignore the errors that are given by the data-flag. Instead everything is computed directly on the raw data. If you perform a correlated fit, the same random numbers per n_τ value will be used. If not, different random numbers will be chosen to break up the correlation. This will add "_bs-fit" to the output file names.
`--no-median`	With this flag, all bootstrap routines compute the error by the standard deviation and not by the distribution using quantiles. This will add `no-median` to the output file names.
`--scnd-btstr`	Perform a second bootstrap on each bootstrap sample to determine the error. This will add `_scnd-bs-fit-` to the output file names.
`--ratio-fit`	Perform a direct fit on the ratio $G(n_\tau)/G(n_\tau+1)$. Implies `--ratio-data`. This will add "`_ratio-fit`" to the output file names.

`--xlabel XLABEL`	X-label in all the plots.
`--ylabel YLABEL`	Y-label in all the plots.
`--plot-size SIZE_X SIZE_Y`	Size of the plots.
`--plot-no-ylog`	Do not use logarithmic y-scale for correlator plots.
`--font-size FONT_SIZE`	The font size of the plots.
`--plot-file RES_FILENAME`	Plot the correlator from a file instead of performing a fit. You can pass a `fitmass...` file here.
`--plot-start`	Do not perform a fit. Instead generate a plot with the start parameters. Has to be passed along with `--start-params`

best_fit.py

Simple program to select the best fit from the output of `corrfitter.py` according to the Akaike information criterion. Simply pass all the `fitmass*` files that stem from correlator fits as arguments to this program.

Argument	Description
`files`	Fit output files files to be used.
`-h, --help`	Show this help message and exit.
`--folder FOLDER`	Output folder.
`--corr-file CORR_FILE`	For an additional correlator plot, you can pass the original correlator file using this flag.
`--run-bs`	Run an additional bootstrap. Currently bootstrap parameters are hard-coded to a second level bootstrap.
`--ns NSAMPLES`	number of bootstrap samples.
`--change-sign`	Change sign of the correlator. Same as for corrfitter.py.
`--auto-sign`	Automatically change sign of the correlator. Same as for corrfitter.py.
`--no-tex`	Do not use LaTeX for text rendering.
`--state-no STATE_NO`	Non-oscillating state that should be extracted. (Default = ground state)
`--state-osc STATE_OSC`	Oscillating state that should be extracted. (Default = ground state)
`--acc ACC, -acc ACC`	The plot ranges for the mass plots are chosen automatically. Use this flag to define how many points shall enter into the plot. Higher value = more points.
`--acc-aicc ACC_AICC`	The plot ranges for the AICc plots are chosen automatically. Use this flag to define how many points shall enter into the plot. Higher value = more points.

find_plateau.py

Program to select a plateau of data points. To compute the expectation value of that plateau, Gaussian noise is generated around each data point. The resulting distributions are added and the final expectation value is computed using the median. The corresponding error is computed using 68% percentiles. The final result is printed to `stdout`.

Argument	Description
`-h, --help`	Show this help message and exit.
`--xdata-col XDATA_COL, -xc XDATA_COL`	Column in text file in which the xdata is stored.
`--data-col DATA_COL, -dc DATA_COL`	Column in text file in which the ydata is stored.
`--edata-col EDATA_COL, -ec EDATA_COL`	Column in text file in which the error is stored.
`--chi-col CHI_COL`	Column in text file in which the $\chi^2/\mathrm{d.o.f}$ is stored.
`--amp-col AMP_COL`	Column in text file in which the amplitude is stored. For instance the amplitude of a mass fit.
`--xmin XMIN`	Minimal x-value for data.
`--xmax XMAX`	Maximal x-value for data.
`--range BOUNDS BOUNDS`	Do not select the range with a plot. Use the range given by this values.
`--auto`	Automatically select the range. Usually imprecise.
`--npoints NPOINTS`	How many points shall be used for the automatic plateau selection.
`--out-name OUT_NAME`	Output name of the plateau plot.
`--title TITLE`	Title in plateau plot.
`--xlabel XLABEL`	X-label of plot.
`--ylabel YLABEL`	X-label of plot.
`--amp-label AMP_LABEL`	Label of the amplitude corresponding to `--amp-col`.
`--show-plot`	Open a window with the results after the plateau selection.
`--no-tex`	Do not use LaTeX for text rendering.
`--hist-name HIST_NAME`	Name of a histogram that shows the error estimation. No histogram is plotted without this option.
`--acc ACC_FACTOR`	The plot ranges for the mass plot are chosen automatically. Use this flag to define how many points shall enter into the plot. Higher value = more points.
`--err-threshold ERR_THRESHOLD`	Points whose error/value ratio is larger than this threshold will not enter the plateau calculation.

extrapolator.py

Very handy tool to perform continuum extrapolation using splines. Each data set corresponding to a different N_τ shall be passed in a different file. The extrapolation is performed linear in $1/N_\tau^2$. The continuum extrapolation is performed in two steps. First, the data are read in. One can distinguish whether these data stem from each lattice configuration, from a bootstrap sample or if they are already averaged and have error bars. Use the `--data` input flag to define the read-in-method. Afterwards the data are processed and a continuum extrapolation is performed. You can specify how the errors shall be computed using the `--method` flag.

Argument	description
`files`	The files to be used. (Required).
`-h, --help`	Show this help message and exit.
`--Nts NTS [NTS ...]`	The N_τ values that correspond to the data. Not necessary if the file names look like `*_Nt8_*` etc.
`--method METHOD`	The method used to calculate the error: Use `btstr` for a standard bootstrapping on the raw data. Use `gauss_btstr` for a Gaussian bootstrapping around the mean value and error bars. Use `from_sample` if the data stem from a bootstrap sample. In each case, the mean value and error are calculated using the median and 68% percentiles. Use direct, if you only want to calculate a quick estimate without error computation.
`--data-input DATA_INPUT`	Specify how the data shall be interpreted: `raw` for raw lattice data. `direct` for data that are already averaged and have error bars. `sample` for data that stem from a bootstrap sample.
`--order ORDER`	Order of the spline.
`--constraints CONSTRAINTS [CONSTRAINTS ...]`	Constraints to stabilize the spline: Pass as multiple of three: `constraint_position order_of_derivative constraint_value`.
`--nknots NKNOTS [NKNOTS ...]`	Number of knots for the spline. Multiple values possible.
`--knots KNOTS [KNOTS ...]`	Explicitly define the knots. This overwrites `--nknots`.
`--outname OUTNAME`	Output name of the files.
`--folder FOLDER`	Output folder. Default = ./

`--plot-results PLOT_RESULTS [PLOT_RESULTS ...]`	Plot results from previous extrapolation. Arguments shall be `extr_parameters.txt extr_cont.txt extr_coeffs.txt`.
`--xmin XMIN`	Minimal x-value for the extrapolation.
`--xmax XMAX`	Maximal x-value for the extrapolation.
`--tol TOL`	Tolerance for the fit.
`--nsamples NSAMPLES, -ns NSAMPLES`	Number of samples for the bootstrap.
`--randomization-factor RANDOMIZATION_FACTOR`	The position of the knots is randomized during the bootstrap. Specify how much randomization shall be used. (0 = None, 1 = max).
`--xdata-col XDATA_COL`	Column where the x-values are stored.
`--ydata-col YDATA_COL`	Column where the y-values are stored.
`--edata-col EDATA_COL`	Column where the error-values (if present) are stored.
`--base-point BASE_POINT`	Base point of the spline. Shift this if you want to use constraints at x = 0.
`--no-tex`	Do not use LaTeX for text rendering.
`--show-plot`	Open a window of a plot after the bootstrap.
`--plot-xmin PLOT_XMIN`	Minimal value that shall be plotted.
`--plot-xmax PLOT_XMAX`	Maximal value that shall be plotted.
`--title TITLE`	Title in plots.
`--xlabel XLABEL`	x-label in plots.
`--ylabel YLABEL`	y-label in plots.
`--save-sample SAVE_SAMPLE`	Save the sample of the extrapolated data. This file is large.
`--log-level LOG_LEVEL`	Log level. Available are `WARN`, `INFO`, `PROGRESS`, `DETAILS`, `DEBUG`, `NONE`.

B. Supplementary data for section 5

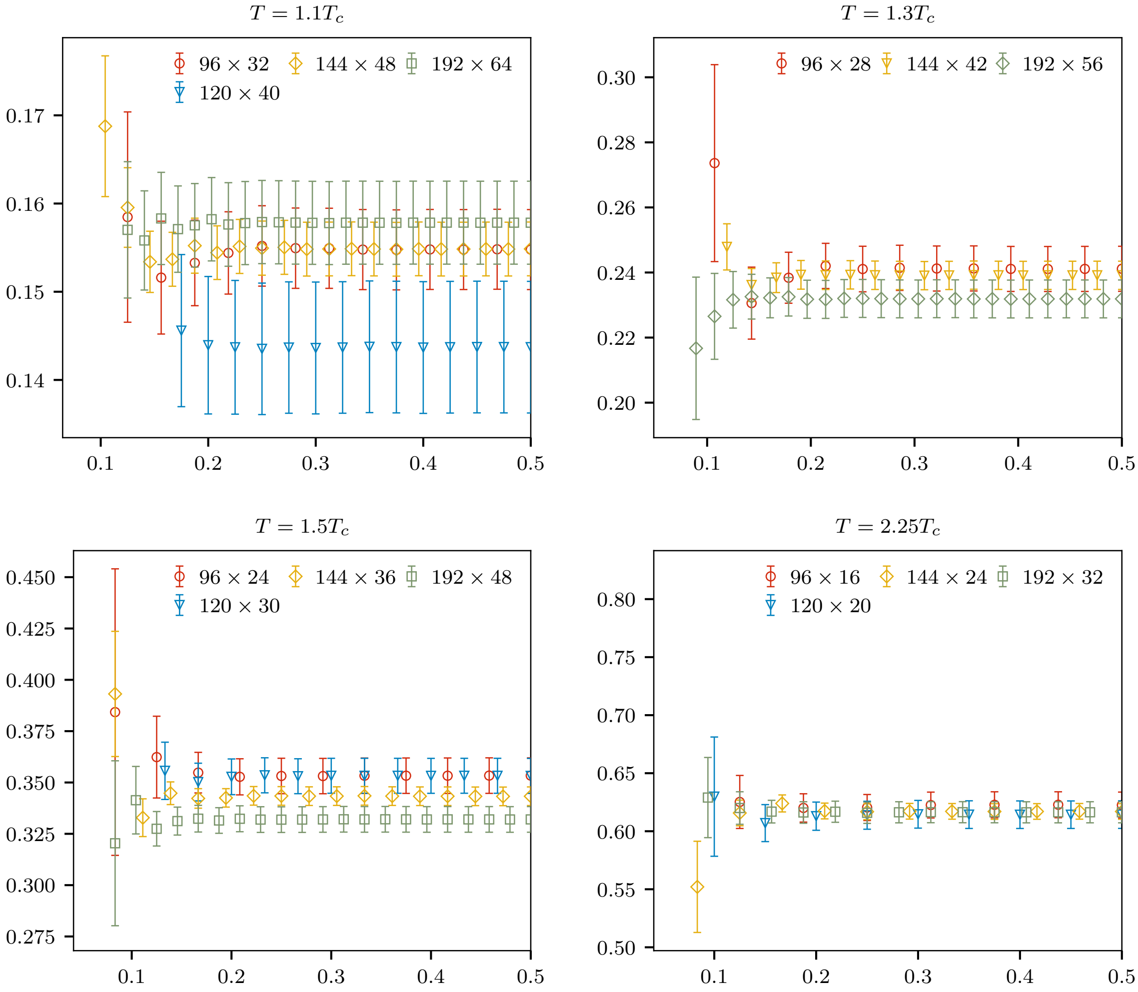

Figure B.1: Time (4th) component of the vector correlators at different temperature and lattice size. For the determination of the quark number susceptibility, we use $G_{\gamma_4}(\tau T = 0.5) = \chi_q/T^2$.

n_τ	τT	$G_{\mathrm{massless}}(n_\tau)/T^3$	$G_{\mathrm{massive}}(n_\tau)/T^3$	$G(n_\tau)T'^2/(T^3\chi_q)$
1	0.0104	$1.64(7) \cdot 10^5$	$1.72(7) \cdot 10^5$	$2.8(2) \cdot 10^5$
2	0.0208	$2.31(4) \cdot 10^4$	$2.45(4) \cdot 10^4$	$4.0(2) \cdot 10^4$
3	0.0312	6000(200)	6300(200)	$1.02(3) \cdot 10^4$
4	0.0417	2200(30)	2290(30)	3700(200)
5	0.0521	1050(20)	1090(20)	1780(50)
6	0.0625	599(9)	630(20)	1020(30)
7	0.0729	376(4)	394(5)	640(20)
8	0.0833	250(3)	262(4)	426(9)
9	0.0938	172(2)	181(3)	294(6)
10	0.1042	122(2)	128(2)	209(5)
11	0.1146	89.4(8)	94(1)	153(4)
12	0.1250	67.0(7)	70.4(9)	115(3)
13	0.1354	51.2(5)	53.8(6)	87(2)
14	0.1458	39.6(4)	41.7(4)	68(2)
15	0.1562	31.0(3)	32.6(3)	53(2)
16	0.1667	24.5(2)	25.8(3)	41.9(9)
17	0.1771	19.5(2)	20.5(2)	33.4(7)
18	0.1875	15.7(2)	16.5(2)	26.9(6)
19	0.1979	12.7(2)	13.4(2)	21.8(5)
20	0.2083	10.39(9)	10.92(9)	17.8(4)
21	0.2188	8.51(7)	8.95(8)	14.6(3)
22	0.2292	7.01(6)	7.37(7)	12.0(3)
23	0.2396	5.79(5)	6.09(5)	9.9(2)
24	0.2500	4.81(4)	5.05(5)	8.2(2)
25	0.2604	4.00(4)	4.21(4)	6.8(2)
26	0.2708	3.34(3)	3.51(3)	5.7(2)
27	0.2812	2.80(3)	2.95(3)	4.8(1)
28	0.2917	2.36(2)	2.47(3)	4.02(8)
29	0.3021	1.98(2)	2.08(2)	3.39(7)
30	0.3125	1.67(2)	1.76(2)	2.86(6)
31	0.3229	1.42(2)	1.49(2)	2.42(5)
32	0.3333	1.20(2)	1.26(2)	2.05(5)
33	0.3438	1.02(1)	1.07(1)	1.75(4)
34	0.3542	0.872(8)	0.916(9)	1.49(4)
35	0.3646	0.745(7)	0.783(8)	1.27(3)
36	0.3750	0.639(6)	0.671(7)	1.09(3)
37	0.3854	0.550(6)	0.578(6)	0.94(2)
38	0.3958	0.476(5)	0.499(5)	0.81(2)
39	0.4062	0.413(5)	0.434(5)	0.70(2)
40	0.4167	0.362(4)	0.380(4)	0.62(2)
41	0.4271	0.319(4)	0.335(4)	0.54(2)
42	0.4375	0.284(3)	0.298(3)	0.48(2)
43	0.4479	0.256(3)	0.268(3)	0.44(1)
44	0.4583	0.234(3)	0.245(3)	0.398(9)
45	0.4688	0.217(3)	0.228(3)	0.370(8)
46	0.4792	0.205(3)	0.216(3)	0.350(8)
47	0.4896	0.199(3)	0.208(3)	0.339(7)
48	0.5000	0.196(3)	0.206(3)	0.335(7)

Table B.1: Continuum extrapolated correlator in units of the temperature for charmonium in the vector channel using different renormalization at $T = 0.75T_c$: The massless renormalization corresponds to equation (3.61) and the massive renormalization is given by equation (3.62). In the last column, the correlator is divided by the quark number susceptibility at $T' = 2.25T_c$.

n_τ	τT	$G_{1-\mathrm{loop}}(n_\tau)/T^3$	$G_{2-\mathrm{loop}}(n_\tau)/T^3$
1	0.0104	$4.8(2) \cdot 10^4$	$4.6(2) \cdot 10^4$
2	0.0208	7680(70)	7340(80)
3	0.0312	2250(30)	2160(30)
4	0.0417	913(8)	876(8)
5	0.0521	462(6)	444(5)
6	0.0625	271(4)	260(3)
7	0.0729	174(2)	167(2)
8	0.0833	118(2)	113(2)
9	0.0938	83(2)	80(1)
10	0.1042	60.1(8)	57.6(7)
11	0.1146	44.7(6)	42.8(6)
12	0.1250	33.9(5)	32.5(5)
13	0.1354	26.2(4)	25.1(4)
14	0.1458	20.5(3)	19.7(3)
15	0.1562	16.2(3)	15.6(2)
16	0.1667	13.0(2)	12.4(2)
17	0.1771	10.5(2)	10.0(2)
18	0.1875	8.5(2)	8.1(2)
19	0.1979	6.9(2)	6.6(1)
20	0.2083	5.69(9)	5.45(8)
21	0.2188	4.70(8)	4.50(7)
22	0.2292	3.90(6)	3.73(6)
23	0.2396	3.25(6)	3.11(5)
24	0.2500	2.71(5)	2.60(5)
25	0.2604	2.27(4)	2.18(4)
26	0.2708	1.91(4)	1.83(3)
27	0.2812	1.61(3)	1.54(3)
28	0.2917	1.36(3)	1.30(3)
29	0.3021	1.15(2)	1.11(2)
30	0.3125	0.98(2)	0.94(2)
31	0.3229	0.83(2)	0.80(2)
32	0.3333	0.71(2)	0.68(2)
33	0.3438	0.61(2)	0.58(1)
34	0.3542	0.522(9)	0.500(9)
35	0.3646	0.449(8)	0.430(8)
36	0.3750	0.387(7)	0.371(7)
37	0.3854	0.335(6)	0.321(6)
38	0.3958	0.291(6)	0.279(5)
39	0.4062	0.255(5)	0.244(5)
40	0.4167	0.224(4)	0.215(4)
41	0.4271	0.199(4)	0.191(4)
42	0.4375	0.178(4)	0.171(4)
43	0.4479	0.161(3)	0.155(3)
44	0.4583	0.148(3)	0.142(3)
45	0.4688	0.138(3)	0.132(3)
46	0.4792	0.131(3)	0.126(3)
47	0.4896	0.127(3)	0.122(3)
48	0.5000	0.126(3)	0.121(3)

Table B.2: Continuum extrapolated correlator in units of the temperature for charmonium in the pseudoscalar channel using 1-loop and 2-loop renormalization from equation (3.65) at $T = 0.75T_c$.

n_τ	τT	$G_{\mathrm{massless}}(n_\tau)/T^3$	$G_{\mathrm{massive}}(n_\tau)/T^3$	$G(n_\tau)T'^2/(T^3\chi_q)$
1	0.0156	$4.9(2)\cdot 10^4$	$5.2(2)\cdot 10^4$	$8.4(6)\cdot 10^4$
2	0.0312	6800(100)	7270(90)	$1.18(3)\cdot 10^4$
3	0.0469	1770(40)	1860(40)	3000(80)
4	0.0625	654(7)	683(7)	1100(30)
5	0.0781	313(5)	326(6)	530(20)
6	0.0938	177(2)	185(3)	302(8)
7	0.1094	110(1)	116(2)	189(5)
8	0.1250	73.1(8)	77(1)	125(3)
9	0.1406	50.4(5)	53.0(5)	86(2)
10	0.1562	35.9(3)	37.8(3)	62(2)
11	0.1719	26.3(2)	27.7(3)	45(1)
12	0.1875	19.8(2)	20.8(2)	33.9(7)
13	0.2031	15.1(1)	15.9(2)	25.9(6)
14	0.2188	11.70(8)	12.31(9)	20.0(5)
15	0.2344	9.17(7)	9.65(7)	15.7(4)
16	0.2500	7.27(5)	7.65(6)	12.5(3)
17	0.2656	5.82(4)	6.12(4)	10.0(3)
18	0.2812	4.71(4)	4.95(4)	8.1(2)
19	0.2969	3.85(3)	4.04(3)	6.6(2)
20	0.3125	3.16(3)	3.33(3)	5.4(2)
21	0.3281	2.62(2)	2.76(2)	4.5(1)
22	0.3438	2.19(2)	2.31(2)	3.76(8)
23	0.3594	1.85(2)	1.95(2)	3.17(7)
24	0.3750	1.58(2)	1.66(2)	2.70(6)
25	0.3906	1.36(1)	1.43(2)	2.33(5)
26	0.4062	1.187(9)	1.25(1)	2.03(5)
27	0.4219	1.051(8)	1.105(9)	1.80(4)
28	0.4375	0.947(8)	0.996(8)	1.62(4)
29	0.4531	0.871(7)	0.915(8)	1.49(4)
30	0.4688	0.818(7)	0.860(7)	1.40(4)
31	0.4844	0.787(7)	0.827(7)	1.35(3)
32	0.5000	0.777(6)	0.817(7)	1.33(3)

Table B.3: Continuum extrapolated correlator in units of the temperature for charmonium in the vector channel using different renormalization at $T = 1.1T_c$: The massless renormalization corresponds to equation (3.61) and the massive renormalization is given by equation (3.62). In the last column, the correlator is divided by the quark number susceptibility at $T' = 2.25T_c$.

n_τ	τT	$G_{1-\text{loop}}(n_\tau)/T^3$	$G_{2-\text{loop}}(n_\tau)/T^3$
1	0.0156	$1.41(4)\cdot 10^4$	$1.36(4)\cdot 10^4$
2	0.0312	2270(20)	2170(20)
3	0.0469	668(7)	640(6)
4	0.0625	271(3)	260(2)
5	0.0781	137(2)	131(2)
6	0.0938	79.8(8)	76.5(7)
7	0.1094	50.9(5)	48.8(5)
8	0.1250	34.4(4)	32.9(4)
9	0.1406	24.2(3)	23.1(3)
10	0.1562	17.5(2)	16.8(2)
11	0.1719	13.0(2)	12.5(2)
12	0.1875	9.9(2)	9.5(2)
13	0.2031	7.66(9)	7.33(8)
14	0.2188	5.99(7)	5.74(7)
15	0.2344	4.74(6)	4.54(6)
16	0.2500	3.79(5)	3.63(5)
17	0.2656	3.06(4)	2.93(4)
18	0.2812	2.49(4)	2.39(3)
19	0.2969	2.04(3)	1.96(3)
20	0.3125	1.69(3)	1.62(3)
21	0.3281	1.40(2)	1.34(2)
22	0.3438	1.17(2)	1.13(2)
23	0.3594	0.99(2)	0.95(2)
24	0.3750	0.84(2)	0.81(2)
25	0.3906	0.73(2)	0.70(1)
26	0.4062	0.63(1)	0.608(9)
27	0.4219	0.560(9)	0.537(8)
28	0.4375	0.503(8)	0.483(7)
29	0.4531	0.461(8)	0.442(7)
30	0.4688	0.433(7)	0.415(7)
31	0.4844	0.416(7)	0.399(6)
32	0.5000	0.411(7)	0.394(6)

Table B.4: Continuum extrapolated correlator in units of the temperature for charmonium in the pseudoscalar channel using 1-loop and 2-loop renormalization from equation (3.65) at $T = 1.1T_c$.

n_τ	τT	$G_{\text{massless}}(n_\tau)/T^3$	$G_{\text{massive}}(n_\tau)/T^3$	$G(n_\tau)T'^2/(T^3\chi_q)$
1	0.0179	$3.3(2)\cdot 10^4$	$3.4(2)\cdot 10^4$	$5.6(5)\cdot 10^4$
2	0.0357	4600(100)	4900(200)	7900(300)
3	0.0536	1190(30)	1260(30)	2040(60)
4	0.0714	437(7)	458(9)	750(30)
5	0.0893	209(3)	218(4)	357(9)
6	0.1071	119(3)	125(4)	203(6)
7	0.1250	74.7(8)	78.3(9)	127(3)
8	0.1429	49.6(7)	52.1(8)	85(2)
9	0.1607	34.2(6)	35.9(7)	59(2)
10	0.1786	24.3(3)	25.6(3)	42(1)
11	0.1964	17.8(2)	18.7(2)	30.6(7)
12	0.2143	13.4(2)	14.1(2)	22.9(5)
13	0.2321	10.2(1)	10.8(2)	17.6(4)
14	0.2500	7.96(7)	8.39(8)	13.7(3)
15	0.2679	6.28(5)	6.61(6)	10.8(3)
16	0.2857	5.00(5)	5.27(5)	8.6(2)
17	0.3036	4.04(4)	4.25(4)	6.9(2)
18	0.3214	3.30(3)	3.47(3)	5.7(2)
19	0.3393	2.72(2)	2.87(3)	4.7(1)
20	0.3571	2.28(2)	2.40(2)	3.92(9)
21	0.3750	1.93(2)	2.04(2)	3.32(7)
22	0.3929	1.66(2)	1.75(2)	2.86(7)
23	0.4107	1.46(2)	1.53(2)	2.50(6)
24	0.4286	1.30(2)	1.37(2)	2.23(5)
25	0.4464	1.184(9)	1.25(2)	2.03(5)
26	0.4643	1.105(9)	1.16(2)	1.90(5)
27	0.4821	1.060(9)	1.12(1)	1.82(4)
28	0.5000	1.045(9)	1.10(1)	1.79(4)

Table B.5: Continuum extrapolated correlator in units of the temperature for charmonium in the vector channel using different renormalization at $T = 1.3T_c$: The massless renormalizations corresponds to equation (3.61) and the massive renormalizations is given by equation (3.62). In the last column, the correlator is divided by the quark number susceptibility at $T' = 2.25T_c$

.

n_τ	τT	$G_{1-\text{loop}}(n_\tau)/T^3$	$G_{2-\text{loop}}(n_\tau)/T^3$
1	0.0179	9400(400)	9000(400)
2	0.0357	1520(20)	1460(20)
3	0.0536	448(7)	430(6)
4	0.0714	182(2)	174(2)
5	0.0893	92(2)	88(1)
6	0.1071	53.7(7)	51.4(7)
7	0.1250	34.3(4)	32.8(4)
8	0.1429	23.2(3)	22.2(3)
9	0.1607	16.3(2)	15.6(2)
10	0.1786	11.8(2)	11.3(2)
11	0.1964	8.8(1)	8.41(9)
12	0.2143	6.66(8)	6.38(8)
13	0.2321	5.15(6)	4.93(6)
14	0.2500	4.04(5)	3.87(5)
15	0.2679	3.20(4)	3.07(4)
16	0.2857	2.57(3)	2.46(3)
17	0.3036	2.08(3)	2.00(3)
18	0.3214	1.70(3)	1.63(2)
19	0.3393	1.41(2)	1.35(2)
20	0.3571	1.18(2)	1.13(2)
21	0.3750	1.00(2)	0.96(2)
22	0.3929	0.86(2)	0.82(2)
23	0.4107	0.75(1)	0.718(9)
24	0.4286	0.666(9)	0.638(9)
25	0.4464	0.605(8)	0.579(8)
26	0.4643	0.563(8)	0.539(8)
27	0.4821	0.539(8)	0.516(7)
28	0.5000	0.531(8)	0.509(7)

Table B.6: Continuum extrapolated correlator in units of the temperature for charmonium in the pseudoscalar channel using 1-loop and 2-loop renormalization from equation (3.65) at $T = 1.3T_c$.

n_τ	τT	$G_{\mathrm{massless}}(n_\tau)/T^3$	$G_{\mathrm{massive}}(n_\tau)/T^3$	$G(n_\tau)T'^2/(T^3\chi_q)$
1	0.0208	$2.06(9)\cdot 10^4$	$2.16(8)\cdot 10^4$	$3.6(3)\cdot 10^4$
2	0.0417	2870(50)	3050(50)	5000(200)
3	0.0625	740(20)	780(20)	1270(40)
4	0.0833	273(3)	286(4)	470(20)
5	0.1042	131(3)	136(3)	222(6)
6	0.1250	74(2)	78(2)	126(3)
7	0.1458	46.5(5)	48.8(5)	79(2)
8	0.1667	30.9(4)	32.4(5)	53(2)
9	0.1875	21.3(3)	22.4(3)	36.5(8)
10	0.2083	15.2(2)	16.0(2)	26.0(6)
11	0.2292	11.2(1)	11.7(2)	19.1(4)
12	0.2500	8.43(9)	8.9(1)	14.4(3)
13	0.2708	6.50(6)	6.83(7)	11.1(3)
14	0.2917	5.10(4)	5.36(4)	8.7(2)
15	0.3125	4.07(4)	4.28(4)	7.0(2)
16	0.3333	3.30(3)	3.47(3)	5.6(2)
17	0.3542	2.72(2)	2.86(3)	4.7(1)
18	0.3750	2.29(2)	2.40(2)	3.92(8)
19	0.3958	1.96(2)	2.06(2)	3.36(7)
20	0.4167	1.72(2)	1.81(2)	2.95(6)
21	0.4375	1.55(2)	1.63(2)	2.65(6)
22	0.4583	1.43(2)	1.51(2)	2.45(5)
23	0.4792	1.37(1)	1.44(2)	2.34(5)
24	0.5000	1.34(2)	1.41(2)	2.30(5)

Table B.7: Continuum extrapolated correlator in units of the temperature for charmonium in the vector channel using different renormalization at $T = 1.5T_c$: The massless renormalization corresponds to equation (3.61) and the massive renormalization is given by equation (3.62). In the last column, the correlator is divided by the quark number susceptibility at $T' = 2.25T_c$.

n_τ	τT	$G_{1-\mathrm{loop}}(n_\tau)/T^3$	$G_{2-\mathrm{loop}}(n_\tau)/T^3$
1	0.0208	6000(200)	5700(200)
2	0.0417	957(8)	914(9)
3	0.0625	280(4)	267(4)
4	0.0833	113(1)	108(1)
5	0.1042	57.0(7)	54.6(6)
6	0.1250	33.2(4)	31.8(4)
7	0.1458	21.2(2)	20.3(2)
8	0.1667	14.3(2)	13.7(2)
9	0.1875	10.0(2)	9.6(2)
10	0.2083	7.24(8)	6.94(8)
11	0.2292	5.38(6)	5.15(6)
12	0.2500	4.08(5)	3.91(5)
13	0.2708	3.16(4)	3.03(4)
14	0.2917	2.49(3)	2.38(3)
15	0.3125	1.99(3)	1.90(3)
16	0.3333	1.61(2)	1.54(2)
17	0.3542	1.32(2)	1.27(2)
18	0.3750	1.10(2)	1.06(2)
19	0.3958	0.94(2)	0.90(2)
20	0.4167	0.82(2)	0.79(2)
21	0.4375	0.73(1)	0.70(1)
22	0.4583	0.67(1)	0.646(9)
23	0.4792	0.640(9)	0.613(9)
24	0.5000	0.628(9)	0.602(9)

Table B.8: Continuum extrapolated correlator in units of the temperature for charmonium in the pseudoscalar channel using 1-loop and 2-loop renormalization from equation (3.65) at $T = 1.5T_c$.

n_τ	τT	$G_{\mathrm{massless}}(n_\tau)/T^3$	$G_{\mathrm{massive}}(n_\tau)/T^3$	$G(n_\tau)T'^2/(T^3\chi_q)$
1	0.0312	6200(200)	6400(200)	$1.05(7)\cdot 10^4$
2	0.0625	860(10)	908(8)	1480(40)
3	0.0938	221(4)	233(5)	380(20)
4	0.1250	81.6(8)	85.3(9)	139(4)
5	0.1562	39.3(6)	41.0(8)	67(2)
6	0.1875	22.5(3)	23.6(3)	38(1)
7	0.2188	14.2(2)	14.9(2)	24.3(6)
8	0.2500	9.6(2)	10.1(2)	16.4(4)
9	0.2812	6.77(6)	7.11(8)	11.6(3)
10	0.3125	5.01(4)	5.27(5)	8.6(2)
11	0.3438	3.88(4)	4.08(5)	6.7(2)
12	0.3750	3.14(3)	3.30(4)	5.4(2)
13	0.4062	2.65(3)	2.79(3)	4.5(1)
14	0.4375	2.34(3)	2.46(3)	4.01(9)
15	0.4688	2.16(2)	2.27(2)	3.71(8)
16	0.5000	2.10(2)	2.21(2)	3.61(8)

Table B.9: Continuum extrapolated correlator in units of the temperature for charmonium in the vector channel using different renormalization at $T = 2.25T_c$: The massless renormalization corresponds to equation (3.61) and the massive renormalization is given by equation (3.62). In the last column, the correlator is divided by the quark number susceptibility at $T' = 2.25T_c$.

n_τ	τT	$G_{1-\mathrm{loop}}(n_\tau)/T^3$	$G_{2-\mathrm{loop}}(n_\tau)/T^3$
1	0.0312	1760(50)	1680(50)
2	0.0625	285(2)	272(2)
3	0.0938	83.6(9)	80.1(8)
4	0.1250	33.9(3)	32.5(3)
5	0.1562	17.1(2)	16.4(2)
6	0.1875	10.0(2)	9.6(1)
7	0.2188	6.36(7)	6.10(7)
8	0.2500	4.30(5)	4.13(5)
9	0.2812	3.05(4)	2.92(4)
10	0.3125	2.24(3)	2.15(3)
11	0.3438	1.71(2)	1.64(2)
12	0.3750	1.36(2)	1.31(2)
13	0.4062	1.13(2)	1.08(2)
14	0.4375	0.98(2)	0.94(2)
15	0.4688	0.90(2)	0.86(2)
16	0.5000	0.87(2)	0.84(2)

Table B.10: Continuum extrapolated correlator in units of the temperature for charmonium in the pseudoscalar channel using 1-loop and 2-loop renormalization from equation (3.65) at $T = 2.25T_c$.

C. Supplementary data for section 6

β	T[MeV]	m_l	m_s	point	wall
5.850	119.19	0.00712	0.1424	1166	1166
5.900	125.45	0.00660	0.1320	1000	1000
5.950	132.07	0.00615	0.1230	1000	1000
6.000	139.08	0.00569	0.1138	3073	3073
6.025	142.73	0.00550	0.1100	1000	1000
6.050	146.48	0.00532	0.1064	1000	1000
6.062	148.32	0.005235	0.1047	1000	1000
6.075	150.33	0.00518	0.1036	1000	1000
6.090	152.70	0.00504	0.1008	1001	1001
6.100	154.29	0.00499	0.0998	3363	3363
6.120	157.54	0.004845	0.0969	1001	1001
6.125	158.36	0.00483	0.0966	1003	1003
6.150	162.54	0.00468	0.0936	1000	1000
6.165	165.10	0.00457	0.0914	1000	1000
6.185	168.58	0.004455	0.0891	1000	1000
6.195	170.35	0.00440	0.0880	1000	1000
6.245	179.46	0.00415	0.0830	1000	1000

β	T[MeV]	m_l	m_s	point	wall
6.050	109.86	0.00532	0.1064	2108	2108
6.125	118.77	0.00483	0.0966	2241	2241
6.195	127.76	0.00440	0.0880	1690	1690
6.245	134.60	0.00415	0.0830	2710	2710
6.285	140.32	0.00395	0.0790	2000	2000
6.341	148.74	0.00370	0.0740	1713	1713
6.354	150.76	0.00364	0.0728	1249	1249
6.390	156.50	0.00347	0.0694	2604	2604
6.423	161.93	0.00335	0.0670	2031	2031
6.460	168.24	0.00320	0.0640	1644	1644
6.488	173.16	0.00310	0.0620	1790	1790
6.515	178.03	0.00302	0.0604	3067	3067
6.575	189.29	0.00282	0.0564	3206	3206
6.608	195.75	0.00271	0.0542	2379	2379
6.664	207.17	0.00257	0.0514	2001	2001
6.740	223.58	0.00238	0.0476	831	831
6.800	237.32	0.00224	0.0448	500	500
6.880	256.75	0.00206	0.0412	500	500
7.030	296.81	0.00178	0.0356	500	500
7.280	375.26	0.00142	0.0284	500	500
7.373	408.63	0.00125	0.0250	500	500
7.596	499.30	0.00101	0.0202	500	500
7.825	610.60	0.00082	0.0164	500	500
8.000	710.45	0.00070	0.0140	500	500
8.200	843.20	0.0005835	0.0116	250	250
8.400	999.39	0.0004875	0.00975	250	250
8.570	1153.83	0.0004188	0.008376	200	200
8.710	1298.31	0.0003697	0.007394	200	200
8.850	1460.54	0.0003264	0.006528	200	200
9.060	1742.17	0.0002417	0.004834	200	0
9.230	2009.14	0.0002074	0.004148	200	200
9.360	2240.48	0.00018455	0.003691	200	200
9.490	2498.41	0.00016425	0.003285	200	200
9.670	2905.28	0.00013990	0.002798	0	200

Table C.1: Summary of statistics for $m_l = m_s/20$ with lattice size $24^3 \times 6$ (left) and $32^3 \times 8$ (right)..

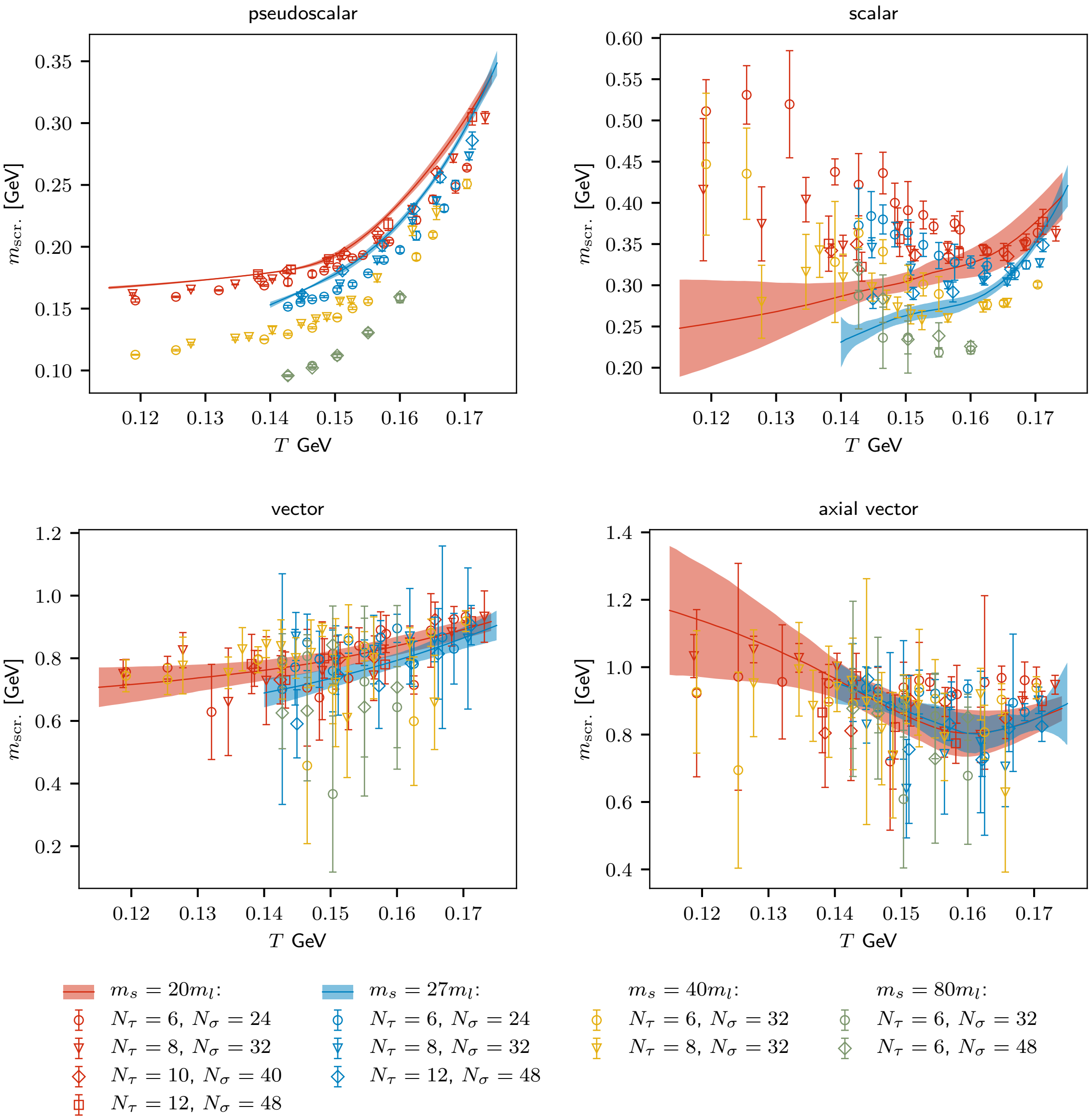

Figure C.1: Screening masses for different quark mass ratios approaching the chiral limit. For $m_s = 20m_l$ and $m_s = 27m_l$, the bands correspond to the continuum extrapolation.

β	T[MeV]	m_l	m_s	point	wall
6.488	138.53	0.00310	0.0620	9534	9534
6.515	142.42	0.00302	0.0604	2525	2525
6.575	151.43	0.00282	0.0564	2512	2512
6.608	156.60	0.00271	0.0542	2685	2685
6.664	165.73	0.00257	0.0514	1071	1071
6.740	178.86	0.00238	0.0476	1021	1021
6.800	189.85	0.00224	0.0448	800	800
6.880	205.40	0.00206	0.0412	650	650
6.950	219.87	0.00193	0.0386	500	500
7.030	237.45	0.00178	0.0356	600	600
7.150	266.03	0.00160	0.0320	500	500
7.500	366.65	0.00111	0.0222	450	450
7.650	419.00	0.00096	0.0192	250	250
7.825	488.48	0.00082	0.016	250	250
8.000	568.36	0.00070	0.0140	500	500
8.200	674.56	0.0005835	0.0116	551	551
8.400	799.51	0.0004875	0.00975	300	300
8.570	923.07	0.0004188	0.008376	250	250

β	T[MeV]	m_l	m_s	point	wall
6.664	138.11	0.00257	0.0514	372	372
6.700	143.20	0.00248	0.0496	649	649
6.740	149.05	0.00238	0.0476	2214	2214
6.800	158.21	0.00224	0.0448	2008	2008
6.880	171.17	0.00206	0.0412	2001	2001
6.950	183.22	0.00193	0.0386	1300	1300
7.030	197.87	0.00178	0.0356	1000	1000
7.150	221.69	0.00160	0.0320	730	730
7.280	250.18	0.00142	0.0284	800	800
7.373	272.42	0.00125	0.0250	800	800
7.596	332.87	0.00101	0.0202	800	800
7.825	407.06	0.00082	0.0164	900	900
8.000	473.63	0.00070	0.0140	310	310
8.200	562.13	0.0005835	0.0116	500	500
8.400	666.26	0.0004875	0.00975	500	500
8.570	769.22	0.0004188	0.008376	250	250
8.710	865.54	0.0003697	0.007394	250	250
8.850	973.70	0.0003264	0.006528	250	250

Table C.2: Summary of statistics for $m_l = m_s/20$ with lattice size $40^3 \times 10$ (left) and $48^3 \times 12$ (right)
.

β	T[MeV]	m_l	m_s	point	wall
6.025	142.73	0.004074	0.1100	990	990
6.038	144.66	0.004	0.1082	1581	1581
6.050	146.48	0.003941	0.1064	1649	1649
6.062	148.32	0.003878	0.1047	1650	1650
6.075	150.33	0.003837	0.1036	1393	1749
6.090	152.70	0.003733	0.1008	1386	1386
6.105	155.10	0.003659	0.0988	1749	1749
6.120	157.54	0.003589	0.0969	1649	1649
6.135	160.02	0.003519	0.0950	1749	1749
6.150	162.54	0.003467	0.0936	990	990
6.175	166.83	0.003356	0.0906	1472	1472
6.185	168.58	0.0033	0.0891	1475	1550

β	T[MeV]	m_l	m_s	point	wall
6.315	144.77	0.00281	0.0759	1115	1115
6.354	150.76	0.00270	0.0728	3731	3731
6.390	156.50	0.00257	0.0694	3514	3514
6.423	161.93	0.00248	0.0670	3250	3250
6.445	165.66	0.00241	0.0652	1912	2373
6.474	170.68	0.00234	0.0632	1937	2425

Table C.3: Summary of statistics for $m_l = m_s/27$ with lattice size $24^3 \times 6$ (left) and $32^3 \times 8$ (right)..

β	T[MeV]	m_l	m_s	point	wall
6.712	144.94	0.00181	0.0490	1955	1955
6.754	151.15	0.00173	0.0468	1484	1484
6.794	157.28	0.00167	0.0450	1407	1407
6.825	162.17	0.00161	0.0436	1946	1946
6.850	166.21	0.00157	0.0424	2081	2081
6.880	171.17	0.00153	0.0412	1960	1960

β	T[MeV]	m_l	m_s	point	wall
6.973	140.50	0.00139	0.0376	4817	2757
7.010	145.59	0.00132	0.0357	5919	6168
7.054	151.84	0.00129	0.0348	123	622
7.095	157.87	0.00124	0.0334	0	308
7.130	163.17	0.00119	0.0322	3697	3697
7.156	167.20	0.00116	0.0314	5774	6107
7.188	172.29	0.00113	0.0306	4451	4324

Table C.4: Summary of statistics for $m_l = m_s/27$ with lattice size $48^3 \times 12$ (left) and $64^3 \times 16$ (right)..

β	T[MeV]	m_l	m_s	point	wall
5.850	119.19	0.00356	0.1424	720	720
5.900	125.45	0.00330	0.1320	1099	1099
6.000	139.08	0.002845	0.1138	1200	1200
6.025	142.73	0.00275	0.1100	1511	1511
6.050	146.48	0.00266	0.1064	1618	1618
6.075	150.33	0.00259	0.1036	1418	1418
6.090	152.70	0.00252	0.1008	1273	1273
6.105	155.10	0.00247	0.0988	685	685
6.150	162.54	0.002340	0.0936	1000	1000
6.165	165.10	0.002285	0.0914	1581	1581
6.195	170.35	0.00220	0.0880	1460	1460

β	T[MeV]	m_l	m_s	point	wall
6.195	127.76	0.00220	0.0880	401	401
6.245	134.60	0.002075	0.0830	822	822
6.260	136.72	0.002025	0.0810	1080	1080
6.285	140.32	0.001975	0.0790	1150	1157
6.300	142.53	0.00193	0.0772	0	1162
6.315	144.77	0.00190	0.0760	1200	1146
6.330	147.05	0.001865	0.0746	1263	1264
6.341	148.74	0.00185	0.0740	450	450
6.354	150.76	0.00182	0.0728	1248	1248
6.365	152.49	0.00179	0.0716	1194	1194
6.390	156.50	0.001735	0.0694	1300	1300
6.423	161.93	0.001675	0.0670	728	728
6.445	165.66	0.001630	0.0652	942	942

Table C.5: Summary of statistics for $m_l = m_s/40$ with lattice size $32^3 \times 6$ (left) and $32^3 \times 8$ (right). .

β	N_σ	T[MeV]	m_l	m_s	point	wall
6.025	32	142.73	0.001375	0.1100	1750	1750
6.050	32	146.48	0.001330	0.1064	1518	1518
6.075	32	150.33	0.001295	0.1036	1750	1750
6.105	32	155.10	0.001235	0.0988	1947	1947
6.135	32	160.02	0.0011875	0.0950	1250	1250
6.025	48	142.73	0.001375	0.1100	992	992
6.050	48	146.48	0.00133	0.1064	1359	1359
6.075	48	150.33	0.001295	0.1036	1192	1192
6.105	48	155.10	0.001235	0.0988	1045	1045
6.135	48	160.02	0.0011875	0.0950	706	706

Table C.6: Summary of statistics for $m_l = m_s/80$ with $N_\tau = 6$.

T [GeV]	m_{P} [GeV]	m_{V} [GeV]	m_{S} [GeV]	m_{A} [GeV]
0.132	0.129(5)	0.7(2)	0.22(2)	1.0(2)
0.136	0.139(4)	0.69(9)	0.23(2)	0.96(9)
0.140	0.150(2)	0.70(7)	0.24(1)	0.94(7)
0.144	0.1615(9)	0.71(5)	0.245(8)	0.91(5)
0.148	0.174(2)	0.72(4)	0.254(6)	0.88(4)
0.152	0.187(2)	0.73(5)	0.263(6)	0.85(4)
0.156	0.202(3)	0.75(6)	0.274(7)	0.83(6)
0.160	0.221(3)	0.78(5)	0.286(7)	0.81(6)
0.164	0.245(2)	0.82(4)	0.303(6)	0.82(5)
0.168	0.275(4)	0.85(5)	0.326(6)	0.84(4)
0.172	0.310(7)	0.88(4)	0.356(9)	0.87(4)
0.176	0.352(8)	0.90(4)	0.39(2)	0.90(4)
0.180	0.399(7)	0.93(4)	0.44(2)	0.94(4)
0.184	0.445(9)	0.96(4)	0.48(2)	0.97(3)
0.188	0.50(1)	0.99(4)	0.53(2)	1.00(3)
0.192	0.54(1)	1.02(4)	0.58(3)	1.04(3)
0.196	0.59(2)	1.05(4)	0.63(3)	1.07(3)
0.200	0.64(2)	1.09(4)	0.68(3)	1.11(3)
0.240	1.08(4)	1.41(2)	1.10(4)	1.43(1)
0.280	1.45(3)	1.73(1)	1.43(3)	1.729(8)
0.320	1.76(2)	2.03(2)	1.74(3)	2.03(2)
0.360	2.06(2)	2.32(2)	2.04(2)	2.32(2)
0.400	2.34(3)	2.61(3)	2.33(2)	2.60(2)
0.440	2.61(3)	2.88(3)	2.61(3)	2.87(3)
0.480	2.88(3)	3.15(4)	2.89(4)	3.14(4)
0.520	3.15(4)	3.41(4)	3.16(4)	3.40(4)
0.560	3.42(5)	3.66(5)	3.42(4)	3.66(5)
0.600	3.68(4)	3.92(5)	3.68(4)	3.92(5)
0.640	3.94(4)	4.17(4)	3.93(3)	4.17(5)
0.680	4.19(4)	4.43(4)	4.19(3)	4.43(5)
0.720	4.45(4)	4.68(4)	4.44(3)	4.68(5)
0.760	4.71(4)	4.94(4)	4.70(3)	4.94(5)
0.800	4.97(4)	5.21(5)	4.96(3)	5.21(5)
0.840	5.23(4)	5.48(5)	5.22(4)	5.48(6)
0.880	5.49(4)	5.76(5)	5.49(3)	5.75(5)
0.920	5.76(6)	6.04(5)	5.75(4)	6.03(6)
0.960	6.02(9)	6.33(6)	6.03(4)	6.32(6)
1.000	6.3(2)	6.63(9)	6.30(5)	6.62(9)

Table C.7: Continuum-extrapolated values of the $\bar{u}d$-screening masses.

T [GeV]	m_{P} [GeV]	m_{V} [GeV]	m_{S} [GeV]	m_{A} [GeV]
0.132	0.50(2)	0.88(2)	0.66(3)	1.17(6)
0.136	0.51(1)	0.89(2)	0.67(3)	1.16(6)
0.140	0.519(5)	0.90(2)	0.67(2)	1.14(5)
0.144	0.527(2)	0.91(2)	0.67(2)	1.12(3)
0.148	0.537(4)	0.923(9)	0.67(2)	1.10(3)
0.152	0.547(9)	0.936(9)	0.675(9)	1.08(2)
0.156	0.559(7)	0.950(9)	0.679(8)	1.06(2)
0.160	0.574(4)	0.965(9)	0.682(7)	1.04(2)
0.164	0.590(7)	0.982(9)	0.686(5)	1.04(2)
0.168	0.604(4)	1.00(1)	0.690(6)	1.04(2)
0.172	0.621(6)	1.020(9)	0.698(8)	1.05(2)
0.176	0.642(9)	1.041(9)	0.71(2)	1.07(2)
0.180	0.667(9)	1.063(9)	0.73(2)	1.09(2)
0.184	0.697(9)	1.086(9)	0.75(2)	1.11(2)
0.188	0.73(2)	1.11(1)	0.77(2)	1.13(2)
0.192	0.76(2)	1.13(1)	0.80(2)	1.15(2)
0.196	0.80(2)	1.16(1)	0.83(2)	1.18(2)
0.200	0.83(3)	1.19(2)	0.86(2)	1.20(2)
0.240	1.16(2)	1.461(8)	1.16(2)	1.463(9)
0.280	1.46(2)	1.748(7)	1.46(2)	1.743(7)
0.320	1.76(2)	2.04(2)	1.75(2)	2.03(2)
0.360	2.05(2)	2.32(2)	2.04(2)	2.32(2)
0.400	2.34(2)	2.60(2)	2.33(2)	2.60(2)
0.440	2.62(2)	2.88(3)	2.61(2)	2.88(3)
0.480	2.89(3)	3.15(3)	2.89(3)	3.15(3)
0.520	3.16(3)	3.41(3)	3.16(4)	3.41(3)
0.560	3.42(4)	3.67(3)	3.42(4)	3.67(4)
0.600	3.68(4)	3.93(4)	3.68(4)	3.92(4)
0.640	3.93(4)	4.18(4)	3.94(4)	4.17(4)
0.680	4.19(4)	4.44(4)	4.19(4)	4.43(4)
0.720	4.45(4)	4.69(4)	4.44(4)	4.68(4)
0.760	4.71(4)	4.95(5)	4.69(5)	4.94(5)
0.800	4.97(4)	5.21(4)	4.95(5)	5.21(5)
0.840	5.23(4)	5.48(4)	5.21(5)	5.48(5)
0.880	5.50(4)	5.75(4)	5.47(5)	5.75(4)
0.920	5.77(5)	6.02(5)	5.74(6)	6.03(5)
0.960	6.05(7)	6.29(7)	6.02(8)	6.31(6)
1.000	6.3(1)	6.6(1)	6.3(2)	6.60(8)

Table C.8: Continuum-extrapolated values of the $\bar{u}s$-screening masses.

T [GeV]	m_{P} [GeV]	m_{V} [GeV]	m_{S} [GeV]	m_{A} [GeV]
0.132	0.71(2)	1.026(7)	1.01(3)	1.36(5)
0.136	0.711(8)	1.032(6)	1.01(2)	1.34(5)
0.140	0.714(4)	1.040(5)	1.00(2)	1.33(4)
0.144	0.717(1)	1.048(4)	0.99(2)	1.32(3)
0.148	0.720(6)	1.056(3)	0.99(2)	1.30(2)
0.152	0.724(9)	1.065(3)	0.98(2)	1.29(2)
0.156	0.730(9)	1.075(3)	0.97(1)	1.27(2)
0.160	0.744(6)	1.086(3)	0.965(9)	1.25(2)
0.164	0.758(6)	1.098(3)	0.957(7)	1.24(2)
0.168	0.772(5)	1.110(4)	0.949(7)	1.23(2)
0.172	0.783(8)	1.124(4)	0.944(9)	1.22(2)
0.176	0.796(9)	1.138(5)	0.94(2)	1.22(2)
0.180	0.81(1)	1.154(5)	0.95(2)	1.23(2)
0.184	0.831(9)	1.171(6)	0.96(2)	1.24(2)
0.188	0.85(1)	1.189(6)	0.97(2)	1.25(1)
0.192	0.88(2)	1.208(7)	0.98(2)	1.26(1)
0.196	0.90(2)	1.229(7)	1.00(2)	1.277(9)
0.200	0.93(2)	1.250(7)	1.02(2)	1.294(9)
0.240	1.20(3)	1.492(7)	1.25(2)	1.512(7)
0.280	1.48(2)	1.763(7)	1.50(2)	1.772(7)
0.320	1.78(2)	2.04(2)	1.78(2)	2.05(2)
0.360	2.07(2)	2.32(2)	2.06(2)	2.33(2)
0.400	2.35(2)	2.60(3)	2.34(2)	2.61(3)
0.440	2.63(3)	2.88(3)	2.62(3)	2.88(3)
0.480	2.90(3)	3.15(3)	2.89(3)	3.15(3)
0.520	3.17(4)	3.41(3)	3.16(4)	3.41(3)
0.560	3.43(4)	3.68(4)	3.42(4)	3.67(4)
0.600	3.68(4)	3.93(4)	3.68(4)	3.93(4)
0.640	3.94(4)	4.19(5)	3.93(4)	4.19(5)
0.680	4.19(4)	4.45(6)	4.19(4)	4.44(5)
0.720	4.45(3)	4.71(6)	4.44(4)	4.70(5)
0.760	4.70(3)	4.96(6)	4.70(4)	4.96(5)
0.800	4.96(4)	5.22(5)	4.95(4)	5.22(5)
0.840	5.23(4)	5.48(4)	5.21(4)	5.49(5)
0.880	5.50(4)	5.74(4)	5.48(6)	5.76(4)
0.920	5.77(5)	6.01(5)	5.75(8)	6.03(4)
0.960	6.05(6)	6.27(7)	6.0(2)	6.31(6)
1.000	6.3(1)	6.5(2)	6.3(2)	6.59(9)

Table C.9: Continuum-extrapolated values of the $\bar{s}s$-screening masses.

References

[1] J. C. Collins and M. J. Perry. “Superdense Matter: Neutrons or Asymptotically Free Quarks?” *Phys. Rev. Lett.* 34 (21 May 1975), pp. 1353–1356.

[2] I. Arsene et al. “Quark gluon plasma and color glass condensate at RHIC? The Perspective from the BRAHMS experiment”. *Nucl. Phys.* A757 (2005), pp. 1–27. arXiv: `nucl-ex/0410020`.

[3] J. Adams et al. “Experimental and theoretical challenges in the search for the quark gluon plasma: The STAR Collaboration’s critical assessment of the evidence from RHIC collisions”. *Nucl. Phys.* A757 (2005), pp. 102–183. arXiv: `nucl-ex/0501009`.

[4] B. B. Back et al. “The PHOBOS perspective on discoveries at RHIC”. *Nucl. Phys.* A757 (2005), pp. 28–101. arXiv: `nucl-ex/0410022`.

[5] K. Adcox et al. “Formation of dense partonic matter in relativistic nucleus-nucleus collisions at RHIC: Experimental evaluation by the PHENIX collaboration”. *Nucl. Phys.* A757 (2005), pp. 184–283. arXiv: `nucl-ex/0410003`.

[6] T. Bhattacharya et al. “QCD Phase Transition with Chiral Quarks and Physical Quark Masses”. *Phys. Rev. Lett.* 113.8 (2014), p. 082001. arXiv: `1402.5175`.

[7] Y. Aoki et al. “The Order of the quantum chromodynamics transition predicted by the standard model of particle physics”. *Nature* 443 (2006), pp. 675–678. arXiv: `hep-lat/0611014`.

[8] K. G. Wilson. “Confinement of quarks”. *Phys. Rev. D* 10 (8 Oct. 1974), pp. 2445–2459.

[9] T. Matsui and H. Satz. “J/ψ Suppression by Quark-Gluon Plasma Formation”. *Phys. Lett.* B178 (1986), pp. 416–422.

[10] R. Arnaldi. “J/ψ production in p-A and A-A collisions at fixed target experiments”. *Nucl. Phys.* A830 (2009), pp. 345C–352C. arXiv: `0907.5004`.

[11] A. Adare et al. “Suppression pattern of neutral pions at high transverse momentum in Au + Au collisions at $\sqrt{s_{NN}} = 200$ GeV and constraints on medium transport coefficients”. *Phys. Rev. Lett.* 101 (2008), p. 232301. arXiv: `0801.4020`.

[12] B. Abelev et al. “J/ψ suppression at forward rapidity in Pb-Pb collisions at $\sqrt{s_{NN}} = 2.76$ TeV”. *Phys. Rev. Lett.* 109 (2012), p. 072301. arXiv: `1202.1383`.

[13] G. Aad et al. “Measurement of the centrality dependence of J/ψ yields and observation of Z production in lead–lead collisions with the ATLAS detector at the LHC”. *Phys. Lett.* B697 (2011), pp. 294–312. arXiv: `1012.5419`.

[14] S. Chatrchyan et al. “Suppression of non-prompt J/ψ, prompt J/ψ, and Y(1S) in PbPb collisions at $\sqrt{s_{NN}} = 2.76$ TeV”. *JHEP* 05 (2012), p. 063. arXiv: `1201.5069`.

[15] S. Chatrchyan et al. “Observation of sequential Upsilon suppression in PbPb collisions”. *Phys. Rev. Lett.* 109 (2012), p. 222301. arXiv: `1208.2826`.

[16] M. Aaboud et al. “Prompt and non-prompt J/ψ and $\psi(2\mathrm{S})$ suppression at high transverse momentum in 5.02 TeV Pb+Pb collisions with the ATLAS experiment”. *Eur. Phys. J.* C78.9 (2018), p. 762. arXiv: `1805.04077`.

[17] A. K. Chaudhuri. “Sequential melting of charmonium states in an expanding Quark Gluon Plasma and J/ψ suppression at RHIC and LHC energy collisions”. *J. Phys.* G35 (2008), p. 095107. arXiv: `0804.1455`.

[18] B. Abelev et al. “D meson elliptic flow in non-central Pb-Pb collisions at $\sqrt{s_{NN}} =$ 2.76TeV”. *Phys. Rev. Lett.* 111 (2013), p. 102301. arXiv: `1305.2707`.

[19] L. Massacrier. “J/ψ elliptic flow measurement in Pb–Pb collisions at $\sqrt{s_{NN}} = 2.76$ TeV at forward rapidity with the ALICE experiment”. *Nuclear Physics A* 910-911 (2013). Hard Probes 2012, pp. 235–238.

[20] A. Adare et al. “Heavy-quark production and elliptic flow in Au$+$Au collisions at $\sqrt{s_{_{NN}}} = 62.4$ GeV”. *Phys. Rev.* C91.4 (2015), p. 044907. arXiv: `1405.3301`.

[21] R. Vértesi. “Heavy Flavor Measurements at STAR”. *Nucl. Part. Phys. Proc.* 273-275 (2016), pp. 1588–1594. arXiv: `1410.3959`.

[22] I. Montvay and G. Münster. *Quantum Fields on a Lattice*. Cambridge Monographs on Mathem. Cambridge University Press, 1997.

[23] T. DeGrand and C. DeTar. *Lattice methods for quantum chromodynamics*. World Scientific, 2006.

[24] C. Gattringer and C. Lang. *Quantum Chromodynamics on the Lattice: An Introductory Presentation*. Lecture Notes in Physics. Springer, 2009.

[25] H. J. Rothe. *Lattice gauge theories: an introduction; 3th ed.* World Scientific Lecture Notes in Physics. Singapore: World Scientific, 2006.

[26] H.-W. Lin and H. B. Meyer. *Lattice QCD for Nuclear Physics*. Springer, 2015.

[27] L. G. Yaffe and B. Svetitsky. “First-order phase transition in the SU(3) gauge theory at finite temperature”. *Phys. Rev. D* 26 (4 Aug. 1982), pp. 963–965.

[28] S. Aoki et al. “Light hadron spectrum and quark masses from quenched lattice QCD”. *Phys. Rev.* D67 (2003), p. 034503. arXiv: `hep-lat/0206009`.

[29] M. Creutz. “Overrelaxation and Monte Carlo simulation”. *Phys. Rev. D* 36 (2 July 1987), pp. 515–519.

[30] S. L. Adler. “Over-relaxation method for the Monte Carlo evaluation of the partition function for multiquadratic actions”. *Phys. Rev. D* 23 (12 June 1981), pp. 2901–2904.

[31] N. Cabibbo and E. Marinari. “A new method for updating SU(N) matrices in computer simulations of gauge theories”. *Physics Letters B* 119.4 (1982), pp. 387–390.

[32] A. D. Kennedy and B. J. Pendleton. “Improved Heat Bath Method for Monte Carlo Calculations in Lattice Gauge Theories”. *Phys. Lett.* 156B (1985), pp. 393–399.

[33] S. Duane, A. Kennedy, B. J. Pendleton, and D. Roweth. “Hybrid Monte Carlo”. *Physics Letters B* 195.2 (1987), pp. 216–222.

[34] B. Sheikholeslami and R. Wohlert. “Improved Continuum Limit Lattice Action for QCD with Wilson Fermions”. *Nucl. Phys.* B259 (1985), p. 572.

[35] M. Luscher and P. Weisz. “$O(a)$ improvement of the axial current in lattice QCD to one loop order of perturbation theory”. *Nucl. Phys.* B479 (1996), pp. 429–458. arXiv: `hep-lat/9606016`.

[36] M. Luscher et al. “Nonperturbative O(a) improvement of lattice QCD”. *Nucl. Phys.* B491 (1997), pp. 323–343. arXiv: `hep-lat/9609035`.

[37] A. D. Kennedy, I. Horvath, and S. Sint. “A New exact method for dynamical fermion computations with nonlocal actions”. *Nucl. Phys. Proc. Suppl.* 73 (1999). [,834(1998)], pp. 834–836. arXiv: `hep-lat/9809092`.

[38] M. Hasenbusch. “Speeding up the hybrid Monte Carlo algorithm for dynamical fermions”. *Phys. Lett.* B519 (2001), pp. 177–182. arXiv: `hep-lat/0107019`.

[39] A. S. Kronfeld. “Lattice gauge theory with staggered fermions: How, where, and why (not)”. *PoS* LAT2007 (2007), p. 016. arXiv: `0711.0699`.

[40] E. Follana et al. “Further improvements to staggered quarks”. *Nucl. Phys. Proc. Suppl.* 129 (2004), pp. 447–449. arXiv: `hep-lat/0311004`.

[41] P. Steinbrecher. “The QCD crossover up to $O(\mu_6^B)$ from Lattice QCD”. PhD thesis. 2018.

[42] D. J. Gross and F. Wilczek. “Ultraviolet Behavior of Non-Abelian Gauge Theories”. *Phys. Rev. Lett.* 30 (26 June 1973), pp. 1343–1346.

[43] R. Sommer. “Scale setting in lattice QCD”. *PoS* LATTICE2013 (2014), p. 015. arXiv: `1401.3270`.

[44] A. Gray et al. “The Upsilon spectrum and m(b) from full lattice QCD”. *Phys. Rev.* D72 (2005), p. 094507. arXiv: `hep-lat/0507013`.

[45] A. Francis et al. “Critical point and scale setting in SU(3) plasma: An update”. *Phys. Rev.* D91.9 (2015), p. 096002. arXiv: `1503.05652`.

[46] Y. Burnier et al. “Thermal quarkonium physics in the pseudoscalar channel”. *JHEP* 11 (2017), p. 206. arXiv: `1709.07612`.

[47] M. Tanabashi et al. “Review of Particle Physics”. *Phys. Rev. D* 98 (3 Aug. 2018), p. 030001.

[48] A. Bazavov et al. “The chiral and deconfinement aspects of the QCD transition”. *Phys. Rev.* D85 (2012), p. 054503. arXiv: `1111.1710`.

[49] A. Bazavov et al. “Equation of state in (2+1)-flavor QCD”. *Phys. Rev.* D90 (2014), p. 094503. arXiv: `1407.6387`.

[50] K. Fukushima and T. Hatsuda. “The phase diagram of dense QCD”. *Rept. Prog. Phys.* 74 (2011), p. 014001. arXiv: `1005.4814`.

[51] H. Suganuma, T. M. Doi, K. Redlich, and C. Sasaki. “Relating Quark Confinement and Chiral Symmetry Breaking in QCD”. *J. Phys.* G44 (2017), p. 124001. arXiv: `1709.05981`.

[52] S. Digal, E. Laermann, and H. Satz. “Interplay between chiral transition and deconfinement”. *Nucl. Phys.* A702 (2002), pp. 159–163.

[53] B. B. Brandt et al. “On the strength of the $U_A(1)$ anomaly at the chiral phase transition in $N_f = 2$ QCD”. *Journal of High Energy Physics* 2016.12 (Dec. 2016), p. 158.

[54] H. T. Ding et al. “Chiral phase transition of (2+1)-flavor QCD”. *27th International Conference on Ultrarelativistic Nucleus-Nucleus Collisions (Quark Matter 2018) Venice, Italy, May 14-19, 2018*. 2018. arXiv: `1807.05727`.

[55] G. Endrodi and L. Gonglach. “Chiral transition via the Banks-Casher relation”. *36th International Symposium on Lattice Field Theory (Lattice 2018) East Lansing, MI, United States, July 22-28, 2018*. 2018. arXiv: `1810.09173`.

[56] F. Burger et al. “Thermal QCD transition with two flavors of twisted mass fermions”. *Phys. Rev.* D87.7 (2013), p. 074508. arXiv: `1102.4530`.

[57] J. S. Bell and R. Jackiw. “A PCAC puzzle: $\pi_0 \to \gamma\gamma$ in the σ-model”. *Il Nuovo Cimento A (1965-1970)* 60.1 (Mar. 1969), pp. 47–61.

[58] S. L. Adler. “Axial-Vector Vertex in Spinor Electrodynamics”. *Phys. Rev.* 177 (5 Jan. 1969), pp. 2426–2438.

[59] J. J. Binney, N. J. Dowrick, A. J. Fisher, and M. Newman. *The theory of critical phenomena: an introduction to the renormalization group*. Oxford University Press, Inc., 1992.

[60] P. Steinbrecher. “The QCD crossover at zero and non-zero baryon densities from Lattice QCD” (2018). arXiv: `1807.05607`.

[61] F. Burger et al. “Thermal QCD transition with two flavors of twisted mass fermions”. *Phys. Rev.* D87.7 (2013), p. 074508. arXiv: `1102.4530`.

[62] F. Cuteri, O. Philipsen, and A. Sciarra. “Progress on the nature of the QCD thermal transition as a function of quark flavors and masses”. *36th International Symposium on Lattice Field Theory (Lattice 2018) East Lansing, MI, United States, July 22-28, 2018*. 2018. arXiv: `1811.03840`.

[63] H. T. Ding et al. “Chiral phase transition of (2+1)-flavor QCD”. *27th International Conference on Ultrarelativistic Nucleus-Nucleus Collisions (Quark Matter 2018) Venice, Italy, May 14-19, 2018*. 2018. arXiv: `1807.05727`.

[64] O. Philipsen and C. Pinke. “$N_f = 2$ QCD chiral phase transition with Wilson fermions at zero and imaginary chemical potential”. *Phys. Rev. D* 93 (11 June 2016), p. 114507.

[65] P. de Forcrand and O. Philipsen. “Constraining the QCD Phase Diagram by Tricritical Lines at Imaginary Chemical Potential”. *Phys. Rev. Lett.* 105 (15 Oct. 2010), p. 152001.

[66] C. Czaban et al. “Roberge-Weiss transition in $N_f = 2$ QCD with Wilson fermions and $N_\tau = 6$”. *Phys. Rev. D* 93 (5 Mar. 2016), p. 054507.

[67] L. G. Yaffe and B. Svetitsky. “First-order phase transition in the SU(3) gauge theory at finite temperature”. *Phys. Rev. D* 26 (4 Aug. 1982), pp. 963–965.

[68] R. D. Pisarski and F. Wilczek. “Remarks on the chiral phase transition in chromodynamics”. *Phys. Rev. D* 29 (2 Jan. 1984), pp. 338–341.

[69] A. Butti, A. Pelissetto, and E. Vicari. “On the nature of the finite temperature transition in QCD”. *JHEP* 08 (2003), p. 029. arXiv: `hep-ph/0307036`.

[70] A. Pelissetto and E. Vicari. “Relevance of the axial anomaly at the finite-temperature chiral transition in QCD”. *Phys. Rev.* D88.10 (2013), p. 105018. arXiv: `1309.5446`.

[71] S. Aoki. “Axial U(1) symmetry in the chiral symmetric phase of 2-flavor QCD at finite temperature”. *PoS* CD15 (2016), p. 045. arXiv: `1603.00997`.

[72] S. Aoki, H. Fukaya, and Y. Taniguchi. “1st or 2nd the order of finite temperature phase transition of $N_f = 2$ QCD from effective theory analysis”. *PoS* LATTICE2013 (2014), p. 139. arXiv: `1312.1417`.

[73] H. B. Nielsen and M. Ninomiya. “Absence of Neutrinos on a Lattice. 1. Proof by Homotopy Theory”. *Nucl. Phys.* B185 (1981). [,533(1980)], p. 20.

[74] R. Narayanan and H. Neuberger. “Chiral fermions on the lattice”. *Phys. Rev. Lett.* 71.20 (1993), p. 3251. arXiv: `hep-lat/9308011`.

[75] H. Neuberger. “Exactly massless quarks on the lattice”. *Phys. Lett.* B417 (1998), pp. 141–144. arXiv: `hep-lat/9707022`.

[76] D. B. Kaplan. “A Method for simulating chiral fermions on the lattice”. *Phys. Lett.* B288 (1992), pp. 342–347. arXiv: `hep-lat/9206013`.

[77] R. Narayanan and H. Neuberger. “Infinitely many regulator fields for chiral fermions”. *Phys. Lett.* B302 (1993), pp. 62–69. arXiv: `hep-lat/9212019`.

[78] Y. Shamir. “New domain wall fermion actions”. *Phys. Rev.* D62 (2000), p. 054513. arXiv: `hep-lat/0003024`.

[79] M. Cheng. “Equation of State for physical quark masses”. *Phys. Rev.* D81 (2010), p. 054504. arXiv: `0911.2215`.

[80] A. Bazavov. “Equation of state and QCD transition at finite temperature”. *Phys. Rev.* D80 (2009), p. 014504. arXiv: `0903.4379`.

[81] J. E. Cavanaugh. “Unifying the derivations for the Akaike and corrected Akaike information criteria”. *Statistics & Probability Letters* 33.2 (1997), pp. 201–208.

[82] M. Cheng et al. “Meson screening masses from lattice QCD with two light and the strange quark”. *Eur. Phys. J.* C71 (2011), p. 1564. arXiv: `1010.1216`.

[83] H.-T. Ding et al. “Charmonium properties in hot quenched lattice QCD”. *Phys. Rev. D* 86 (1 July 2012), p. 014509.

[84] Z. Fodor and C. Hoelbling. “Light Hadron Masses from Lattice QCD”. *Rev. Mod. Phys.* 84 (2012), p. 449. arXiv: `1203.4789`.

[85] Y. Saad. *Iterative Methods for Sparse Linear Systems: Second Edition*. Other Titles in Applied Mathematics. Society for Industrial and Applied Mathematics (SIAM, 3600 Market Street, Floor 6, Philadelphia, PA 19104), 2003.

[86] P. Chakraborty, M. Mustafa, and M. H. Thoma. “Quark Number Susceptibility, Thermodynamic Sum Rule, and Hard Thermal Loop Approximation”. *Physical Review D* 68 (Mar. 2003).

[87] W. Florkowski and B. L. Friman. “Spatial dependence of meson correlation functions at high temperature”. *Zeitschrift für Physik A Hadrons and Nuclei* 347.4 (Dec. 1994), pp. 271–276.

[88] W. Florkowski and B. L. Friman. “Spatial dependence of meson correlation functions at high temperature”. *Zeitschrift für Physik A Hadrons and Nuclei* 347.4 (Dec. 1994), pp. 271–276.

[89] M. F. Golterman. “Irreducible representations of the staggered fermion symmetry group”. *Nuclear Physics B* 278.2 (1986), pp. 417–435.

[90] M. F. Golterman. “Staggered mesons”. *Nuclear Physics B* 273.3 (1986), pp. 663–676.

[91] M. F. Golterman and J. Smit. “Self-energy and flavor interpretation of staggered fermions”. *Nuclear Physics B* 245 (1984), pp. 61–88.

[92] R. Altmeyer et al. “The hadron spectrum in QCD with dynamical staggered fermions”. *Nuclear Physics B* 389.2 (1993), pp. 445–510.

[93] E. Laermann and F. Pucci. “Taste symmetry breaking at finite temperature”. *Eur. Phys. J.* C72 (2012), p. 2200. arXiv: `1207.6615`.

[94] R. Gupta, G. Guralnik, G. W. Kilcup, and S. R. Sharpe. “Quenched spectrum with staggered fermions”. *Phys. Rev. D* 43 (6 Mar. 1991), pp. 2003–2026.

[95] C. Bernard, C. E. DeTar, Z. Fu, and S. Prelovsek. “Scalar meson spectroscopy with lattice staggered fermions”. *Phys. Rev.* D76 (2007), p. 094504. arXiv: `0707.2402`.

[96] M. Lüscher, S. Sint, R. Sommer, and H. Wittig. “Non-perturbative determination of the axial current normalization constant in $O(a)$ improved lattice QCD”. *Nuclear Physics B* 491.1 (1997), pp. 344–361.

[97] A. Skouroupathis and H. Panagopoulos. “Two-loop renormalization of scalar and pseudoscalar fermion bilinears on the lattice”. *Phys. Rev.* D76 (2007). [Erratum: Phys. Rev.D78,119901(2008)], p. 094514. arXiv: `0707.2906`.

[98] G. P. Lepage and P. B. Mackenzie. “On the viability of lattice perturbation theory”. *Phys. Rev.* D48 (1993), pp. 2250–2264. arXiv: `hep-lat/9209022`.

[99] S. Sint and P. Weisz. “Further results on O(a) improved lattice QCD to one loop order of perturbation theory”. *Nucl. Phys.* B502 (1997), pp. 251–268. arXiv: `hep-lat/9704001`.

[100] M. Gockeler et al. “Perturbative and Nonperturbative Renormalization in Lattice QCD”. *Phys. Rev.* D82 (2010). [Erratum: Phys. Rev.D86,099903(2012)], p. 114511. arXiv: `1003.5756`.

[101] A. Athenodorou, H. Panagopoulos, and A. Tsapalis. “The Lattice Free Energy of QCD with Clover Fermions, up to Three-Loops”. *Phys. Lett.* B659 (2008), pp. 252–259. arXiv: `0710.3856`.

[102] T. R. Klassen. “The (Lattice) QCD potential and coupling: How to accurately interpolate between multiloop QCD and the string picture”. *Phys. Rev.* D51 (1995), pp. 5130–5152. arXiv: `hep-lat/9408016`.

[103] S. A. Larin. “The Renormalization of the axial anomaly in dimensional regularization”. *Phys. Lett.* B303 (1993), pp. 113–118. arXiv: `hep-ph/9302240`.

[104] H. B. Meyer. “Transport Properties of the Quark-Gluon Plasma: A Lattice QCD Perspective”. *Eur. Phys. J.* A47 (2011), p. 86. arXiv: `1104.3708`.

[105] A. Francis. “Thermal dilepton rates from quenched lattice QCD : a study of thermal spectral functions in the continuum limit of quenched lattice QCD, at vanishing and finite momentum”. PhD thesis. 2011.

[106] G. D. Moore and D. Teaney. “How much do heavy quarks thermalize in a heavy ion collision?” *Phys.Rev.* C71 (2005), p. 064904. arXiv: `hep-ph/0412346`.

[107] P. Petreczky and D. Teaney. “Heavy quark diffusion from the lattice”. *Phys. Rev.* D73 (2006), p. 014508. arXiv: `hep-ph/0507318`.

[108] G. Aarts and J. M. Martinez Resco. “Continuum and lattice meson spectral functions at nonzero momentum and high temperature”. *Nucl. Phys.* B726 (2005), pp. 93–108. arXiv: `hep-lat/0507004`.

[109] H. Ding. “Charmonium correlation and spectral functions in quenched lattice QCD at finite temperature”. PhD thesis. 2010.

[110] Y. Burnier and A. Rothkopf. “Bayesian Approach to Spectral Function Reconstruction for Euclidean Quantum Field Theories”. *Phys. Rev. Lett.* 111 (18 Oct. 2013), p. 182003.

[111] M. Asakawa, T. Hatsuda, and Y. Nakahara. “Maximum entropy analysis of the spectral functions in lattice QCD”. *Prog. Part. Nucl. Phys.* 46 (2001), pp. 459–508. arXiv: `hep-lat/0011040`.

[112] G. Aarts et al. “Charmonium at high temperature in two-flavor QCD”. *Phys. Rev.* D76 (2007), p. 094513. arXiv: `0705.2198`.

[113] S. Fuchs, T. Pruschke, and M. Jarrell. “Analytic continuation of quantum Monte Carlo data by stochastic analytical inference”. *Phys. Rev. E* 81 (5 May 2010), p. 056701.

[114] K. S. D. Beach. “Identifying the maximum entropy method as a special limit of stochastic analytic continuation”. *arXiv e-prints*, cond-mat/0403055 (Mar. 2004), cond–mat/0403055. arXiv: `cond-mat/0403055`.

[115] A. S. Mishchenko, N. V. Prokof’ev, A. Sakamoto, and B. V. Svistunov. “Diagrammatic quantum Monte Carlo study of the Fröhlich polaron”. *Phys. Rev. B* 62 (10 Sept. 2000), pp. 6317–6336.

[116] H.-T. Ding et al. “Stochastic reconstructions of spectral functions: Application to lattice QCD”. *Phys. Rev.* D97.9 (2018), p. 094503. arXiv: `1712.03341`.

[117] G. Backus and F. Gilbert. “The Resolving Power of Gross Earth Data”. *Geophysical Journal International* 16.2 (1968), pp. 169–205.

[118] B. B. Brandt, A. Francis, B. Jäger, and H. B. Meyer. “Charge transport and vector meson dissociation across the thermal phase transition in lattice QCD with two light quark flavors”. *Phys. Rev. D* 93 (5 Mar. 2016), p. 054510.

[119] S. Caron-Huot. “Asymptotics of thermal spectral functions”. *Phys. Rev.* D79 (2009), p. 125009. arXiv: `0903.3958`.

[120] P. A. Baikov, K. G. Chetyrkin, and J. H. Kuhn. “Order $\alpha^4(s)$ QCD Corrections to Z and τ Decays”. *Phys. Rev. Lett.* 101 (2008), p. 012002. arXiv: `0801.1821`.

[121] Y. Burnier and M. Laine. “Towards flavour diffusion coefficient and electrical conductivity without ultraviolet contamination”. *Eur. Phys. J.* C72 (2012), p. 1902. arXiv: `1201.1994`.

[122] Y. Burnier, M. Laine, and M. Vepsalainen. “Heavy quarkonium in any channel in resummed hot QCD”. *JHEP* 01 (2008), p. 043. arXiv: `0711.1743`.

[123] M. Laine, O. Philipsen, P. Romatschke, and M. Tassler. “Real-time static potential in hot QCD”. *JHEP* 03 (2007), p. 054. arXiv: `hep-ph/0611300`.

[124] Y. Schröder. “The Static potential in QCD to two loops”. *Phys. Lett.* B447 (1999), pp. 321–326. arXiv: `hep-ph/9812205`.

[125] A. Bazavov et al. “In-medium modifications of open and hidden strange-charm mesons from spatial correlation functions”. *Phys. Rev.* D91.5 (2015), p. 054503. arXiv: `1411.3018`.

[126] M. Lüscher and U. Wolff. “How to calculate the elastic scattering matrix in two-dimensional quantum field theories by numerical simulation”. *Nuclear Physics B* 339.1 (1990), pp. 222–252.

[127] A. collaboration et al. “On the generalized eigenvalue method for energies and matrix elements in lattice field theory”. *Journal of High Energy Physics* 2009.04 (2009), p. 094.

[128] D. Guadagnoli, M. Papinutto, and S. Simula. “Extracting excited states from lattice QCD: the Roper resonance”. *Physics Letters B* 604.1 (2004), pp. 74–81.

[129] G. P. Lepage et al. “Constrained curve fitting”. *Nucl. Phys. Proc. Suppl.* 106 (2002), pp. 12–20. arXiv: `hep-lat/0110175`.

[130] Y. Chen et al. “The Sequential empirical bayes method: An Adaptive constrained-curve fitting algorithm for lattice QCD” (2004). arXiv: `hep-lat/0405001`.

[131] H. Akaike. “A new look at the statistical model identification”. *IEEE Transactions on Automatic Control* 19.6 (Dec. 1974), pp. 716–723.

[132] J. E. Cavanaugh. “Unifying the derivations for the Akaike and corrected Akaike information criteria”. *Statistics & Probability Letters* 33.2 (1997), pp. 201–208.

[133] S. Digal, P. Petreczky, and H. Satz. “Quarkonium feed down and sequential suppression”. *Phys. Rev.* D64 (2001), p. 094015. arXiv: `hep-ph/0106017`.

[134] F. Karsch, D. Kharzeev, and H. Satz. “Sequential charmonium dissociation”. *Phys. Lett.* B637 (2006), pp. 75–80. arXiv: `hep-ph/0512239`.

[135] P. Braun-Munzinger and J. Stachel. “On charm production near the phase boundary”. *Nucl. Phys.* A690 (2001), pp. 119–126. arXiv: `nucl-th/0012064`.

[136] L. Kluberg and H. Satz. “Color Deconfinement and Charmonium Production in Nuclear Collisions”. *Relativistic Heavy Ion Physics*. Ed. by R. Stock. 2010. arXiv: `0901.3831`.

[137] H.-T. Ding et al. “Charmonium dissociation and heavy quark transport in hot quenched lattice QCD”. *EPJ Web Conf.* 70 (2014), p. 00061. arXiv: `1210.0292`.

[138] H.-T. Ding, O. Kaczmarek, and F. Meyer. “Thermal dilepton rates and electrical conductivity of the QGP from the lattice”. *Phys. Rev.* D94.3 (2016), p. 034504. arXiv: `1604.06712`.

[139] H.-T. Ding et al. “Charmonium and bottomonium spectral functions in the vector channel”. *27th International Conference on Ultrarelativistic Nucleus-Nucleus Collisions (Quark Matter 2018) Venice, Italy, May 14-19, 2018*. 2018. arXiv: `1807.06315`.

[140] A. Frommer and P. Maass. “Fast CG-Based Methods for Tikhonov-Phillips Regularization”. *SIAM Journal on Scientific Computing* 20 (Feb. 1970).

[141] Y. Burnier and M. Laine. “Massive vector current correlator in thermal QCD”. *JHEP* 11 (2012), p. 086. arXiv: `1210.1064`.

[142] Y. Burnier, O. Kaczmarek, and A. Rothkopf. “Quarkonium at finite temperature: Towards realistic phenomenology from first principles”. *JHEP* 12 (2015), p. 101. arXiv: `1509.07366`.

[143] S. Kim, P. Petreczky, and A. Rothkopf. “Quarkonium in-medium properties from realistic lattice NRQCD”. *JHEP* 11 (2018), p. 088. arXiv: `1808.08781 [hep-lat]`.

[144] N. Brambilla, M. A. Escobedo, A. Vairo, and P. Vander Griend. “Transport coefficients from in medium quarkonium dynamics” (2019). arXiv: `1903.08063 [hep-ph]`.

[145] S. Borsanyi et al. “Charmonium spectral functions from 2+1 flavour lattice QCD”. *JHEP* 04 (2014), p. 132. arXiv: `1401.5940`.

[146] M. Laine and M. Vepsalainen. “Mesonic correlation lengths in high temperature QCD”. *JHEP* 02 (2004), p. 004. arXiv: `hep-ph/0311268`.

[147] C. W. Bernard et al. “The QCD spectrum with three quark flavors”. *Phys. Rev.* D64 (2001), p. 054506. arXiv: `hep-lat/0104002`.

[148] O. Kaczmarek, E. Laermann, and M. Müller. “The thermodynamic and the continuum limit of meson screening masses”. *PoS* LATTICE2013 (2014), p. 150. arXiv: `1311.3889`.

[149] S. Prelovsek. “Effects of staggered fermions and mixed actions on the scalar correlator”. *Phys. Rev.* D73 (2006), p. 014506. arXiv: `hep-lat/0510080`.

[150] M. Laine and Y. Schröder. “Two-loop QCD gauge coupling at high temperatures”. *JHEP* 03 (2005), p. 067. arXiv: `hep-ph/0503061`.

[151] D. Banerjee, R. V. Gavai, and S. Gupta. “Quasi-static probes of the QCD plasma”. *Phys. Rev.* D83 (2011), p. 074510. arXiv: `1102.4465 [hep-lat]`.

[152] A. Bazavov et al. “The chiral transition and $U(1)_A$ symmetry restoration from lattice QCD using Domain Wall Fermions”. *Phys. Rev.* D86 (2012), p. 094503. arXiv: `1205.3535 [hep-lat]`.

[153] L. Mazur, O. Kaczmarek, E. Laermann, and S. Sharma. “The fate of axial U(1) in 2+1 flavor QCD towards the chiral limit”. *PoS* LATTICE2018 (2018), p. 153. arXiv: `1811.08222`.

[154] A. Bazavov et al. “Chiral crossover in QCD at zero and non-zero chemical potentials” (2018). arXiv: `1812.08235`.

[155] H.-T. Ding et al. “The chiral phase transition temperature in (2+1)-flavor QCD” (2019). arXiv: `1903.04801`.

[156] K. Suzuki et al. “Axial $U(1)$ symmetry at high temperature in 2-flavor lattice QCD”. *EPJ Web Conf.* 175 (2018), p. 07025. arXiv: `1711.09239 [hep-lat]`.

[157] F. Pedregosa et al. “Scikit-learn: Machine Learning in Python ”. *Journal of Machine Learning Research* 12 (2011), pp. 2825–2830.

Danksagung

Als erstes möchte ich Edwin Laermann danken. Er war es, der mich in die Gittereichtheorie eingeführt hat. Edwin war immer freundlich, immer gutmütig und herzlich zu mir. Schon während meiner Bachelorarbeit hat er es geschafft, mich für die Hochenergiephysik und gerade auch für die Programmierung auf Superrechnern zu begeistern. Es steht außer Frage, dass ich ohne Edwin heute nicht dort wäre, wo ich bin. Es ist unglaublich schade und einfach nicht richtig, dass du so früh von uns gegangen bist.

Effektiv und am Ende auch offiziell als meinen Betreuer möchte ich Olaf Kaczmarek meinen Dank aussprechen. Die Kommunikation mit Olaf war immer auf Augenhöhe und äußerst angenehm. Auf magische Art und Weise hat Olaf immer Zeit, wenn es etwas zu besprechen gibt, ja scheint sich fast zu freuen mir zu helfen. Olaf war immer freundlich und auch persönlich waren die Gespräche immer sehr nett. Gleichzeitig hat es Olaf immer geschafft mich durch seine Anerkennung meiner Leistung weiter zu motivieren. Ich weiß aus vielen Gesprächen mit anderen Studenten, dass eine derart gute Betreuung nicht die Regel, sondern die absolute Ausnahme ist. Dafür möchte ich mich zutiefst bedanken!

Weiterhin möchte ich Frithjof Karsch für seine Unterstützung während meiner Dissertation danken. Auch mit Frithjof zusammen zu arbeiten war immer sehr angenehm und äußerst produktiv und es gibt nichts, was mich an dieser Zusammenarbeit stören würde.

Viel Dank gilt den anderen Mitgliedern unserer Arbeitsgruppe, insbesondere Anirban, Christian, Wolfgang, Hiroshi, Swagato, Patrick und Heng-Tong. Viele Diskussionen haben signifikant zur Vervollständigung dieser Arbeit beigetragen.

Sehr viel Dank geht an David und Simon für das Korrekturlesen dieser Arbeit.

Darüber hinaus möchte ich meinen Büro-Kollegen, das sind David, Lukas und Anna-Lena für die viele gemeinsame Zeit danken. Es war immer so, dass man gerne mit den anderen im Büro saß und sich einsam fühlte, wenn mal die anderen nicht da waren. Vielen Dank gilt auch der Biomolecular Photonics Gruppe für das gemeinsamen Mittag-Essen. Darüber hinaus danke ich Marc, Stephan, Daniel, Florian und meiner Familie für die angenehme Zeit neben der Dissertation.

Während der ganzen Zeit hatte ich immer Unterstützung von meiner Frau Alice, gerade auch in Zeiten, wo es mal nicht so lief. Sehr vielen Dank dafür.

Disclaimer

I hereby declare that the work done in this thesis is that of the author alone with the help of no more than the mentioned literature and auxiliary means.

Bielefeld, July 2, 2019

Hauke Sandmeyer

Gedruckt auf alterungsbeständigem Papier gemäß DIN ISO 9706.